

Utah State University

DigitalCommons@USU

All Graduate Theses and Dissertations

Graduate Studies

5-2012

Raman Microspectroscopy, Atomic Force Microscopy, and Electric Cell-Substrate Impedance Sensing For Characterization of Bio-Interfaces: Molecular, Bacteria, and Mammalian Cells

Gerald Dustin McEwen
Utah State University

Follow this and additional works at: <https://digitalcommons.usu.edu/etd>

 Part of the [Engineering Commons](#)

Recommended Citation

McEwen, Gerald Dustin, "Raman Microspectroscopy, Atomic Force Microscopy, and Electric Cell-Substrate Impedance Sensing For Characterization of Bio-Interfaces: Molecular, Bacteria, and Mammalian Cells" (2012). *All Graduate Theses and Dissertations*. 1251.

<https://digitalcommons.usu.edu/etd/1251>

This Dissertation is brought to you for free and open access by the Graduate Studies at DigitalCommons@USU. It has been accepted for inclusion in All Graduate Theses and Dissertations by an authorized administrator of DigitalCommons@USU. For more information, please contact digitalcommons@usu.edu.



RAMAN MICROSPECTROSCOPY, ATOMIC FORCE MICROSCOPY, AND ELECTRIC
CELL-SUBSTRATE IMPEDANCE SENSING FOR CHARACTERIZATION OF BIO-
INTERFACES: MOLECULAR, BACTERIA, AND MAMMALIAN CELLS

by

Gerald Dustin McEwen

A dissertation submitted in partial fulfillment
of the requirements for the degree

of

DOCTOR OF PHILOSOPHY

in

Biological Engineering

Approved:

Anhong Zhou, Ph.D.
Major Professor

Ronald C. Sims, Ph.D.
Committee Member

Timothy A. Gilbertson, Ph.D.
Committee Member

Charles D. Miller, Ph.D.
Committee Member

Lisa M. Berreau, Ph.D.
Committee Member

Mark R. McLellan, Ph.D.
Vice President for Research and
Dean of the School of Graduate Studies

UTAH STATE UNIVERSITY
Logan, Utah

2012

Copyright © Gerald Dustin McEwen 2012

All Rights Reserved

ABSTRACT

Raman Microspectroscopy, Atomic Force Microscopy, and Electric Cell-substrate

Impedance Sensing for Characterization of Bio-Interfaces:

Molecular, Bacteria, and Mammalian Cells

by

Gerald D. McEwen, Doctor of Philosophy

Utah State University, 2012

Major Professor: Dr. Anhong Zhou
Department: Biological Engineering

A fundamental understanding of bio-interfaces will facilitate improvement in the design and application of biomaterials that can beneficially interact with biological objects such as nucleic acids, molecules, bacteria, and mammalian cells. Currently, there exist analytical instruments to investigate material properties and report information on electrical, chemical, physical, and mechanical natures of biomaterials and biological samples. The overall goal of this research was to utilize advanced spectroscopy techniques coupled with data mining to elucidate specific characteristic properties for biological objects and how these properties imply interaction with environmental biomaterials.

My studies of interfacial electron transfer (ET) of DNA-modified gold electrodes aided in understanding that DNA surface density is related to the step-wise order of which a self-assembled monolayer is created on a gold substrate. Further surface modification plays a role in surface conductivity, and I found that electro-oxidation of the

DNA involved the oxidation of guanine and adenine nucleotides. Scanning tunneling microscopy (STM) was used to create topography and current images of the SAM surfaces. I also used Raman microspectroscopy (RM) to obtain spectra and spectral maps of DNA-modified gold surfaces.

For studies of bacteria, atomic force microscopy (AFM) and scanning electron microscopy (SEM) images showed similar morphological features of Gram-positive and Gram-negative bacteria. Direct classical least squares (DCLS) analysis aided to distinguish co-cultured strains. Fourier transform infrared (FTIR) spectroscopy proved insightful for characteristic bands for Gram-positive bacteria and a combined AFM/RM image revealed a relationship between culture height/density and peak Raman intensity.

In our mammalian cell studies we focused on human lung adenocarcinoma epithelial cells (A549), metastatic human breast carcinoma cells MDA-MB-435 (435), and non-metastatic MDA-MB-435/BRMS1 (435/BRMS1). RM revealed similarities between metastatic 435 and non-metastatic 435/BRMS1 cells compared to epithelial A549 cells. AFM showed increases in biomechanical properties for 435/BRMS1 in the areas of cell adhesion, cell spring constant, and Young's modulus. Fluorescent staining illustrates F-actin rearrangement for 435 and 435/BRMS1. Electric cell-substrate impedance sensing (ECIS) revealed that 435 cells adhere tightly to substrata and migrate rapidly compared with 435/BRMS1. For ECIS, ≤ 10 -fold diesel exhaust particles (DEP) concentration exposure caused clastogenic DNA degradation whereas ≥ 25 -fold DEP exposure caused cytotoxic results. Resveratrol (RES) at 10 μM showed minimal to mild protection against DEP before and after exposure and aided in improving injury recovery.

PUBLIC ABSTRACT

Raman Microspectroscopy, Atomic Force Microscopy, and Electric Cell-substrate
Impedance Sensing for Characterization of Bio-Interfaces:
Molecular, Bacteria, and Mammalian Cells

Gerald D. McEwen

Understanding bio-interfaces will help improve the design and application of biomaterials that can interact with biological objects like nucleic acids, molecules, bacteria, and mammalian cells. Currently, there exist instruments to investigate material properties for the electrical, chemical, physical, and mechanical nature of biomaterials or biological samples. Our goal is to use advanced spectroscopic methods and data analysis to find specific properties of biological objects and see how these properties show the biological object's response to their environment.

My studies of interfacial electron transfer (ET) of DNA coated gold electrodes aided to understand that the density of DNA on the surface is related to the order at which it is added during surface coating. Furthermore, surface coating affects the conductivity of the electrode and I found that guanine and adenine are destroyed through current induced oxidation. Scanning tunneling microscopy (STM) was used to see the height of surface coatings and verify decreased conductivity. I also used Raman microspectroscopy (RM) to obtain Raman peaks and spectral images of DNA coated on the gold surfaces.

For bacteria studies atomic force microscopy (AFM) and scanning electron microscopy (SEM) images showed visually similar features of Gram-positive and Gram-

negative bacteria. Data analysis aided to visually separate mixed strains of bacteria and Fourier transform infrared (FTIR) spectroscopy showed specific peaks for Gram-positive bacteria. A combined AFM/RM image showed that there was a relationship between the sample height and the Raman peak intensity.

For mammalian cell studies, RM revealed similarities between two types of breast cancer cell lines. AFM showed increases in biomechanical properties for breast cancer cells that do not metastasize versus those that spread. Fluorescent staining illustrates breast cancer cell physical arrangement of the cytoplasm. Electric cell-substrate impedance sensing (ECIS) revealed that breast cancer cells which do not metastasize, grow more slowly compared to those that do metastasize, and do not spread when wounded (i.e. surgically removed). It was found that for ECIS, diesel exhaust particles (DEP) concentration caused lung cells to either mutate or rapidly die. Resveratrol (RES) showed some protection against DEP before and after exposure and aided in improving injury recovery of airway epithelial cells.

DEDICATION

I would like to dedicate this work to my wife and children. To my wife, Amber, thank you for your support and patience (I do not take either for granted!). Graduate school brought trials and sacrifices that tested every facet of our relationship and ultimately made us stronger. I have to be the luckiest man alive to have you at my side. To say you are a remarkable woman does not begin to sum up my indebtedness to you!

To my three sons: Jonathon, Timothy, and Peter – you made innumerable sacrifices in your young lives and I hope that my success will be the foundation for your successes in life. My eldest son, Jonathon, you were just four months old when I began the graduate program at Utah State University. Just like you, curious and thriving to learn, I had no idea of what lie ahead for either myself or my family. Life has a way of teaching lessons that are crafted specifically for us and graduate school was a succession of life lessons. My second son, Timmy, you came along in the second year of graduate school, probably the most trying time our family has ever faced, and definitely the most fragile time in your young life. I am grateful, to this day, that you are here with our family. My youngest, Peter, you were born in the fourth year of graduate school. At this point my tenure as a graduate student was slowly winding down.

Looking back on the journey, I want to thank each of you for your love, support, and all the good memories. This time does not end with my completing a degree; it now closes a season filled with trials, family growth, and precious miracles.

ACKNOWLEDGMENTS

I would like to acknowledge all those who have made possible the completion of this doctoral program. First and foremost I would like to thank my major advisor, Dr. Anhong Zhou, whose tutelage and guidance have proven both invaluable and inspiring. He has taught me to push myself and has encouraged me to continuously seek new insights from existing knowledge. With his mentorship and patience, I have grown as a scientist; moreover, I have learned about my true nature as a person and, for this, I am deeply indebted to this dear friend.

My sincere appreciation goes to Dr. Ron Sims for advice, correction, and encouragement. You always warmly encouraged discipline, helped me to see my flaws, and then, incredibly, made me feel better about having mistakes to correct in the first place. Thanks to my other committee members, Drs. Tim Gilbertson, Charlie Miller, and Lisa Berreau, for your advice and assistance through this entire process.

Next, I want to thank the myriad of undergraduate and graduate students that I have worked with at USU. I am also grateful for Dr. Yangzhe Wu, Dr. Dane Hansen, Tian Yu, Qian Chen, and Mingjie Tang. Also special thanks to Dr. Richard Bormett and Dr. Zhenhaun Chi from Renishaw Co.; Dr. Charles Keese, Dr. David Biggs, Ms. Catherine Toniatti from Applied BioPhysics Co.; and Mr. Juan Ciorciari from Thermo Fisher Scientific Co., for your training and support. Especially students and staff in the Zhou, Gilbertson, and DeWald labs, you have all been amazing – Thank you!

Also, I need to specifically acknowledge entities and individuals who made the work possible: the Utah Water Research Laboratory (UWRL), Utah Water Initiative funds, USU New Faculty Research Initiative, Huntsman Environmental Research Center

(Logan, UT), with partial support by National Institute of Health (#ES013688-01A1), and Department of Defense DURIP grant (#W911NF-06-01-0139). I am also grateful for the USU Presidential Graduate Fellowship, the USU Center for Integrated Biosystems Graduate Research Support Program (CIB-R) for their support, and the USU School of Graduate Studies for the Dissertation Fellowship. Dr. Daniel Costa and Dr. Ian Gilmour from the U.S. EPA National Health and Environmental Effects Research Laboratory (NEERL) contributed diesel exhaust particles (DEP) for these studies. I appreciate Dr. Daryll B. DeWald and Dr. Tim A. Gilbertson from Utah State University Department of Biology for aid in funding the rental of the ECIS workstation. I need to thank my colleagues in the new product development (NPD) group at Thermo Fisher Scientific (TFS) for all of their encouragement and support in completing the written portion of my dissertation, my defense, and subsequent revisions of my dissertation.

I thank all my friends, the Biological Engineering (BE) department faculty and staff, and my Grandma Marilyn Veater, parents, brothers and sister, and extended family for all of their support during my academic life and education. Finally, and most importantly, thank you Heavenly Father and Jesus Christ for your guidance and unconditional love.

Gerald D. McEwen

CONTENTS

	Page
ABSTRACT	iii
PUBLIC ABSTRACT	v
DEDICATION	vii
ACKNOWLEDGMENTS	viii
LIST OF TABLES	xvi
LIST OF FIGURES	xix
NOMENCLATURE	xxxvii
 CHAPTER	
1 INTRODUCTION	1
1.1 Rationale for proposed research.....	1
1.2 Background.....	1
1.3 Electrochemical sensing.....	2
1.4 Raman microspectroscopy	3
1.5 Atomic force microscopy.....	7
1.6 Electric cell-substrate impedance sensing	10
1.6.1 Diesel exhaust particles.....	14
1.6.2 Resveratrol	15
1.7 Dissertation outline	16
1.8 References.....	18
2 IMMOBILIZATION, HYBRIDIZATION, AND OXIDATION OF SYNTHETIC DNA ON GOLD SURFACE: ELECTRON TRANSFER INVESTIGATED BY ELECTROCHEMISTRY AND SCANNING TUNNELING MICROSCOPY AND RAMAN MICROSPECTROSCOPY	23
2.1 Abstract.....	23
2.2 Introduction.....	24
2.3 Materials and Methods.....	27

		xi
2.3.1	Chemicals and reagents.....	27
2.3.2	Surface treatment of gold electrode	27
2.3.3	DNA modification of gold electrode surface.....	28
2.3.4	Electrochemical measurements.....	30
2.3.5	Scanning tunneling microscopy	31
2.3.6	Electron transfer characterization by CV and EIS.....	31
2.3.7	Raman microspectroscopy	34
2.4	Results.....	35
2.4.1	STM image of DNA immobilized on Au (111).....	35
2.4.2	Electron transfer behaviors of the Hoechst/t-DNA/MCH/ss-DNA modified electrode surface	37
2.4.3	Electron transfer behaviors of the Hoechst/CV oxidation/Hoechst/MCH/dsS-DNA modified electrode surface.....	45
2.4.4	Hoechst interactions with ss-DNA, hybridized ds-DNA, dsS-DNA, and oxidatively damaged dsS-DNA.....	51
2.4.5	Comparison of current vs. time curves of DNA oxidations on electrode surfaces with different modifications.....	53
2.4.6	STM imaging of electro-oxidation of DNA modified gold surface.....	57
2.5	Raman microspectroscopy	62
2.6	Conclusions.....	63
2.7	References.....	65
3	CHARACTERIZATION AND ANALYSIS OF GRAM-POSITIVE AND GRAM-NEGATIVE BACTERIA AND CO-CULTURE MIXTURES BY RAMAN MICROSPECTROSCOPY, FOURIER TRANSFORM INFRARED SPECTROSCOPY, AND ATOMIC FORCE MICROSCOPY.....	68
3.1	Abstract.....	68
3.2	Introduction.....	69
3.3	Methods and materials	71
3.3.1	Bacterial culture	71
3.3.2	Morphology observations via Atomic Force Microscopy (AFM) and Scanning Electron Microscopy (SEM).....	72
3.3.3	Raman microspectroscopy	72
3.3.4	Fourier transform infrared spectroscopy.....	73

		xii
	3.3.5	Coupled AFM/Raman microspectroscopy.....73
	3.3.6	Gram staining.....74
	3.3.7	DCLS analysis of Raman spectra and spectral image74
3.4		Results and Discussion76
	3.4.1	Morphological observation of bacterial cells under AFM and SEM.....76
	3.4.2	Raman microspectroscopy characterization of Gram- positive and Gram-negative bacteria76
	3.4.3	DCLS analysis of <i>P. putida</i> KT244085
	3.4.4	Interaction analysis of mixture of <i>Mycobacteria MCS</i> with <i>Pseudomonas putida</i> KT 2440.....86
	3.4.5	Fourier transform infrared spectroscopy (FTIR)88
	3.4.6	Combined AFM/Raman microspectroscopy of mycobacterium.....92
3.5		Conclusions.....92
3.6		References.....94
4		SUBCELLULAR SPECTROSCOPIC MARKERS, TOPOGRAPHY AND NANOMECHANICS OF HUMAN LUNG CANCER AND BREAST CANCER CELLS EXAMINED BY COMBINED RAMAN MICROSPECTROSCOPY AND ATOMIC FORCE MICROSCOPY97
	4.1	Abstract.....97
	4.2	Introduction.....98
	4.2.1	Breast cancer metastasis suppressor 1 (BRMS1) gene.....98
	4.2.2	Raman microspectroscopy99
	4.2.3	Atomic force microscopy.....100
	4.3	Materials and Methods.....101
	4.3.1	Preparation of human breast cancer cell line 435 and 435/BRMS1 and human lung adenocarcinoma cell A549.....101
	4.3.2	Raman microspectroscopy102
	4.3.3	Chemometric analysis of Raman spectra and spectral images103
	4.3.4	Atomic force microscopy.....104
4.4		Results.....106

4.4.1	Raman spectral analysis - Biochemical markers of three cell lines	106
4.4.2	Raman spectral image analysis – Biochemical markers of three cell lines	113
4.4.3	AFM observation of cell membrane nanostructure	116
4.4.4	Measurements of nanomechanical properties of cancer cell lines	117
4.5	Discussion	119
4.5.1	Raman spectral analysis – Biochemical markers of three cell lines	119
4.5.2	Raman spectral image analysis – Biochemical markers of three cell lines	123
4.5.3	Measurement of nanomechanical properties of cancer cell lines	125
4.6	Conclusions	126
4.7	References	127
5	BRMS1 EXPRESSION ALTERS THE ULTRASTRUCTURAL, BIOMECHANICAL AND BIOCHEMICAL PROPERTIES OF MDA-MB-435 HUMAN BREAST CARCINOMA CELLS: AN INSTRUMENTAL APPROACH TO STUDY CANCER CELLS	131
5.1	Abstract	131
5.2	Introduction	132
5.3	Materials and methods	135
5.3.1	Preparation of breast cancer cell line 435 and 435/BRMS1	135
5.3.2	Atomic force microscopy	136
5.3.3	Raman microspectroscopy	138
5.3.4	Electric cell-substrate impedance sensing	139
5.3.5	Immuno-fluorescent staining for F-actin localization in 435 and 435/BRMS1 cells.	139
5.4	Results	140
5.4.1	Topography and ultrastructure of 435 and 435/BRMS1 cells	140
5.4.2	Homogeneity in adhesion behavior and elasticity of membrane surface	141
5.4.3	Biomechanics of 435 and 435/BRMS1 cells.	142

		xiv
	5.4.4 Cellular components of 435 and 435/BRMS1 cells.....	145
	5.4.5 435 and 435/BRMS1 wound healing and migration rate.....	150
	5.4.6. Immuno-fluorescent imaging for F-actin localization in 435 and 435/BRMS1 cells	152
	5.5 Discussion.....	155
	5.6 References.....	157
6	TOXIC EFFECTS OF DIESEL EXHAUST PARTICLES AND ANTI- OXIDANT PROTECTIVE ACTIVITIES ON HUMAN LUNG EPITHELIAL CELLS: ENHANCED STUDIES USING ELECTRIC- CELL SUBSTRATE IMPEDANCE SENSING AND RAMAN MICROSPECTROSCOPY	163
	6.1 Abstract.....	163
	6.2 Introduction.....	164
	6.3 Electric cell-substrate impedance sensing	164
	6.4 Material and Methods	168
	6.4.1 Chemicals.....	168
	6.4.2 Cell culture.....	168
	6.4.3 Electric cell-substrate impedance sensing	169
	6.4.4 Cell viability staining.....	169
	6.4.5 Raman microspectroscopy	170
	6.4.6 Raman data processing	170
	6.5 Results and Discussion	171
	6.5.1 Approach #1 – Sequential array modification	172
	6.5.2 Approach #2 – Simultaneous array modification	198
	6.6 Raman Microspectroscopy.....	207
	6.6.1 Raman spectra and light images of DEP exposure A549 with and without resveratrol protection	207
	6.6.2 Hierarchical Cluster Analysis of DEP exposed A549 with and without resveratrol protection	209
	6.7 Conclusion	217
	6.8 References.....	218
7	SUMMARY AND FUTURE DIRECTIONS.....	221
	7.1 Summary.....	221

	xv
7.2 Future Work	223
7.2.1 Raman outlook	223
7.2.2 Electric cell-substrate impedance sensing outlook	225
7.2.3 Traditional biology methods to validate EC, RM, AFM, and ECIS	226
APPENDICES	228
APPENDIX A	229
APPENDIX B	256
APPENDIX C	266
APPENDIX D	268
CURRICULUM VITAE	281

LIST OF TABLES

Table	Page
2.1. Diffusion coefficients (D_0) for successive modifications on bare gold by ss-DNA, MCH, t-DNA, and Hoechst binding	40
2.2. Diffusion coefficients (D_0) for successive modifications on bare gold by ss-DNA, MCH, t-DNA, and Hoechst binding	44
2.3. Diffusion coefficients (D_0) for successive modifications on bare gold by dsS-DNA, MCH, Hoechst, CV oxidation, and Hoechst binding	48
2.4. Oxidation/Reduction charges for cyclic voltammetric oxidations of different modified gold electrodes	57
3.1. Tentative peak assignments of Gram-positive and Gram-negative bacteria	80
3.2. Assignment of functional groups associated with major vibration bands in IR spectra of bacteria	90
4.1. Tentative Raman band assignments for human lung adenocarcinoma epithelial cell (A549) and human metastatic (435) and non-metastatic (435/BRMS1) breast carcinoma cells	109
6.1. Sectional overview for the ECIS experimental setup	171
6.2. Array seeding density and treatment for array A and B in Figure 6.2	172
6.3. Array seeding density and treatment for array A and B in Figure 6.3	175
6.4. Array seeding density and treatment for array A and B in Figure 6.4	176
6.5. Array seeding density and treatment for array A and B in Figure 6.7	181
6.6. Array seeding density and treatment for array A and B in Figure 6.10	185

6.7.	Well seeding density and treatment for array A and B in Figure 6.13 and Figure 6.14.	190
6.8.	Array seeding density and treatment for array A and B in Figure 6.15 and Figure 6.16.	193
6.9.	Array seeding density and treatment for array A and B in Figure 6.19.....	198
6.10.	Array seeding density and treatment for array A and B in Figure 6.20.....	200
6.11.	Array seeding density and treatment for array A in Figure 6.21 and B in Figure 6.22.	202
6.12.	Array seeding density and treatment for array A in Figure 6.23 and B in Figure 6.24.	204
B2.5.	Measured EIS parameters for successive modifications on bare gold by dsS-DNA, MCH, Hoechst, CV oxidation, and Hoechst binding.	258
B2.6.	Diffusion coefficients (D_0) for successive modifications on bare gold by MCH, dsS-DNA, CV oxidation, and Hoechst binding.....	260
B2.7.	Measured EIS parameters for successive modifications on bare gold by MCH, dsS-DNA, CV oxidation, and Hoechst binding.....	261
B2.8.	The charges (μC) for individual electro-oxidation reactions on different modified gold electrodes.	264
D6.13.	Array seeding density and treatment for array A and B in Figure D6.32.....	268
D6.14.	Array seeding density and treatment for array A and B in Figure D6.34.....	270
D6.15.	Array seeding density and treatment for array A and B in Figure D6.35.....	271
D6.16.	Array seeding density and treatment for array A and B in Figure D6.38.....	273

D6.17.	Array seeding density and treatment for array A and B in Figure D6.39.....	275
D6.18.	Array seeding density and treatment for array A and B in Figure D6.40.....	276

LIST OF FIGURES

Figure	Page
1.1.	A schematic overview of the instrumentation used to study the bio-interfaces of molecules, bacteria, and mammalian cells.....2
1.2.	Schematic of DNA mediated electron transfer at the modified gold surface. DNA is indirectly probed by monitoring the reduction or oxidation reaction within the redox probe solution (0.5 mM $K_3Fe(CN)_6$ + 0.01 M PBS) at various scan rates. Hoechst 33258 is used to increase the conductivity of the double stranded DNA. The inset cyclic voltogram illustrates a typical reduction peak (A) and oxidation peak (B) of the semi-reversible reaction. [Image inspired from [2]]. MB = methylene blue and LB = leucomethylene blue, where LB goes on to reduce ferricyanide in solution.3
1.3.	A classical-simple representation of the energy states for the different forms of scatter. The shift in the Raman effect is due to the spacing between the vibrational energy states and the ground state (A). Inset illustrates a Raman profile of A549 mammalian cells (B). [Image adapted from [3]]4
1.4.	A schematic of the beam deflection system used in AFM (A) and a potential energy diagram of a probe and sample (B). Respective topographical image (C) and force map (D).8
1.5.	An 8W10E+ array containing >40 working electrodes (A), an 8W1E array with a single working electrode (B), ECIS time versus capacitance profile (C), and a simplified depiction of the ECIS model (D). Barrier resistance (R_b), current flow between the ventral side of the cell and the substratum (α), average capacitance of the cell plasma membrane (C_m), cell radius (r_c), and the average distance (h) between the electrode and the basal membrane of the cell. [image adapted from Applied BioPhysics, NY, USA].11
1.6.	ECIS time profiles for resistance (A) and capacitance (B). Cell to cell-free ratio for confluent cells measured at different frequencies for resistance (C) and capacitance (D). Surface response for resistance (E) and capacitance (F) at each frequency and with respect to time.13

1.7.	Chemical structure of resveratrol (3,5,4'-trihydroxystilbene) [Image courtesy of www.sigmaaldrich.com].....	16
2.1.	The sequential modification of the gold working electrode beginning with the bare Au substrate (1), addition of single strand-DNA (ss-DNA) (2), addition of 6-mercapto-1-hexanol (MCH) (3), hybridization with target-DNA (t-DNA) (4), binding Hoechst 33258 (5), and the cyclic voltammetric oxidation of the DNA modified on electrode surface (6).	29
2.2.	STM topography images of (A) bare Au (111) electrode (-0.5 V, 0.01 nA), (B) ss-DNA modified 13 hr (-0.5 V, 0.03 nA), (C) MCH modified 6 hr (-0.5 V, 0.01 nA), (D) ss-DNA 24 hr/MCH 6 hr (-0.5 V, 0.03 nA), (E) dsS-DNA 24 hr (-0.5 V, 0.05 nA), (F) dsS-DNA 24 hr/MCH 6 hr (-0.5 V, 0.05 nA), (G) MCH 6 hr/dsS-DNA 24 hr (-0.5 V, 0.05 nA). The numbers in parenthesis are the bias and tunneling current set points under which the images are collected. All coatings of DNA and MCH are conducted in 5 mM phosphate buffer. dsS-DNA is designated as the synthetic double strand DNA. Arrow in (E) indicate the DNA cluster structures and aggregates. The arrows in (G) show the rod-like structure.....	36
2.3.	Voltammetric behaviors of $\text{Fe}(\text{CN})_6^{3-/4-}$ redox couple (0.5 mM $\text{K}_3\text{Fe}(\text{CN})_6$ + 0.01 M PBS) on step-by-step ss-DNA modified electrodes. The data corresponds to electrode modifications: bare Au (1), ss-DNA/Au (2), MCH/ss-DNA/Au (3), t-DNA/MCH/ss-DNA/Au (4), and Hoechst/t-DNA/MCH/ss-DNA/Au (5) (all scans performed in 0.5 mM $\text{K}_3\text{Fe}(\text{CN})_6$ + 0.01 M PBS, pH 7.4; at scan rate 60 mV s^{-1}). Inset: Dependence of i_{pa} and i_{pc} on $v^{1/2}$, for scan rates; 0.005, 0.01, 0.02, 0.03, 0.04, 0.05, 0.06, 0.08, 0.1, 0.15, 0.2, 0.3, and 0.4 V s^{-1}	39
2.4.	Electrochemical impedance spectroscopy (EIS) of step-by-step ss-DNA modified electrodes: bare Au (1), ss-DNA/Au (2), MCH/ss-DNA/Au (3), t-DNA/MCH/ss-DNA/Au (4), and Hoechst/t-DNA/MCH/ss-DNA/Au (5). Inset: modified equivalent Randles circuit used to model impedance data; R_{Ω} , electrolyte resistance; Z_W , Warburg impedance; R_{ct} , charge-transfer resistance; and C_d , double-layer capacitance. The coating conditions are the same as Figure 2.3. EIS was conducted in 0.5 mM $\text{K}_3\text{Fe}(\text{CN})_6$ + 0.5 mM $\text{K}_4\text{Fe}(\text{CN})_6$ in 0.01 M PBS, pH 7.4 with 10 mV AC amplitude.....	41

- 2.5. Voltammetric behaviors of $\text{Fe}(\text{CN})_6^{3-/4-}$ redox couple (0.5 mM $\text{K}_3\text{Fe}(\text{CN})_6$ + 0.01 PBS) on step-by-step synthetic ds-DNA modified electrodes: bare Au (1), dsS-DNA/Au (2), MCH/dsS-DNA/Au (3), Hoechst/MCH/dsS-DNA/Au (4), Oxidation/Hoechst/MCH/dsS-DNA/Au (5), and Hoechst/Oxidation/Hoechst/MCH/dsS-DNA/Au (no data) (6). Inset: 5 mM Na_2HPO_4 + 5 mM NaH_2PO_4 between 0 - 1.3 V at 30 mV s^{-1}46
- 2.6. Voltammetric behaviors of modified electrodes between 0 V to 0.9 V in 100 μM Hoechst 33258 + 0.01 M PBS buffer: bare Au (1), ss-DNA for 1 hr (2), t-DNA and ss-DNA hybrid (3), dsS-DNA for 12 hrs (4), and oxidized dsS-DNA (5). Scan rate: 100 mV s^{-1} . Oxidation was conducted in 5 mM Na_2HPO_4 + 5 mM NaH_2PO_4 between 0 - 1.3 V at 30 mV s^{-1} for three cycles. All DNA concentrations are 1 μM49
- 2.7. Cyclic voltammograms (A) oxidation of dsS-DNA (pre-immobilized for 12 hours) in 5 mM Na_2HPO_4 + 5 mM NaH_2PO_4 solution between 0 - 1.3 V at 30 mV s^{-1} for three cycles; (B) continuous scanning of Hoechst bound dsS-DNA-modified gold electrode in 100 μM Hoechst 33258 + 0.01 M PBS, pH 7.4; scan rate 100 mV s^{-1} . The first scan in (B) is the same from curve 5 in Figure 2.6.51
- 2.8. Chemical structure of Hoechst 33258 in solution as used in this study. [Image courtesy of www.sigmaaldrich.com].53
- 2.9. STM topography (A) and current (B) images of Au (111) surface after being modified by dsS-DNA for 12 hrs, subsequently by voltammetric oxidation, and then binding with Hoechst 33258 for 5 min. scan area 100 \times 100 nm. The bring spot (black arrow) of the inset in topography image (A) corresponds to that spot (black arrow) of the inset in current image (B). Magnified in images are shown in topography image (C) and current image (D). Scan area 5.3 \times 5.3 nm. Cross section profiles (c1) and (c2) correspond to the green line and red line in (C), respectively. Similarly, (d1) and (d2) correspond to the green line and red line in (D), respectively. Voltammetric oxidation was conducted in 5 mM Na_2HPO_4 + 5 mM NaH_2PO_4 between 0 - 1.3 V at 30 mV s^{-1} for three cycles.59

2.10.	Current distributions obtained from STM current images for 24 hours dsS-DNA modified gold surface at different surface oxidation status with the following modification order: dsS-DNA modification, MCH modification, voltammetric oxidation, and binding with Hoechst 33258. Triplicate images are analyzed at each modification.....	61
2.11.	Bright field image of DNA modified Au (111) surface (A), Raman map with wavenumber center at 760.4 cm^{-1} (B), and typical Raman spectrum for nucleic acid bands (C). Image acquired by 50x objective, 100% laser power and 5 second exposure.....	63
3.1.	AFM deflection images of <i>M. JLS</i> (A), <i>M. KMS</i> (B), <i>M. MCS</i> (D), <i>E. Coli</i> (E), <i>P. putida</i> KT2440 (F), and SEM images of <i>M. KMS</i> (C), and <i>P. putida</i> KT2400 (G).....	77
3.2.	A typical schematic of the Gram-positive bacteria cell wall. Gram-positive bacteria lack an outer membrane and the associated lipopolysaccharide (LPS) that is present in Gram-negative organisms (Figure 3.5). In the Gram-positive bacteria cell wall, the peptidoglycan layer is thicker than the Gram-negative cell wall and contains teichoic acids (derived from ³¹).....	78
3.3.	Schematic of mycobacteria cell wall structure (derived from ^{37,38}).....	80
3.4.	Raman spectra of Gram-positive <i>M. JLS</i> , <i>M. KMS</i> , and <i>M. MCS</i> grown on LB agar.	81
3.5.	Schematic of Gram-negative bacteria cell wall with several layers of polysaccharides and glycoconjugates. The periplasmic space contains peptidoglycan and proteins. The outer leaflet of the outer membrane is rich in lipopolysaccharide (LPS) and (n) variable number of O-antigen repeats. With permission from ²⁵	82
3.6.	Raman spectra of Gram-negative bacteria; <i>E. coli</i> TOP 10, <i>E. coli</i> J4S, and <i>P. putida</i> KT2440 grown on agar.....	83

- 3.7. Raman mapping on the agar surface containing KT2440. Bright field image (A), the crosshair of the image indicates the actual spectra (B); DCLS spectral data fit to a spectrum of KT2440 (C) (blue curve); DCLS spectral data fit to a spectrum of *M. KMS* (D) (blue curve). The rainbow color image is a concentration distribution of KT2440 (E). Raman spectra of the four color regions (F). Red and yellow represents higher concentration and green and blue represents lower concentration.84
- 3.8. Raman spectral map of LB agar surface containing both *M. MCS* and *P. putida* KT2440. Bright field image (A), Raman spectral map of both co-cultured *M. MCS* and KT2440 (B). Individual Raman spectral maps of *M. MCS* (C) and KT2440 (D). DCLS spectral data fit to a spectrum of *M. MCS* (E, blue curve = reference, red curve = actual) and DCLS spectral data fit to a spectrum of KT2440 (F, blue curve = reference, red curve = actual).87
- 3.9. Representative IR absorbance spectra ($700 - 4000 \text{ cm}^{-1}$) of *M. KMS* on four different substrates: gold surface (A), multibounce ZnSe crystal (B), Orbit with a diamond crystal (C), and Ge ATR crystal (D).89
- 3.10. FTIR spectrum and mapping of *M. KMS* coated on gold surface. Bright field view (A), concentration heat map (B, red = high, blue = low), selected points with the heat map (C), and a 3D surface image of the heat map (D).90
- 3.11. Combined AFM/Raman measurement of *M. JLS* on gold coated mica (A) acquired in phase feedback mode in air. Raman spectral intensity map at 1154 cm^{-1} (B). Raman spectrum at crosshair on AFM image (C) acquired at 100% laser power with 1 second exposure and a center of 1040 cm^{-1} . Scale is = $30 \times 30 \mu\text{m}$. *M. JLS* was cultured Luria Broth (LB), concentrated by centrifugation at 2000 rpm for 2 minutes and spotted on the gold coated mica substrate and allowed to dry in air.93

- 4.1. Averaged Raman spectra for three cancer cell lines and background, respectively: A549 (A-black), 435 (B-red), 435/BRMS1 (C-blue), and background (D-magenta). For each cell line the Raman spectrum represent an average of five separate spectra and the background is an average of fifteen spectra. Spectra are offset vertically for clarity.....107
- 4.2. Mean Raman spectra of three cancer cell lines: A549 (A-black), 435 (B-red), and 435/BRMS1 (C-blue). Each spectrum is the average of five spectra, the averaged background was subtracted by finding a local minimum area, spectra were baseline corrected, and then normalized using peak intensity at 1450 cm^{-1} [32]. Spectra are offset vertically for clarity.....108
- 4.3. Difference spectra computed from the 1450 cm^{-1} normalized spectrum in Figure 4.2 using A549, 435, and 435/BRMS1: 435/BRMS1 – A549 (A), 435/BRMS1 – A549 (B), A549 – 435 (C).111
- 4.4. PCA score plot of pre-processed Raman spectra for each cell line. Each cancer cell line is coded by color and shape (435/BRMS1 - red star, 435 - green pentagram, and A549 - blue diamond)112
- 4.5. Dendrogram analysis based on PCA score values for the first six principal components. The data is color coded into three groups. By including six PCs, the dendrogram shows that the spectral data can be correctly categorized according to cancer cell line type.....113
- 4.6. Raman spectral images for relative biochemical distribution within single cells; A549, 435 and 435/BRMS1. White light images (A-C). Different biochemical components were identified by characteristic wavenumber as follows; DNA (D-F, red) – 720 cm^{-1} , carbohydrate (G-I, blue) – 940 cm^{-1} , protein (J-L, cyan) – 1006 cm^{-1} , and lipid (M-O, yellow) – 1095 cm^{-1} . Complete biochemical distribution overlays (P-R). Scale bar: $10\text{ }\mu\text{m}$ (horizontal), $5\text{ }\mu\text{m}$ (vertical).114
- 4.7. Single cell Raman spectral image maps for A549, 435, 435/BRMS1: first column (white image), 2nd column (PCA1 score image), 3rd column (PCA2 score image). The colors were scaled for better visualization and displaying purpose. Scale bar: $10\text{ }\mu\text{m}$ (horizontal), $5\text{ }\mu\text{m}$ (vertical).115

- 4.8. Topography and membrane surface nanostructures of A549, 435, and 435/BRMS1 acquired in PBS. The 1st column shows the topography images; 2nd column the respective deflection images, 3rd and 4th columns show the membrane surface nanostructures (roughness values marked) obtained at two different locations for each cell line. The 5th column presents the cross section profiles taken along the green dash lines. Scale bar: 5 μm (A,B,E,F,I,J), 1 μm (C,D,G,K,L), 500 nm (H).....116
- 4.9. Biomechanical evaluation of A549 (column 1), 435 (column 2) and 435/BRMS1 (column 3). Row 1 shows representative topography images acquired in culture medium. The maps of adhesion force (F), spring constant (k_{cell}), and Young's modulus (E) of three cell lines are shown row 2, row 3, and row 4, respectively, and their respective distribution histogram (mean \pm SD is marked) is displayed under the corresponding map. The color bars arranged at the right of maps illustrate the value scale of color-coded maps of adhesion force (nN), k_{cell} (mN/m), and E (kPa). Scale bar: 5 μm (A549), 1 μm (435 and 435/BRMS1).....118
- 5.1. Comparison of topography, ultrastructures, and biomechanics of 435 (A-F) and 435/BRMS1 (G-L) cells. The cells were fixed by 1% glutaraldehyde plus 1% paraformaldehyde. (A-C) and (G-I) are deflection images of 435 and 435/BRMS1 cells, respectively; (D-F) and (J-L) present ultrastructures of 435 and 435/BRMS1 cells, respectively. The inset in (G) indicates the height mode image of cell (G). Images (H) and (J) are the magnified views of square frame in (G) and (I), respectively. Scale bar: A-C, G-I, 5 μm ; D-F, J-L, 1 μm142

- 5.2. Biomechanical evaluation of living breast cancer cell line 435 (A-E) and 435/BRMS1 (G-K). (A) and (G) are representative deflection images of 435 and 435/BRMS1 cells scale acquired in culture medium, respectively, and their respective statistical results of adhesion force and spring constant (k_{cell}) are shown in (B, D) or in (H, J). The maps of adhesion force and k_c of 435 and 435/BRMS1 cells are shown in (C, E) and (I, K), respectively. (F) Two representative deflection (nm)-distance (nm) curves measured on 435 cells (black curve) and 435/BRMS1 cell (red curve). (L) presents the merged compliance portion of approaching branch of one deflection (nm)-distance (nm) curve acquired on 435 cell (green curve), 435/BRMS1 cell (red curve), or on Petri dish (black curve); the Young's moduli of the two cell lines were calculated by substituting the indentation depth and the corresponding compliance force into the equation (2). Scale bar for (A, G): $5\mu\text{m}$144
- 5.3. Raman spectra of 435 cells (upper) and 435/BRMS1 cells (lower).147
- 5.4. Raman mapping of biochemical information for cell line 435 and 435/BRMS1. Different biochemical components were identified by characteristic wavenumbers as follows; DNA (red) – 785 cm^{-1} , carbohydrate (blue) – 939 cm^{-1} , protein (green) – 1006 cm^{-1} , and lipid (yellow) – 1092 cm^{-1} . Scale bar: $10\mu\text{m}$ (horizontal), $5\mu\text{m}$ (vertical).149
- 5.5. Electric cell-substrate impedance sensing (ECIS) of wounding and healing for 435 and 435/BRMS1. Each cell line was seeded, in culture-ware containing integrated electrodes on the substrate, at a final density of 2×10^5 cells/well (1). A confluent layer was allowed to form after initial attachment and proliferation (2). Arrays were charged with a $1400\mu\text{A}$ pulse for 20 seconds at 60 kHz to wound cells attached on the electrode surface (3), time then allowed for the cell layer to recover – migrate/proliferate back over electrode surface (4). Re-wounding was performed (5) and then more time was allowed for healing (6).152

- 5.6. Bright field images of array A wells imaged with IX – 71 Olympus Microscope at 10x magnification. Well were imaged pre- and post-wounding. Note wells A1 and A5 contained only culture medium, A2, A3, A4 contained 435 cells and A6, A7, A8 contained 435/BRMS1 cells. Arrows indicated areas where cell monolayer has changed after wounding.....153
- 5.7. F-actin localization in 435 and 435/BRMS1 cells: Cells were cultured on cover slips for 24 hours; F-actin was visualized by phalloidin staining. Multiple cells and single cells were imaged for 435 (A and C) and 435/BRMS1 (B and D).....154
- 6.1. An 8W10E+ array containing >40 working electrodes (A) compared with 8W1E array that has a single working electrode (B) [images courtesy of ABP, NY, USA].166
- 6.2. Two 8W10E+ arrays were seeded with 2×10^5 cells/well (A1 – A7 and B1 – B7) with control wells containing culture medium (A8 and B8). When the cells were confluent at ~25 hours an increasing amount of methanol was added to each well, and then at 50 hours wells were wounded (60 kHz, 5000 μ A, for 20 sec) and allowed to recover. The experiment was performed twice with similar results. Legend “AnBn” refers to averaging the responses in duplicate wells An and Bn (where n = 1, 2, 3 ... 8 see insert of well configuration).....174
- 6.3. Two 8W10E+ arrays were seeded with 2×10^5 cells/ml (A1 – A7 and B1 – B7) with control wells containing culture medium (A8 and B8). When the cells were confluent at ~28 hours, then an increasing amount of DEP (ranging from 10 μ g/ml to 1000 μ g/ml), dissolved in methanol, was added to each of the wells. Each data line is an average of two wells, except for A6 (B6 data was erroneous).175

- 6.4. Two 8W10E+ arrays (array A and B) were seeded with 2×10^5 cells/ml of A549 (A1 – A7 and B1 – B7). After attachment and proliferation (0 – 24 hours), the media in wells A1 – A8 was replaced with fresh media (~24 hours) and wells B1 – B8 was replaced with medium containing 10 μ M resveratrol. Next cells were treated with different concentrations of DEP (45 – 70 hours), then media was changed again and cells were allowed to adjust to new media (70 – 90 hours), next cells were wounded (90 hours) and allowed to recover (90~120 hours), and finally cells were re-wounded (~120 hours) and allowed to recover (120 – 165 hours).177
- 6.5. Array A. A549 was seeded at 2×10^5 cells/well in 8W10E+ arrays. After attachment and proliferation (0 – 24 hours), the media in the wells was replaced with fresh media (~24 hours). Next cells were treated with different concentrations of DEP (45 – 70 hours), then media was changed again and cells were allowed to adjust to new media (70 – 90 hours), next cells were wounded (90 hours) and allowed to recover (90~120 hours), and finally cells were re-wounded (~120 hours) and allowed to recover (120 – 165 hours).178
- 6.6. Array B. After attachment and proliferation (0 – 24 hours), the cells were treated with 10 μ M resveratrol (~24 – 45 hours). Next cells were treated with different concentrations of DEP (45 – 70 hours), then media was changed and cells were allowed to recover (70 – 90 hours), next cells were wounded (90 hours) and allowed to recover (90 – 120 hours), and finally cells were re-wounded and allowed to recover (120 – 165 hours).179
- 6.7. Two 8W1E arrays were seeded with 2×10^5 cells/ml of A549 (A1 – A7) and (B1 – B7) with control wells containing culture medium (A8 and B8). Cells were monitored until approximately confluent (27 hours), then 10 μ M (final) resveratrol was added to array B for 24 hours (culture medium, without resveratrol, in array A), DEP was added for the final~24 hours.182
- 6.8. Array A. A549 was seeded at 2×10^5 cells/well in an 8W1E array. After attachment and proliferation (0 – 27 hours), the medium in each well was replaced with fresh medium (~27 hours) and cells were allowed to continue in culture (28 – 50 hours). Next cells were treated with different concentrations of DEP (50 – 75 hours).183

- 6.9. Array B. A549 was seeded at 2×10^5 cells/well in an 8W1E array. After attachment and proliferation (0 – 27 hours), the medium in each well was replaced with fresh medium containing a final concentration of 10 μ M resveratrol (~27 hours) and cells were allowed to continue in culture (28 – 50 hours). Next cells were treated with different concentrations of DEP (50 – 75 hours).184
- 6.10. Two 8W1E arrays were seeded with 2×10^5 cells/well of A549 (A1–A8 and B1–B8) and cells were allowed to become confluent. After ~24 hours, the medium was changed and medium with DEP (50, 125, and 500 μ g/ml) was added to the arrays. The arrays were then wounded (A5 – 8 and B5 – 8 @ 180 seconds, 3000 μ A and 60 kHz), and then allowed to recover. It appears each of the wells begin to recover, but not to the baseline of the un-wounded wells.186
- 6.11. Bright field and fluorescent images of array A imaged with IX – 71 Olympus Microscope at 10x magnification. Note that the first column (A1 – A4) was not wounded and the second column (A5 – A8) was wounded and the 250 μ m electrode is still covered after partial recovery.188
- 6.12. Bright field and fluorescent images of array B imaged with IX – 71 Olympus Microscope at 10x magnification. Note that the first column (B1 – B4) was not wounded and the second column (B5 – B8) was wounded and the 250 μ m electrode is mostly covered, but the dead cells are visible above the electrode.189
- 6.13. A549 cells were seeded at 1×10^5 cells/well, allowed to attach and spread until 30 hours. Next cells were treated with increasing concentrations of DEP and allowed to continue to grow for ~15 hours (note each data line is an average of two wells).191
- 6.14. A549 cells were seeded at 1×10^5 cells/well, allowed to attach and spread until 30 hours. Next cells were treated with increasing concentrations of DEP combined with 10 μ M resveratrol and allowed to continue to grow for ~15 hours (note each data line is an average of two wells).192

- 6.15. A549 cells were seeded at 2×10^5 cells/well plus 10 μ M resveratrol, allowed to attach and spread until ~ 30 hours. Then cells were treated with increasing concentrations of DEP, wounded (60 kHz and 3000 μ A for 180 seconds) and allowed to continue to grow for ~ 36 hours (note each data line is an average of two wells, expect for the media and media + cells wells).194
- 6.16. A549 cells were seeded at 2×10^5 cells/well + 10 μ M resveratrol, allowed to attach and spread until ~ 30 hours. Then cells were treated with increasing concentrations of DEP and allowed to continue to grow for ~ 36 hours (note each data line is an average of two wells, expect for the media and media +cells wells).195
- 6.17. Bright field and fluorescent images of Array A imaged with IX – 71 Olympus Microscope at 40x magnification. Note that most of the wounded cells detached and may have washed away – except for well A4 and some in well A6.196
- 6.18. Bright field and fluorescent images of Array A imaged with IX – 71 Olympus Microscope at 40x magnification. It also appears that some of the cells have washed off in the rinsing with EBSS.....197
- 6.19. Two 8W10E+ arrays were seeded with 2×10^5 cells/well + methanol (A1 – A7 and B1 – B7) and culture media without methanol in the other two wells (A8 and B8). A549 cells become confluent at ~ 24 hours.199
- 6.20. Two 8W10E+ arrays were seeded with 2×10^5 cells/ml + DEP/MTH (A1 – A7 and B1 – B7) and culture media in the other two wells (A8 and B8). A549 cells become confluent at $\sim 15 - 20$ hours.....200
- 6.21. Array A (8W10E+ array) seeded with 2×10^5 cells/ml of A549 + media/DEP (A1–A7) and culture medium in A8. Cells were monitored until approximately confluent (~ 23 hours) and were wounded at 6500 μ A, 20 seconds, and 60 kHz.....202
- 6.22. Array B (8W10E+ array) seeded with 2×10^5 cells/ml of A549 + media/RES/DEP (B1–B7) and culture medium + RES in B8. Cells were monitored until approximately confluent (~ 23 hours) and were wounded at 6500 μ A, 20 seconds, and 60 kHz.....203

- 6.23. Array A (8W1E array) was seeded with 2×10^5 cells/ml of A549 + DEP (50, 125, and 500 $\mu\text{g/ml}$) + 10 μM resveratrol (A1–A8 and B1–B8) and cells were allowed to become confluent. After ~28 hours, the arrays were then wounded (B1–B8 @ 180 seconds, 3000 μA and 60 kHz), then the wells were allowed to recover.....205
- 6.24. Array B (8W1E array) was seeded with 2×10^5 cells/ml of A549 + DEP (50, 125, and 500 $\mu\text{g/ml}$) + 10 μM RES (A1–A8 and B1–B8) and cells were allowed to become confluent. After ~28 hours, the arrays were then wounded (B1–B8 @ 180 seconds, 3000 μA and 60 kHz), then the wells were allowed to recover.....206
- 6.25. Raman spectra and bright field images of A549 cells during culture/treatment. Row 1 – Raman spectra of untreated A549 cells for 0 and 4 hours of culture. Row 2 – Raman spectra of 25 $\mu\text{g/ml}$ DEP treated A549 cells. Row 3 – Raman spectra of 25 $\mu\text{g/ml}$ DEP + 10 μM RES treated A549 cells. Row 4 – Raman spectra of 50 $\mu\text{g/ml}$ DEP treated A549 cells. Row 5 – Raman spectra of 50 $\mu\text{g/ml}$ DEP + 10 μM RES treated A549 cells. Each Raman spectral profile represent the following locations of A549; nucleus (black), cytoplasm (red), cellular membrane (blue), and background substrate (magenta) and corresponding arrows accompany bright filed images. Raman spectra are an average of four spectra per cell for four separate imaged cells (16 total spectra per profile). Scale bar = 10 μm210
- 6.26. Raman spectra and bright field images of A549 cells during culture/treatment. Row 1 – Raman spectra of untreated A549 cells for 8 and 16 hours of culture. Row 2 – Raman spectra of 25 $\mu\text{g/ml}$ DEP treated A549 cells. Row 3 – Raman spectra of 25 $\mu\text{g/ml}$ DEP + 10 μM RES treated A549 cells. Row 4 – Raman spectra of 50 $\mu\text{g/ml}$ DEP treated A549 cells. Row 5 – Raman spectra of 50 $\mu\text{g/ml}$ DEP + 10 μM RES treated A549 cells. Each Raman spectral profile represent the following locations of A549; nucleus (black), cytoplasm (red), cellular membrane (blue), and background substrate (magenta) and corresponding arrows accompany bright filed images. Raman spectra are an average of four spectra per cell for four separate imaged cells (16 total spectra per profile). Scale bar = 10 μm211

- 6.27. Raman spectra and bright field images of A549 cells during culture/treatment. Row 1 – Raman spectra of untreated A549 cells for 24 and 48 hours of culture. Row 2 – Raman spectra of 25 $\mu\text{g/ml}$ DEP treated A549 cells. Row 3 – Raman spectra of 25 $\mu\text{g/ml}$ DEP + 10 μM RES treated A549 cells. Row 4 – Raman spectra of 50 $\mu\text{g/ml}$ DEP treated A549 cells. Row 5 – Raman spectra of 50 $\mu\text{g/ml}$ DEP + 10 μM RES treated A549 cells. Each Raman spectral profile represent the following locations of A549; nucleus (black), cytoplasm (red), cellular membrane (blue), and background substrate (magenta) and corresponding arrows accompany bright filed images. Raman spectra are an average of four spectra per cell for four separate imaged cells (16 total spectra per profile). Scale bar = 10 μm212
- 6.28. Dendrogram obtained by hierarchical cluster analysis of Raman spectra of A549 cells during 48 hour culture period. Each tree, three per figure, represent a different set of cell culture treatment conditions; control (red), 25 $\mu\text{g/ml}$ DEP (green), and 50 $\mu\text{g/ml}$ DEP (blue). Row 1 – Dendrogram clusters of A549 nucleus at 0, 4, and 8 hours of culture. Row 2 – Dendrogram clusters of A549 cytoplasm. Row 3 – Dendrogram clusters of A549 membrane. Row 4 – Dendrogram clusters of A549 background.213
- 6.29. Dendrogram obtained by hierarchical cluster analysis of Raman spectra of A549 cells during 48 hour culture period. Each tree, three per figure, represent a different set of cell culture treatment conditions; control (red), 25 $\mu\text{g/ml}$ DEP (green), and 50 $\mu\text{g/ml}$ DEP (blue). Row 1 – Dendrogram clusters of A549 nucleus at 16, 24, and 48 hours of culture. Row 2 – Dendrogram clusters of A549 cytoplasm. Row 3 – Dendrogram clusters of A549 membrane. Row 4 – Dendrogram clusters of A549 background.....214
- 6.30. Dendrogram obtained by hierarchical cluster analysis of Raman spectra of A549 cells during 48 hour culture period. Each tree, three per figure, represent a different set of cell culture treatment conditions; control (red), 25 $\mu\text{g/ml}$ DEP (green), and 25 $\mu\text{g/ml}$ DEP + 10 μM RES (blue). Row 1 – Dendrogram clusters of A549 nucleus at 0, 4, 8, 16, 24, and 48 hours of culture. Row 2 – Dendrogram clusters of A549 cytoplasm. Row 3 – Dendrogram clusters of A549 membrane. Row 4 – Dendrogram clusters of A549 background.....215

- 6.31. Dendrogram obtained by hierarchical cluster analysis of Raman spectra of A549 cells during 48 hour culture period. Each tree, three per figure, represent a different set of cell culture treatment conditions; control (red), 25 $\mu\text{g/ml}$ DEP (green), and 25 $\mu\text{g/ml}$ DEP + 10 μM RES (blue). Row 1 – Dendrogram clusters of A549 nucleus at 0, 4, 8, 16, 24, and 48 hours of culture. Row 2 – Dendrogram clusters of A549 cytoplasm. Row 3 – Dendrogram clusters of A549 membrane. Row 4 – Dendrogram clusters of A549 background.....216
- B2.11. Electrochemical impedance spectroscopy (EIS) of step-by-step synthetic ds-DNA modified electrode: bare Au (1), dsS-DNA/Au (2), MCH/dsS-DNA/Au (3), Hoechst/MCH/dsS-DNA/Au (4), Oxidation/Hoechst/MCH/dsS-DNA/Au (5), and Hoechst/Oxidation/Hoechst/MCH/dsS-DNA/Au (6). Inset: modified equivalent Randles circuit used to model impedance data. EIS was conducted in 0.5 mM $\text{K}_3\text{Fe}(\text{CN})_6$ + 0.5 mM $\text{K}_4\text{Fe}(\text{CN})_6$ in 0.01 M PBS, pH 7.4 with 10 mV AC amplitude.259
- B2.12. Voltammetric behaviors of $\text{Fe}(\text{CN})_6^{3-/4-}$ redox couple (0.5 mM $\text{K}_3\text{Fe}(\text{CN})_6$ + 0.01 M PBS) on step-by-step synthetic ds-DNA modified electrodes: bare Au (1), MCH/Au (2), dsS-DNA/MCH/Au (3), Oxidation/dsS-DNA/MCH/Au (4), and Hoechst/Oxidation/dsS-DNA/MCH/Au (5). Inset: 5 mM Na_2HPO_4 + 5 mM NaH_2PO_4 between 0 - 1.3 V at 30 mV s^{-1}260
- B2.13. Electrochemical impedance spectroscopy (EIS) of step-by-step synthetic ds-DNA modified electrode: bare Au (1), MCH/Au (2), dsS-DNA/MCH/Au (3), Oxidation/dsS-DNA/MCH/Au (4), and Hoechst/Oxidation/dsS-DNA/MCH/Au (5). Inset: modified equivalent Randles circuit used to model impedance data. EIS was conducted in 0.5 mM $\text{K}_3\text{Fe}(\text{CN})_6$ + 0.5 mM $\text{K}_4\text{Fe}(\text{CN})_6$ in 0.01 M PBS, pH 7.4 with 10 mV AC amplitude.261
- B2.14. Depiction of current vs. time curves for three cases; (A) Hoechst 33258 (5 min)/MCH (6 hrs)/dsS-DNA (24 hrs)/Au (corresponding to the inset in Figure 2.5), (B) dsS-DNA (24 hrs)/MCH (6 hrs)/Au (corresponding to the inset in Figure B2.12), and (C) dsS-DNA (12 hrs)/Au (corresponding to the curves in Figure 2.7-A. Each CV illustrates the first three cyclic voltammetry scans numbered 1, 2, and 3.262

- C4.10. Mean Raman spectra of three cancer cell lines: A549 (a-black), 435 (b-red), and 435/BRMS1 (c-blue). Each spectrum is the average of five spectra, the averaged background was subtracted by finding a local minimum area, spectra were baseline corrected, and, then normalized using peak intensity at 1660 cm^{-1} . Spectra are offset vertically for clarity.266
- C4.11. Difference spectra computed from the 1660 cm^{-1} normalized spectrum in Figure C4.10 using A549, 435, and 435/BRMS1: 435/BRMS1 – A549 (a); 435/BRMS1 – A549 (b); A549 – 435 (c).....267
- D6.32. Two 8W10E+ arrays were seeded with 2×10^5 cells/ml (A1 – A7 and B1 – B7) and media in the other two wells (A8 and B8). When the cells were confluent at $\sim 27 - 28$ hours, an increasing amount of methanol was added to each of the wells.268
- D6.33. Means comparison (mean \pm SD) of modeled parameters R_b , α , and C_m obtained from Figure 6.7. Means were computed for six wells over a 10 hour period. Seed = 15 – 25 hours (A), Media/RES = 35 – 45 hours (B), and DEP = 55 – 65 hours (C). Array A and B were seeded at 0 hour, media was exchanged at 29 hour with medium control in array A and 10 μM resveratrol plus medium in array B, and DEP exposure was at performed 50 hours.269
- D6.34. This was an experiment to test the migration rate of A549 at two different concentrations of DEP (50 and 125 $\mu\text{g/ml}$ – dark red and dark yellow) at the previously defined wounding settings of at 60 kHz, 2600 μA and 180 seconds. A549 cells were seeded as outlined above (see Table D6.14). At ~ 22.5 hours the experiment was paused, DEP was added to wells A2, 3, 4, 6, 7 and B2, 3, 4, 6, and 7. Arrays were replaced, values were checked and wounding was applied while measurements were still paused. Then measurement was resumed.270
- D6.35. Two 8W1E arrays were seeded with 2×10^5 cells/ml of A549 cells and were allowed to become confluent. At ~ 22 hours the media was changed and DEP was added to wells A2, 3, 4, 6, 7, and 8. Cells were allowed to continue to culture for ~ 42 hours. Array B was then wounded at 2600 μA , for 30 seconds. and 32 kHz. Cells were allowed to heal until ~ 42 hours.271

- D6.36. Bright field images of Array A and B imaged with IX – 71 Olympus Microscope at 10x magnification. Note increasing DEP concentrations in Wells A2 & 6, 3 & 7, 4 & 8 and B2 & 6, 3 & 7, 4 & 8 – respectively 50, 125, and 500 µg/ml.....272
- D6.37. Bright field images of Array A and B imaged with IX – 71 Olympus Microscope at 40x magnification. Note increasing DEP concentrations in Wells A2 & 6, 3 & 8, 4 & 8 and B2 & 6, 3 & 7, 4 & 8 – respectively 50, 125, and 500 µg/ml.....273
- D6.38. Two 8W1E arrays were seeded with 2×10^5 cells/ml of A549 (A1–A8 and B1–B8) and cells were allowed to become confluent. After ~18 hours, the media was changed and media and DEP (50, 125, and 500 µg/ml) were added to the arrays. The arrays were then wounded (A5 – 8 and B5 – 8 @ 180 seconds, 3000 µA and 64 kHz), then the wells were allowed to recover. It appears that control and the 50 µg/ml DEP wells start to recover while the 125 and 500 µg/ml treated wells do not recover.....274
- D6.39. 8W10E+ Second seeding using a final dilution (2×10^5 cells/well) combined with methanol + media treatment (~0 hours) *note MTH + media was prepared fresh on day of runs.275
- D6.40. A repeat of the suspension/DEP work was performed to verify the concentration and test if media+ antibiotics make a difference in the bacterial contamination of the DEP. Two 8W10E+ arrays each seeded with A549 mixed with DEP, final density of A549 was 2×10^5 cells/well. Density of the DEP treatments is listed in the table below.276
- D6.41. Raman spectrum of dry diesel exhaust particles collected over a wavenumber range of 100 – 3200 cm^{-1} at 2.5% laser power for 10 seconds (A). Bright field image of DEP (B). Scale bar = 20 µm.277
- D6.42. SEM images of DEP powder. Micrographs reveal DEP size and morphology. Size of DEP clusters range from 3.0 µm (A), 500 nm (B), 333 nm (C), and 231 nm (D).278
- D6.43. Raman spectrum of resveratrol powder collected over a wavenumber range of 200 – 3200 cm^{-1} at 0.5% laser power for 10 seconds (A). Bright field image of resveratrol powder (B). Scale bar = 20 µm.279

D6.44.	Raman spectral overlay of resveratrol powder (blue), DEP (red), and A549 (black). Count intensities are absolute values.	280
--------	--	-----

NOMENCLATURE

α	charge transfer coefficient (chapter 2)
α	current flow under cells [$\Omega \text{ cm}^2$] (chapter 4, 5)
C_d	double-layer capacitance [μF]
C_m	average capacitance of the cell plasma membrane [$\mu\text{F cm}^{-2}$]
C_0	bulk solution concentration [M]
D_0	diffusion coefficient [$\text{cm}^2 \text{ s}^{-1}$]
d_i	thickness of the i^{th} layer [nm]
$\text{Fe}(\text{CN})_6^{3-/4-}$	redox probe [M]
h	height between substratum and cell basal membrane [cm]
I	current [μA]
i_p	peak current [μA]
i_{pa}	anodic peak current [μA]
i_{pc}	cathodic peak current [μA]
K_a^0	heterogeneous standard charge-transfer rate constant [cm s^{-1}]
k_c	cell spring constant [mN m^{-1}]
k_{cell}	cellular spring constant [nN]
k_{tip}	cantilever spring constant [nN]
N	total number of data points
ν	scan rate [mV s^{-1}]
Q_O	oxidation charge [μC]
Q_R	reduction charge [μC]
R_a	average roughness [nm]
R_b	barrier function [$\Omega \text{ cm}^2$]
r_c	cell radius [cm]
R_{ct}	charge-transfer resistance [Ω]

ROS	reactive oxygen species
R_{rms}	root-mean-square roughness [nm]
R_{Ω}	electrolyte resistance [Ω]
R_s	roughness factor
ρ	resistivity of culture medium [Ω cm]
s	slope
θ_R	surface coverage
Γ_{DNA}	surface density of DNA [moles cm^{-2}]
Γ_0	surface density [moles cm^{-2}]
V	potential [Volts]
Z_W	Warburg impedance [$\mu\Omega$ $\text{s}^{-1/2}$]
Z_{im}	imaginary portion of impedance [$\mu\Omega$ $\text{s}^{-1/2}$]
Z_{re}	real portion of impedance [$\mu\Omega$ $\text{s}^{-1/2}$]
Z_n	height of the n^{th} point
8W1E	eight well array with one electrode per well
8W10E+	eight well array with 40 electrodes per well
ABP	Applied BioPhysics
AFM	atomic force microscopy
Au	polycrystalline gold
Au(111)	single crystalline gold
BRMS1	breast cancer metastasis suppressor 1
CCD	charged coupled device
CLS	classical least squares
CRR	cosmic ray removal
CV	cyclic voltammetry
DEP	diesel exhaust particles
DCLS	direct classical least squares

DMEM	Dulbecco's modified eagle's medium
DOE	Design of experiment
ds-DNA	double stranded DNA
EC	electrochemical sensing
ECIS	electric cell-substrate impedance sensing
ECM	extracellular matrix
EGFR	epidermal growth factor receptor
EIS	electrochemical impedance spectroscopy
ELISA	enzyme-linked immunosorbent assay
eNOS	endothelial nitric oxide synthase
EPS	extracellular polymeric substances
ET	electron transfer
EthD	ethidium homodimer
FT-IR	Fourier transform infrared spectroscopy
HCA	hierarchical cluster analysis
IR	infrared
LB	Luria Broth
LPS	lipopolysaccharide
MB	methyl blue
MCH	6-mercapto-1-hexanol
MCSIL	Molecular and Cellular Sensing and Imaging Laboratory
MMP	matrix metalloproteinase
MTB	<i>Mycobacterium tuberculosis</i>
MTH	methanol
NB	Nile blue
NEERL	National Health and Environmental Effects Research Laboratory
NO	nitric oxide

NPD	New product development
OEHHA	Office of Environmental Health Hazard Assessment
OLS	ordinary least squares
PAH	polycyclic aromatic hydrocarbons
PAP _R	<i>p</i> -aminophenol
PAPP	<i>p</i> -aminophenyl phosphate
PBS	phosphate buffered solution
PCA	principal component analysis
RM	Raman microspectroscopy
RES	resveratrol (3,5,4'-trihydroxystilbene)
SAM	self assembled monolayer
SEM	scanning electron microscopy
SERS	surface enhanced Raman scattering
SSC	saline sodium citrate
ss-DNA	single stranded DNA
STM	scanning tunneling microscopy
t-DNA	complementary target DNA
TFS	Thermo Fisher Scientific
USU	Utah State University
XPS	X-ray photoelectron spectroscopy

CHAPTER 1

INTRODUCTION

1.1 RATIONALE FOR PROPOSED RESEARCH

A simple interface is the place or point where two objects come together, meet, and form contact. A bio-interface is the point where a bio-molecule comes into contact with a solid surface. More complex bio-interfaces are formed when more complex biological objects are incorporated at the interface site (i.e. bacteria, mammalian cells, tissues, organs systems, and so on). A fundamental understanding of bio-interfaces is useful to gain insight into how surface modification can allow beneficial coexistence between complex biological objects and surfaces that may not readily be present in nature.

The overall thematic research on bio-interfaces entails several explored areas throughout this dissertation. Therefore, the broad overview of the research can be classified as exploratory; wherein, each individual chapter contains hypothesis driven research along with results and discussion. Also, because the technical Chapters 2 – 6 contain more background specific to the research described therein, a brief background is covered below followed by an outline of the dissertation.

1.2 BACKGROUND

The study of bio-interfaces and biomaterials has been around since the 1960's [1] and has continued to thrive with the increase in the use of sophisticated analytical instruments. The research presented in the following chapters of this dissertation

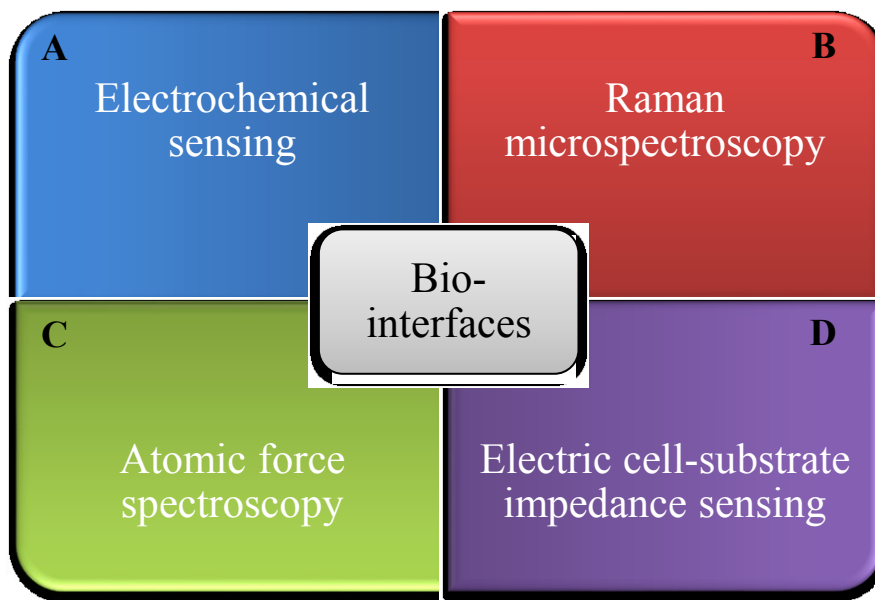


Figure 1.1. A schematic overview of the instrumentation used to study the bio-interfaces of molecules, bacteria, and mammalian cells.

explores different types of bio-interfaces and utilizes several different instruments to perform the experiments.

Figure 1.1 illustrates the four main techniques that we used to probe bio-interfaces. Two of the techniques were electrical (A and D) while the other two were optical (B) and mechanical (C). All of these different techniques utilized specific instruments to investigate bio-interfaces respectively. The bio-interfaces that we focused on in our biological samples, ranged from DNA oligonucleotides, bacterial cell walls, and three types of mammalian cell-lines.

1.3 ELECTROCHEMICAL SENSING

We begin with cyclic voltammetry (I vs. V curves) (Figure 1.1-A), where the DNA mediated electron transfer of the redox probe was facilitated by the conductivity of our modified gold electrode surface (Figure 1.2). When the redox probe is reduced, we

obtain a peak potential (Figure 1.2-A) and the reversible reaction yields an oxidation peak (Figure 1.2-B). Based on cyclic voltograms (similar to the one inset in Figure 1.2), for each surface modification, we can understand the DNA-mediated recyclable conductivity changes of the surface by indirectly monitoring I vs. V curve of the redox probe - potassium ferricyanide ($\text{K}_3\text{Fe}(\text{CN})_6^{3-}$).

1.4 RAMAN MICROSCOPY

With Raman microspectroscopy (Figure 1.1-B) we use monochromatic light to excite molecules, within a sample, to a virtual excited state (Figure 1.3-A). At the decay from the excited state to the ground state energy is given off. The majority of the energy

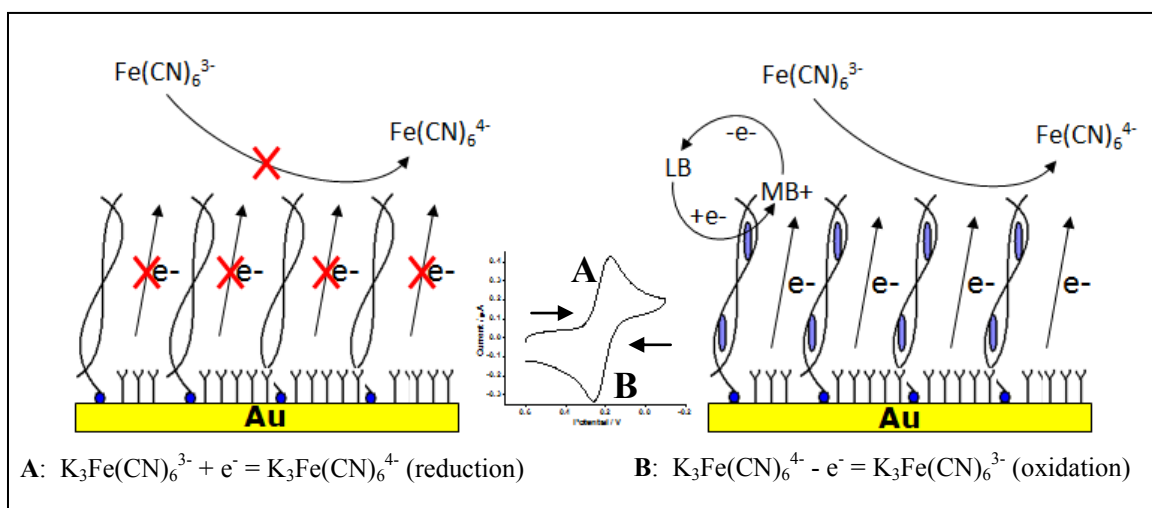


Figure 1.2. Schematic of DNA mediated electron transfer at the modified gold surface. DNA is indirectly probed by monitoring the reduction or oxidation reaction within the redox probe solution (0.5 mM $\text{K}_3\text{Fe}(\text{CN})_6$ + 0.01 M PBS) at various scan rates. Hoechst 33258 is used to increase the conductivity of the double stranded DNA. The inset cyclic voltammogram illustrates a typical reduction peak (A) and oxidation peak (B) of the semi-reversible reaction. [Image inspired from [2]]. MB = methylene blue and LB = leucomethylene blue, where LB goes on to reduce ferricyanide in solution.

scattered returns the molecular energy to the initial ground state. This type of scatter is called Rayleigh scatter. A small change in the energy, either an increase above the ground state or below the ground state is termed Stokes or Anti-Stokes scattering. These small changes in energy are known as the Raman effect and are what we measured in our studies. Due to the differing vibrational frequencies (corresponding to specific chemical bond vibrations), we have a wavenumber range of Raman active bands that produce a spectral profile (Figure 1.3-B).

Raman scattering (also known as the Raman effect) is named for the Indian physicist, C.V. Raman, who was acknowledged with the discovery in 1928. This was a very significant discovery and Professor Raman received the Nobel Prize in Physics for

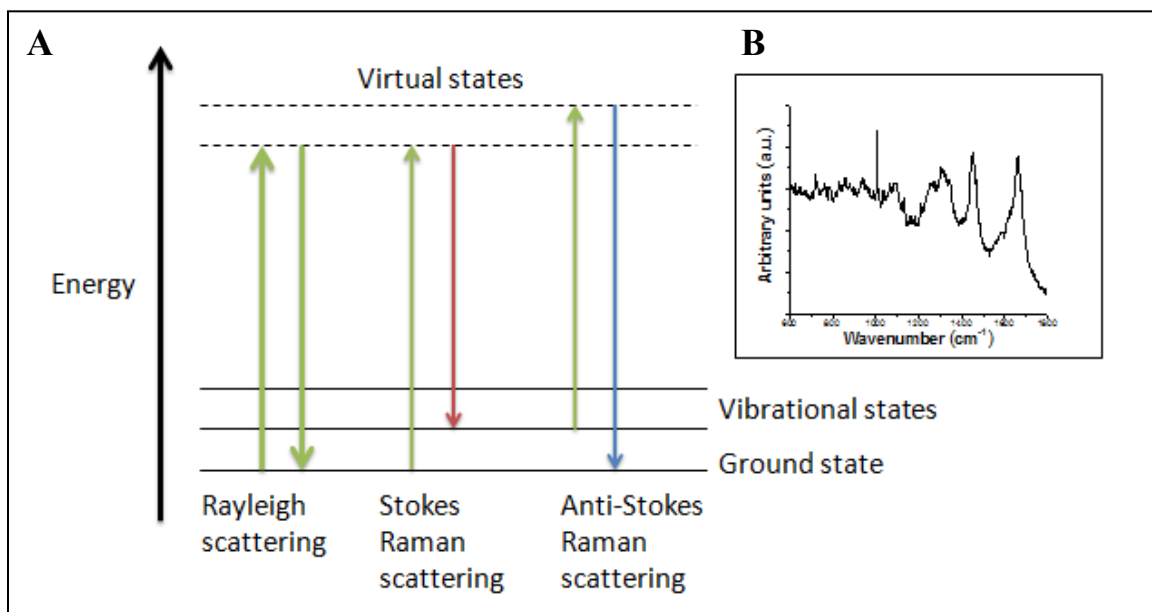


Figure 1.3. A classical-simple representation of the energy states for the different forms of scatter. The shift in the Raman effect is due to the spacing between the vibrational energy states and the ground state (A). Inset illustrates a Raman profile of A549 mammalian cells (B). Image adapted from [3].

this discovery in 1930. Prior to the Nobel Prize the recognition of the Raman effect was cited in more than 150 papers in that year and a half alone [3]. At present Raman microspectroscopy is utilized in a range of industrial applications [4]. Some examples of Raman applications include; pharmaceuticals [5], semiconductors and thin films [6, 7], biocompatibility [8], forensics, and archeometry [9]. As the instrumentation has improved over the past five decades, increased Raman microspectroscopy performance has opened an area in bioanalytical applications for biology, chemistry, and medicine [10-12].

Raman microspectroscopy (RM) is a nondestructive vibrational classification routine that can be utilized to identify characteristic spectroscopic fingerprints of living cells based on chemical compositions and molecular structures [13]. Briefly, Raman spectral frequencies are recorded in wavenumber units which are proportional to vibrational energies based on molecular polarizability [14]. Many former RM studies focused mainly on physical and structural investigations. Over the past few decades, due to advances within instrumentation design [11, 15], biological applications [10, 16], and methods for biochemical information extraction [12, 17], RM has exhibited increased popularity in the field of mammalian cell biology [18, 19]. Short *et al.* demonstrated the use of RM to detect biochemical changes, in tumorigenic versus non-tumorigenic cells, as a result of proliferation [20]. More recently, Abramczyk *et al.* reported the hallmarks of normal, malignant, benign breast tissue characterized by Raman studies [21]. Several other studies reported the appearance of cellular biopolymers (including DNA/RNA, lipids, proteins, and carbohydrates) in cell growth [17, 19, 22]. As RM has increased in popularity, new analysis routines have emerged to extract useful information from Raman

spectra. Advances have been made to obtain Raman scatter from inherent background fluorescence through automation [23, 24], while other groups move toward an automated pre- and post-processing routine to eliminate natural user variability [25] and categorize Raman spectra [26]. Also new and emerging methods have been explored to enhance the usefulness of Raman spectral maps/images. Principal component analysis (PCA) was used to evaluate maps of freeze dried and living cells [27]. Ling *et al.* demonstrated image-processing algorithms to restore Raman image degradation in the study of anticancer drug distribution within living cells [13]. When key molecular components are used, RM becomes a powerful tool for rapid identification of normal and transformed breast epithelial cell-lines [19] and multivariate analysis classification models can discriminate, through distinct Raman bands, normal from abnormal tissue in cervical cancer progression [17].

During recent years Raman microspectroscopy has increased in popularity in the field of microbiology as a tool to identify microorganisms, such as bacteria [12, 28-32]. Gram-positive *Bacillus anthracis*, *B. thuringiensis*, and *B. atropheus* spores, and *B. cereus* vegetative cells have been characterized and differentiated via Raman imaging and using data analysis algorithms [33]. Work continues to explore rapid quality control methods to detect pathogenic Gram-positive and Gram-negative bacteria [34]. Both Gram-positive and Gram-negative bacteria have been characterized by SERS to provide molecular level information [35], and rapid fingerprinting combined with principal component analysis (PCA) to distinguish simulated biological threats [36].

On the clinical side of research, cancerous cell characterization and detection via Raman microspectroscopy has increased rapidly with time. Confocal Raman

microspectroscopy has been used to characterize normal and transformed human breast epithelial cell lines and has shown that, in the tumorigenic cell nuclei, DNA duplication is significantly higher than in normal cell nuclei [37]. Yu *et al.* propose a new technique for rapid cell identification utilizing sub-cellular level Raman bands [37]. Similar studies have been performed for other cancer cell line identification; such as, prostate [38], ovarian [39, 40], liver and other tissues [41], lung [42], pancreatic [43], cervical [17], and leukemia [44]. We employed RM to locally track biochemical changes (DNA/RNA, lipids, proteins, and carbohydrates) during cell growth (Chapters 4, 5, 6) and with DEP and resveratrol treatment (Chapter 6).

1.5 ATOMIC FORCE MICROSCOPY

Atomic force microscopy (Figure 1.1-C) uses a very tiny cantilever and tip to detect the attraction and repulsion forces at the atomic level (Figure 1.4-A). These forces are represented in the force versus distance diagram (Figure 1.4-B). The repulsion, attraction, and no deflection forces move the cantilever and thus move the laser position on the diode and yield measureable forces. These forces can then be used to construct topography images (Figure 1.4-C) and force maps (Figure 1.4-D).

Atomic force microscopy (AFM) is also known as scanning probe microscopy (SPM) and has been around since 1985 when it was invented by Binnig, Quate, and Gerber [45]. It was created to probe and image non-conductive surfaces via direct contact in air [45]. In the simplest form, AFM can be described similar to workings of an audio phonograph or vinyl record player. For the AFM, an extremely small tip is used

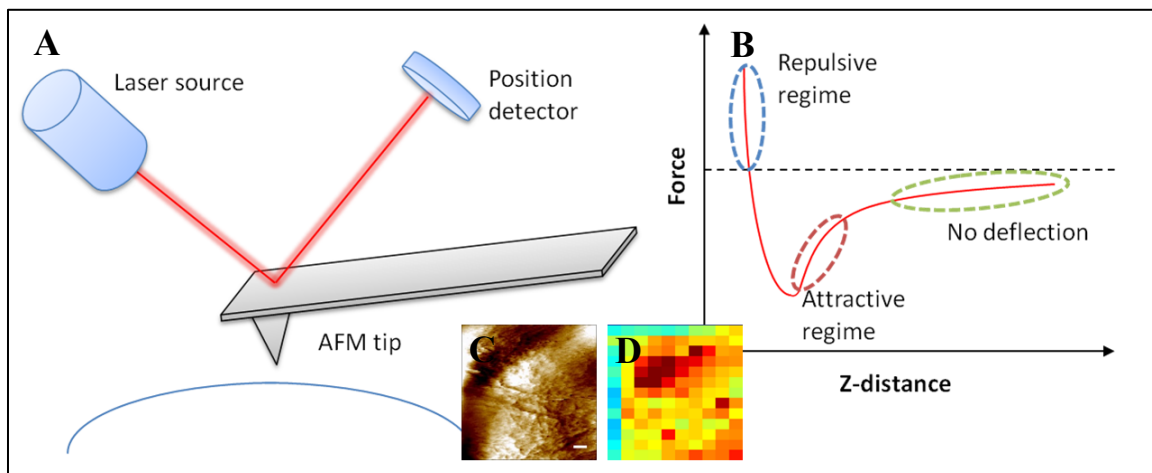


Figure 1.4. A schematic of the beam deflection system used in AFM (A) and a potential energy diagram of a probe and sample (B). Respective topographical image (C) and force map (D).

(10 – 30 nm) to move along the “grooves” or topography of a sample. The sample topography is relayed back to a computer and an image is created based on the distance the AFM tip moves in the Z-direction. Tip movement is usually measured by laser deflection off the back of the tip and onto a position sensitive detector (Figure 1.4-A). All of the collected data is then used to create an image of the surface that was probed by the AFM tip.

The force sensor for an AFM will only work if the probe tip can interact with the associated force field of a surface. A force distance curve is illustrated in Figure 1.4-B. In the repulsive regime (contact region), the AFM cantilever tip is held very close (just a few angstroms) to the sample surface and the interatomic forces between the cantilever and sample surface are repulsive (causing deflection) [46]. In the attractive regime (non-contact region), the tip is far away from the surface (tens to hundreds of angstroms) and the interatomic forces between the cantilever and sample surface are attractive [46].

When the tip is very far from the surface, there is no deflection. By using Hook's law, the stiffness cantilever, and the deflection distance [47], we can calculate the interatomic forces of the sample. Then by utilizing this force distance curve, one can begin to study the biomechanical properties of a biological sample (e.g. mammalian cells) [48].

AFM offers some advantages compared with other imaging techniques such as scanning electron microscopy. One advantage for AFM is that it can be used to image samples in fluids and therefore, biological samples can be imaged in near physiological conditions. Also, fluids can be changed or modified during scanning to image real-time processes. Since the introduction of AFM, as an imaging technique, there have been many studies of biological samples/materials [49]. Some examples of AFM characterization of biological materials included here are DNA/RNA, bacterial cells, cancerous cell lines, and viruses. The potential for new applications of AFM has expanded as it has been used across multiple disciplines compared to the traditional area for which it was originally designed [50].

AFM has been used to characterize synthetic DNA oligonucleotides adsorbed onto an electro-analytical sensor surface to better understand surface coverage, pores in the self-assembled layer, and areas where non-specific binding may occur [51]. A fundamental understanding such as this can enable better electro-analytical biosensors to be developed. AFM has been utilized to visualize the movement of RNA polymerase along a DNA template – aiding in understanding the cellular decision making process [52]. Circular plasmid DNA has been characterized before and after heat denaturing to reveal that DNA takes on a compact particle shape once denatured [53].

Bacillus spores were imaged via AFM to determine if characteristic surface features could be used to distinguish related species and the information rich surface can be used, with statistical analysis, to distinguish *B. anthracis* and close relatives [54]. Similarly, contrasts for Gram-positive and Gram-negative bacteria have been reported in air and in liquid environments with superior results depending on the method of bacterial culture [55]. AFM has shown the visible deterioration of the bacterial cell envelope to nitric oxide [56], oritavancin [57], natural herbs [58], and antimicrobials [59].

Breast cancer characterization of BT-20 cells has shown cellular uptake and internalization of poly-(ethylene glycol) or folic acid coated nanoparticles for targeted intracellular delivery [60]. AFM has been used in studies to view topographical features for J82 bladder cancer cells [61] and also to view anti-cancer drug induced cellular membrane changes in human cervical carcinoma, human hepatocellular liver, and rat glioma cells following treatment [62]. AFM studies have reported that cellular tumorigenicity and transformation have a decrease in cell modulus and elasticity – implicating these in cellular metastatic potential [63]. The above mentioned and other applications of AFM are providing new insights into the realm of cell biology [64].

1.6 ELECTRIC CELL-SUBSTRATE IMPEDANCE SENSING

Electric cell-substrate impedance sensing (ECIS) – is another electrical technique to monitor cellular behavior in real-time (Figure 1.1-D). The cells are modeled as disks and parameters for the cell membrane capacitance, barrier function, electron flow under the cells, and the tightness of attachment can be calculated. ECIS can also be used for electroporation and wounding cells on the working portion of the electrode.

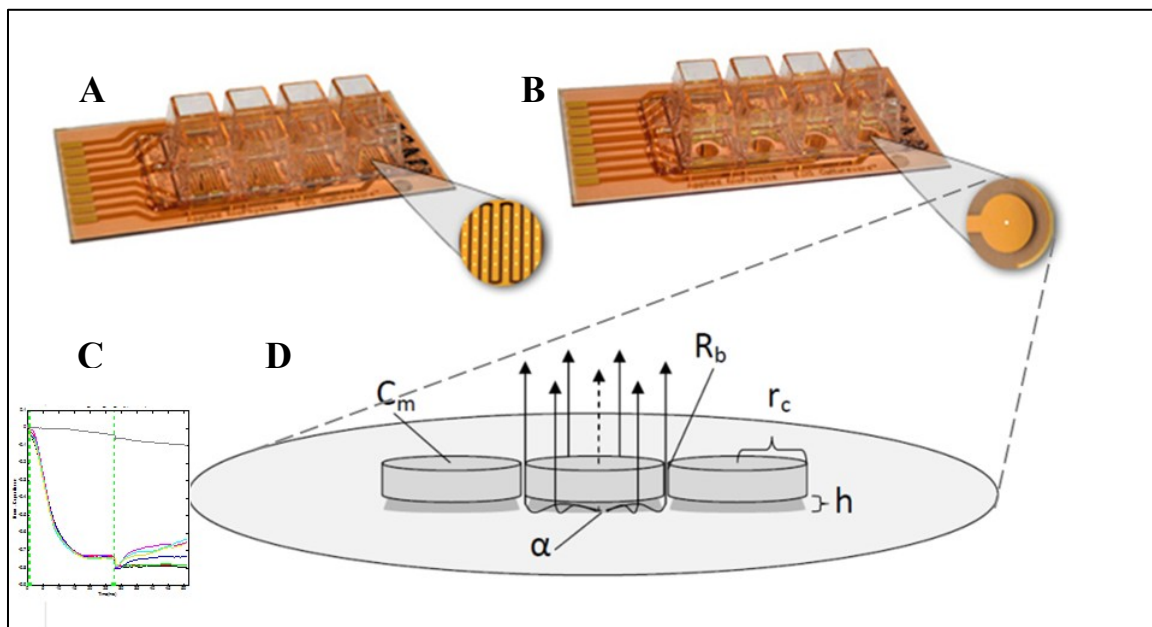


Figure 1.5. An 8W10E+ array containing >40 working electrodes (A), an 8W1E array with a single working electrode (B), ECIS time versus capacitance profile (C), and a simplified depiction of the ECIS model (D). Barrier resistance (R_b), current flow between the ventral side of the cell and the substratum (α), average capacitance of the cell plasma membrane (C_m), cell radius (r_c), and the average distance (h) between the electrode and the basal membrane of the cell. [image adapted from Applied BioPhysics, NY, USA].

Figure 1.5 illustrates ECIS arrays that contain multiple electrodes (Figure 1.5-A) or a single electrode (Figure 1.5-B). Also, a respective capacitance versus time profile is shown in Figure 1.5-C. A simplified example of the ECIS model is illustrated in Figure 1.5-D, where mammalian cells are modeled as spherical disks that have an insulated membrane surface and contain a conducting electrolyte (a more in-depth study of the model is developed in reference [65]).

Briefly, ECIS utilizes a mathematical model of impedance changes based on cell presence on the gold working electrode. Because the cells are attached to the gold working surface via focal adhesion plaques the cells are considered, for modeling

purposes, to be hovering above the surface substratum. Considering that the current changes are caused by the surface coverage of the electrode, a bare electrode is used as a reference and changes in the impedance are used to calculate the following morphological parameters; barrier resistance (R_b), the current flow between the ventral side of the cell and the substratum (α), and the average capacitance of the cell plasma membrane (C_m). R_b is important for endothelial and epithelial cell permeability. As related to r_c , α can be used to evaluate the average distance (h) between the electrode and the basal membrane of the cell. C_m gives the average capacitance of the cell plasma membrane, but cannot distinguish between the apical and basal membranes [65]. Furthermore, R_b (ohm cm^2) is related to cell-to-cell junctions and decreases with smaller cell-to-cell junction formation, α (ohm cm^2) is linearly related to r_c and inversely related to h by the equation $\alpha^2 = r_c^2 \times \rho/h$, where ρ is the resistivity of the medium, and C_m ($\mu\text{F}/\text{cm}^2$) is the average capacitance of the cell plasma membrane.

To more fully appreciate ECIS, it is helpful to understand what a typical time profile illustrates. For example, Figure 1.6-A and Figure 1.6-B illustrate ECIS time profiles for both resistance and impedance changes with cell adhesion and spreading. In Figure 1.6-A cells were inoculated at time zero and allowed to settle to the bottom of the wells and begin to attach and proliferate. This attachment and proliferation is illustrated by an increase in resistance with time, due to the thin barrier that the cells create above the electrode. Conversely in Figure 1.6-B the capacitance decreases, as we would expect for normal cell adhesion and proliferation during culture. To model our data and extract quantitative values, we utilized various frequencies (62.5, 125, 500, 1000, 2000, 4000, 8000, 16000, 32000, and 64000 Hz). Figure 1.6-C and Figure 1.6-D show the ratio of the

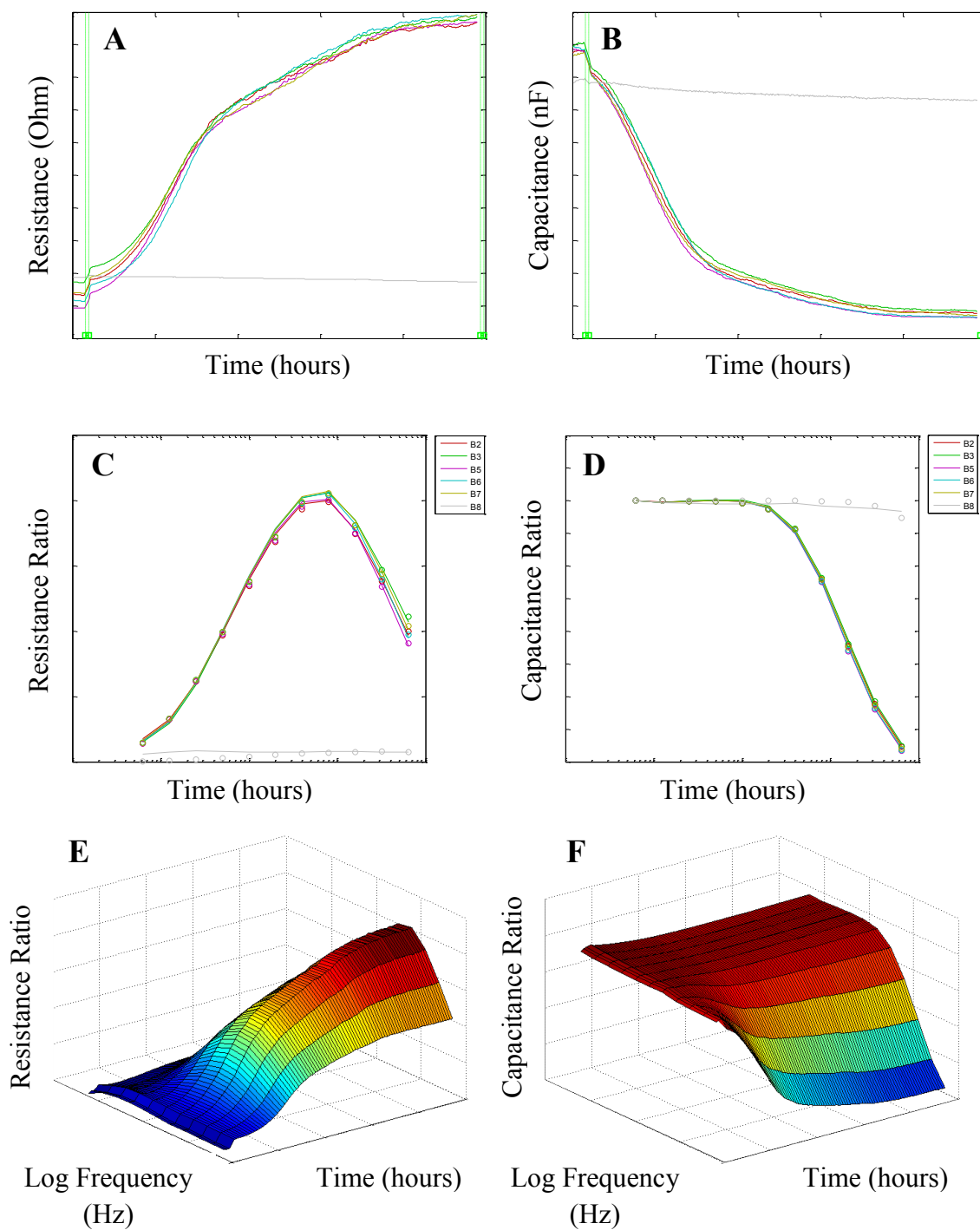


Figure 1.6. ECIS time profiles for resistance (A) and capacitance (B). Cell to cell-free ratio for confluent cells measured at different frequencies for resistance (C) and capacitance (D). Surface response for resistance (E) and capacitance (F) at each frequency and with respect to time.

cell covered well (“cell”) to the open wells (“cell-free”) for each frequency when the mammalian cells were completely confluent (~24 hours). Finally, Figure 1.6-E and Figure 1.6-F are response surface graphs of the change in cell to cell-free ratio with time and frequency. Cell to cell-free ratios were calculated using Applied BioPhysics – ECIS Software (v1.2.71.5, Applied BioPhysics, NY, USA). Figure 1.6-E illustrates that the greatest difference in the cell ratio, for resistance measurements, is at 4000 Hz and Figure 1.6-F shows the greatest difference, for capacitive measurements, is at 64000 Hz, respectively. Therefore, we have chosen to look at resistance values at 4000 Hz and capacitance values at 64000 Hz to get the most valuable information from our collected data.

1.6.1 Diesel exhaust particles

Diesel exhaust particles (DEP) are produced from compression-ignition engines that burn diesel fuels. It has been shown, that on the basis of equal horsepower, diesel engine exhaust is 100 times more toxic than gasoline engine exhaust [66]. In 1998 the California Environmental Protection Agency's Office of Environmental Health Hazard Assessment (OEHHA) completed a comprehensive health assessment of diesel exhaust and determined that DEP is an assorted mixture of gases and particulates with over 40 toxic air pollutants [67]. In humans, there are a number of these pollutants that have been shown to cause a range of illness and disorders ranging from cardiac, pulmonary, cancer, hypertension, neurotoxicity, prenatal health, and infertility [68]. Some of the pulmonary effects include: airway inflammation induced bronchial asthma [69], bacterial infection [70], endotoxic inflammation [71], and gene regulation [72]. We utilized DEP to incite

cytotoxic responses in human lung carcinoma (A549) cells and monitored the growth and viability responses using ECIS and RM with respect to exposure time and concentration.

1.6.2 Resveratrol

Figure 1.7, Resveratrol (3,5,4'-trihydroxystilbene), is a naturally occurring polyphenol, found in red grapes, peanuts, and other plant sources, that exhibits potential health benefits. Studied benefits include anti-oxidant, anti-inflammatory, cardio-protective, and anti-tumor activities [73] along with benefits against age-related diseases, like cancer, diabetes (type 2), cardiovascular, and neurological conditions [74]. Resveratrol has also been shown to target components for intracellular signaling pathways which include: pro-inflammatory mediators, apoptosis and cellular survival regulators, upstream kinases for angiogenic tumor and metastasis switches, and transcription factors and regulators [72]. In cultured cells, some specific anti-cytotoxic and -genotoxic effects range from cancer prevention due to increased metabolism of polycyclic aromatic hydrocarbons (PAH) by inhibiting cytochrome P450 enzymes [75, 76], by increasing phase II enzymes to excrete potentially harmful carcinogenic chemicals [77, 78], activate NAD⁺-dependent deacetylases which affect protein targets and other transcription factors [74], and stimulate endothelial nitric oxide synthase (eNOS) activity to catalyze nitric oxide (NO) formation [79, 80]. Our desire in this dissertation was to monitor *in vitro* protective effects of resveratrol treated human lung cells pre- and post-DEP exposure.

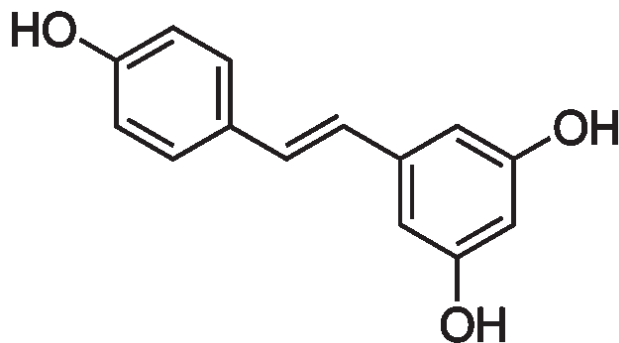


Figure 1.7. Chemical structure of resveratrol (3,5,4'-trihydroxystilbene) [Image courtesy of www.sigmaaldrich.com].

1.7 DISSERTATION OUTLINE

In Chapter 2, our research explored the interfacial electron transfer (ET) of DNA modified gold surfaces to better understand DNA-mediated electron transfer mechanism. Synthetic DNA was self-assembled on a gold substrate and then electrochemically studied. Cyclic voltammetry and electrochemical impedance spectroscopy were used to evaluate the effects of immobilization order on interface electron transfer related parameters. Scanning tunneling microscopy (STM) and Raman microspectroscopy were used to create topography and current images and to obtain a Raman spectrum and a spectral image.

The area of focus in Chapter 3 was to distinguish between Gram-positive and Gram-negative bacteria. Atomic force microscopy (AFM) and scanning electron microscopy (SEM) were used to collect topography images. Raman microspectroscopy was used to obtain characteristic spectra for both Gram-positive and Gram-negative bacteria. Raman spectral images were obtained for Gram-negative and co-cultured Gram-positive and negative bacteria. Raman spectral images were analyzed using direct classic least squares (DCLS) to separate Raman spectra based on pure reference spectra.

Fourier transform infrared (FTIR) spectroscopy was used to collect Gram-positive spectra and mapping on gold coated surface. A tandem AFM/Raman measurement of Gram-positive bacteria was collected to create a combined Raman spectral map and topography image.

In Chapter 4 we studied two mammalian cell lines with the goal to develop a combined Raman and AFM technique to detect subtle differences in the membrane components and nanomechanics of both; A549 and MDA-MB-435 (breast cancer ductal carcinoma) with and without expression of breast metastasis suppressor 1 (BRMS1) gene. We further explored ways to apply PCA for data mining and clustering.

The research focus in Chapter 5 was to employ AFM and fluorescent staining of MDA-MB-435 (435) and MDA-MB-435/BRMS1 (435/BRMS1) to look at alterations in cell topography and ultrastructures. Raman was used to compare spectroscopic bands between both cell lines 435 and 435/BRMS1. Electric cell-substrate impedance sensing (ECIS) was used to monitor cell line attachment, proliferation, and death during growth and wounding assays.

In Chapter 6, my research focused on a novel arrangement of ECIS and Raman microspectroscopy to explore cytotoxic response in A549 cell line exposed to diesel exhaust particles (DEP). I monitored cellular adhesion and growth, wound healing, toxic effects of DEP, and protective effects of resveratrol against DEP exposure. Confocal Raman spectra were acquired for different locations of the cell and relative Raman spectra locations and intensities are compared. Data mining was also used to cluster different monitored locations for the treated A549 cells.

In Chapter 7, I conclude with a brief review of the results from each of the technical chapters outlined above. I also explore some recommendations for future research.

1.8 REFERENCES

- [1] L.C.J. Clark, C. Lyons, *Ann. NY Acad. Sci.* 102 (1962) 29.
- [2] T.G. Drummond, M.G. Hill, J.K. Barton, *Nat. Biotechnol.* 21 (2003) 1192.
- [3] P. Coombe, B. Barber, C. Best, D. Brook, K. Sandeman, *Raman Spectroscopy, Dissemination of IT for the Promotion of Material Science, DoITPoMS, Department of Materials Science and Metallurgy, University of Cambridge, Cambridge, Mass, 2009.*
- [4] P.V. Huong, *Vib. Spectrosc.* 11 (1996) 17.
- [5] P.V. Huong, *Pharmaceut. Biomed.* 4 (1986) 811.
- [6] J. Wagner, *Appl. Surf. Sci.* 50 (1991) 79.
- [7] S. Jimenez-Sandoval, *Microelectr. J.* 31 (2000) 419.
- [8] A. Bertoluzza, C. Fagnano, P. Monti, R. Simoni, A. Tinti, M.R. Tosi, R. Caramazza, *Clin. Mater.* 9 (1992) 49.
- [9] G.D. Smith, R.J.H. Clark, *J. Archaeol. Sci.* 31 (2004) 1137.
- [10] H. Fabian, P. Anzenbacher, *Vib. Spectrosc.* 4 (1993) 125.
- [11] D. Pappas, B.W. Smith, J.D. Winefordner, *Talanta* 51 (2000) 131.
- [12] J.R. Baena, B. Lendl, *Curr. Opin. Chem. Biol.* 8 (2004) 534.
- [13] J. Ling, S.D. Weitman, M.A. Miller, R.V. Moore, A.C. Bovik, *Appl. Opt.* 41 (2002) 6006.
- [14] D.W. Ball, *Spectroscopy* 16 (2001) 32.
- [15] P. Carey, *Trac-Trend. Anal. Chem.* 2 (1983) 275.
- [16] P. Hildebrandt, S. Lecomte, C.L. John, *Encyclopedia of Spectroscopy and Spectrometry*, Elsevier, Oxford, 1999.
- [17] F.M. Lyng, E.Ó. Faoláin, J. Conroy, A.D. Meade, P. Knief, B. Duffy, M.B. Hunter, J.M. Byrne, P. Kelehan, H.J. Byrne, *Exp. Mol. Pathol.* 82 (2007) 121.

- [18] C.M. Krishna, G.D. Sockalingum, G. Kegelaer, S. Rubin, V.B. Kartha, M. Manfait, *Vib. Spectrosc.* 38 (2005) 95.
- [19] C. Yu, E. Gestl, K. Eckert, D. Allara, J. Irudayaraj, *Cancer Detect. Prev.* 30 (2006) 515.
- [20] K.W. Short, S. Carpenter, J.P. Freyer, J.R. Mourant, *Biophys. J.* 88 (2005) 4274.
- [21] H. Abramczyk, J. Surmacki, B. Brozek-Pluska, Z. Morawiec, M. Tazbir, *J. Mol. Struct.* 924-926 (2009) 175.
- [22] I. Notingher, *Sensors* 7 (2007) 1343.
- [23] C.A. Lieber, A. Mahadevan-Jansen, *Appl. Spectrosc.* 57 (2003) 1363.
- [24] J. Zhao, H. Lui, D.I. McLean, H. Zeng, *Appl. Spectrosc.* 61 (2007) 1225.
- [25] F.W.L. Esmonde-White, M.V. Schulmerich, K.A. Esmonde-White, M.D. Morris, *Automated Raman spectral preprocessing of bone and other musculoskeletal tissues, Optics in Bone Biology and Diagnostics*, SPIE, San Jose, CA, USA, 2009, p. 716605.
- [26] E.M. Kanter, S. Majumder, E. Vargis, A. Robichaux-Viehoever, G.J. Kanter, H. Shappell, I. Howard W. Jones, A. Mahadevan-Jansen, *J. Raman Spectrosc.* 40 (2009) 205.
- [27] C. Krafft, T. Knetschke, A. Siegner, R.H.W. Funk, R. Salzer, *Vib. Spectrosc.* 32 (2003) 75.
- [28] P.R. Carey, *J. Biol. Chem.* 274 (1999) 26625.
- [29] P. Rösch, M. Schmitt, W. Kiefer, J. Popp, *J. Mol. Struct.* 661-662 (2003) 363.
- [30] P. Rösch, M. Harz, M. Schmitt, K.-D. Peschke, O. Ronneberger, H. Burkhardt, H.-W. Motzkus, M. Lankers, S. Hofer, H. Thiele, J. Popp, *Appl. Environ. Microbiol.* 71 (2005) 1626.
- [31] J. De Gelder, K. De Gussem, P. Vandenabeele, M. Vancanneyt, P. De Vos, L. Moens, *Anal. Chim. Acta* 603 (2007) 167.
- [32] G.I. Petrov, R. Arora, V.V. Yakovlev, X. Wang, A.V. Sokolov, M.O. Scully, *P. Natl. Acad. Sci.* 104 (2007) 7776.
- [33] A. Tripathi, R.E. Jabbour, J.A. Guicheteau, S.D. Christesen, D.K. Emge, A.W. Fountain, J.R. Bottiger, E.D. Emmons, A.P. Snyder, *Anal. Chem.*, 81 (2009) 6981.
- [34] Z. Schmilovitch, A. Mizrach, V. Alchanatis, G. Kritzman, R. Korotic, J. Irudayaraj, C. Debroy, *Trans. ASAE* 48 (2005) 1843.

- [35] M. Çulha, A. Adigüzel, M.M. Yazici, M. Kahraman, F. Şahin, M. Güllüce, *Appl. Spectrosc.* 62 (2008) 1226.
- [36] J. Guicheteau, L. Argue, D. Emge, A. Hyre, M. Jacobson, S. Christesen, *Appl. Spectrosc.* 62 (2008) 267.
- [37] C. Yu, E. Gestl, K. Eckert, D. Allara, J. Irudayaraj, *Cancer Detect. Prev.* 30 (2006) 515.
- [38] P. Crow, N. Stone, C.A. Kendall, J.S. Uff, J.A.M. Farmer, H. Barr, M.P.J. Wright, *Brit. J. Cancer* 89 (2003) 106.
- [39] C.M. Krishna, G.D. Sockalingum, R.A. Bhat, L. Venteo, P. Kushtagi, M. Pluot, M. Manfait, *Anal. Bioanal. Chem.* 387 (2007) 1649.
- [40] K. Maheedhar, A.B. Rani, R. Malini, N.B. Prathima, K. Patil, K. Pralhad, C.M. Krishna, *Photomed. Laser Surg.* 26 (2008) 83.
- [41] C. Krafft, V. Sergo, *Spectroscopy: An International Journal*, 20 (2006) 195.
- [42] D.M. Nicholas, S.V. Julien, T.M. Eric, E. Madeleine, J.S. Elborn, J.M. John, *J. Phys. Chem. B* 113 (2009) 8137.
- [43] V. Backman, H.K. Roy, *Dis. Markers* 25 (2008) 279.
- [44] J.W. Chan, D.S. Taylor, S.M. Lane, T. Zwerdling, J. Tuscano, T. Huser, *Anal. Chem.* 80 (2008) 2180.
- [45] G. Binnig, C.F. Quate, C. Gerber, *Phys. Rev. Lett.* 56 (1986) 930.
- [46] A. Vilalta-Clemente, K. Gloystein, *Principles of Atomic Force Microscopy (AFM)*, Physics of Advanced Materials Winter School 2008, Thessaloniki, Greece, 2008.
- [47] B. Cappella, G. Dieter, *Surface Science Reports* 34 (1999) 1.
- [48] K.A. Addae-Mensah, J.P. Wikswo, *Exp. Biol. Med.* 233 (2008) 792.
- [49] D. P. Allison, N. P. Mortensen, C. J. Sullivan, M.J. Doktycz, *WIREs Nanomed. Nanobiotechnol.* 2 (2010) 618.
- [50] N.C. Santos, M.A.R.B. Castanho, *Biophys. Chem.* 107 (2004) 133.
- [51] A.M. Oliveira Brett, A.M. Chiorcea Paquim, V. Diculescu, T.S. Oretskaya, *Bioelectrochem.* 67 (2005) 181.
- [52] C.W. Gibson, N.H. Thomson, W.R. Abrams, J. Kirkham, *Gene* 350 (2005) 15.
- [53] S. Hou, K. Yang, Z. Liu, X.-Z. Feng, *J. Biochem. Biophys. Met.* 70 (2008) 1066.
- [54] R.A. Zolock, G. Li, C. Bleckmann, L. Burggraf, D.C. Fuller, *Micron* 37 (2006) 363.

- [55] M.J. Doktycz, C.J. Sullivan, P.R. Hoyt, D.A. Pelletier, S. Wu, D.P. Allison, *Ultramicroscopy* 97 (2003) 209.
- [56] S.M. Deupree, M.H. Schoenfish, *Acta Biomater.* 5 (2009) 1405.
- [57] O. Domenech, G. Francius, P.M. Tulkens, F. Van Bambeke, Y. Dufrière, M.-P. Mingeot-Leclercq, *BBA - Biomembranes* 1788 (2009) 1832.
- [58] X. Jiang, P. Yu, J. Jiang, Z. Zhang, Z. Wang, Z. Yang, Z. Tian, S.C. Wright, J.W. Larrick, Y. Wang, *Eur. J. Med. Chem.* 44 (2009) 2936.
- [59] A. da Silva, O. Teschke, *BB – Mol. Cell Res.* 1643 (2003) 95.
- [60] Y. Zhang, J. Zhang, *J. Colloid Interf. Sci.* 283 (2005) 352.
- [61] S.-H. Jung, J.-Y. Park, J.-O. Yoo, I. Shin, Y.-M. Kim, K.-S. Ha, *Ultramicroscopy* 109 (2009) 1428.
- [62] J. Wang, Z. Wan, W. Liu, L. Li, L. Ren, X. Wang, P. Sun, L. Ren, H. Zhao, Q. Tu, Z. Zhang, N. Song, L. Zhang, *Biosens. Bioelectron.* 25 (2009) 721.
- [63] E.M. Darling, S. Zauscher, J.A. Block, F. Guilak, *Biophys. J.* 92 (2007) 1784.
- [64] V. Shahin, N.P. Barrera, W.J. Kwang, *International Review of Cytology*, Academic Press, 2008.
- [65] I. Giaever, C.R. Keese, *P. Natl. Acad. Sci.* 88 (1991) 7896.
- [66] P. Gilman, Health assessment document for diesel engine exhaust, in: EPA/600/8–90/057F (Ed.), US Environmental Protection Agency, Washington, DC, 2002.
- [67] C.A.R. Board, Proposed identification of diesel exhaust as a toxic air contaminant, in: O.o.E.H.H.A. Air Resources Board (Ed.), California, 1998.
- [68] I.N. Krivoshto, J.R. Richards, T.E. Albertson, R.W. Derlet, *J. Am. Board. Fam. Med.* 21 (2008) 55.
- [69] M. Sagai, A. Furuyama, T. Ichinose, *Free Radical Bio. Med.* 21 (1996) 199.
- [70] X.J. Yin, C.C. Dong, J.Y.C. Ma, J.M. Antonini, J.R. Roberts, M.W. Barger, J.K.H. Ma, *Toxicol. Sci.* 88 (2005) 73.
- [71] H. Takano, R. Yanagisawa, T. Ichinose, K. Sadakane, S. Yoshino, T. Yoshikawa, M. Morita, *Am. J. Respir. Crit. Care Med.* 165 (2002) 1329.
- [72] J. Liu, M. Ballaney, U. Al-alem, C. Quan, X. Jin, F. Perera, L.-C. Chen, R.L. Miller, *Toxicol. Sci.* 102 (2008) 76.
- [73] J.K. Kundu, Y.-J. Surh, *Cancer Lett.* 269 (2008) 243.
- [74] F.Z. Marques, M.A. Markus, B.J. Morris, *Int. J. Biochem. Cell B.* 41 (2009) 2125.

- [75] Z.-H. Chen, Y.-J. Hurh, H.-K. Na, J.-H. Kim, Y.-J. Chun, D.-H. Kim, K.-S. Kang, M.-H. Cho, Y.-J. Surh, *Carcinogenesis* 25 (2004) 2005.
- [76] H.P. Ciolino, G.C. Yeh, *Mol. Pharmacol.* 56 (1999) 760.
- [77] M. Jang, L. Cai, G.O. Udeani, K.V. Slowing, C.F. Thomas, C.W.W. Beecher, H.H.S. Fong, N.R. Farnsworth, A.D. Kinghorn, R.G. Mehta, R.C. Moon, J.M. Pezzuto, *Science* 275 (1997) 218.
- [78] S.H.K. Yang, J S : Oh, T J : Kim, M S : Lee, S W : Woo, S K : Cho, H S : Choi, Y H : Kim, Y H : Rha, S Y : Chung, H C : An, S W, *Int. J. Oncol.* 22 (2003) 741.
- [79] C.M. Klinge, K.A. Blankenship, K.E. Risinger, S. Bhatnagar, E.L. Noisin, W.K. Sumanasekera, L. Zhao, D.M. Brey, R.S. Keynton, *J. Biol. Chem.* 280 (2005) 7460.
- [80] T. Wallerath, G. Deckert, T. Ternes, H. Anderson, H. Li, K. Witte, U. Forstermann, *Circulation* 106 (2002) 1652.

CHAPTER 2

IMMOBILIZATION, HYBRIDIZATION, AND OXIDATION OF SYNTHETIC DNA ON GOLD SURFACE: ELECTRON TRANSFER INVESTIGATED BY ELECTROCHEMISTRY AND SCANNING TUNNELING MICROSCOPY AND RAMAN MICROSPECTROSCOPY ¹**2.1 ABSTRACT**

Fundamental understanding of interfacial electron transfer (ET) among electrolyte/DNA/solid-surface will facilitate the design of sensors for the electrical detection of DNA molecules. In this report, the electron transfer characteristics of synthetic DNA (sequence from pathogenic *Cryptosporidium parvum*) self-assembled on a gold surface was electrochemically studied. The effects of immobilization order on the interface ET related parameters such as diffusion coefficient (D_0), surface coverage (θ_R), and monolayer thickness (d_i) were determined by cyclic voltammetry (CV) and electrochemical impedance spectroscopy (EIS). DNA surface density (Γ_{DNA}) was determined by the integration of the charge of the electro-oxidation current peaks during the initial cyclic voltammetry scans and was imaged via Raman microspectroscopy. It was found that the DNA surface density on the gold electrode (Au), at different modifications of synthetic double-stranded DNA (dsS-DNA) and 6-mercapto-1-hexanol (MCH), followed the order: $\Gamma_{\text{DNA}}(\text{dsS-DNA/Au}) > \Gamma_{\text{DNA}}(\text{MCH/dsS-DNA/Au}) > \Gamma_{\text{DNA}}(\text{dsS-DNA/MCH/Au})$. It was also revealed that the electro-oxidation of the DNA modified gold surface would involve the oxidation of nucleotides (guanine and adenine) with a rate constant of 5.51 electron transfer and the oxidative desorption of DNA and

¹ Gerald D. McEwen, Fan Chen, and Anhong Zhou, *Analytica Chimica Acta*, 643 (2009) 26-37.

MCH molecules by a 3 electron transfer rate constant. STM topography and current image analysis indicated that the surface conductivity after each surface modification followed the order: dsS-DNA/Au < MCH/dsS-DNA/Au < oxidized MCH/dsS-DNA/Au < Hoechst/oxidized MCH/dsS-DNA/Au. The results from this study suggest that varying the immobilization order on the gold surface may provide an alternative approach for the optimization of DNA hybridization and the further development for the electrical detection of DNA.

2.2 INTRODUCTION

Electrochemical biosensors play an important role in biological, pharmaceutical, clinical, and agricultural areas of study because of their association with viruses, microorganisms, and genetic and biological materials. The introduction of the electrochemical DNA hybridization biosensor initiated an area of research which has continually grown in popularity over the past decade [1]. Compared with other biosensing techniques, such as fluorescence-based DNA analysis, which has some limitations (e.g., expensive instrumentation and sophisticated numerical algorithms to interpret the data), electrochemical biosensors have gained great attention in molecular diagnostics due to their high sensitivity, small dimension, low cost, ease-of-use and compatibility with micro-fabrication, and integrated array technology [2, 3]. A basic DNA hybridization biosensor consists of single stranded DNA (ss-DNA) immobilized on a transducer surface which can then hybridize a complementary target DNA (t-DNA) sequence. The double strand DNA duplex, which is formed on the transducer surface, is known as a hybrid [4] and can be electrochemically studied by measuring the interfacial ET behaviors.

The DNA hybridization event can be converted into a measurable analytical signal via interaction with redox active molecules. Different redox active molecules, coupled with electrochemical techniques, can be used to specify and amplify detection signals. Metal complexes like hexaamineruthenium(III) chloride and tris(2,2'-bipyridyl) cobalt(III) perchlorate have shown that electrostatic binding to DNA is not affected with nucleic immobilization to an electrode surface [5]. Electroactive tags such as ferrocene yield higher electron transfer rates than $[\text{Ru}(\text{NH}_3)_6]^{3+}$ [6]. Cationic phenoxazine dyes such as methyl blue (MB) [7] and Nile blue (NB) have been utilized because of π -stacking intercalation [8]. External labels such as bisbenzimidazole dyes (Hoechst 33258) bind to the minor groove and are more selective than intercalators [9]. More recently, these external small electroactive molecules have been applied to probe the electron transfer characteristic of DNA lesion [10] and single base mutations [11] on a modified gold electrode surface.

Cryptosporidium parvum, a deadly waterborne pathogenic parasite, has been recognized by the World Health Organization as a significant global threat [12, 13]. There is an increasing need for fast, reliable, and cost-effective methods of detection. Electrochemical hybridization biosensors for the detection of *Cryptosporidium parvum* DNA have been reported. One approach utilized a metal complex, $\text{Co}(\text{phen})_3^{3+}$ to improve the signal of adsorptive immobilized probe DNA on a carbon paste transducer for the capture and detection of an rRNA oligonucleotide specific to *C. parvum* [14]. Another approach was a DNA-hybridization assay with electrochemical detection through covalent attachment on a gold location that was separate from the working electrode. An alkaline phosphatase conjugate was used to produce an electrochemically

active species, *p*-aminophenol (PAP_R) and *p*-aminophenyl phosphate (PAPP), for detection at the working electrode, which was amplified with time [15]. These reported electrochemical approaches to detect *C. parvum* DNA focused on the improvement of detection limits; however, they did not reveal specific interfacial electrochemical (or ET related) characteristics of *C. parvum* DNA.

Scanning tunneling microscopy (STM) has also been utilized to investigate modified and unmodified DNA with a variety of substrates [16, 17, 18]. This surface imaging technique offers the unique capability of high resolution imaging of DNA at the atomic or nanoscale, and provides insight into surface electric properties [16]. STM has also been used to observe the binding of Hoechst 33258 with DNA [19]. Raman microspectroscopy, a non-destructive vibrational/structural characterization method, was utilized to identify the characteristic Raman peaks of nucleotide bases [20].

In this study, we used synthetic DNA (40 bases) from the heat shocked protein (hsp 70) of the human genotype *C. parvum* (Genebank Access No. AF221535). Our present paper is divided into two main sections. In the first section, we investigated the interfacial electron transfer of DNA molecules at a gold modified electrode surface by electrochemical techniques. Then, in the second section, we investigated oxidation events that occurred at the gold surface by electrochemical techniques and scanning tunneling microscopy. A final section contains a Raman spectral image of a DNA immobilized gold surface. The ultimate goal of this work is to develop a highly specific and sensitive biosensor array to detect different genotypes of *C. parvum*. An understanding of the interfacial ET behaviors will assist to achieve this goal.

2.3 MATERIALS AND METHODS

2.3.1 Chemicals and reagents

All chemicals were of analytical reagent grade and were supplied by Sigma-Aldrich unless otherwise stated. Molecular biology grade water was used in all solutions. Probe DNA (5'-HS-(CH₂)₆-AAATCGAAGATCAATACATTTCTCTCGCCAGTTCCTTTCT-3'), target DNA (t-DNA), (5'-AGAAAGGAACTGGCGAGAGAAATGTATTGATCGATTT-3'), and synthetic double strand DNA (dsS-DNA), a complementary hybrid of the probe and target DNA, were synthesized and purified from SynGen Inc. (San Carlos, CA) and were diluted to a 100 mM concentration stock solution. The DNA stock solution was then diluted in 0.01 M PBS buffer to desired concentrations for further experiments. One millimolar 6-mercapto-1-hexanol (MCH) was prepared in molecular biology grade water. A 100 μM Hoechst 33258 solution was prepared by dissolving powder in 0.01 M phosphate buffered solution. Hoechst solution was stored at 4 °C and used within a 1-week period.

2.3.2 Surface treatment of gold electrode

A gold electrode (diameter 2 mm; 0.0314 cm²) was cleaned with piranha solution (75% H₂SO₄ + 25% H₂O₂) for 10 minutes to remove organic impurities and then rinsed with double distilled water (Milli-Q). *CAUTION*: Piranha solution reacts violently with organic solvents and is a skin irritant. Extreme caution should be exercised when making, storing (do not store air tight), and working with piranha solution. The gold surface was then 'renewed' by sequential hand polishing with a polishing kit (CHI120) (CH Instruments, Austin, TX, USA), with 1.0 micron alpha alumina powder on a nylon

polishing pad for ~60 seconds, then with 0.3 micron alpha alumina powder on a nylon polishing pad for ~90 seconds, and finally with 0.05 micron gamma alumina powder on a micro-cloth polishing pad for ~120 seconds. The gold surface was rinsed with double distilled water between each polishing step.

It has been discussed in the literature that effectiveness in the monolayer is correlated to the method of substrate preparation [21]. In order to reduce the surface roughness and improve reproducibility [22] the hand polished gold electrode was then electrochemically cycled (~ 15 cycles at 60 mV s^{-1}) from a potential of 0.0 to +1.57 V in 1 M H_2SO_4 solution until stable gold oxidation peaks at $\sim 1.06 \text{ V vs. Ag/AgCl}$ were observed. The reactivity of the gold electrode is distinctly affected by the presence of absorbed layers of organic contaminants used in the common polishing step [22, 23, 24]. In each cycle, a monolayer of chemisorbed oxygen was formed and reduced. The reduction charge per microscopic unit area has been experimentally determined as $390 \pm 10 \text{ } \mu\text{C cm}^{-2}$ [25]. The microscopic surface area was obtained by integrating the reduction current peak to obtain the reduction charge, and dividing this by $390 \text{ } \mu\text{C cm}^{-2}$. By this method, our polished gold electrode indicated a roughness of ca. 1.

2.3.3 DNA modification of gold electrode surface

Figure 2.1 is an illustration of the gold substrate modification that we used in this study. The freshly prepared gold electrode (step 1) was immersed in 1 μM ss-DNA in 0.01 M PBS buffer at 4 $^\circ\text{C}$ for 24 hours. The ss-DNA modified electrode was then rinsed with 0.01 M PBS, pH 7.4, to remove any probes that were non-specifically absorbed. The electrode was mounted in an electrode holder for CV and EIS measurements. Next, ss-DNA/Au electrode (step 2) was immersed in 1 mM MCH solution for a period of 1 to 12

hours, and then rinsed with PBS buffer to form MCH/ss-DNA/Au (step 3). After that, the resulting probe DNA modified gold electrode was then incubated with 2×SSC (saline sodium citrate) buffer containing t-DNA (1 μM) for 90 min at 37 °C with interval agitation. After the reaction, the substrate was washed with 2×SSC buffer solution to remove non-specifically bound DNA, to form a t-DNA/MCH/ss-DNA/Au (step 4) modification. After being rinsed with PBS buffer, the modified gold electrode was then immersed in a 100 μM Hoechst 33258 in 0.1 M KCl solution for 5 minutes at 25 °C to form the Hoechst/t-DNA/MCH/ss-DNA/Au (step 5) modification. The electrode was then rinsed with Tris-HCl (10 mM) buffer to remove non-specifically adsorbed Hoechst

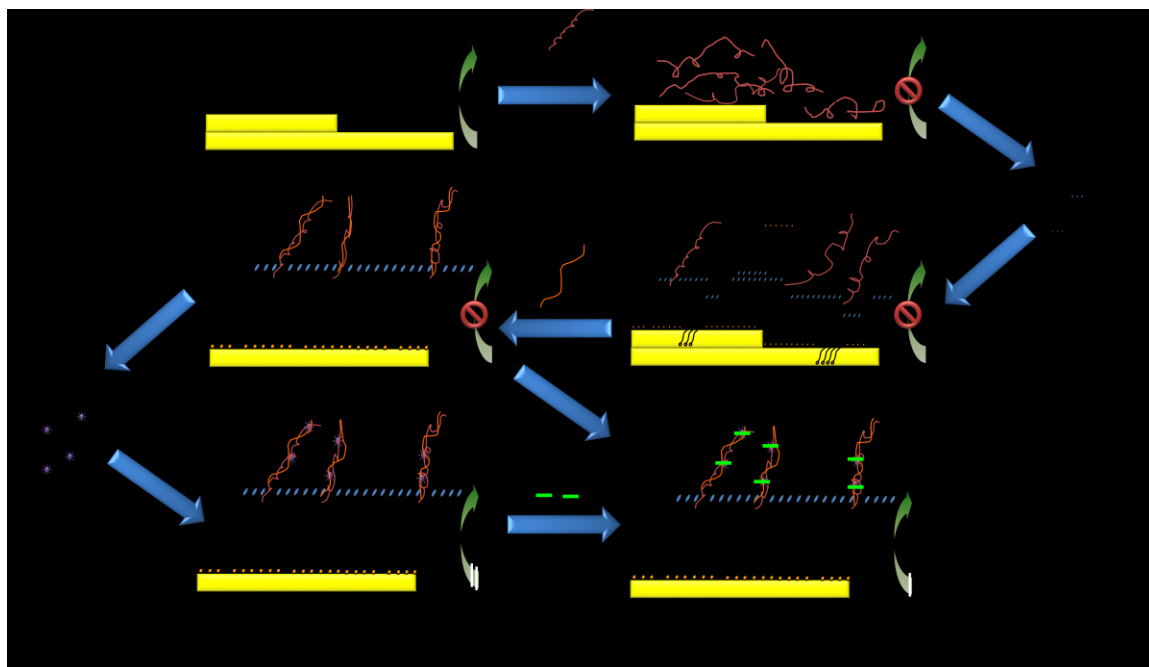


Figure 2.1. The sequential modification of the gold working electrode beginning with the bare Au substrate (1), addition of single strand-DNA (ss-DNA) (2), addition of 6-mercapto-1-hexanol (MCH) (3), hybridization with target-DNA (t-DNA) (4), binding Hoechst 33258 (5), and the cyclic voltammetric oxidation of the DNA modified on electrode surface (6).

33258. Finally, the Oxidation/Hoechst/t-DNA/MCH/ss-DNA/Au (step 6) modification was achieved by running cyclic voltammetry oxidation of the gold electrode surface (step 5) in 5 mM Na_2HPO_4 + 5 mM NaH_2PO_4 between 0 - 1.3 V at 30 mV s^{-1} to irreversibly oxidize Hoechst 33258 (bound to hybridized ds-DNA) [9] and/or oxidize immobilized DNA during the substrate gold oxidation [26]. All experiments were carried out at ambient laboratory temperature ($25 \text{ }^\circ\text{C}$). Finally, if necessary, the oxidized electrode surface (step 6) was re-immersed in 100 μM Hoechst 33258 solution for 5 min to see if the CV behavior changed after the DNA or bound Hoechst was oxidatively damaged.

2.3.4 Electrochemical measurements

Cyclic voltammetry (CV) was performed with a CHI 1220 Electrochemical Analyzer via the CHI software Version 4.30 (CH Instruments, Austin, TX, USA). Initial experiments were undertaken using a three-electrode setup consisting of a platinum wire counter electrode (CHI115), a Ag/AgCl reference electrode (CHI111), and a gold working electrode (CHI101) (CH Instruments, Austin, TX, USA). All potentials refer to the Ag/AgCl reference electrode. The CV curves were measured between 0.6 V and -0.1 V in a solution of 0.5 mM $\text{K}_3\text{Fe}(\text{CN})_6$ + 0.01 M PBS over a range of scan rates; 0.005, 0.01, 0.02, 0.03, 0.04, 0.05, 0.06, 0.08, 0.1, 0.15, 0.2, 0.3, and 0.4 V s^{-1} . Electrochemical impedance spectroscopy (EIS) was performed using a VMP2/Z multi-channel potentiostat (Princeton Applied Research, TN, USA) via the EC-Lab software Version 9.32 (Bio-Logic, France). These EIS measurements were conducted in a solution of 0.5 mM $\text{K}_3\text{Fe}(\text{CN})_6$ + 0.5 mM $\text{K}_4\text{Fe}(\text{CN})_6$ + 0.01 M PBS under an alternating current (AC) amplitude of 0.01 V and a frequency range from 100 kHz to 0.01 Hz. The EIS parameters

(R_{Ω} , C_d , R_{ct} , Z_W , K_a^0 , θ_R , and d_i) were obtained by modeling the EC-Lab data using ZSimpWin 3.21 (EChem Software, Ann Arbor, Michigan, USA).

2.3.5 Scanning tunneling microscopy

STM imaging for DNA/MCH coated Au (111) substrate in air was conducted with a PicoPlus AFM system (Agilent Technologies, AZ) with Picoscan 5.3 version data acquisition software. STM tips (Pt_{0.8}Ir_{0.2} wire) were used. The Au (111) substrate used for STM imaging consisted of a fresh mica substrate coated with a ~200 nm thick, gold deposited, layer (Agilent Technologies, AZ). Immediately before use, the gold substrates were annealed in a hydrogen flame for 90 seconds. A gas chamber was used to provide an argon environment, and an STM scanner with a maximum scan range of 1.5 μm was used. The annealed gold substrate was immersed in 1.0 μM of oligonucleotide solution (HS-ssDNA or HS-dsDNA) of 1.0 M phosphate buffer at 4 $^{\circ}\text{C}$ for different coating times. Then, the gold substrate was removed from the solution, rinsed thoroughly with distilled water, and dried in an argon gas stream. Unless otherwise stated, the images were acquired using the same parameters with the tip scanning from left to right. The scan rate was kept at 2.7~3.1 lines/second. The modifications of the Au (111) followed the same aforementioned procedure as the CV/EIS gold working electrode (polycrystalline gold surface).

2.3.6 Electron transfer characterization by CV and EIS

The association of electroactive species (Hoechst 33258) with DNA structure facilitates the electron transfer of immobilized DNA at the electrode surface. The

electrode reaction mechanisms of the electroactive species at the electrode surface can be determined by either CV or EIS measurements.

The Randles–Sevcik equation [27], Eq. 1, depicts a linear relationship between the peak current (i_p) and scan rate ($v^{1/2}$) where T is ~ 25 °C.

$$i_p = 2.69 \times 10^5 n^3 A D_0^{1/2} C v^{1/2} \quad (1)$$

In Eq. 1, n is the number of electrons transferred, A the area of the working electrode, and C the concentration of the redox species in solution. The slope can then be used to determine the rate of species diffusion, or the diffusion coefficient (D_0), of the electroactive species to or away from the electrode surface. The magnitude of D_0 reflects the mass transport characteristic of electroactive species diffusing to or away from the electrode surface.

The electron transfer through a DNA self-assembled monolayer on metal substrates has been intensively studied using EIS [28, 29, 30], and is generally described as an equivalent circuit model [31]. The basic equivalent circuit model (Randles model) consists of four components; the electrolyte resistance (R_Ω), charge-transfer resistance (R_{ct}), double-layer capacitance (C_d), and Warburg impedance (Z_W) due to mass transport at the electrode surface. A Nyquist plot, imaginary part (Z_{im}) versus real part (Z_{re}), was used for the impedance analysis. The Nyquist plot for an electrode is generally a semicircular region lying on the Z_{re} axis followed by a straight line. The semicircle portion, measured at higher frequencies, corresponds to a direct electron transfer limited process, whereas the straight linear portion, observed at lower frequencies, represents a diffusion-controlled electron transfer process. Modification of the working electrode

surface with an organic layer tends to decrease the double layer capacitance and delays the interfacial electron transfer rate as compared to a bare working electrode [32, 33, 34].

The general features of the Nyquist plot are understood intuitively [35]. The imaginary component of the impedance comes solely from C_d . The C_d contributions fall to zero at high frequencies because it offers no impedance. All the current is the charging current, and the only impedance seen is the ohmic resistance. As the frequency continues to drop, the finite impedance of C_d is manifest as a significant Z_{im} . At the very low frequencies, the capacitance (C_d) offers high impedance; hence the flow passes mostly through R_{ct} and R_Ω . Therefore, the imaginary impedance component falls off again. Generally, a departure from the low frequency regime is expected and the Warburg impedance (Z_W) will become important [31]. When the Nyquist data is modeled, the above mentioned parameters are determined and can be further explored.

Kinetic parameters related to the electron transfer at the DNA modified electrode surface can also be obtained by EIS analysis. The heterogeneous standard charge-transfer rate constant (K_a^0) was obtained by using Eq. 2 [27],

$$R_{ct} = \frac{RT}{n^2 F^2 A K_a^0} \frac{1}{C_0^{*(1-\alpha)} C_R^\alpha} \quad (2)$$

where the charge-transfer coefficient α is assumed to be 0.5, $C_0^{*(1-\alpha)} = C_R^\alpha = C_0$, C_0 being the concentration of the bulk solution. The other constants in Eq. 2 are as follows; $T = 298$ K, $A = 0.0314$ cm², $n = 1$ (for the Fe(CN)₆^{3-/4-} redox probe used here), F Faraday's constant (96485 C mol⁻¹), and R universal gas constant (8.31 J mol⁻¹ K⁻¹)

Furthermore, the surface coverage (θ_R) for each addition to the monolayer was calculated by using Eq. 3 [36], where R_{ct}^{Au} and R_{ct}^{SAM} are the charge-transfer resistance

values for the bare and DNA-modified Au electrode, respectively. An increase in R would yield a decrease in D_0 .

$$\theta_R = 1 - \frac{R_{ct}^{Au}}{R_{ct}^{SAM}} \quad (3)$$

On the other hand, Eq. 4 was used [37] to estimate the monolayer thickness (d_i) from the capacitance values:

$$d_i = \frac{\epsilon_0 \epsilon_i A}{C_d} \quad (4)$$

where d_i is the thickness of the i th layer, C_d is the differential capacitance of the double layer, ϵ_0 is the permittivity of free space ($8.854 \times 10^{-12} \text{ s}^4 \text{ A}^2 \text{ kg}^{-1} \text{ m}^{-3}$), ϵ_i is the dielectric constant of the layer, and A is the electrode area (0.0314 cm^2). For our calculations, we use the dielectric constant of water (80) as the ϵ_i value [38].

2.3.7 Raman microspectroscopy

Raman spectra were recorded using a Renishaw inVia Raman microscope (controlled by WiRE 3.0 software) equipped with a 785 nm near-IR laser. Laser light was focused through a Leica 50×0.75 N PLAN optical glass microscope objective. Rayleigh scattering was eliminated by the use of filters. Within the spectrometer, Raman scattering passed through a 50 μm slit, then was collected and dispersed by a holographic diffraction grating (1200 l/mm), and finally the entire Raman shift was recorded as a spectrum by a thermoelectrically cooled charge coupled device (CCD). The instrument was wavelength calibrated with silicon at a static spectrum centered at 520.5 cm^{-1} for 1 second. The Au (111) mica slide was mounted on a standard stage (Leica 11501200) of the Olympus microscope, focused under the collection assembly, and spectra were collected in static

mode of 1 accumulation at 5 second laser exposure at a fixed wavenumber range of 760.4 cm^{-1} .

2.4 RESULTS

2.4.1 STM image of DNA immobilized on Au (111)

Figure 2.2 gives the STM topography images of Au (111) surface with different modifications under constant current mode: (A) bare Au (111), (B) ss-DNA modified 13 hour, (C) MCH modified 6 hour, (D) ss-DNA 24 hour/MCH 6 hour, (E) ds-DNA 24 hour, (F) ds-DNA 24 hour/MCH 6 hour, (G) MCH 6 hour/ds-DNA 24 hour. Figure 2.2 (A) illustrates the atomically flat Au (111) surface with a depth of $\sim 2.5 \text{ \AA}$ between two adjacent terraces. The surface topography modified with 40 base pair ss-DNA is shown in Figure 2.2-B. The gold atom layers are still observed and wave-like features appear on the flat gold surface which is related to the immobilized ss-DNA. The zig-zag-like structure [39] was observed on the Au (111) surface for shorter DNA oligonucleotide as well (not shown). Compared to ss-DNA modification, MCH modification presents smoother surface features; however, MCH modification is rougher than the bare Au (111). It is expected that MCH, like other alkanethiol molecules, form self-assembled monolayer structures on the gold surface after 6 hour immobilization. However, the immobilizations of ss-DNA for 24 hours and then subsequent MCH for 6 hours result in atomically flat, non-distinctive, gold layers shown in Figure 2.2-D. This observation is because the MCH molecules have filled in the boundaries of the gold atom layers. The role of MCH in DNA immobilization is to remove any non-specifically bound ss-DNA from the gold surface by replacement of ss-DNA [5].

Different surface topography features are observed for the synthetic double strand DNA (denoted as dsS-DNA) modified Au (111) surface. Immobilization of dsS-DNA for 24 hours forms DNA cluster structures which aggregate on the Au (111) surface, as indicated in Figure 2.2-E.

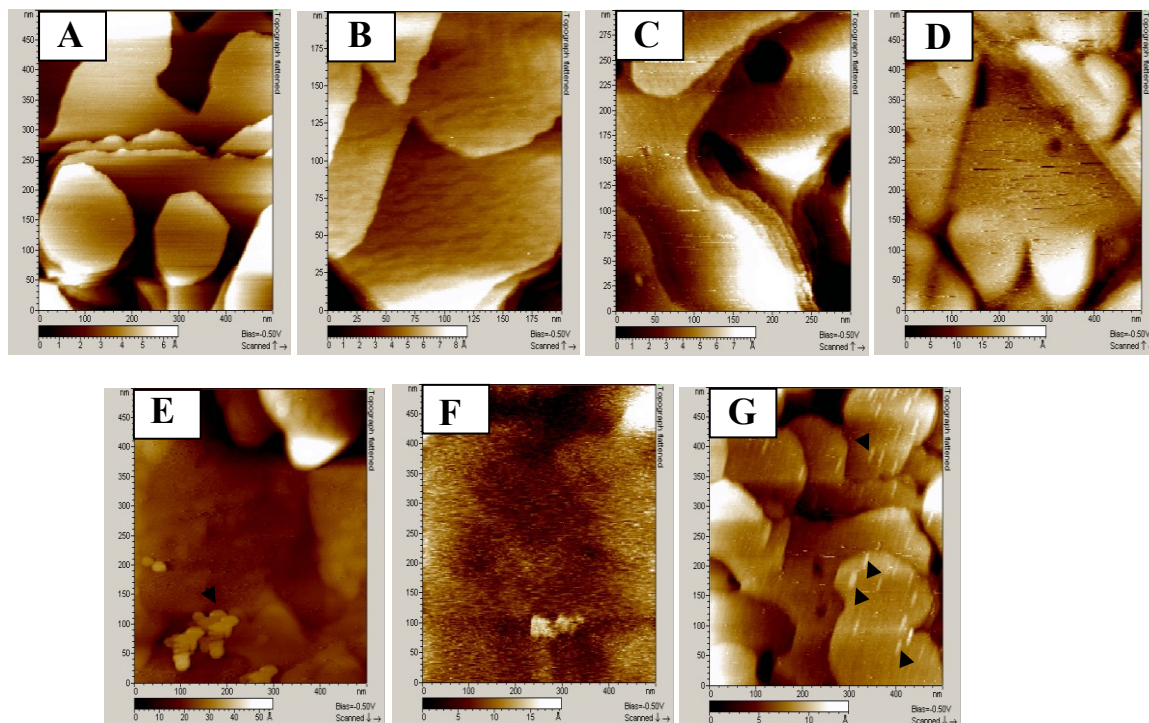


Figure 2.2. STM topography images of (A) bare Au (111) electrode (-0.5 V, 0.01 nA), (B) ss-DNA modified 13 hr (-0.5 V, 0.03 nA), (C) MCH modified 6 hr (-0.5 V, 0.01 nA), (D) ss-DNA 24 hr/MCH 6 hr (-0.5 V, 0.03 nA), (E) dsS-DNA 24 hr (-0.5 V, 0.05 nA), (F) dsS-DNA 24 hr/MCH 6 hr (-0.5 V, 0.05 nA), (G) MCH 6 hr/dsS-DNA 24 hr (-0.5 V, 0.05 nA). The numbers in parenthesis are the bias and tunneling current set points under which the images are collected. All coatings of DNA and MCH are conducted in 5 mM phosphate buffer. dsS-DNA is designated as the synthetic double strand DNA. Arrow in (E) indicate the DNA cluster structures and aggregates. The arrows in (G) show the rod-like structure.

The cross section analysis from one of these clusters (not shown here) indicates a size of 20×10 nm (length \times height), which is similar in size for ds-DNA imaged by STM in air [40], but much larger than the heights for ds-DNA imaged by AFM [41]. For AFM investigation in air, the heights for ds-DNA immobilized on a solid substrate vary from 0.5 to 1.9 nm [41], which is smaller than the helix diameter, probably due to elastic deformations of the ds-DNA caused by the AFM tip [41]. The ds-DNA, “forest” as shown in Figure 2.2-F, is observed for the coating of dsS-DNA for 24 hours, followed by MCH for 6 hours. Figure 2.2-F and -D give different surface topography features, respectively, for the dsS-DNA and ss-DNA confined gold surfaces. In both cases, the DNA molecules are perpendicularly oriented to the electrode surface due to the replacement by MCH. The former produces more densely packed DNA molecules and no observable gold atom layer as compared with the latter where the terrace of the gold atom layer is vague yet distinguishable. If the coating order is reversed with MCH for 6 hours and then dsS-DNA for 24 hours, then 20×10 nm (length \times width) rod-like structures are observed, as in Figure 2.2-G. Similar rod-like structures have been reported in literature for ds-DNA with mercapto-hexyls on the 5' end of each chain [40]. It is apparent that by reversing the immobilization order between MCH and dsS-DNA yields visible differences seen in AFM surface topography.

2.4.2 Electron transfer behaviors of the Hoechst/t-DNA/MCH/ss-DNA modified electrode surface

Figure 2.3 illustrates cyclic voltammograms in 0.5 mM $K_3Fe(CN)_6$ + 0.01 M PBS of the sequentially modified gold electrode. The electrochemical behaviors of the

electroactive $\text{Fe}(\text{CN})_6^{3-/4-}$ redox couple is used to reflect the ET characteristic of the gold surface at each modification. As for bare Au (curve 1), a pair of redox peaks for $\text{Fe}(\text{CN})_6^{3-/4-}$ appeared at 0.176 V and 0.263 V at a scan rate (ν) of 60 mV s^{-1} giving a formal potential $E^{0'}$ of 0.22 V and the peak potential difference ΔE_p of 0.087 V. The ΔE_p increased with increasing the scan rate and the peak current was directly proportional to $\nu^{1/2}$ (Figure 2.3 insert), which indicates a quasi-reversible surface electrode process [8].

After the immersion in $1 \mu\text{M}$ ss-DNA for 24 hours, ss-DNA/Au (curve 2), there was a decrease in the redox peak current and an increase in the ΔE_p . This could be attributed to a modification of the gold surface with the 5'-end thiolated 40-mer ss-DNA (via gold-thiol bond) that blocks the interfacial electron transfer between the gold surface and bulk solution [42]. Next, with the addition of 1 mM MCH for 1 hour to form MCH/ss-DNA/Au, the redox peaks are completely suppressed (curve 3), which indicate further coverage by MCH on the gold surface. As mentioned previously for the STM work, it is believed that MCH plays a two-fold role in the treatment of ss-DNA modified electrodes. First, it can take part in the replacement of thiolated ss-DNA (via thiol-thiol exchange) to remove or decrease non-specifically bound ss-DNA, and second, it can form a barrier (via the gold-thiol bond) to electron transfer [42]. Next, the probe DNA modified gold electrode is then immersed in $1 \mu\text{M}$ t-DNA in $2\times\text{SSC}$ hybridization buffer for 1.5 hours to form t-DNA/MCH/ss-DNA/Au (curve 4).

At this stage a ds-DNA duplex is formed, yet the $\text{Fe}(\text{CN})_6^{3-/4-}$ redox peaks remained negligible. The DNA prevents a redox response of the bulk solution (potassium

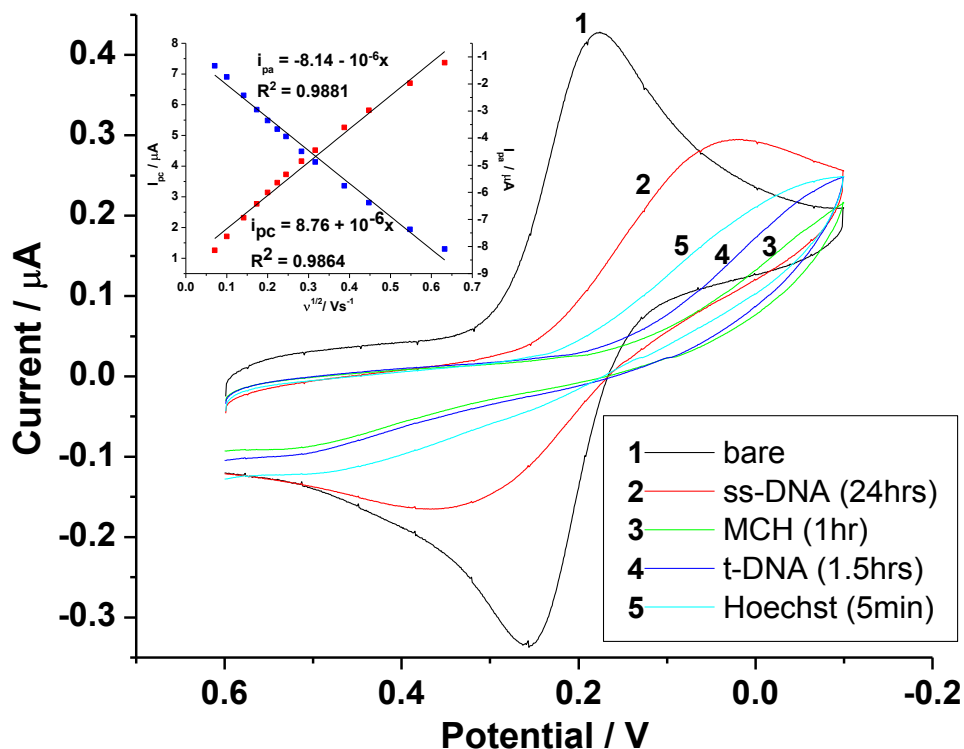


Figure 2.3. Voltammetric behaviors of $\text{Fe}(\text{CN})_6^{3-/4-}$ redox couple (0.5 mM $\text{K}_3\text{Fe}(\text{CN})_6$ + 0.01 PBS) on step-by-step ss-DNA modified electrodes. The data corresponds to electrode modifications: bare Au (1), ss-DNA/Au (2), MCH/ss-DNA/Au (3), t-DNA/MCH/ss-DNA/Au (4), and Hoechst/t-DNA/MCH/ss-DNA/Au (5) (all scans performed in 0.5 mM $\text{K}_3\text{Fe}(\text{CN})_6$ + 0.01 M PBS, pH 7.4; at scan rate 60 mV s^{-1}). Inset: Dependence of i_{pa} and i_{pc} on $v^{1/2}$, for scan rates; 0.005, 0.01, 0.02, 0.03, 0.04, 0.05, 0.06, 0.08, 0.1, 0.15, 0.2, 0.3, and 0.4 V s^{-1} .

ferricyanide ions) after the immobilization or hybridization of DNA on the gold electrode surface [24]. Finally, the interaction of $100 \mu\text{M}$ Hoechst 33258 with the t-DNA hybridized gold surface for 5 minutes (curve 5, Hoechst/t-DNA/MCH/ss-DNA/Au) restores some of the modified surface conductivity, as compared with curve 4. This

means that Hoechst bound ds-DNA duplexes facilitate the interfacial electron transfer reaction [9].

Table 2.1 lists the calculated diffusion coefficient (D_0) of the $\text{Fe}(\text{CN})_6^{3-/4-}$ ions obtained by cyclic voltammetry and the Randles-Sevick equation (Eq. 1). For simplicity, the cathodic peak currents were used in this calculation. The bare gold electrode gives rise to D_0 of $6.59 \times 10^{-6} \text{ cm}^2 \text{ s}^{-1}$, which is close to the literature reported value [43]. After ss-DNA immobilization, D_0 decreases to $1.54 \times 10^{-6} \text{ cm}^2 \text{ s}^{-1}$ because the DNA layer acts as a barrier to block the diffusion of electroactive $\text{Fe}(\text{CN})_6^{3-/4-}$ ions at the ss-DNA modified gold surface. This role is further evidenced by the subsequent immobilization of MCH and the t-DNA hybridization where no D_0 values are obtained. However, D_0 returns to a very low level of $9.3 \times 10^{-9} \text{ cm}^2 \text{ s}^{-1}$ after Hoechst binds with the hybrid ds-DNA duplex.

Figure 2.4 shows the EIS Nyquist plots after each electrode modification as described in Figure 2.3. Bare Au (curve 1) possesses a straight line in the low frequency region with unit slope, but has no semicircular portion in the higher frequency region.

Table 2.1. Diffusion coefficients (D_0) for successive modifications on bare gold by ss-DNA, MCH, t-DNA, and Hoechst binding.

Step	Modifications	$D_0^{\text{a}} / \text{cm}^2 \text{ s}^{-1}$
1	Bare gold	6.59E-06
2	ss-DNA	1.54E-06
3	MCH	undetectable
4	t-DNA	undetectable
5	Hoechst	9.30E-09

^aCalculated from Equation 1 by using cathodic peak currents.

The low frequency signal indicates that the redox couple electron transfer process is diffusion-controlled. On the other hand, for the ss-DNA/Au (curve 2) modified electrode immersed in $1\mu\text{M}$ ss-DNA for 24 hours, there is a semicircular portion in the higher frequency region, which corresponds to a direct electron transfer limited process, and a

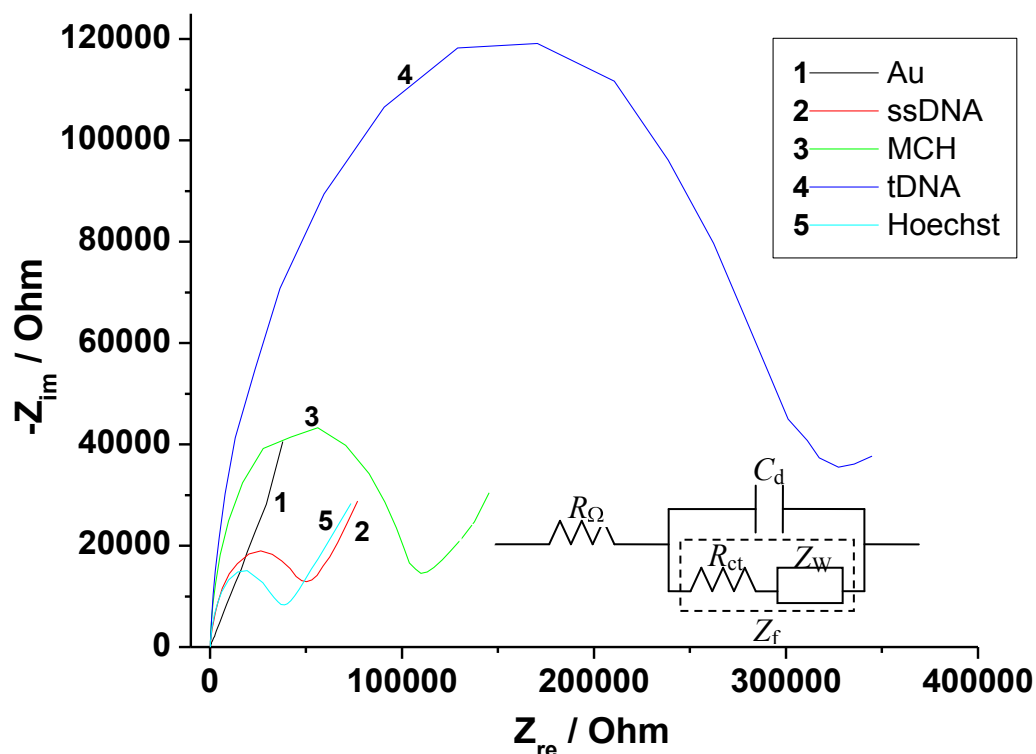


Figure 2.4. Electrochemical impedance spectroscopy (EIS) of step-by-step ss-DNA modified electrodes: bare Au (1), ss-DNA/Au (2), MCH/ss-DNA/Au (3), t-DNA/MCH/ss-DNA/Au (4), and Hoechst/t-DNA/MCH/ss-DNA/Au (5). Inset: modified equivalent Randles circuit used to model impedance data; R_{Ω} , electrolyte resistance; Z_w , Warburg impedance; R_{ct} , charge-transfer resistance; and C_d , double-layer capacitance. The coating conditions are the same as Figure 2.3. EIS was conducted in $0.5\text{ mM K}_3\text{Fe}(\text{CN})_6 + 0.5\text{ mM K}_4\text{Fe}(\text{CN})_6$ in 0.01 M PBS , pH 7.4 with 10 mV AC amplitude.

straight line in the low frequency region which represents a diffusion-controlled electron transfer process.

After immersion in 1 mM MCH for 1 hour, MCH/ss-DNA/Au (curve 3), the semicircular portion in the higher frequency region increased and the straight line in the low frequency region has a decreasing slope. For the hybridization with 1 μ M t-DNA for 1.5 hours, t-DNA/MCH/ss-DNA/Au (curve 4), the semicircular portion in the higher frequency region increased substantially revealing increased barrier properties of the resultant hybridized ds-DNA duplex on the modified gold surface. The effect of immersion in 100 μ M Hoechst for 5 minutes on the hybridized ds-DNA is evidenced in curve 5 (Hoechst/t-DNA/MCH/ss-DNA/Au) where there is a greater decrease in the semicircular portion. The insert in Figure 2.4 is the modified Randles circuit used to model the EIS data.

The values for circuit components R_{Ω} , C_d , R_{ct} , Z_W , K_a^0 , R , and d_i are listed in Table 2.2. For this set of experiments, the solution resistance (R_{Ω}) had an average value of 155.2 Ω , which is expected for measurements under identical experimental conditions. The interfacial double-layer capacitance (C_d) for the bare gold electrode is estimated at 1.12 μ F, which is in the range of 20~50 μ F cm^{-2} [44] (considering our electrode geometric area 0.0314 cm^2). C_d increases to 9.64 μ F with the ss-DNA modification due to the fact that ss-DNA is a charged macromolecule, then this value decreases to 2.92 μ F with the subsequent MCH modification due to the replacement of ss-DNA by MCH, and increases to 3.76 μ F after the formation of the hybrid ds-DNA duplex, and remains constant (3.75 μ F) with the final binding of Hoechst. It is not surprising that Hoechst

interaction does not affect the C_d due to Hoechst attachment with the inner duplex of the helical ds-DNA via a minor groove binding mechanism [9], and this binding may not significantly change the surface charge of the ds-DNA modified electrode surface. The electron transfer characteristics of the step-by-step modification could be reflected by the changes in the charge transfer (R_{ct}) and heterogeneous charge-transfer rate constant (K_a^0), which are associated with each other by Eq. 2. In each step, from bare gold to t-DNA, the modification results in the rapid increase of R_{ct} and an inversely significant decrease in K_a^0 . For example, the immobilization of ss-DNA on the bare gold surface leads to a 37-fold increase of R_{ct} , from 1 k Ω to 37 k Ω ; correspondingly, K_a^0 decreases from 1.51×10^{-2} cm s $^{-1}$ to 4.54×10^{-4} cm s $^{-1}$ (approximately a two order of magnitude decrease). The subsequent increase of R_{ct} (or decrease of K_a^0) is due to the formation of the thiolated ss-DNA layer on the gold surface after this modification, which prevents the electron transfer of the redox couple $\text{Fe}(\text{CN})_6^{3-/4-}$ at the modified Au/solution interface. It is interesting to note that the binding of Hoechst to the hybridized ds-DNA duplex yields an approximate 10-fold decrease of R_{ct} (conversely a ~ 10 -fold increase of K_a^0), compared to that obtained from the t-DNA/MCH/ss-DNA/Au modified surface. This is evidence that the binding of Hoechst to the ds-DNA on the modified gold surface increases conductivity, and thus facilitates the ET of $\text{Fe}(\text{CN})_6^{3-/4-}$ at this modified electrode surface. This effect is seen in the restored D_0 value (Table 2.1) after the Hoechst binding. There is not much change in the Warburg impedance (Z_W) and the electrolyte resistance (R_Ω) for each modification, except the variations in R_Ω and Z_W after the t-DNA hybridization step.

Table 2.2. Diffusion coefficients (D_0) for successive modifications on bare gold by ss-DNA, MCH, t-DNA, and Hoechst binding.

Step	Modifications	${}^{\forall}R_{\Omega} / \Omega$	${}^{\forall}C_d / \mu\text{F}$	${}^{\forall}R_{ct} / \Omega$	${}^{\forall}Z_w / \mu\Omega \text{ s}^{-1/2}$	${}^{\xi}K_a^0 / \text{cm s}^{-1}$	${}^{\epsilon}\theta_R$	${}^{\psi}d_i / \text{nm}$
1	Bare gold	147.9	1.12	1120	80.4	1.51E-02	-	-
2	ss-DNA	150.2	9.64	37360	68.7	4.54E-04	0.970	2.31
3	MCH	145.7	2.92	95930	63.9	1.77E-04	0.988	7.63
4	t-DNA	184.5	3.76	255400	32.3	6.63E-05	0.995	5.92
5	Hoechst	147.9	3.75	32360	72.7	5.24E-04	0.965	5.93

${}^{\forall}$ Calculated based on the modified Randles equivalent circuit; ${}^{\xi}$ Calculated using Equation 2; ${}^{\epsilon}$ Calculated using Equation 3; and ${}^{\psi}$ Calculated using Equation 4.

It is also found that there are changes in surface coverage (θ_R) and thickness (d_i) for each modification of the gold electrode surface (Table 2.2). For each modification step, the values for both θ_R and d_i are calculated from Eq. 3 and 4. The initial immobilization of ss-DNA results in θ_R of 0.97 and d_i of 2.31 nm. The subsequent modification with MCH may replace some immobilized ss-DNA and/or non-specifically bound ss-DNA to allow more ss-DNA molecules to stand-up vertically due to charge repulsion (step 3 in Figure 2.1). Therefore, it is not surprising to observe a slight increase in θ_R (to 0.988) and a significant increase in d_i (to 7.63 nm), the latter resulting in a thickness increase (Δd_i) of 5.32 nm due to the MCH modification. Considering that the estimated (or theoretical) thickness of MCH is closer to a height of 7~8 Å (with a 30° tilt angle toward the substrate), this increased thickness would imply the formation of a multi-layer MCH structure as seen in step 3 of Figure 2.1, similar to other thiol multi-layers formed on gold surfaces [45, 46, 47]. This multi-layer MCH structure could be due to hydrogen bonding between the -O~H and -S~H that exist between the inter-layer MCH molecules. This hypothesis of multi-layer MCH structures will need to be further

verified by other surface analysis tools such as X-ray photoelectron spectroscopy (XPS), and/or ellipsometry. The further hybridization of t-DNA with MCH/ss-DNA/Au causes a slight increase of θ_R from 0.988 to 0.995 despite a decrease in d_i from 7.63 nm to 5.92 nm. It is understandable that the formed ds-DNA duplex might have a decreased thickness compared to the MCH/ss-DNA/Au, where MCH helps the ss-DNA to orient vertically. After the hybridization with t-DNA, the resulting ds-DNA would have an increased probability to orient more parallel to the electrode substrate surface, which could account for the decreased thickness at the ds-DNA/MCH/ss-DNA/Au modification. On the other hand, during hybridization, the t-DNA could replace the multi-layer MCH structures previously formed on the modified gold surface shown in step 3 of Figure 2.1. This replacement would also result in the decrease of the layer thickness. The K_a^0 value increases about by one order of magnitude with the binding of Hoechst to the ds-DNA (due to the increase of the conductivity of the bound ds-DNA duplex), at this modification step, the interfacial double layer capacitance C_d (3.75 μF) and layer thickness d_i (5.93 nm) remain unchanged. This reaffirms the idea that Hoechst binding within the minor groove [48, 49] of the helical structure of the hybrid ds-DNA duplex does not significantly change C_d and d_i but facilitates the interfacial electron transfer indicated by an increase in K_a^0 .

2.4.3 Electron transfer behaviors of the Hoechst/CV oxidation/Hoechst/MCH/dsS-DNA modified electrode surface

To compare the ET characteristic difference between ss- and ds-DNA, the electrochemical behaviors of synthetic ds-DNA (“dsS-DNA”) were also investigated. This ds-DNA duplex was formed by the hybridization of ss-DNA (probe DNA) with t-

DNA (each 40 base pairs). Figure 2.5 depicts cyclic voltammograms of the sequentially modified gold electrode beginning with bare Au, followed by dsS-DNA, MCH, Hoechst binding, CV oxidation, and Hoechst re-binding. In this comparison study, the same bare gold electrode CV curve in Figure 2.3 (curve 1) is used. After the bare electrode is immersed in 1 μM dsS-DNA for 24 hours, dsS-DNA/Au (curve 2), there is a pair of compressed redox peaks for $\text{Fe}(\text{CN})_6^{3-/4-}$ and an increase in the peak potential difference, similar to the ss-DNA/Au modification seen in curve 2, Figure 2.3.

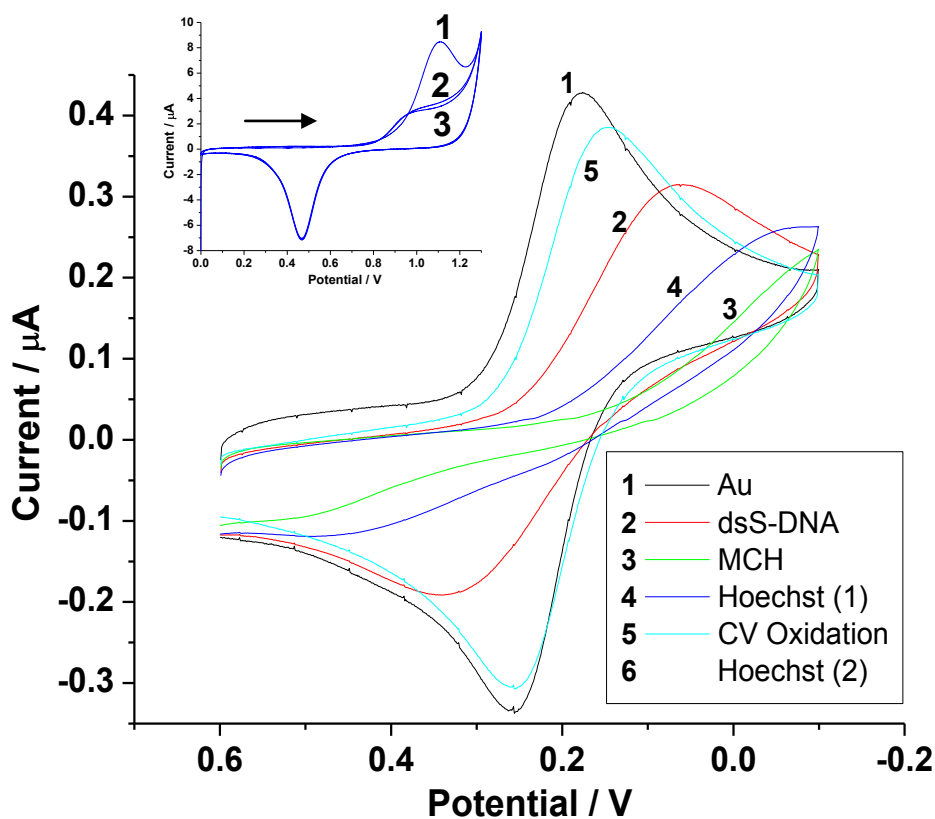


Figure 2.5. Voltammetric behaviors of $\text{Fe}(\text{CN})_6^{3-/4-}$ redox couple (0.5 mM $\text{K}_3\text{Fe}(\text{CN})_6$ + 0.01 PBS) on step-by-step synthetic ds-DNA modified electrodes: bare Au (1), dsS-DNA/Au (2), MCH/dsS-DNA/Au (3), Hoechst/MCH/dsS-DNA/Au (4), Oxidation/Hoechst/MCH/dsS-DNA/Au (5), and Hoechst/Oxidation/Hoechst/MCH/dsS-DNA/Au (no data) (6). Inset: 5 mM Na_2HPO_4 + 5 mM NaH_2PO_4 between 0 - 1.3 V at 30 mV s^{-1} .

However the diffusion coefficient D_0 for dsS-DNA, $3.84 \times 10^{-6} \text{ cm}^2 \text{ s}^{-1}$ (Table 2.3), is more than double that of ss-DNA, $1.54 \times 10^{-6} \text{ cm}^2 \text{ s}^{-1}$ (Table 2.1). This implies that the ss-DNA would form a more densely compact or uniform DNA layer, than dsS-DNA, on the bare gold electrode for the same 24 hour immobilization time. This is also verified by the d_i value difference shown in Table 2.2 and Table B2.5 (Appendix B). Similarly, the subsequent modification of the DNA immobilized gold in 1 mM MCH for 6 hours exhibits no $\text{Fe}(\text{CN})_6^{3-/4-}$ redox peaks. This also suggests that the replacement of dsS-DNA by MCH could have achieved better surface coverage for the MCH/dsS-DNA/Au modification (curve 3). Next, the immersion in 100 μM Hoechst 33258 for 5 minutes to form the Hoechst/MCH/dsS-DNA/Au modification (curve 4), shows a little more conductivity of the modified gold electrode, seen by a slight increase in the current responses for both the reduction and oxidation branches of the CV curve (compared to curve 3). The binding of Hoechst with the immobilized dsS-DNA yields the same D_0 of $9.3 \times 10^{-9} \text{ cm}^2 \text{ s}^{-1}$ (Table 2.3) as that of the hybrid ds-DNA duplex as shown in Table 2.1. After three cycles of voltammetric oxidation (Figure 2.5, inset) in 5 mM Na_2HPO_4 + 5 mM NaH_2PO_4 between 0 - 1.3 V at 30 mV s^{-1} , the CV oxidation/Hoechst/MCH/dsS-DNA/Au is formed and the well-defined $\text{Fe}(\text{CN})_6^{3-/4-}$ redox peaks return (curve 5), giving peak potential and peak current heights that are close to those of the bare gold electrode (curve 1). We propose that a combined effect of the oxidative DNA damage and oxidative desorption of the immobilized dsS-DNA and MCH due to this CV oxidation increases surface conductivity and contributes to the return of the $\text{Fe}(\text{CN})_6^{3-/4-}$ redox peaks in curve 5. This cyclic oxidation of the Hoechst bound dsS- DNA modified gold

Table 2.3. Diffusion coefficients (D_0) for successive modifications on bare gold by dsS-DNA, MCH, Hoechst, CV oxidation, and Hoechst binding.

Step	Modifications	D_0 /cm ² s ⁻¹
1	Bare gold	6.59E-06
2	dsS-DNA	3.84 E-06
3	MCH	undetectable
4	Hoechst (1)	9.30 E-09
5	CV Oxidation	7.26 E-06
6	Hoechst (2)	--

^oCalculated from Equation 1 by using cathodic peak currents.

surface results in an increase of D_0 by three orders of magnitude, from $9.3 \times 10^{-9} \text{ cm}^2 \text{ s}^{-1}$ to $7.26 \times 10^{-6} \text{ cm}^2 \text{ s}^{-1}$ (Table 2.3). A second immersion in 100 μM Hoechst 33258 (5 minutes) of the oxidized Hoechst bound dsS-DNA would form the Hoechst/Oxidation/Hoechst/MCH/dsS-DNA/Au modification (curve 6). Unfortunately, the D_0 value for Step 6 in Table 2.3 was not obtained.

The EIS Nyquist plots for the steps described above are displayed in (Appendix B) Figure B2.11. The same EIS equivalent circuit model from Figure 2.4 was used and the simulated values for R_Ω , C_d , R_{ct} , Z_W , K_a^0 , R , and d_i are listed in Table B2.5.

Compared to the ss-DNA (Table 2.2), with the same immobilization time (24 hours) and probe concentration (1 μM), the first step in the immobilization of the synthetic dsS-DNA gives smaller values: double layer capacitance ($C_d = 7.64 \mu\text{F}$), charge transfer resistance ($R_{ct} = 4.8 \text{ k}\Omega$) and surface coverage ($R = 0.766$) (Table B2.5). The larger values of these three parameters for the ss-DNA immobilization imply the ss-DNA

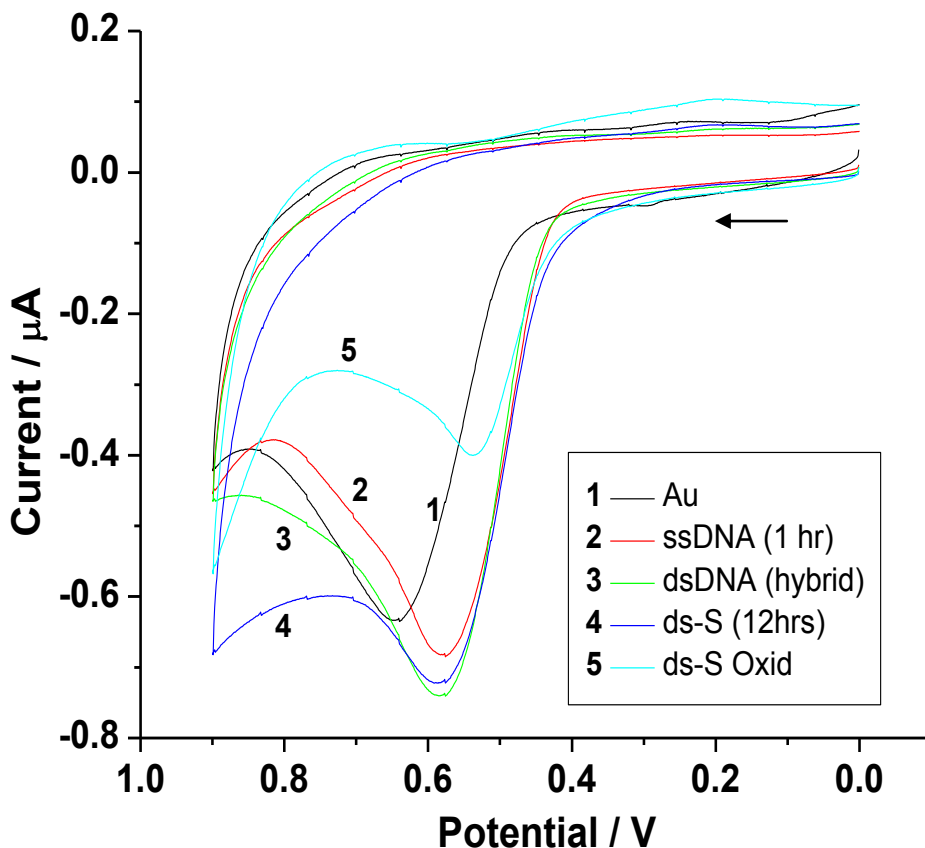


Figure 2.6. Voltammetric behaviors of modified electrodes between 0 V to 0.9 V in 100 μM Hoechst 33258 + 0.01 M PBS buffer: bare Au (1), ssDNA for 1 hr (2), t-DNA and ss-DNA hybrid (3), dsS-DNA for 12 hrs (4), and oxidized dsS-DNA (5). Scan rate: 100 mV s^{-1} . Oxidation was conducted in 5 mM Na_2HPO_4 + 5 mM NaH_2PO_4 between 0 - 1.3 V at 30 mV s^{-1} for three cycles. All DNA concentrations are 1 μM .

layer is more densely spaced than the ds-DNA layer on the gold electrode surface under current experimental conditions. A larger K_a^0 ($3.54 \times 10^{-3} \text{ cm s}^{-1}$) is observed due to the dsS-DNA immobilization. This K_a^0 value is approximately one order of magnitude greater than the ss-DNA immobilization of $4.54 \times 10^{-4} \text{ cm s}^{-1}$ (Table 2.2). The measured thickness for dsS-DNA is about 2.91 nm, which is a little larger than the ss-DNA layer of

2.31 nm. After further modification with MCH, a decrease in both C_d (3.1 μF) and K_a^0 ($1.86 \times 10^{-4} \text{ cm s}^{-1}$) are observed, which are 40% and 5.3% of the respective values obtained for the ss-DNA immobilization. As expected, the MCH modification shows an increase in R_{ct} (91 k Ω), R (0.988), and d_i (7.19 nm), respectively. At step 4, the self-assembled dsS-DNA (with MCH) molecules are then bound with Hoechst (CV curve shown in Figure 2.5 and not shown in EIS plot Figure B2.11). In step 5 a very conductive gold surface is produced, due to the oxidative damage of the dsS-DNA and oxidative desorption of the dsS-DNA and MCH, as evidenced by the increase in K_a^0 ($4.04 \times 10^{-3} \text{ cm s}^{-1}$). In spite of the similarity between the values for R_{ct} and R in step 2 versus those of R_{ct} (4.2 k Ω) and R (0.733) in step 5, the values for C_d (2.63 μF) and d_i (0.85 nm) in step 5 (CV oxidation) are significantly less than those at step 2 (7.64 μF and 2.91 nm), respectively. The significant decrease in both R and d_i , (compared to step 3), are a result of the desorption of dsS-DNA and MCH from the gold surface, after the electrochemical oxidation at a high positive potential (up to 1.3 V). The resulting surface conductivity would be comparable to the immobilized dsS-DNA only in terms of R_{ct} (or K_a^0). Especially, the thickness d_i (0.85 nm) after the CV oxidation, which is similar to a single layer of MCH (or the length of the linking spacer, $-\text{S}(\text{CH}_2)_6-$, of the synthetic dsS-DNA or pure MCH). After the re-binding with Hoechst for the oxidized gold surface, the increase of R_{ct} (5.5 k Ω), R (0.799), and d_i (2.13 nm) are accounted for by non-specifically bound Hoechst. Most dsS-DNA molecules have been oxidized and removed away from the modified gold surface at step 5, thus there is a less likely chance for Hoechst to bind with dsS-DNA.

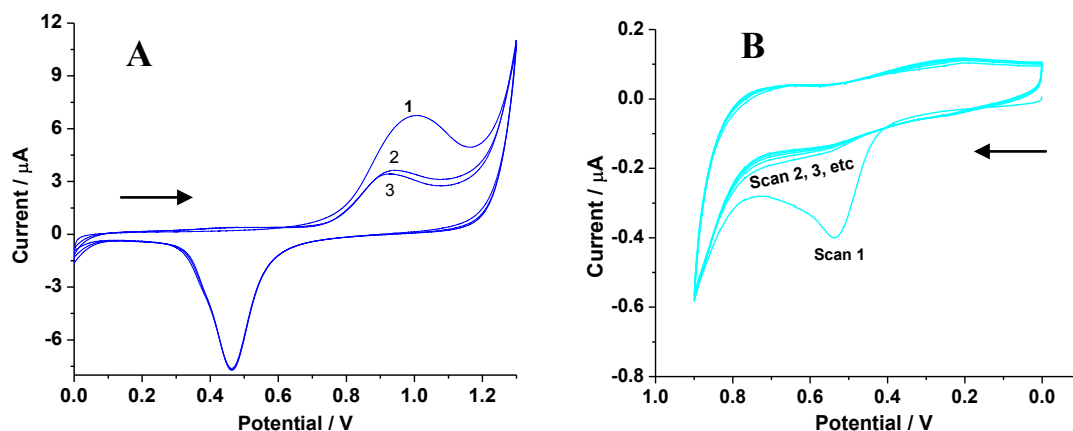


Figure 2.7. Cyclic voltammograms (A) oxidation of dsS-DNA (pre-immobilized for 12 hours) in 5 mM Na_2HPO_4 + 5 mM NaH_2PO_4 solution between 0 - 1.3 V at 30 mV s^{-1} for three cycles; (B) continuous scanning of Hoechst bound dsS-DNA-modified gold electrode in 100 μM Hoechst 33258 + 0.01 M PBS, pH 7.4; scan rate 100 mV s^{-1} . The first scan in (B) is the same from curve 5 in Figure 2.6.

For comparison purposes, the electron transfer behaviors of the Hoechst/CV oxidation/dsS-DNA/MCH modified electrode surface was also investigated by CV and EIS. The results are shown in Figure B2.12 - Figure B2.13 and Table B2.6 - Table B2.7.

2.4.4 Hoechst interactions with ss-DNA, hybridized ds-DNA, dsS-DNA, and oxidatively damaged dsS-DNA

Figure 2.6 shows cyclic voltammograms of Hoechst 33258 bound to DNA modified gold electrodes in 0.01 M PBS buffer. Curve 1 represents the CV response of the bare gold electrode between 0 to 0.9 V in a 100 μM Hoechst 33258 + 0.01 M PBS solution. It exhibits an irreversible oxidation peak for Hoechst at the peak potential of 0.647 V and peak current of $-0.634 \times 10^{-6} \text{ A}$, which is consistent with values reported in the literature [50]. After modification with ss-DNA for 1 hour, the ss-DNA modified electrode is run by CV with the same conditions, as shown in curve 2. Hoechst bound ss-

DNA in the presence of the Hoechst solution shows an oxidation peak shifted to the potential 0.580 V with a larger current response of -0.682×10^{-6} A (I_{ss}), indicating the oxidation potential of Hoechst is more negative than that measured on the bare gold surface. Then the ss-DNA modified gold electrode is hybridized with t-DNA to form a ds-DNA(hybrid)/Au. This ds-DNA duplex interaction with Hoechst results in a slightly positively shifted peak current at 0.586 V and a further increase in current to -0.74×10^{-6} A (curve 3, $I_{ds,hybrid}$). As a control, synthetic ds-DNA (dsS-DNA) is immobilized on the bare gold surface for 12 hours and then moved to the same Hoechst PBS buffer solution for CV analysis, as shown in curve 4. This voltammogram gives a similar shape, peak potential (0.588 V), and peak current (-0.722×10^{-6} A, I_{ds-S}) as those in curve 3 (dsS-DNA hybrid). This means the Hoechst prefers to bind with ds-DNA other than ss-DNA, which yields a larger current response ($I_{ds,hybrid} \sim I_{ds-S} > I_{ss}$). Finally, the (12 hour) dsS-DNA modified gold electrode is first oxidized in 5 mM Na_2HPO_4 + 5 mM NaH_2PO_4 by cycling at 100 mV s^{-1} (as illustrated in Figure 2.7-A), and then run with CV in the $100 \mu\text{M}$ Hoechst 33258 PBS buffer. As shown in curve 5, the Hoechst binding to the oxidatively damaged dsS-DNA leads to a significant negatively shifted oxidation peak of Hoechst at 0.539 V and a decreased peak current of -0.40×10^{-6} A ($I_{ds,damaged}$). The binding of Hoechst 33258 with ds-DNA is attributed to a minor groove binding mechanism [51, 52, 53], where Hoechst selectively binds to A-T base pairs [48, 49]. The first scan in Figure 2.7-B is the same as curve 5 in Figure 2.6. The continuous scans (scan 2, 3, etc) gives rise to almost no further oxidation of Hoechst due to irreversible oxidation on the electrode surface (Figure 2.6, curve 5). It is interesting to observe that the oxidation currents of Hoechst on the DNA modified electrode follow the order: $I_{ds,hybrid} \sim I_{ds-S} > I_{ss} > I_{ds,damaged}$.

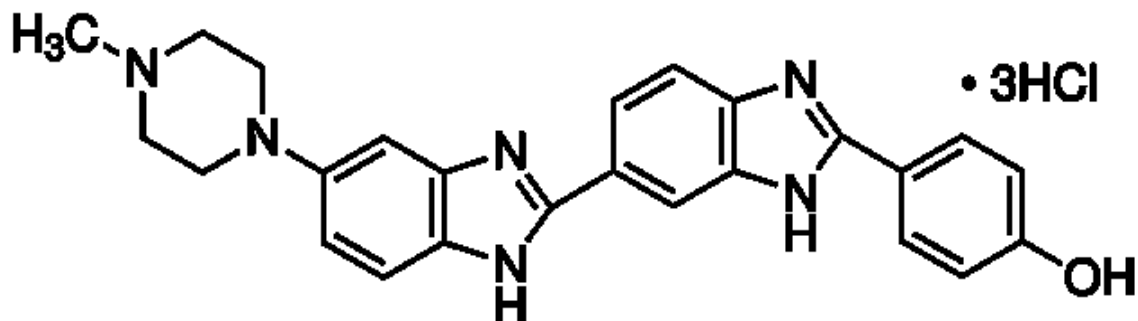


Figure 2.8. Chemical structure of Hoechst 33258 in solution as used in this study. [Image courtesy of www.sigmaaldrich.com].

From the chemical structure of Hoechst 33258 (Figure 2.8), the most probable oxidation sites are in the N-3 and N'-3 of the two benzimidazole rings [53]. Since the imidazole ring shows a partial electrostatic charge, when binding with ss-DNA, it would bind to the phosphate groups of DNA by electrostatic binding in the ss-DNA state [24]. The Hoechst 33258 binding mode changes to a minor groove binding for the ds-DNA duplex.

2.4.5 Comparison of current vs. time curves of DNA oxidations on electrode surfaces with different modifications

The current versus time curves of three cases: (A) Hoechst 33258 (5 min)/MCH (6 hours)/dsS-DNA (24 hours)/Au (corresponding to the inset in Figure 2.5), (B) dsS-DNA (24 hours)/MCH (6 hours)/Au (corresponding to the inset in Figure B2.12), and (C) dsS-DNA (12 hours)/Au (corresponding to Figure 2.7-A) are shown in Figure B2.14 (see Appendix B). Each CV illustrates the first three cyclic voltammetry scans and are numbered 1, 2, and 3. The surface densities of ds-DNA in these cases can also be obtained from the electro-oxidation charges of A or G nucleotides [26, 54] on a ds-DNA

modified gold electrode. From the CV scans in each case, it can be seen that the oxidation of the gold substrate is not prevented but only retarded. The first current peaks for these cases (A) through (C) appear at 1.11 V, 1.11 V, and 1.00 V, respectively, whereas the reduction peaks for all cases appear, ca. 0.46~0.47 V. The small reduction peaks observed in each of the cases (A) through (C) may be attributed to the electro-reduction of electro-oxidation products produced on the electrode surface at each oxidation process. It is not clear what the small reduction peaks actually represent in Figure B2.14-D. These small reduction peaks (are absent in A-C) are from the last three CV scans of the electro-polishing processes by repetitive CV cycles of the bare gold electrode in a solution of 1.0 M H₂SO₄ between 0 - 1.3 V at 60 mV s⁻¹. Table 2.4 lists all the charges for the first three electro-oxidation peaks and corresponding electro-reduction peaks obtained from the individual CV curves.

The surface density (Γ_0) of the DNA immobilized on the gold surface can be obtained from Eq. 5, where Q_{DNA} is the oxidation charge difference between the first scan (Q_{o1}) and the second scan (Q_{o2}):

$$Q_{\text{DNA}} = Q_{o1} - Q_{o2} \quad (5)$$

$$\Gamma_0 = \frac{Q_{\text{DNA}}}{nFAR} \quad (6)$$

In Eq. 6, R_s is the roughness factor (R_s is approximately 1 for the gold electrodes used here). The surface density (Γ_{DNA} , mol cm⁻²) of DNA immobilized on the gold surface can be calculated from Eq. 7 below:

$$\Gamma_{\text{DNA}} = \Gamma_0 \frac{z}{m} \quad (7)$$

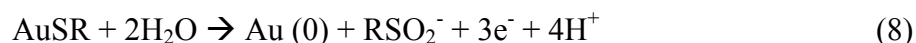
where m is the number of base pairs in the DNA strand and z is the charge of the redox molecules.

Therefore, the surface DNA densities (Γ_{DNA}) on the different modified gold electrodes are determined as: 3.33×10^{-11} mol cm⁻² for Hoechst/MCH/ds-DNA/Au, 2.94×10^{-11} mol cm⁻² for ds-DNA/MCH/Au, and 3.92×10^{-11} mol cm⁻² for ds-DNA/Au, by the DNA electro-oxidation charge ($Q_{\text{DNA,ox}}$) given in Table B2.8, assuming an average electron-transfer of 5.51 electrons per base pair. The calculation for the number of electrons transferred through DNA is carried out as follows: if we assume 6 and 4.7 electrons for the electrochemical oxidation of the adenine and guanine moieties [26], the average number of electrons needed for the oxidation of each base pair is given by the relationship $(0.625 \times 6) + (0.375 \times 4.7) = 5.51$ electrons, because the current 40 bp oligonucleotide contains A-T and G-C in a ratio of 0.625/0.375 (25 A-T pairs/15 G-C pairs). The immobilization of ds-DNA directly on the bare electrode for 12 hours gives a DNA density of 3.92×10^{-11} mol cm⁻², which is close to the literature value [6, 55]. Our results show that the treatment of MCH on the DNA-modified gold surface leads to a slightly lower DNA surface density than that of the gold surface without the MCH treatment. A similar observation has been reported [42]. It is found that the DNA densities at these modifications follows this order: $\Gamma_{\text{DNA}} (\text{dsS-DNA/Au}) > \Gamma_{\text{DNA}} (\text{MCH/dsS-DNA/Au}) > \Gamma_{\text{DNA}} (\text{dsS-DNA/MCH/Au})$.

On the other hand, assuming that ds-DNA molecules are adsorbed flat on the gold substrate surface in a saturated monolayer, a surface density of 6.1×10^{-12} mol cm⁻² can be estimated from the area of a single ds-DNA molecule (length \times width) of 27.2 nm² for a 40 bp duplex. It is obvious that the actual surface density obtained from the CV is larger than the theoretical calculation. This may be due to the fact that ds-DNA is not actually laying flat on the substrate, but more likely it is in a “coiled” state, rather than in a

compact (flat) state, on the gold surface. The former state would yield a smaller single molecule area, and thus lead to a larger surface density. This coiled effect becomes more plausible for the long 40 bp oligonucleotide. From the EIS measurement, ss-DNA/Au and ds-DNA/Au give the thickness values of 2.31 nm for ss-DNA (Table 2.2) and 2.91 nm for ds-DNA (Table B2.5), both are greater than the theoretical 2 nm thickness (using a DNA width of 2 nm).

Meanwhile, according to the oxidative desorption charge ($Q_{\text{ox-des}}$) for each individual modified electrode at voltammetric scans, one could calculate the surface density of the oxidatively desorbed thiolated molecules immobilized on the gold surface by assuming a three-electron transfer of desorption [56].



It is seen that the $Q_{\text{ox-des}}$ decreases with an increase in the number of scans for all three modified electrodes (Table B2.8). Applying the individual $Q_{\text{ox-des}}$ to Eq. 6 and 7, one can obtain the DNA oxidative desorption density. For instance, if the gold electrode is immobilized with dsS-DNA (i.e., dsS-DNA/Au, case C), the surface density due to DNA oxidative desorption is $1.26 \times 10^{-10} \text{ mol cm}^{-2}$ for the 1st scan, $1.15 \times 10^{-10} \text{ mol cm}^{-2}$ for the 2nd scan, and $1.02 \times 10^{-10} \text{ mol cm}^{-2}$ for the 3rd scan, respectively, which are about three times larger than the surface density due to DNA oxidation, $3.92 \times 10^{-11} \text{ mol cm}^{-2}$. These calculation details can be found in Appendix B. It is understandable that the surface density, due to DNA oxidative desorption, decreases over the cyclic scanning time, because more and more of the adsorbed thiol-group DNA molecules (and MCH in the cases of the other two modifications) are oxidized to a more soluble RSO_2^- species that results in the gradual removal of the DNA from the gold surface.

Table 2.4. Oxidation/Reduction charges for cyclic voltammetric oxidations of different modified gold electrodes.

	Modifications	Q_{O1}	Q_{R1}	Q_{O2}	Q_{R2}	Q_{O3}	Q_{R3}
A	Hoechst 33258 (5 min)/MCH (6 hrs)/dsS-DNA (24 hrs)/Au	102.04	47.38	77.18	48.33	74.47	47.94
B	dsS-DNA (24 hrs)/MCH (6 hrs)/Au	120.33	47.41	96.77	48.34	92.80	47.96
C	dsS-DNA (12 hrs)/Au	119.08	47.49	89.42	47.48	85.72	48.50

(A)-(C) were conducted in 5 mM Na_2HPO_4 + 5 mM NaH_2PO_4 between 0 - 1.3 V at 30 mV s^{-1} ; Q_{O1} (Q_{R1}), Q_{O2} (Q_{R2}), and Q_{O3} (Q_{R3}) are the charges for the 1st, 2nd, 3rd oxidation (reduction) peaks, respectively. The columns Q_{O1} , Q_{O2} , and Q_{O3} can be broken down to three columns shown in Table B2.8. Unit of charge: μC .

2.4.6 STM imaging of electro-oxidation of DNA modified gold surface

In order to observe the DNA modified gold electrode surface details of before and after electro-oxidation, we used the same immobilization procedures mentioned above to modify a single crystalline gold surface (111). This Au (111) electrode surface is atomically flat and suitable to image DNA. In this study, we utilized the nanoscale resolution of STM imaging to assess the surface topography and surface conductivity of the gold surface for different modifications. Figure 2.9 illustrates typical STM topography (A) and current (B) images that were obtained using a constant current mode, at different oxidation stages for the dsS-DNA modified Au (111) surface. The procedures to process these STM images are described in detail in Appendix B. A bright spot was chosen at random as indicated by arrow in images (A) and (B) and then, for further analysis, magnified images (5.3×5.3 nm) for both topography (C) and current (D) were created. One simple way to analyze both images can easily be done by cross section analysis for both the topography and current images (see Appendix B). The cross section profiles (c1) and (c2) correspond to the green line and red line in the topography image

(C), respectively. Similarly, (d1) and (d2) correspond to the green line and the red line in the current image (D), respectively.

It is interesting to note that the area where the green line crosses in the topography image (C) yields a different cross section profile as does the red line. The red line crosses a dark area in the topography image (C) and yields a decrease in height (c2), whereas the green line shows an increase for the height of the area it crosses (c1). This implies that the bright spots on the Au (111) surface are probably accounted for as modified molecules and the dark areas (or pinholes) are the gold substrate. These pinholes are often observed in the reductive desorption of alkanethiols due to the breaking of the Au-S bond formed on the Au (111) surface [39, 57, 58]. It is also noteworthy to observe that the corresponding bright spot in the current image (D) is at the same location for the topography image (C). The bright spot crossed by the green line (d1) gives a much higher conductance than the spot crossed by the red line (d2). Considering that our sample is a ds-DNA modified flat gold (111) surface, it is plausible to tentatively assign the bright spot in both the topography (height information) and current images (conductance information) to at least three possible species: i) the oxidized thiol linker ($-\text{HS}(\text{CH}_2)_6-$) of the adsorbed ds-DNA molecules, ii) the electroactive Hoechst molecules that could be bound with oxidized DNA or native DNA molecules on gold surface, and iii) oxidized and/or broken DNA fragments.

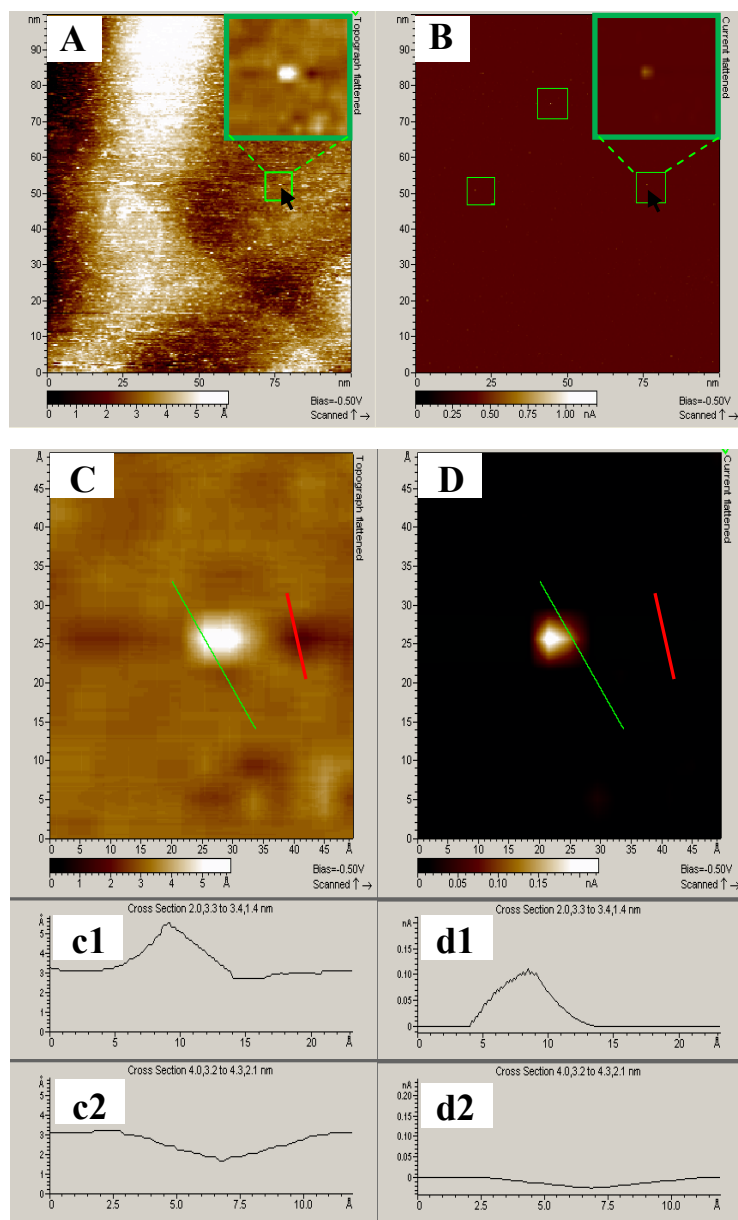


Figure 2.9. STM topography (A) and current (B) images of Au (111) surface after being modified by ds-DNA for 12 hrs, subsequently by voltammetric oxidation, and then binding with Hoechst 33258 for 5 min. scan area 100×100 nm. The bring spot (black arrow) of the inset in topography image (A) corresponds to that spot (black arrow) of the inset in current image (B). Magnified in images are shown in topography image (C) and current image (D). Scan area 5.3×5.3 nm. Cross section profiles (c1) and (c2) correspond to the green line and red line in (C), respectively. Similarly, (d1) and (d2) correspond to the green line and red line in (D), respectively. Voltammetric oxidation was conducted in 5 mM Na_2HPO_4 + 5 mM NaH_2PO_4 between 0 - 1.3 V at 30 mV s^{-1} for three cycles.

For i) the charged species is most likely in the format of $-\text{O}_2\text{S}(\text{CH}_2)_6^-$, as shown in Eq. 8. When the STM tip approaches the conductive species, like $-\text{O}_2\text{S}(\text{CH}_2)_6^-$, the topography image will give an increase in the height and the current image will exhibit an increase in conductivity. From the cross section of the green line (c1) in the topography image (C), the height of the bright spot is estimated to be $\sim 6\text{--}7 \text{ \AA}$ (depth relevant to the substrate). Considering the length of MCH to be 1.2 nm [59], this bright spot corresponds to a tilt angle of about 30° toward the substrate for mercaptohexane groups. For ii), the dimension of the bright spot in image (C) is about $1.3 \times 0.48 \text{ nm}$, which is comparable to the theoretical size of single Hoechst 33258 [9], $2.12 \times 0.48 \text{ nm}$ (length \times width). Finally, for iii), since it does not resemble the observed island structure as shown in Figure 2.2-E after the electro-oxidation on the dsS-DNA modified gold electrode, it is speculated that the thiolated 40 bp dsS-DNA previously immobilized on the gold surface could be broken down to DNA fragments or pieces of nucleotides (by opening the duplex helix), after voltammetric oxidation. On the other hand, the $6\text{--}7 \text{ \AA}$ height of the bright spot is close to the thickness of ss-DNA [59]. Thus, after the oxidization of bases at a very positive potential, it could be likely that the helical duplex structure of ds-DNA would be opened to become either single strand DNA or DNA fragments.

Nevertheless, it is difficult to definitively distinguish which species or combination of species could be assigned to the numerous bright spots shown on the gold surface after the electro-oxidation (it is known that these bright spots represent a conductive species on the electrode surface).

After analysis of the gold surface immobilized dsS-DNA for 24 hours, we obtained a current distribution of conductance from the STM current images for that gold

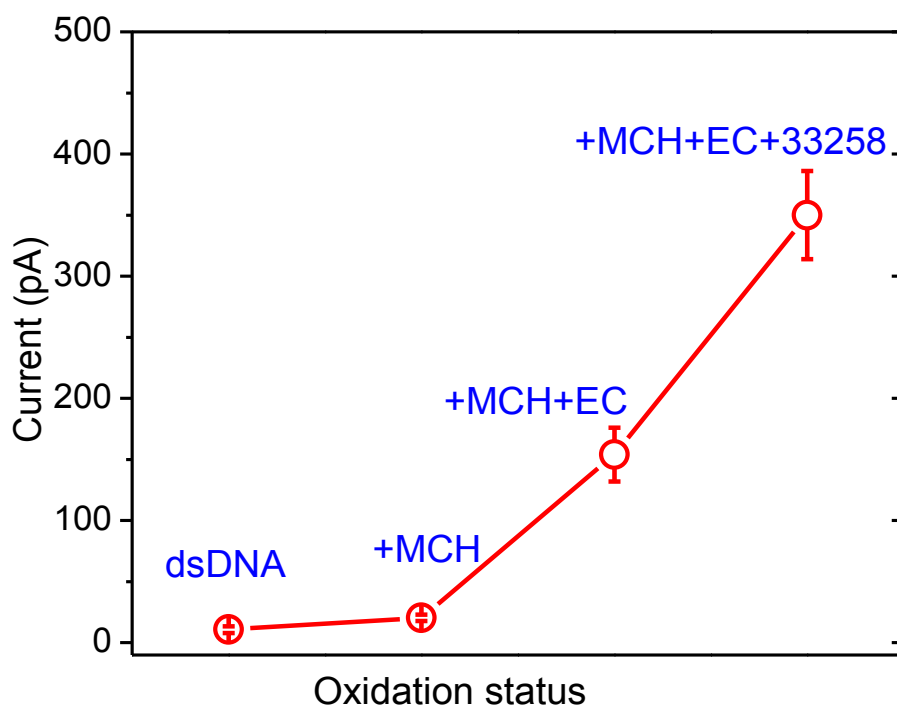


Figure 2.10. Current distributions obtained from STM current images for 24 hours dsS-DNA modified gold surface at different surface oxidation status with the following modification order: dsS-DNA modification, MCH modification, voltammetric oxidation, and binding with Hoechst 33258. Triplicate images are analyzed at each modification.

surface at different oxidation stages for the successive modifications of dsS-DNA, MCH, voltammetric oxidation, and binding with Hoechst 33258. Images were analyzed in triplicate for each surface modification and the results are shown in Figure 2.10. It was observed that the surface conductivity (based on the current of the bright spots in Figure 2.9) after each modification follows the order: dsS-DNA/Au < MCH/dsS-DNA/Au < oxidized MCH/dsS-DNA/Au < Hoechst/oxidized MCH/dsS-DNA/Au. This trend is consistent with the results shown in the CV curves of Figure 2.5 and the EIS plots of

Figure B2.11 which was obtained for the polycrystalline gold electrode using the same surface modifications. STM was previously applied to observe the Hoechst 33258 bound ds-DNA [19]; however, no quantitative information was obtained in that application.

From the results obtained in this present work, conductivity changes of the gold electrode surface could be estimated by at least three methods: cyclic voltammetry (cyclic shape changes), electrochemical impedance spectroscopy (EIS parameter changes, e.g., R_{ct}), and STM current image (changes in current). Furthermore, it will be of interest to utilize the combined *in situ* electrochemical STM (*in situ* EC-STM) to quantitatively correlate results obtained by these different methods.

2.5 RAMAN MICROSPECTROSCOPY

Figure 2.11-A is a bright field image of a DNA modified Au (111) surface and Figure 2.11-B is the accompanying Raman spectral map of the selected area. The white areas of the spectral map represent high Raman intensities while dark areas represent low Raman intensities for the Raman band 760.4 cm^{-1} . Figure 2.11-C is a typical Raman spectrum from the DNA modified Au (111) surface and the bands at $\sim 610\text{ cm}^{-1}$, 760 cm^{-1} , 800 cm^{-1} , and 917 cm^{-1} correspond to the characteristic Raman shifts for nucleotide conformation [20]. Band in the region from $600\text{ to }800\text{ cm}^{-1}$ can be assigned to ring breathing vibrations. These four bases can be divided into purine bases (adenine and guanine) and pyrimidine bases (cytosine and thymine), however further studies would be necessary to distinguish a characteristic band for each nucleotide base.

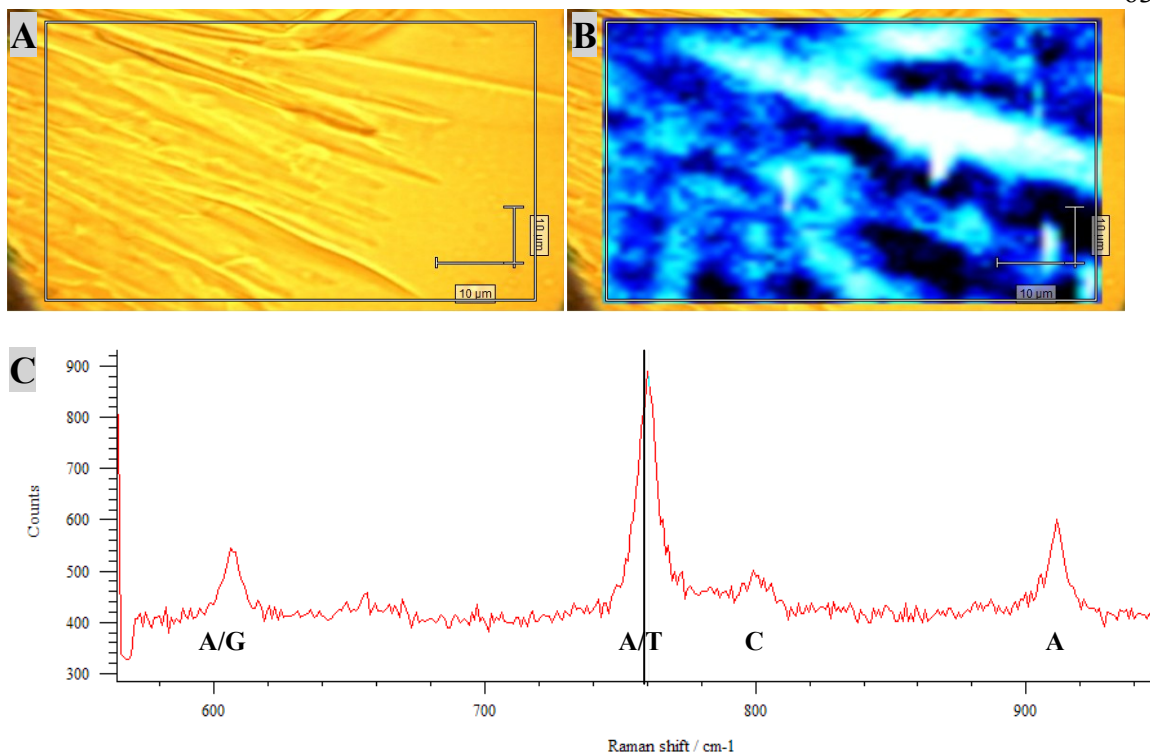


Figure 2.11. Bright field image of DNA modified Au (111) surface (A), Raman map with wavenumber center at 760.4 cm^{-1} (B), and typical Raman spectrum for nucleic acid bands (C). Image acquired by 50x objective, 100% laser power and 5 second exposure.

2.6 CONCLUSIONS

In this study we have demonstrated the formation of DNA SAM by a variety of step-by-step immobilization procedures to understand the DNA-mediated electron transfer behaviors on modified gold electrode surfaces by electrochemical methods (cyclic voltammetry and electrochemical impedance spectroscopy), STM and Raman. As expected, in these immobilization procedures MCH plays an essential role in the replacement of thiolated DNA molecules (via thiol-thiol group exchange) and removal of non-specifically bound DNA from the modified electrode surface, and therefore further adjusting the interfacial electron transfers on electrode/DNA/electrolyte. These roles of

MCH are elucidated by investigating the changes in CV curves and Randles equivalent circuit model parameters for each of the immobilization (i.e. surface modification) procedures. The change of layer thickness (d_i), as shown in Eq. 4, obtained from the change in the interfacial double layer capacitance (C_d) before and after MCH immobilization, implies that there may be a multilayer structure of MCH that could be attached on the modified electrode by the hydrogen bond between MCH molecules (H-S \cdots HO). However, this hypothesis needs to be confirmed by other surface analysis techniques.

It is proposed that the electro-oxidation of the DNA-confined electrode in PBS buffer solution involves oxidative DNA damage (via 5.51 electron transfer rate constant) as well as the oxidative desorption (via 3 electron transfer rate constant) of DNA and MCH (if immobilized), according to the electrical charges obtained from the voltammetric oxidation. Hoechst 33258, as an electroactive non-intercalator, has been introduced to probe the conductivity changes before and after the electro-oxidation of the ds-DNA modified electrode surface. The constant layer thickness and remarkable increase in electron transfer rate before and after Hoechst binding indicate that Hoechst 33258 prefers to bind with ds-DNA, rather than ss-DNA, by a minor groove binding mechanism. STM topography and current image analysis are, for the first time, introduced to study the conductivity of the modified electrode surfaces. The results suggest that there is a possibility of the co-existence for oxidative DNA damage and oxidative desorption on the modified electrode surface at a positive potential (e.g., > 1.1 V vs. Ag/AgCl). Our results highlight that the combined techniques, such as EC-STM, may provide a new tool to qualitatively and quantitatively measure the DNA-mediated

electron transfer passing through the DNA nucleotides/bases, as well as the visualization of the DNA oxidative damage on modified electrode surface at nanoscale resolutions.

2.7 REFERENCES

- [1] K.M. Millan, S.R. Mikkelsen, *Anal. Chem.* 65 (1993) 2317.
- [2] J.W. Schultze, V. Tsakova, *Electrochim. Acta* 44 (1999) 3605.
- [3] W. Ehrfeld, *Electrochim. Acta* 48 (2003) 2857.
- [4] K. Kerman, M. Kobayashi, E. Tamiya, *Meas. Sci. Technol.* 15 (2004) R1.
- [5] A.B. Steel, T.M. Herne, M.J. Tarlov, *Bioconjugate Chem.* 10 (1999) 419.
- [6] M. Chahma, J.S. Lee, H.-B. Kraatz, *J. Electroanal. Chem.* 567 (2004) 283.
- [7] D. Pan, X. Zuo, Y. Wan, L. Wang, J. Zhang, S. Song, C. Fan, *Sensors* 7 (2007) 2825.
- [8] H. Ju, Y. Ye, Y. Zhu, *Electrochim. Acta* 50 (2005) 1361.
- [9] S. Wang, T. Peng, C.F. Yang, *Electroanalysis* 14 (2002) 1648.
- [10] A.K. Boal, J.K. Barton, *Bioconjugate Chem.* 16 (2005) 312.
- [11] E.M. Boon, D.M. Ceres, T.G. Drummond, M.G. Hill, J.K. Barton, *Nat. Biotechnol.* 18 (2000) 1096.
- [12] Anonymous, *ASM News* 56 (1990) 358.
- [13] D.D. Juranek, *Cryptosporidiosis: Hunter's Tropical Medicine and Emerging Infectious Diseases* 8th ed., WB Saunders, Philadelphia, 2000.
- [14] J. Wang, G. Rivas, C. Parrado, X. Cai, M.N. Flair, *Talanta* 44 (1997) 2003.
- [15] Z.P. Aguilar, I. Fritsch, *Anal. Chem.* 75 (2003) 3890.
- [16] S. Kilina, S. Tretiak, D.A. Yarotski, J.X. Zhu, N. Modine, A. Taylor, A.V. Balatsky, *J. Phys. Chem. C* 111 (2007) 14541.
- [17] E. Shapir, H. Cohen, N. Borovok, A.B. Kotlyar, D. Porath, *J. Phys. Chem. B* 110 (2006) 4430.
- [18] W. Mamdouh, M. Dong, R.E.A. Kelly, L.N. Kantorovich, F. Besenbacher, *J. Phys. Chem. B* 111 (2007) 12048.
- [19] M.H. Zareie, F.I. Şahin, M.A. Ergün, C. Koçum, S. Menevşe, A. Menevşe, E. Pişkin, *Int. J. Biol. Macromol.* 23 (1998) 7.

- [20] J. De Gelder, K. De Gussem, P. Vandenabeele, M. Vancanneyt, P. De Vos, L. Moens, *Anal. Chim. Acta* 603 (2007) 167.
- [21] S.E. Creager, L.A. Hockett, G.K. Rowe, *Langmuir* 8 (1992) 854.
- [22] J.C. Hoogvliet, M. Dijkema, B. Kamp, W.P. van Bennekom, *Anal. Chem.* 72 (2000) 2016.
- [23] S.-J. Ding, B.-W. Chang, C.-C. Wu, C.-J. Chen, H.-C. Chang, *Electrochem. Commun.* 9 (2007) 1206.
- [24] Y.-S. Choi, K.-S. Lee, D.-H. Park, *Bull. Korean Soc.* 26 (2005) 379.
- [25] S. Trasatti, O.A. Petrii, *Pure and Appl. Chem.* 65 (1991) 711.
- [26] C. Hinnen, A. Rousseau, R. Parsons, J.A. Reynaud, *J. Electroanal. Chem.* 125 (1981) 193.
- [27] A.J. Bard, L.R. Faulkner, *Electrochemical Methods: Fundamentals and Applications*, Wiley, New York, 1980.
- [28] C. Gautier, C. Esnault, C. Cougnon, J.-F. Pilard, N. Casse, B. Chénais, *J. Electroanal. Chem.* 610 (2007) 227.
- [29] T. Ito, K. Hosokawa, M. Maeda, *Biosens. Bioelectron.* 22 (2007) 1816.
- [30] F. Davis, A.V. Nabok, S.P.J. Higson, *Biosens. Bioelectron.* 20 (2005) 1531.
- [31] A.J. Bard, L.R. Faulkner, *Electrochemical methods: fundamentals and applications* 2nd ed., Wiley, New York, 2001.
- [32] H.O. Finklea, M.S. Ravenscroft, D.A. Snider, *Langmuir* 9 (1993) 223.
- [33] A.B. Kharitonov, L. Alfonta, E. Katz, I. Willner, *J. Electroanal. Chem.* 487 (2000) 133.
- [34] A. Zhou, Q. Xie, Y. Wu, Y. Cai, L. Nie, S. Yao, *J. Colloid Interface Sci.* 229 (2000) 12.
- [35] S.-M. Park, J.-S. Yoo, *Anal. Chem.* 75 (2003) 455A.
- [36] R.P. Janek, W.R. Fawcett, A. Ulman, *Langmuir* 14 (1998) 3011.
- [37] P. Horowitz, W. Hill, *The Art of Electronics* 2nd ed., Cambridge University Press, Cambridge [England]; New York, 1989.
- [38] G. Sanchez-Pomales, L. Santiago-Rodriguez, N.E. Rivera-Velez, C.R. Cabrera, *J. Electroanal. Chem.* 611 (2007) 80.
- [39] H. Wackerbarth, M. Grubb, J. Zhang, A.G. Hansen, J. Ulstrup, *Langmuir* 20 (2004) 1647.

- [40] D. Rekes, Y. Lyubchenko, L.S. Shlyakhtenko, S.M. Lindsay, *Biophys. J.* 71 (1996) 1079.
- [41] H.G. Hansma, I. Revenko, K. Kim, D.E. Laney, *Nucl. Acids Res.* 24 (1996) 713.
- [42] A.B. Steel, R.L. Levicky, T.M. Herne, M.J. Tarlov, *Biophys. J.* 79 (2000) 975.
- [43] I.-F. Hu, D.H. Karweik, T. Kuwana, *J. Electroanal. Chem.* 189 (1985) 59.
- [44] A.B. Steel, T.M. Herne, M.J. Tarlov, *Anal. Chem.* 70 (1998) 4670.
- [45] P. Kohli, K.K. Taylor, J.J. Harris, G.J. Blanchard, *J. Am. Chem. Soc.* 120 (1998) 11962.
- [46] Y.T. Kim, R.L. McCarley, A.J. Bard, *Langmuir* 9 (1993) 1941.
- [47] R.C. Thomas, L. Sun, R.M. Crooks, A.J. Ricco, *Langmuir* 7 (1991) 620.
- [48] P.E. Pjura, K. Grzeskowiak, R.E. Dickerson, *J. Mol. Biol.* 197 (1987) 257.
- [49] M.-k. Teng, N. Usman, C.A. Frederick, A.H.J. Wang, *Nucl. Acids Res.* 16 (1988) 2671.
- [50] K. Hashimoto, K. Ito, Y. Ishimori, *Anal. Chem.* 66 (1994) 3830.
- [51] Y.-S. Choi, D.-H. Park, *J. Korean Phys. Soc.* 44 (2004) 1556.
- [52] Y.-S. Choi, D.-H. Park, *J. Korean Phys. Soc.* 46 (2005) 1445.
- [53] S. Wang, T. Peng, C.F. Yang, *J. Biochem. Biophys.* 55 (2003) 191.
- [54] R.Y. Zhang, D.W. Pang, Z.L. Zhang, J.W. Yan, J.L. Yao, Z.Q. Tian, B.W. Mao, S.G. Sun, *J. Phys. Chem. B* 106 (2002) 11233-11239.
- [55] S.O. Kelley, J.K. Barton, N.M. Jackson, M.G. Hill, *Bioconjugate Chem.* 8 (1997) 31.
- [56] C.A. Widrig, C. Chung, M.D. Porter, *J. Electroanal. Chem.* 310 (1991) 335.
- [57] M. Satjapipat, R. Sanedrin, F. Zhou, *Langmuir* 17 (2001) 7637.
- [58] Y. Song, Y. Liu, M. Yang, B. Zhang, Z. Li, *Appl. Surface Sci.* 252 (2006) 5693.
- [59] R. Levicky, T.M. Herne, M.J. Tarlov, S.K. Satija, *J. Am. Chem. Soc.* 120 (1998) 9787.
- [60] H. Wackerbarth, R. Marie, M. Grubb, J. Zhang, A. Hansen, I. Chorkendorff, C.V. Christensen, A. Boisen, J. Ulstrup, *J. Solid State Electrochem.* 8 (2004) 474.
- [61] V. Vetterl, N. Papadopoulos, V. Drazan, L. Strasák, S. Hason, J. Dvorák, *Electrochim. Acta* 45 (2000) 2961.

CHAPTER 3

CHARACTERIZATION AND ANALYSIS OF GRAM-POSITIVE AND GRAM-NEGATIVE BACTERIA AND CO-CULTURE MIXTURES BY RAMAN MICROSCOPY, FOURIER TRANSFORM INFRARED SPECTROSCOPY, AND ATOMIC FORCE MICROSCOPY²

3.1 ABSTRACT

The molecular composition of Gram-positive and Gram-negative bacteria cell walls is structurally different. In this work, Raman microspectroscopy was applied to discriminate Gram type (Gram-positive and Gram-negative) by assessing specific characteristic spectral features. Analysis of Raman spectra indicated that Gram-positive and Gram-negative bacteria exhibit different spectral patterns under our experimental conditions due to their different extracellular polymeric substances (EPSs). Fourier transform infrared (FTIR) spectroscopy, as a supplementary vibrational spectroscopy, was also applied to analyze the biochemical composition of the representative bacterial strains. As for co-cultured bacterial mixtures, the distribution of individual cell types was obtained by quantitative analysis of Raman and FTIR spectral images and the spectral contribution from each cell type was distinguished by direct classical least-squares (DCLS) analysis. Coupled atomic force microscopy (AFM) and Raman microspectroscopy (RM) realized simultaneous measurements of topography and spectral images for the same sampled surface. This work demonstrated the feasibility of utilizing a combination of Raman microspectroscopy, FTIR, and AFM techniques to effectively characterize spectroscopic fingerprints from bacterial Gram types and mixtures.

² Gerald D. McEwen, M. Tang, Y. Wu, C. D. Miller, A. Zhou (*manuscript in preparation*).

3.2 INTRODUCTION

During recent years Raman spectroscopy has increased in popularity in the field of microbiology as a tool to identify microorganisms, such as bacteria¹⁻⁶. Raman microspectroscopy is a nondestructive vibrational/structural characterization method that can identify a characteristic spectroscopic fingerprint of bacteria based on chemical molecular compositions⁴. A number of applications of Raman microspectroscopy have been reported to monitor the appearance of surface biopolymers (including DNA/RNA, lipids, proteins, and carbohydrates) in growth and antibiotic interaction,⁷ during the cultivation of *Staphylococcus*,⁸ and in metabolism characterization of *Staphylococcus Epidermidis*.⁹ However, studies on characterization of diverse genera of Gram-positive and Gram-negative bacteria by Raman spectroscopy are limited.

FTIR is a physico-chemical method based on the measurement of molecular vibrations when excited by IR radiation at a specific wavelength range. FTIR spectra reflect the overall molecular composition of the sample. The spectra can serve as a spectroscopic fingerprint that can enable accurate identification of microorganisms.¹⁰⁻¹²

In AFM, a sharp probing tip scans the sample surface and the interaction forces between the tip and sample are regulated via a feedback loop. Thus, AFM can provide high resolution topographic images from the micrometer scale to the atomic scale. The technique has been further developed into a versatile tool for the structural and mechanical analysis of biological samples and has been utilized specifically with bacteria.¹³⁻¹⁵

Bacteria studied included Mycobacteria (Gram-positive) and *Pseudomonas putida* and *Escherichia coli* (Gram-negative). Three Gram-positive *Mycobacteria* sp. *JLS*, *KMS*

and *MCS* were isolated and characterized by Dr. Ron Sims's group of Utah State University from the Champion International Superfund site at Libby, Montana. These microorganisms have been demonstrated to degrade polycyclic aromatic hydrocarbons (PAHs).¹⁶ The genomes of these three soil mycobacterium were sequenced by the U.S. Department of Energy/Joint Genome Institute (JGI), and each sequence is available in the NCBI database. *Pseudomonas putida* KT2440 is a Gram-negative bacterium derivative of *P. putida* strain mt-2 (the toluene degrading isolate) and was developed as the first biosafety strain to be considered by the Recombinant DNA Advisory Committee.¹⁷⁻¹⁹ KT2440 is utilized as a model soil bacterium in bioremediation because of diverse metabolism,¹⁸ the complete genome sequence,^{18,20} and an ability to survive in the general environment. Also, KT2440 has been exploited for other applications such as agriculture and biotransformations.²⁰

Studies have shown that bacterial extracellular polymeric substances (EPS) play a major role in bioremediation through the biosorption of heavy metals,²¹ especially in activated sludge,²² and within the marine food chain.²³ Another study focused on the structural analysis of extracted EPS from *P. putida* G7 to the mechanisms of toxic metal binding.²⁴ Our research group presented new insightful views for EPS growth and nanostructural features of the KT2440 cell wall at different culture times by utilization of Raman microspectroscopy and AFM techniques.²⁵

The Gram-positive cell wall is primarily made up of peptidoglycan (ca. 40-80% of the dry weight of the wall), which is a polymer of *N*-acetylglucosamine and *N*-acetylmuramic acid, containing mainly carboxyl, amide, and hydroxyl functional

groups.²⁶ Two other important constituents of the Gram-positive cell wall are teichoic acids, a polymer of glycopyranosyl glycerol phosphate, and teichuronic acid (similar to teichoic acid), but replaces the phosphate functional groups with carboxyls. The Gram-negative bacteria cell wall is more complex due to the presence of an outer membrane in addition to a thin peptidoglycan layer, but does not contain teichoic or teichuronic acids.²⁷ Instead; the outer membrane contains phospholipids, lipoproteins, lipopolysaccharides, and proteins.

This work focused on distinguishing vibrational spectroscopic features between Gram-positive bacteria, including *Mycobacteria KMS*, *JLS*, and *MCS*, and Gram-negative bacteria, including *E. coli* TOP 10, *E. coli* JS4, and *P. putida* KT2440. FTIR spectra of bacterial cells were used to analyze their total composition, including proteins, fatty acids, carbohydrates, nucleic acids, and lipopolysaccharides. The distribution maps obtained from individual Raman, FTIR, and AFM were applied to reveal variation of the bacteria concentration at different locations in co-cultured mixes.

3.3 METHODS AND MATERIALS

3.3.1 Bacterial culture

Mycobacteria KMS, *JLS*, *MCS*, *E. coli* TOP 10, *E. coli* JS4 and *P. putida* KT2440 were obtained from Dr. Charles Miller within the Department of Biological Engineering, Utah State University. Organisms were cultured on plates containing Luria Broth (LB) agar composed of yeast extract, peptone from casein, sodium chloride, and agar (mass ratio, 1:2:1:3) at room temperature in air.

3.3.2 Morphology observations via Atomic Force Microscopy (AFM) and Scanning Electron Microscopy (SEM)

AFM deflection images of bacterial cells were collected using a contact mode AFM controlled by PicoScan 5.4 software (PicoPlus, Agilent Technologies, USA). The measurements were conducted under contact mode at room temperature in air. The spring constants for the AFM probes were 0.58 N/m (or 0.12 N/m),²⁸ and 0.12 N/m (or 0.06 N/m),²⁵ respectively and were used for probing both Gram-positive and Gram-negative bacteria. Electron micrographs for both Gram-positive and Gram-negative bacteria were obtained using a Hitachi (S-4000) scanning electron microscope (SEM).

3.3.3 Raman microspectroscopy

Raman spectra from *Mycobacteria KMS, JLS, MCS, E. coli* TOP 10, *E. coli* JS4 and *P. putida* KT2440 on agar were recorded using a Renishaw inVia Raman microscope (controlled by WiRE 3.0 software) equipped with a 785 nm near-IR laser. Laser light was focused through a Leica 50 × 0.75 N PLAN optical glass microscope objective. Rayleigh scatter was eliminated by the use of notch filters. Within the spectrometer, Raman scatter passed through a 50 μm slit, was then collected and dispersed by a holographic diffraction grating (1200 lines/mm), and finally the entire Raman shift was recorded as a spectrum by a thermoelectrically cooled charge coupled device (CCD). The instrument was wavelength calibrated with silicon at a static spectrum centered at 520.5 cm⁻¹ for 1 second. The bacteria agar plate was mounted on the stage (Leica 11501200) of a Leica microscope, focused under the collection assembly, and spectra were collected in static mode of three accumulations at 10 seconds laser exposure over a wavenumber range of 500-1800 cm⁻¹.

3.3.4 Fourier transform infrared spectroscopy

The FTIR spectra were recorded using a Continuum Microscope (Thermo Fisher) in micro reflectance mode controlled with OMNIC software (Version 7.2). The bacteria sample was prepared in solution and a droplet was allowed to dry on the instrument sampling substrate-interface. Samples were spotted at different concentrations and conglomerations of bacterial colonies were formed and imaged. The cursor was placed on a dark area of the sample to collect a single point spectrum using 64 scans with an 8 cm^{-1} resolution. Following spectral collections, area maps of $\sim 250 \times 200$ microns and 300×150 microns were collected to reveal the transition pattern between the bacteria layers.

3.3.5 Coupled AFM/Raman microspectroscopy

In order to simultaneously collect nanoscale topography and Raman microspectroscopy, a coupled AFM/Raman system was utilized. The phase feedback height image was collected by a Nanonics MV2000 AFM, using a SuperSensorTM tuning fork with 20 nM chromium cantilever with tuning frequency ~ 35 kHz and Q value of ~ 1055 , in non-contact mode in air. The Nanonics MV2000 AFM was controlled using Quartz Software for SPM by Cavendish Instruments (Version 1.4.2.0). After collection, the AFM image was post-processed with the Quartz Software to perform auto plane removal, line normalization, and contrast stretching. These processing steps were performed to remove noise that was added during the simultaneous Raman collection. Concurrent Raman spectra were acquired at 100% laser power with 1 second exposure time for each point on the AFM image. The Renishaw inVia Raman Microscope was controlled using QuartzSpec for Renishaw WiRE3 by Cavendish Instruments with no further post-processing.

3.3.6 Gram staining

The bacterial cell wall is a rigid structure which contributes to bacteria shape and serves as a protective layer that keeps the cytoplasm and internal structures protected for the outside environment. Not all bacterial cell walls are the same and these differences in bacterial cell walls are of great interest both microbiologically and also for clinical diagnostics. In 1888 a Danish physician, Christian Gram, developed the Gram staining procedure.²⁹ This procedure identifies bacteria based on either the retention or loss of crystal violet stain when rinsed with alcohol. Bacteria that retain the crystal violet stain are, generally, classified as Gram-positive and bacteria that do not retain the stain are Gram-negative.

3.3.7 DCLS analysis of Raman spectra and spectral image

When collecting Raman data from complex systems with many different spectral features, it is often inappropriate to use univariate methods to accurately determine the location and proportion of specific biochemical compounds. Thus multivariate data analysis is ideal to investigate these systems. If reference spectra of all pure chemical components are available, direct classical least-squares (DCLS) can be used. DCLS is also referred to as classical least squares (CLS) or ordinary least squares (OLS) in literature.³⁰ In our case reference spectra were obtained by scanning individual plates of bacteria using the same imaging instrument and acquisition settings.

DCLS is based on Beer's law:

$$D = CS^T + E \quad (1)$$

In equation 1, D is the $M \times N$ data matrix, C is the $M \times P$ concentration matrix, S is the $N \times P$ matrix consisting of pure spectra corresponding to unit concentration, E is

the $M \times N$ model residual matrix and P is the number of components and T is the matrix transpose.

DCLS estimates the concentration by a least-square approximation:

$$C = DS'(S'^T S')^{-1} \quad (2)$$

In equation 2, S' is the $N \times P$ reference spectra matrix. If each reference spectrum matrix S' is scaled corresponding to unit concentration, C which consist of estimates of absolute concentrations. However, the absolute amount of a chemical component corresponding to a solid-state spectrum measured with an imaging instrument is usually not available. Thus, determining the absolute concentration is not possible due to the scaling difference between S and S' . This is the so-called intensity ambiguity problem and the situation can be illustrated by the following equation:

$$D = CNN^{-1}S^T = CS'^T \quad (3)$$

For equation 3, D is the reconstructed data matrix, N is a diagonal matrix, $C = CN$ and $S' = SN^{-1}$. Because the diagonal matrix N is not an identity matrix, differences in magnitude between the estimated concentration C and absolute concentration C exist. However, for a given component, the relative concentration distribution is consistent with the actual distribution.

Reference spectra can be used from previously collected spectra or from within the collected image data. There are two general approaches based on DCLS: 1) All reference spectra - for fractional analysis to give repeatable results the reference spectra must all be collected under equivalent conditions (or appropriately scaled) and when creating the images use “no normalisation”. Also for optimum results the reference spectra should have a high signal-noise ratio. With careful use, this technique can give an

indication of component fractional estimates, and could provide a basis for a quantitative calibration approach. 2) Partial reference spectra - now the solution will only be partial as some image data cannot be described by the limited reference spectral information. This will not yield any useful semi-quantitative information; however, the data may be qualitatively useful.

3.4 RESULTS AND DISCUSSION

3.4.1 Morphological observation of bacterial cells under AFM and SEM

Figure 3.1 shows the representative AFM deflection images of Gram-positive strains *M. JLS* (A), *M. KMS* (B), *M. MCS* (D), and SEM images of *M. KMS* (C) and *P. putida* KT2400 (G). Flagella were clearly observed for both *E. Coli* (E) and KT2440 (F) and (G) in both the AFM and SEM images, which are typical cell structures of Gram-negative bacteria. For Gram-positive *Mycobacterium*, both AFM and SEM images show very similar morphology and shape.

3.4.2 Raman microspectroscopy characterization of Gram-positive and Gram-negative bacteria

In Gram-positive bacteria (Figure 3.2), the thick and rigid cell wall structure is composed of many layers of peptidoglycan. This thick cell wall also contains teichoic acids. There are two types of teichoic acids, which are lipoteichoic acid and wall teichoic acid. The lipoteichoic acids span the peptidoglycan and are linked to the plasma membrane and the wall teichoic acids are linked to the peptidoglycan layer. These

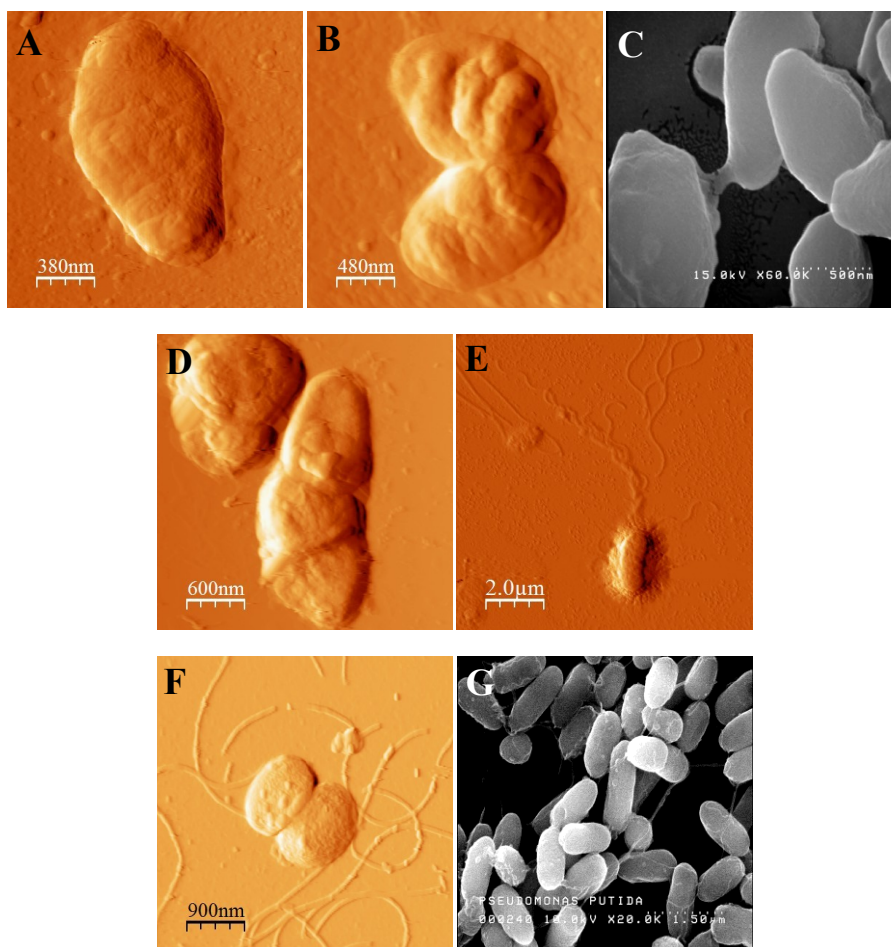


Figure 3.1. AFM deflection images of *M. JLS* (A), *M. KMS* (B), *M. MCS* (D), *E. Coli* (E), *P. putida* KT2440 (F), and SEM images of *M. KMS* (C), and *P. putida* KT2440 (G).

teichoic acids provide much of the antigenic properties of the cell wall.³¹ In recent years, it was determined that vibrational spectroscopy (Raman and infrared) has a high potential for novel imaging in microbiology and medical microbiology.^{32,33} Since that time, Raman has been used to image single bacteria colonies on agar plates and a mixture of colored microorganisms; *Micrococcus luteus* and *Rothia mucilaginosa*,³ *Bacillus atrophaeus* spores and *Escherichia coli* (Gram-negative) in water,³⁴ and biochemical information in

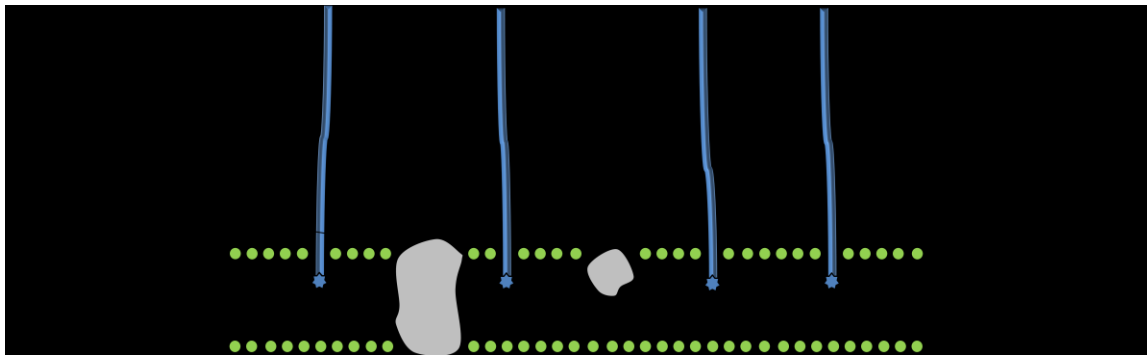


Figure 3.2. A typical schematic of the Gram-positive bacteria cell wall. Gram-positive bacteria lack an outer membrane and the associated lipopolysaccharide (LPS) that is present in Gram-negative organisms (Figure 3.5). In the Gram-positive bacteria cell wall, the peptidoglycan layer is thicker than the Gram-negative cell wall and contains teichoic acids (derived from ³¹).

Cupriavidus metallidurans.⁵ Other Gram-positive bacteria studied with Raman include cultivation conditioned *staphylococcus*,⁸ and the identification of oral *streptococci*.³⁵

Mycobacteria are considered to be Gram-positive eubacteria that are slender, irregular rods and contain a waxy substance in the cell wall. These unique bacteria contain both features of Gram-positive and Gram-negative organisms. Mycobacteria have an outer cell membrane (Figure 3.3) that is covalently bonded to a peptidoglycan layer. After the peptidoglycan layer is the arabinogalactan layer that contains both galactan and arabinan. Lipoarabinomannan can span the peptidoglycan and arabinogalactan layers. Above the arabinogalactan layer is a mycolic acid layer that contains intercalated lipids. Above the mycolic acid layer is a capsule-like material, which lipoarabinomannan can cross. Mycobacterium species can cause tuberculosis and leprosy in humans. Raman spectroscopy has been utilized for rapid identification of mycobacterium to explore the possibility of identifying mycobacterium without biosafety 3 level precautions.³⁶ Due to

the unique structures of the complex glycans; mycolic acid-arabinogalactan-peptidoglycan complex and polysaccharide-rich arabinomannan and mannan capsule, inhibition target drugs are possible against human diseases.³⁷

Our Raman spectral analysis focused on a spectral fingerprint range of 500-1800 cm^{-1} . Vibrational bands typical of proteins, phospholipids, nucleic acids, and polysaccharides are anticipated to contribute to these spectra. Figure 3.4 shows the representative Raman spectra of Gram-positive bacteria in the 500-1800 cm^{-1} region and tentative peak assignments of Gram-positive bacteria are given in Table 3.1. It was found that, *M. KMS*, *M. JLS*, and *M. MCS* share similar characteristic peaks of 780, 1003, 1154, 1186, 1212, 1262, 1524, and 1651 cm^{-1} . Three strong bands at 1003, 1154, and 1524 cm^{-1} could be tentatively assigned as C-CH₃ deformation, C-C stretching, and C=C stretching modes of sarcinaxantin (or carotenoids), respectively. The 780 cm^{-1} peak is related to cytosine and uracil ring stretching, while 1262 and 1651~1657 cm^{-1} are associated with amide III and amide I. It is interesting to note that the peak intensity at 1487 cm^{-1} (CH₂ deformation) follow the order *M. JLS* > *M. KMS* > *M. MCS* (undetectable). For *M. MCS*, peaks at 1062, 1082, and 1128 cm^{-1} imply the presence of unsaturated fatty acids on the cellular surface.

For Gram-negative bacteria (Figure 3.5), the cell wall is made up of a few layers of peptidoglycan and an outer membrane. The peptidoglycan is bonded to the lipoproteins which are covalently bonded to the outer membrane. The periplasmic space is the space between the cell wall and the plasma membrane. Inside the periplasmic space are a host of enzymes and transport proteins. Unlike the Gram-positive cell wall, the

Table 3.1. Tentative peak assignments of Gram-positive and Gram-negative bacteria

Gram-positive bacteria			Gram-negative bacteria		
Wavenumber (cm ⁻¹)	Description	Assignment	Wavenumber (cm ⁻¹)	Description	Assignment
780	m	ν (ring) DNA/RNA C, U	783	m	ρ (ring) DNA/RNA U, T, C
1003	vs	δ (C-CH ₃)	1002	vs	δ (ring) Phenylalanine
1154	vs	ν (C-C)	1126	m, b	ν (C-C)
1262	w	amide III	1342	b	δ (CH ₂)/DNA G
1524	vs	ν (C=C)	1449	b	ν (CH ₂)/asymmetric δ (CH ₃)
1651	m, b	amide I	1661	b	amide I

vs, very strong; m, medium; w, weak; b, broad; ν , stretching; δ , deformation; ρ , breathing.

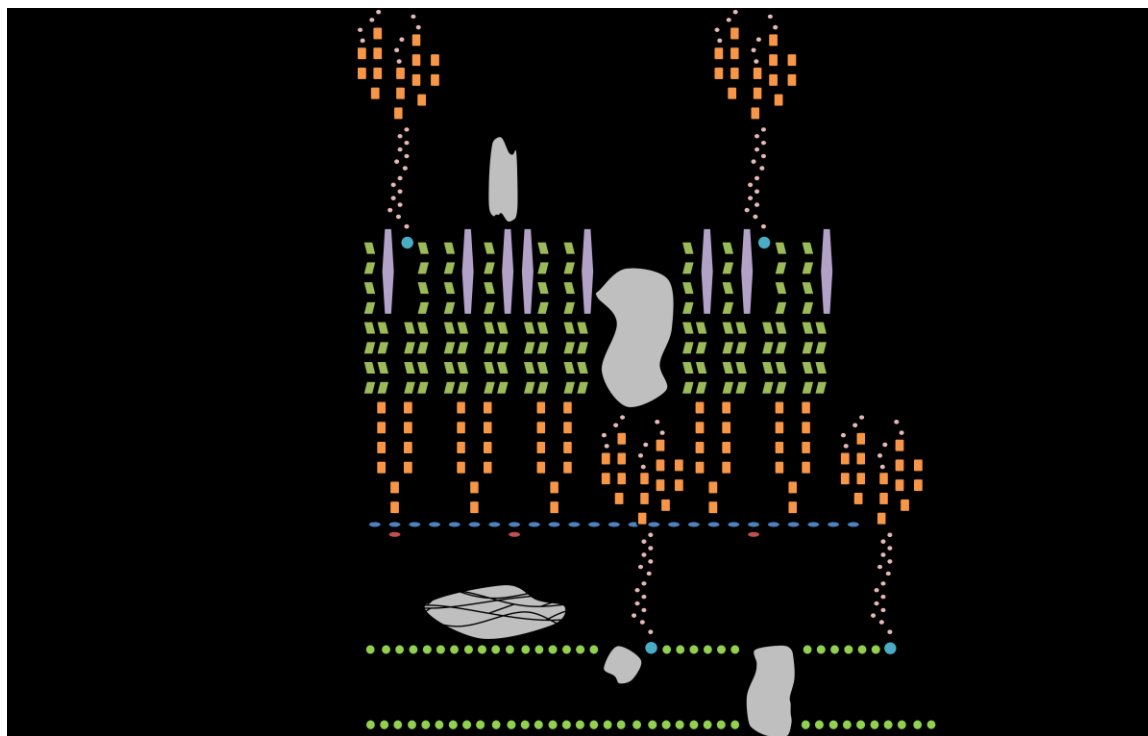


Figure 3.3. Schematic of mycobacterium cell wall structure (derived from ^{37,38}).

Gram-negative cell wall does not contain teichoic acids. The outer membrane of the cell wall is made up of lipopolysaccharides, phospholipids, and lipoproteins. The outer membrane is the first line of defense for the Gram-negative bacteria and aids in evading phagocytosis, and is a barrier for antibiotics, enzymes, detergents, heavy metals, bile salts, and certain dyes.³⁹ The Gram-negative cell wall contains porins that can allow for the passage of molecules. There are also O-polysaccharides that function as antigens and lipid A which is an endotoxin.³⁹ Raman spectroscopy has been used to study carotenoids

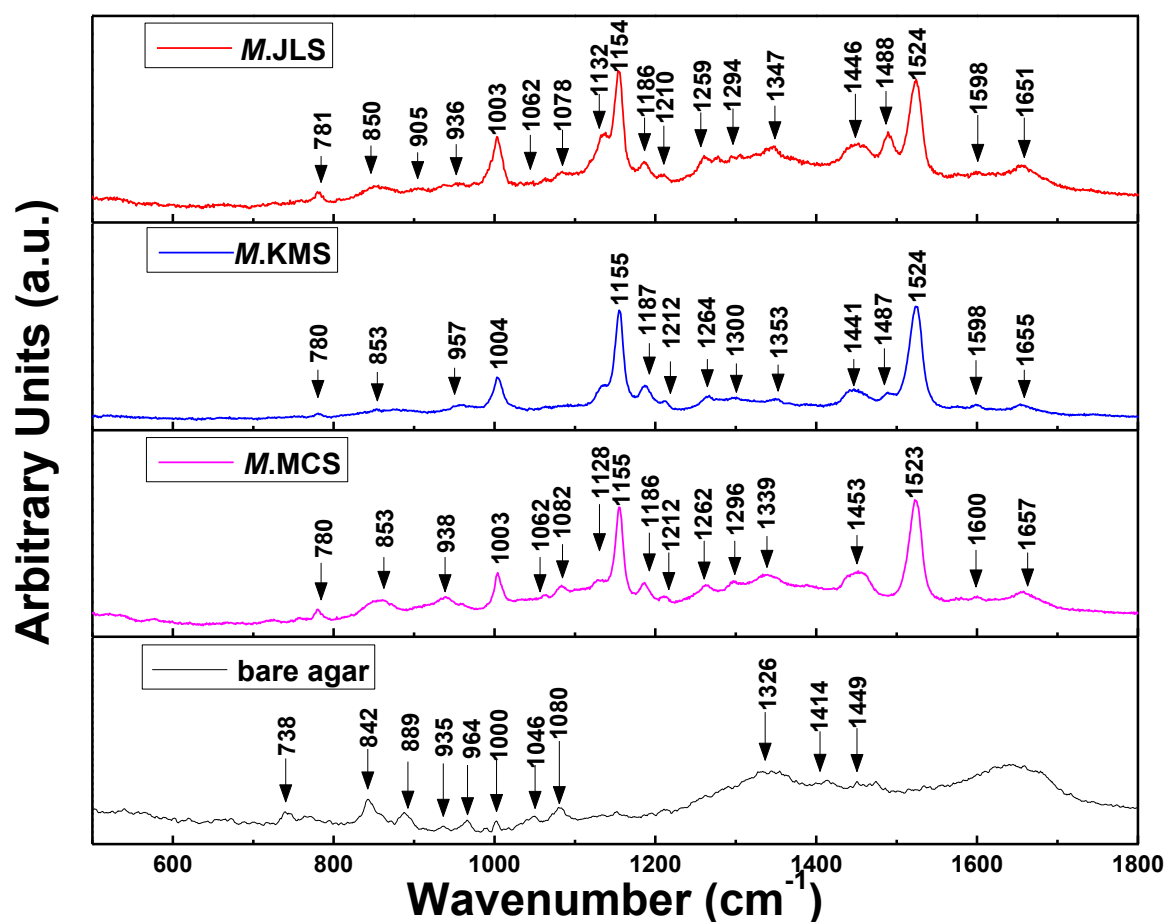


Figure 3.4. Raman spectra of Gram-positive *M. JLS*, *M. KMS*, and *M. MCS* grown on LB agar.

in *Halobacterium salinarium* colonies grown on agar,⁴⁰ distinguishing *Pseudomonas fluorescens* from other bacteria,³ and identifying different constituents of molecular fragments in *Acidithiobacillus ferrooxidans* and secreted extracellular polymeric substances (EPSs).⁴¹

Figure 3.6 show Raman spectra for each Gram-negative bacterium and the characteristic peak assignments for the Gram-negative microorganisms are listed in Table 3.1. There are two dominant peaks observed at 783 and 1002 cm^{-1} and four broad peaks at 1126, 1342, 1449, and 1661 cm^{-1} , respectively. DNA/RNA breathing modes of cytosine, thymine, and uracil bases can be assigned to the band at 785 cm^{-1} . The peak at 1006 cm^{-1} is related to phenylalanine of proteins or $\delta(\text{ring})$ deformation. In the broad bands, peak 1127 cm^{-1} is associated with C-C stretching in saturated fatty acids,

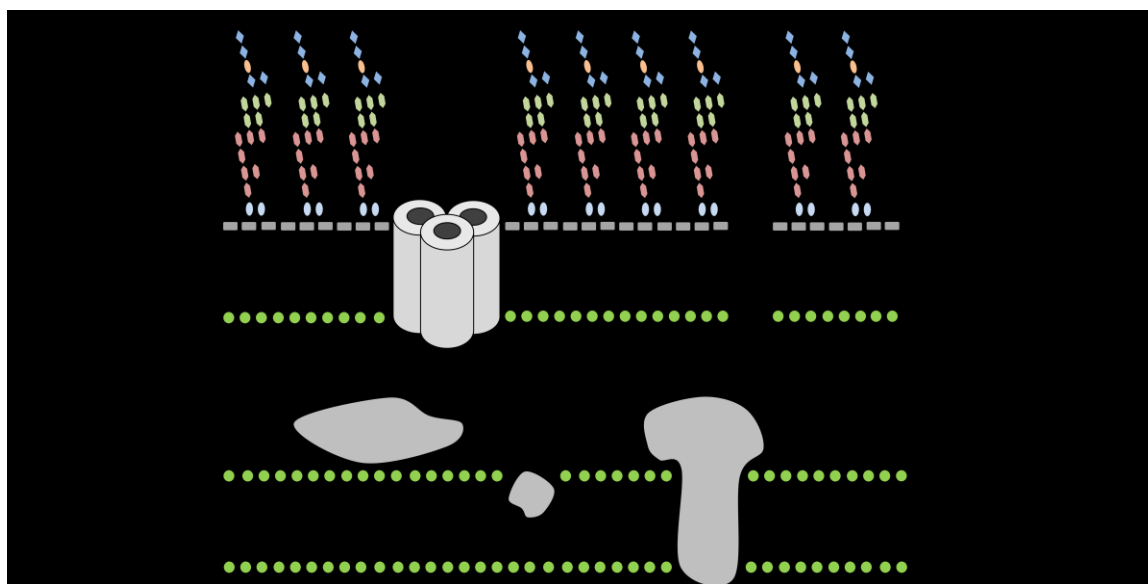


Figure 3.5. Schematic of Gram-negative bacteria cell wall with several layers of polysaccharides and glycoconjugates. The periplasmic space contains peptidoglycan and proteins. The outer leaflet of the outer membrane is rich in lipopolysaccharide (LPS) and (n) variable number of O-antigen repeats. With permission from.²⁵

whereas 1342 cm^{-1} can be assigned to guanine in DNA or $\delta(\text{CH}_2)$ deformation in proteins and carbohydrates and the major peak at 1454 cm^{-1} could correspond to a $\nu(\text{CH}_2)$ stretching or a $\delta(\text{CH}_3)$ deformation associated with lipids, proteins, and carbohydrates. The 1660 cm^{-1} peak is related to the amide I band. Tentative peak assignments for Gram-negative bacteria are listed in Table 3.1.

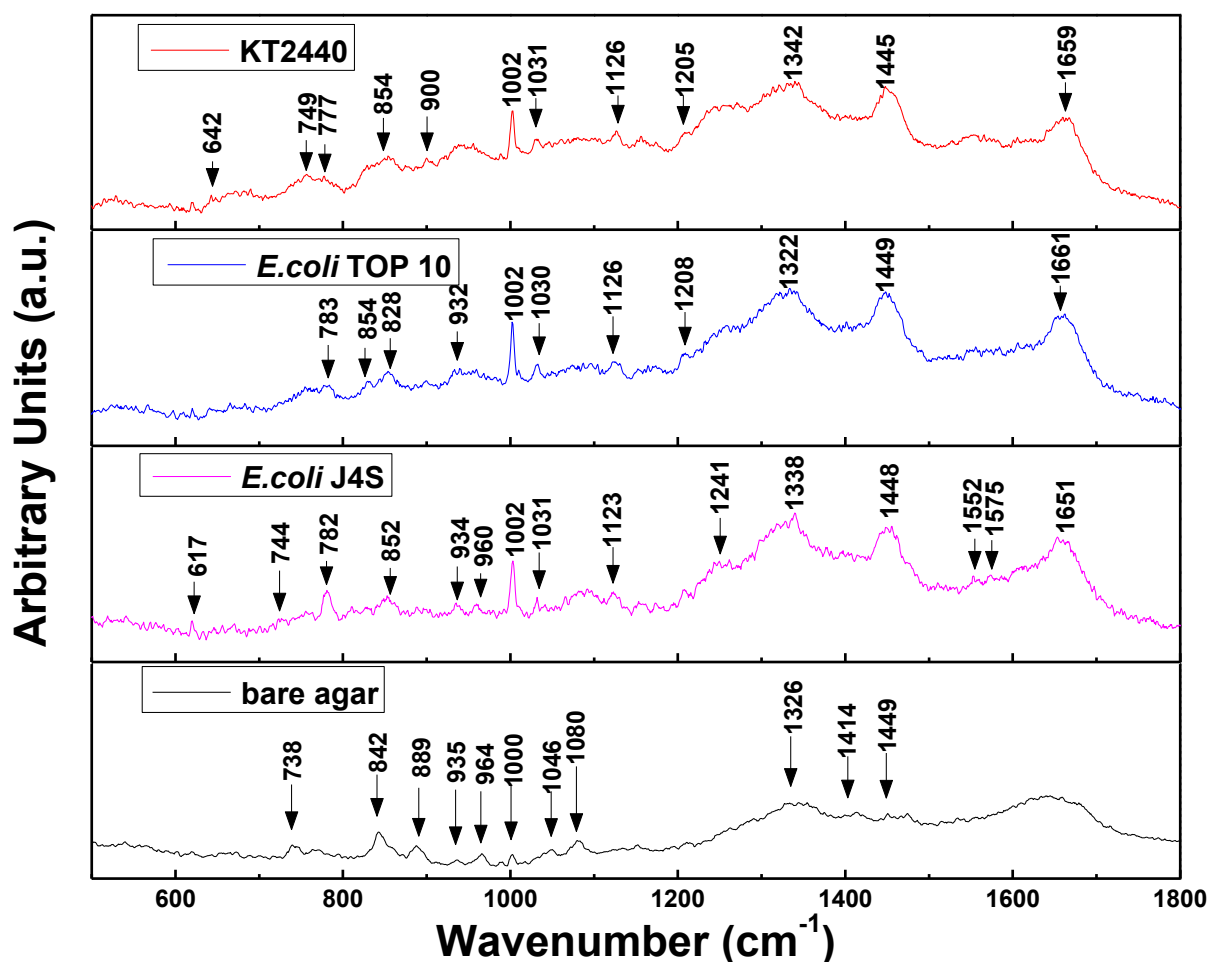


Figure 3.6. Raman spectra of Gram-negative bacteria; *E. coli* TOP 10, *E. coli* J4S, and *P. putida* KT2440 grown on agar.

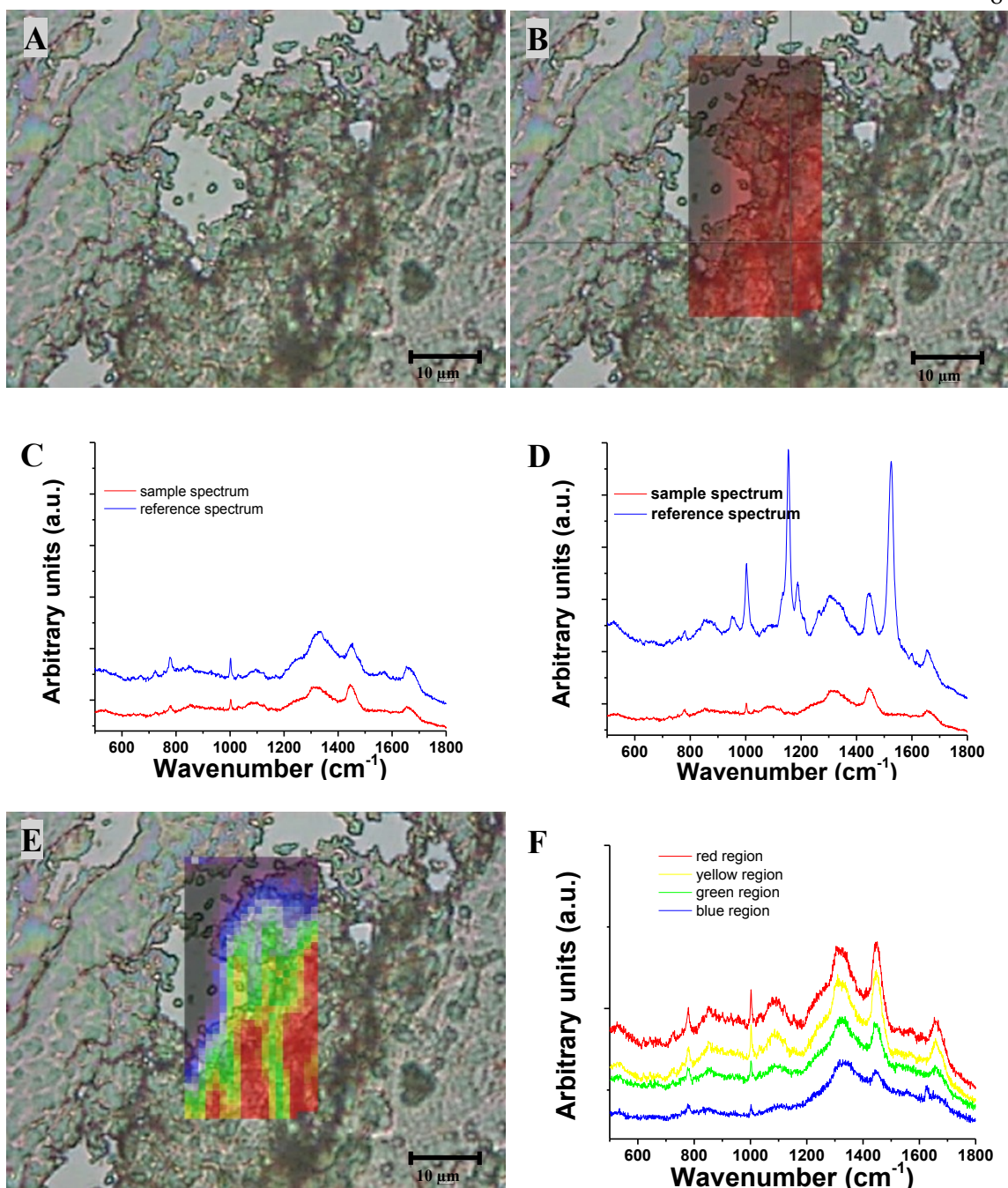


Figure 3.7. Raman mapping on the agar surface containing KT2440. Bright field image (A), the crosshair of the image indicates the actual spectra (B); DCLS spectral data fit to a spectrum of KT2440 (C) (blue curve); DCLS spectral data fit to a spectrum of *M. KMS* (D) (blue curve). The rainbow color image is a concentration distribution of KT2440 (E). Raman spectra of the four color regions (F). Red and yellow represents higher concentration and green and blue represents lower concentration.

3.4.3 DCLS analysis of *P. putida* KT2440

Raman mapping for KT2440 was conducted as a spectral image and was acquired over the fingerprint region $500\text{-}1800\text{ cm}^{-1}$, as shown in Figure 3.7. The data were processed by direct classical least squares (DCLS) fitting of the collected spectra to a linear combination of the specified component spectra. For the DCLS analysis, a number of representative spectra exhibiting similar features to the pure components were needed as an input for the generation of the DCLS map. Such a requirement was achieved by extracting spectra from the mapping data and comparing them to the reference samples of *M. KMS* and KT2440 prepared separately from cultured bacteria. DCLS analysis uses a linear combination of spectra from the pure components from each species contained in the sample that most closely match the Raman spectrum of the sample. It is seen that the crosshair point in Figure 3.7-B (red spectrum in Figure 3.7-C and -D) represent a good match for the KT2440 reference spectrum (blue curve in Figure 3.7-C), while the crosshair point (red spectrum) does not match the *M. KMS* reference spectrum (blue curve in Figure 3.7-D). From the Raman spectral map of KT2440, the Gram-negative organism can be identified (red region in Figure 3.7-B) based on DCLS analysis. It is observed in Figure 3.7-C that the Raman spectra obtained from KT2440 more closely match the reference spectra obtained from pure KT2440 cells. The rainbow color image (Figure 3.7-E) represents variation of KT2440 concentrations at different locations in the map (color gradient represents the variation in cell concentration). Red represents the greatest concentration and blue the lowest concentration. Figure 3.7-F gives Raman spectra of KT2440 for the different color regions in Figure 3.7-E.

3.4.4 Interaction analysis of mixture of *Mycobacteria MCS* with *Pseudomonas putida* KT 2440

One useful application of Raman spectral mapping would be to distinguish co-cultured bioremediation soil bacteria. Figure 3.8 shows the Raman mapping using the Streamline image acquisition mode, on an LB agar surface that contains both *M. MCS* and *P. putida* KT2440. Figure 3.8-B shows the Raman mapping on the agar surface containing both *M. MCS* (red region in Figure 3.8-C) and KT2440 (green region in Figure 3.8-D). Figure 3.8-E shows the DCLS reference spectrum (blue curve) fit to a spectrum of *M. MCS* (red curve) and Figure 3.8-F shows DCLS reference spectrum (blue curve) fit to a spectrum of KT2440 (green curve). Raman mapping (Figure 3.8-B, -C, -D) was then used to distinguish between both *M. MCS* and KT2440 based on DCLS analysis. The red region indicated the presence of *M. MCS* and the green region indicated the presence of KT2440. It was observed that the spectra of *M. MCS* (red curve in Figure 3.8-E) derived from red region was similar with the Raman spectra of *M. MCS* in the range of 842 cm^{-1} to 1212 cm^{-1} in Figure 3.4. The derived spectrum (red curve) in Figure 3.8-E clearly shows two characteristic peaks at 1003 cm^{-1} and 1154 cm^{-1} respectively. Whereas the spectra of KT2440 (green curve in Figure 3.8-F) derived from green region not only shows a characteristic peak at 1002 cm^{-1} , but also shows a weak characteristic peak at 1154 cm^{-1} , the reason was probably due to the combination of bacteria mixed and grown together. Thus, it was shown that Raman mapping and the derived Raman spectrum can be used to identify a mixture of *M. MCS* and KT2440.

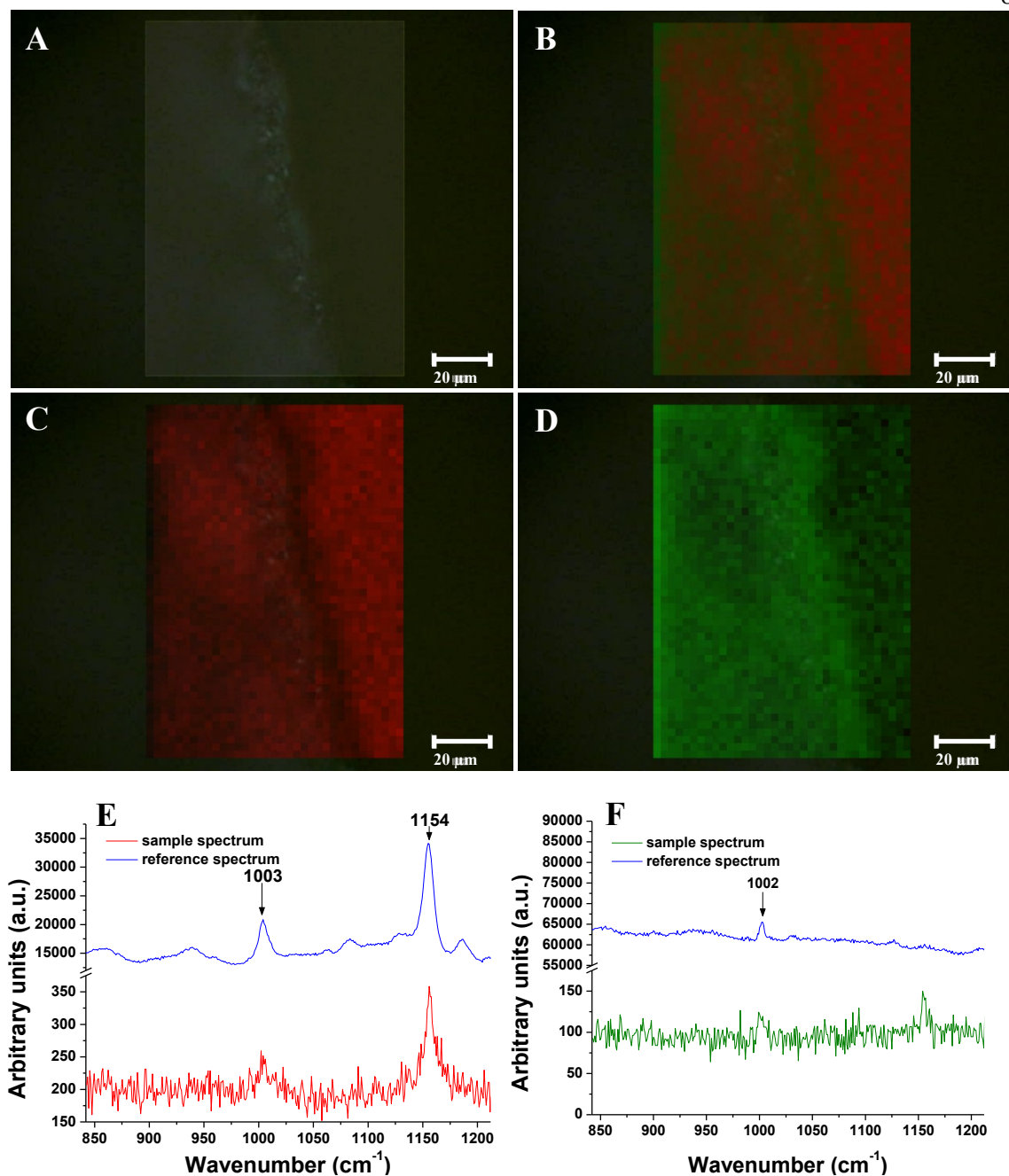


Figure 3.8. Raman spectral map of LB agar surface containing both *M. MCS* and *P. putida* KT2440. Bright field image (A), Raman spectral map of both co-cultured *M. MCS* and KT2440 (B). Individual Raman spectral maps of *M. MCS* (C) and KT2440 (D). DCLS spectral data fit to a spectrum of *M. MCS* (E, blue curve = reference, red curve = actual) and DCLS spectral data fit to a spectrum of KT2440 (F, blue curve = reference, red curve = actual).

3.4.5 Fourier transform infrared spectroscopy (FTIR)

Each bacterial species has a complex cell wall/membrane composition that gives a unique IR fingerprint. This uniqueness is due to the stretching and bending vibrations of molecular bonds or functional groups present in proteins, nucleic acids, lipids, sugars, and lipopolysaccharides within the cell wall. The molecular composition can vary from species to species and even at the strain level. Therefore each bacterium will have a unique and characteristic spectrum, and single microorganisms could be identified from a FTIR spectrum.

Figure 3.9 shows the representative infrared spectrum of *M. KMS* on four different substrates in the 700 – 4000 cm^{-1} range. The main bands were labeled in Figure 3.9 and detailed spectral band assignments for bacteria are listed in Table 3.2. IR spectra measured for intact cells of bacteria are usually complex and the peaks are broad due to superposition of contributions from all the biomolecules present in a bacterial cell (Figure 3.9). In the absence of water, Naumann^{10,42} recommended that five major absorbance regions in IR spectra should be analyzed for the identification of bacteria: the 3000 – 2800 cm^{-1} spectral region is the fatty acid region (region I); 1700 – 1500 cm^{-1} contains the amide I and II bands of proteins and peptides (region II); 1500 – 1200 cm^{-1} is a mixed region of fatty acid bending vibrations, proteins, and phosphate-carrying compounds (region III); 1200 – 900 cm^{-1} contains absorption bands of the carbohydrates in microbial cell walls (region IV); and 900 – 700 cm^{-1} is the “fingerprint region” that contains weak but very unique absorbance values that are characteristic to specific bacteria (region V). Regions I and II are the most useful for routine bacterial identification; however, the other regions may be used to better understand minor variations in the structure and

composition of bacteria. The fingerprint region is significant for the discrimination of microorganisms at the strain level. The wave number positions of absorbance peaks, peak intensities, and peak widths are useful for functional group, cell component, and sample identification.⁴³ There are several interesting peaks that appear on an IR spectrum of bacteria, and most of them represent functional group vibrations in the main biomolecular constituents like protein, fatty acids, nucleic acid, and carbohydrates.

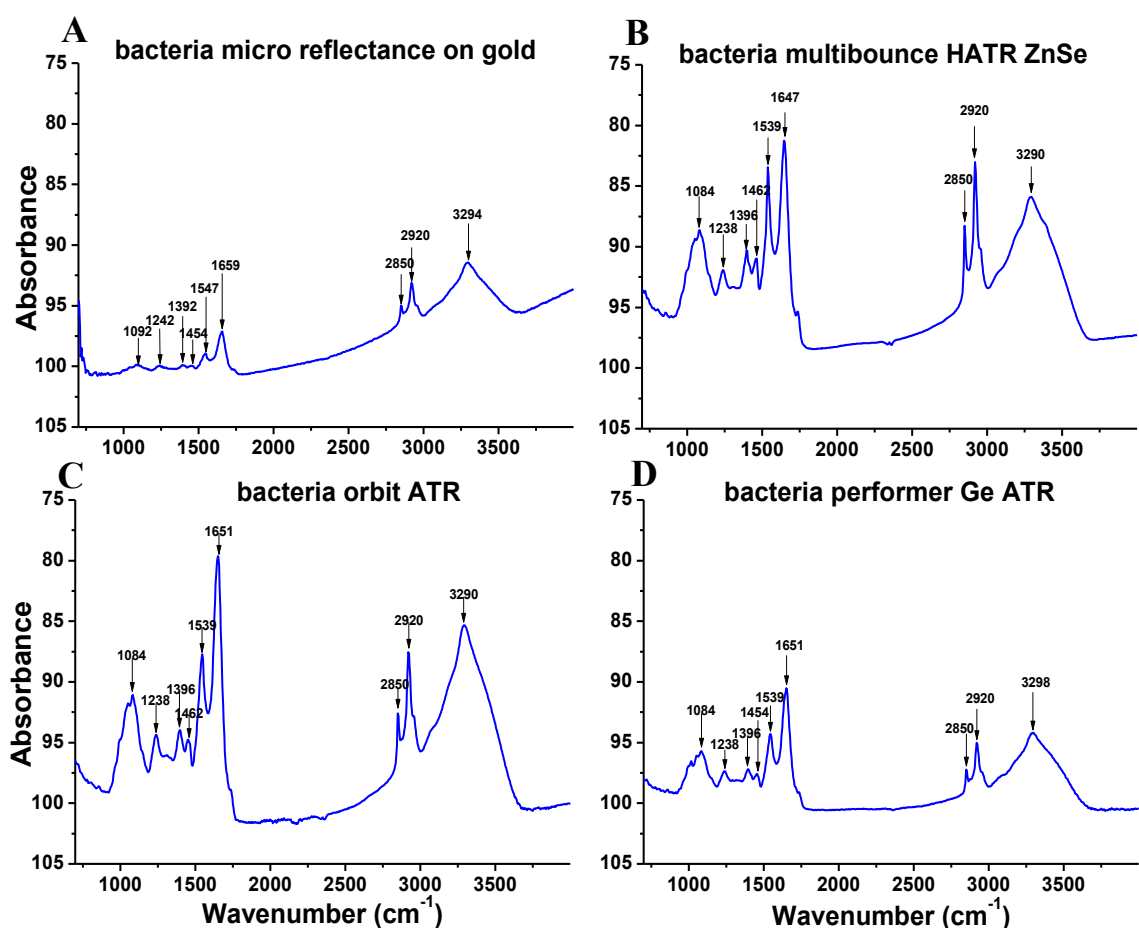


Figure 3.9. Representative IR absorbance spectra (700 – 4000 cm^{-1}) of *M. KMS* on four different substrates: gold surface (A), multibounce ZnSe crystal (B), Orbit with a diamond crystal (C), and Ge ATR crystal (D).

Table 3.2. Assignment of functional groups associated with major vibration bands in IR spectra of bacteria.

Wavenumber (cm^{-1})	Definition of the spectral assignment
3290	N-H and O-H stretching vibration: polysaccharides, proteins
2920	CH_2 asymmetric stretch: mainly lipids, with the little contribution from proteins, carbohydrates, nucleic acids
2850	CH_2 symmetric stretch: mainly lipids, with the little contribution from proteins, carbohydrates, nucleic acids
1651	Amide I (protein C=O stretching): α helices
1539	Amide II (protein N-H bend, C-N stretch): α helices
1462	CH_2 Bending: lipids
1396	COO^- symmetric stretch: amino acid side chains, fatty acids
1238	PO_2^- asymmetric stretching: mainly nucleic acids with the little contribution from phospholipids
1084	PO_2^- symmetric stretching: nucleic acids and phospholipids

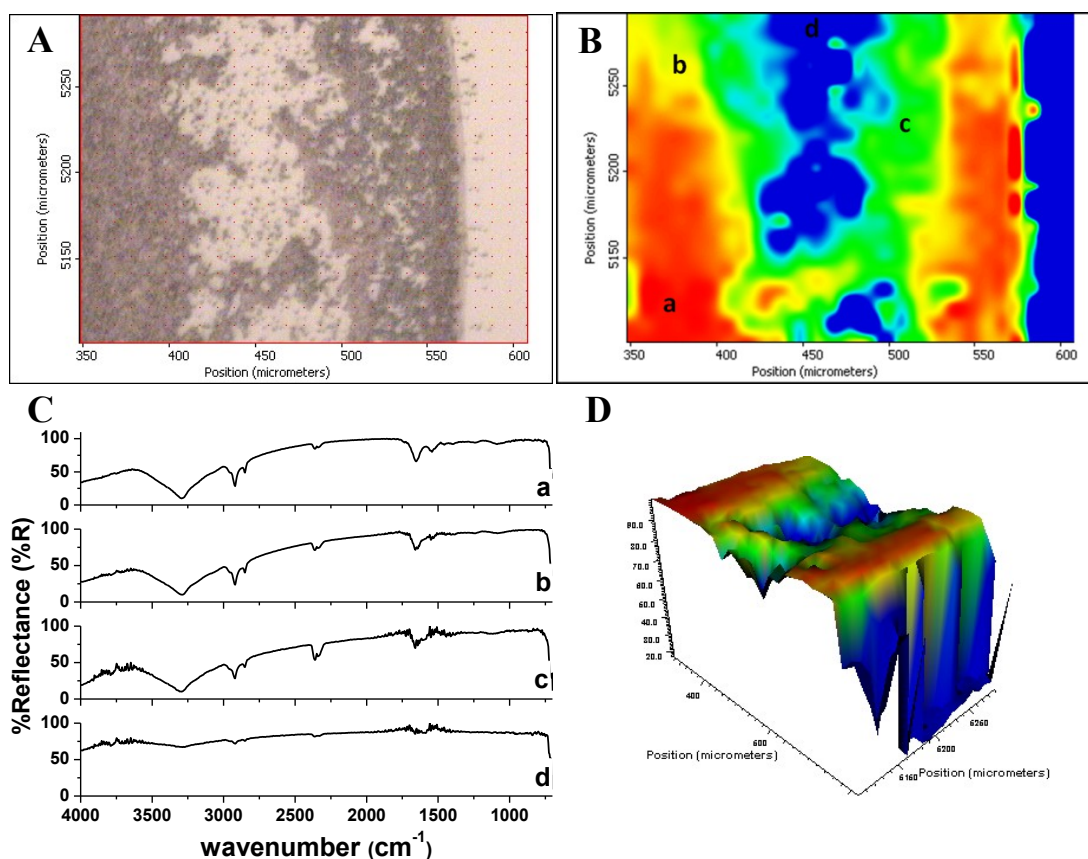


Figure 3.10. FTIR spectrum and mapping of *M. KMS* coated on gold surface. Bright field view (A), concentration heat map (B, red = high, blue = low), selected points with the heat map (C), and a 3D surface image of the heat map (D).

Figure 3.10 gives the FTIR spectrum and mapping of *M. KMS*. The FTIR mapping was conducted at 1653 cm^{-1} , which corresponds to $\delta(\text{NH}_2)$, $\delta(\text{NH}_3^+)$ association, $\delta(\text{CH}_2)$, $\nu(\text{C-O})$, $\delta(\text{NH}_3^+)$ symmetrical vibrations. However, it is apparent that the fingerprint region of $500 - 1800\text{ cm}^{-1}$ did not give detailed chemical composition information due to the low spectral resolution. The major restriction of using FTIR for bacteria characterization is that FTIR is not optimal for application with aqueous samples. Furthermore, the detection limit with IR methods is often not sufficient to quantify low levels of analytes. So it is critical to concentrate bacteria and remove as much liquid (water) from the sample as practical⁴⁴ for qualitative as well as quantitative analysis. In contrast, Raman spectra provided a greater number of spectral features for the bacterial cell membrane compared with FTIR. Raman scattering relies on changes in the polarizability of functional groups as atoms vibrate while IR absorption requires a change in the intrinsic dipole moment to occur with molecular vibrations.⁴⁵ Polar groups such as C=O, N-H, and O-H have strong IR stretching vibrations and non-polar groups, such as C-C and S-S have intense Raman bands.^{46,47} Raman spectroscopy provides some major advantages over IR spectroscopy for investigations of biological samples⁴⁸ since interference of water spectral features is less problematic. In addition, more spectral features are detectable in a Raman spectrum than in an infrared one over the same wavenumber range. Raman bands tend to be narrower than those in the IR range because Raman laser/detectors offer greater specificity. Figure 3.10 shows that the surface distribution can resolve both physical and chemical differences compared with sections that were bacteria free. The rainbow color in the distribution map (Figure 3.10-B) represents variation of the *M. KMS* concentration at different locations in the map. Red

represents an intense presence and blue almost total absence of bacteria. Four spectra were extracted from the map (a, b, c, d curves in Figure 3.10-C derived from red, yellow, green and blue regions in Figure 3.10-B respectively). The lower right image (Figure 3.10-D) is a 3D representation of the distribution based on the absorption intensity in the spectrum at each point.

3.4.6 Combined AFM/Raman microspectroscopy of mycobacterium

Figure 3.11 illustrates a combined AFM/Raman measurement of *M. JLS* coated on a gold (111) coated mica slide. The AFM phase feedback height image Figure 3.11-A was collected in non-contact mode in air and concurrent Raman spectra were acquired for each point on the AFM image. From the software, the respective crosshair indicates one individual Raman spectrum in, Figure 3.11-B, and shows characteristic peaks of mycobacterium at $\sim 1003\text{ cm}^{-1}$ and 1154 cm^{-1} . Next, from the 169 Raman spectra (13×13 matrix), a spectral heat map at Raman band 1154 cm^{-1} was created using QuartzSpec software and the relative intensity of this band is shown in Figure 3.11-C. The significance of the combined AFM/Raman is the ability to gather mechanical/force properties for the sampled specimen from the AFM image and also have the accompanying chemical information from the Raman spectra.

3.5 CONCLUSIONS

Gram-positive and Gram-negative bacteria are biochemically characterized by Raman, FTIR and AFM and can be separated on the basis of either the presence or absence of Raman peaks that can serve as identifiable markers for the analyzed bacteria.

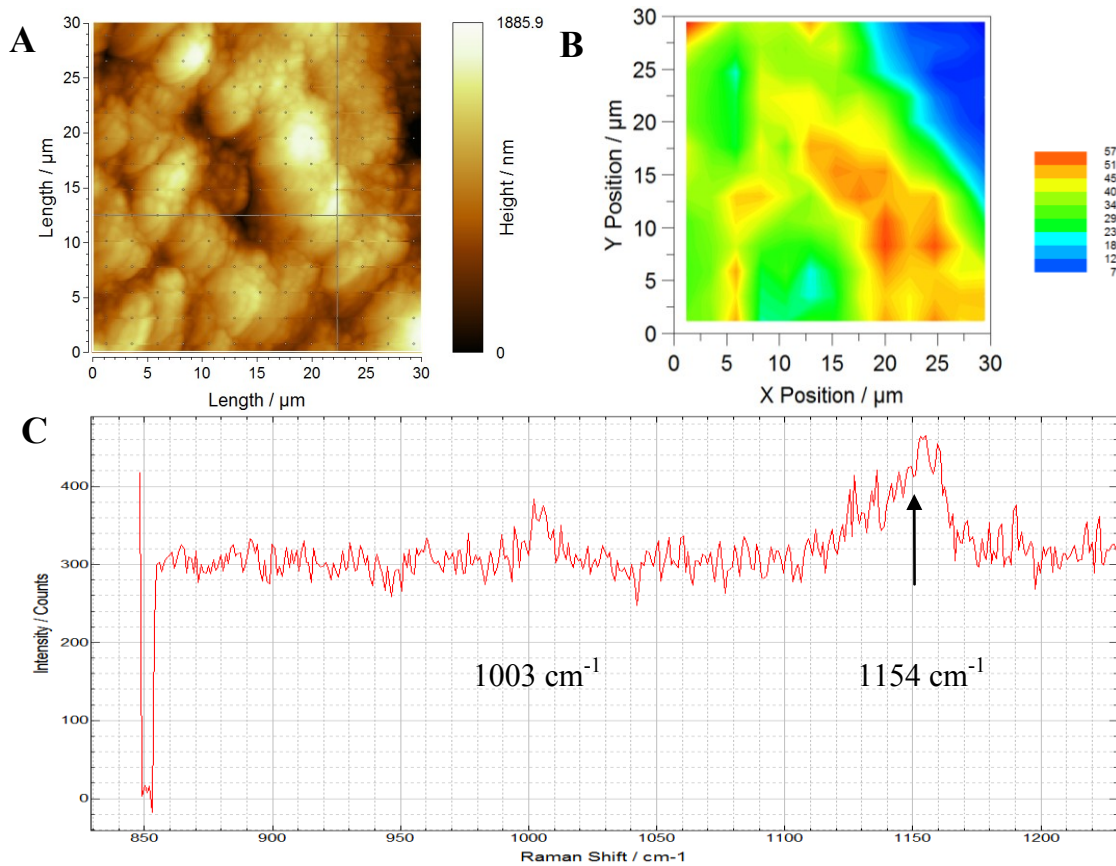


Figure 3.11. Combined AFM/Raman measurement of *M. JLS* on gold coated mica (A) acquired in phase feedback mode in air. Raman spectral intensity map at 1154 cm^{-1} (B). Raman spectrum at crosshair on AFM image (C) acquired at 100% laser power with 1 second exposure and a center of 1040 cm^{-1} . Scale is = $30 \times 30\ \mu\text{m}$. *M. JLS* was cultured Luria Broth (LB), concentrated by centrifugation at 2000 rpm for 2 minutes and spotted on the gold coated mica substrate and allowed to dry in air.

The large differences in molecular composition of the outer membrane and cell wall of Gram-positive and Gram-negative bacteria lead to variation in spectral regions of each individual Raman spectra. This study is an evaluation of Raman spectroscopy as a new method for rapid and nondestructive screening of Gram-positive and Gram-negative bacteria. In addition, the intensities of various peaks from distribution maps of Raman and FTIR give us additional information related to the variation of the bacteria

concentration at different locations within the respective samples. Raman microspectroscopy could therefore serve as a reagentless alternative to routine Gram testing with the advantage of easy automation for spectral analysis and simple sample preparation.

3.6 REFERENCES

1. Carey, P. R. *J Biol Chem* 1999, 274, 26625-26628.
2. Baena, J. R.; Lendl, B. *Curr Opin Chem Biol* 2004, 8, 534-539.
3. Rösch, P.; Schmitt, M.; Kiefer, W.; Popp, J. *J Mol Struct* 2003, 661, 363-369.
4. Rösch, P.; Harz, M.; Schmitt, M.; Peschke, K. D.; Ronneberger, O.; Burkhardt, H.; Motzkus, H. W.; Lankers, M.; Hofer, S.; Thiele, H.; Popp, J. *Appl Environ Microbiol* 2005, 71, 1626-1637.
5. De Gelder, J.; De Gussem, K.; Vandenabeele, P.; Vancanneyt, M.; De Vos, P.; Moens, L. *Anal Chim Acta* 2007, 603, 167-175.
6. Petrov, G. I.; Arora, R.; Yakovlev, V. V.; Wang, X.; Sokolov, A. V.; Scully, M. O. *Proc Natl Acad Sci USA* 2007, 104, 7776-7779.
7. Neugebauer, U.; Schmid, U.; Baumann, K.; Holzgrabe, U.; Ziebuhr, W.; Kozitskaya, S.; Kiefer, W.; Schmitt, M.; Popp, J. *Biopolymers* 2006, 82, 306-311.
8. Harz, M.; Rösch, P.; Peschke, K. D.; Ronneberger, O.; Burkhardt, H.; Popp, J. *Analyst* 2005, 130, 1543-1550.
9. Neugebauer, U.; Schmid, U.; Baumann, K.; Ziebuhr, W.; Kozitskaya, S.; Deckert, V.; Schmitt, M.; Popp, J. *Chemphyschem* 2007, 8, 124-137.
10. Naumann, D.; Helm, D.; Labischinski, H. *Nature* 1991, 351, 81-82.
11. Maquelin, K.; Kirschner, C.; Choo-Smith, L. P.; Ngo-Thi, N. A.; van Vreeswijk, T.; Stammler, M.; Endtz, H. P.; Bruining, H. A.; Naumann, D.; Puppels, G. J. *J Clin Microbiol* 2003, 41, 324-329.
12. Holman, H. Y. N.; Nieman, K.; Sorensen, D. L.; Miller, C. D.; Martin, M. C.; Borch, T.; McKinney, W. R.; Sims, R. C. *Environ Sci Technol* 2002, 36, 1276-1280.
13. Rodriguez, A.; Autio, W. R.; McLandsborough, L. A. *Food Biophys* 2008, 3, 305-311.

14. Yongsunthon, R.; Lower, S. K. *Advances in Appl Microbiol*, Vol 58 2006, 58, 97-124.
15. Beckmann, M. A.; Venkataraman, S.; Doktycz, M. J.; Nataro, J. P.; Sullivan, C. J.; Morrell-Falvey, J. L.; Allison, D. P. *Ultramicroscopy* 2006, 106, 695-702.
16. Miller, C. D.; Hall, K.; Liang, Y. N.; Nieman, K.; Sorensen, D.; Issa, B.; Anderson, A. J.; Sims, R. C. *Microbial Ecology* 2004, 48, 230-238.
17. Bagdasarian, M.; Lurz, R.; Ruckert, B.; Franklin, F. C.; Bagdasarian, M. M.; Frey, J.; Timmis, K. N. *Gene* 1981, 16, 237-247.
18. Nelson, K. E. *Environ Microbiol* 2002, 4, 777-778.
19. Federal Register; Washington, DC, 1982.
20. Nelson, K. E.; Weinel, C.; Paulsen, I. T.; Dodson, R. J.; Hilbert, H.; Martins dos Santos, V. A.; Fouts, D. E.; Gill, S. R.; Pop, M.; Holmes, M.; Brinkac, L.; Beanan, M.; DeBoy, R. T.; Daugherty, S.; Kolonay, J.; Madupu, R.; Nelson, W.; White, O.; Peterson, J.; Khouri, H.; Hance, I.; Chris Lee, P.; Holtzapple, E.; Scanlan, D.; Tran, K.; Moazzez, A.; Utterback, T.; Rizzo, M.; Lee, K.; Kosack, D.; Moestl, D.; Wedler, H.; Lauber, J.; Stjepandic, D.; Hoheisel, J.; Straetz, M.; Heim, S.; Kiewitz, C.; Eisen, J. A.; Timmis, K. N.; Dusterhoft, A.; Tumbler, B.; Fraser, C. M. *Environ Microbiol* 2002, 4, 799-808.
21. Pal, A.; Paul, A. K. *Indian J Microbiol* 2008, 48, 49-64.
22. Tian, Y. *International J Environ Pollut* 2008, 32, 78-89.
23. Bhaskar, P. V.; Bhosle, N. B. *Environ Int* 2006, 32, 191-198.
24. Kachlany, S. C.; Lavery, S. B.; Kim, J. S.; Reuhs, B. L.; Lion, L. W.; Ghiorse, W. C. *Environ Microbiol* 2001, 3, 774-784.
25. McEwen, G. D.; Wu, Y. Z.; Zhou, A. H. *Biopolymers* 2010, 93, 171-177.
26. Beveridge, T. J. *Int Rev Cytol* 1981, 72, 229-317.
27. Perry, J. J.; Staley, J. T.; Lory, S.; Sinauer Associates Incorporated Sunderland 2002.
28. Wu, Y. Z.; Zhou, A. H. *Micron* 2010, 41, 814-820.
29. Solomon, E. P.; Berg, L. R.; Martin, D. W.; Saunders College Publishing: New York, 1999.
30. Martens, H.; Naes, T.; John Wiley and Sons: New York, 1992.
31. Varki, A.; Cummings, R.; Esko, J.; Freeze, H.; Hart, G.; Marth, J., Eds. *Essentials of Glycobiology*; Cold Spring Harbor Laboratory Press: New York, 1999.

32. Maquelin, K.; Kirschner, C.; Choo-Smith, L. P.; van den Braak, N.; Endtz, H. P.; Naumann, D.; Puppels, G. J. *J Microbiol Methods* 2002, 51, 255-271.
33. Thi, N. A. N.; Carolin, K.; Dieter, N. *Proc SPIE* 2000, 36, 36-44.
34. Tripathi, A.; Jabbour, R. E.; Treado, P. J.; Neiss, J. H.; Nelson, M. P.; Jensen, J. L.; Snyder, A. P. *Appl Spectrosc* 2008, 62, 1-9.
35. Berger, A. J.; Zhu, Q. Y. *J Modern Optics* 2003, 50, 2375-2380.
36. Buijtel, P. C. A. M.; Willemse-Erix, H. F. M.; Petit, P. L. C.; Endtz, H. P.; Puppels, G. J.; Verbrugh, H. A.; van Belkum, A.; van Soolingen, D.; Maquelin, K. *J Clin Microbiol* 2008, 46, 961-965.
37. Varki, A.; Cummings, R.; Esko, J.; Freeze, H.; Stanley, P.; Bertozzi, C. R.; Hart, G. W.; Etzler, M. E., Eds. *Essentials of Glycobiology*; Cold Spring Harbor Laboratory Press: New York, 2008.
38. Brennan, P. J.; Crick, D.C. *Current Topics in Medical Chemistry* 2007, 7, 475-488.
39. Tortora, G. J.; Funke, B. R.; Case, C. L.; Addison Wesley Longman, Inc.: Menlo Park, California, 1998.
40. Goodwin, J. R.; Hafner, L. M.; Fredericks, P. M. *J Raman Spectrosc* 2006, 37, 932-936.
41. Pradhan, N.; Pradhan, S. K.; Nayak, B. B.; Mukherjee, P. S.; Sukla, L. B.; Mishra, B. K. *Res Microbiol* 2008, 159, 557-561.
42. Naumann, D. In *Encyclopedia of Analytical Chemistry*; John Wiley and Sons, 2006.
43. Mauer, L. J.; Reuhs, B. L., *Wiley Handbook of Science and Technology for Homeland Security*; John Wiley and Sons, 2008.
44. Fountain, A. W.; Pearman, W. F. *Appl Spectrosc* 2006, 60, 356-365.
45. Naumann, D. *Appl Spectrosc Rev* 2001, 36, 239-298.
46. Oust, A.; Moretro, T.; Naterstad, K.; Sockalingum, G. D.; Adt, I.; Manfait, M.; Kohler, A. *Appl Environl Microbiol* 2006, 72, 228-232.
47. Rasco, B. A.; Lu, X. N.; Al-Qadiri, H. M.; Lin, M. S. *Food Bio Technol* 2011, 4, 919-935.
48. Goodacre, R.; Jarvis, R. M.; Brooker, A. *Anal Chem* 2004, 76, 5198-5202.

CHAPTER 4

SUBCELLULAR SPECTROSCOPIC MARKERS, TOPOGRAPHY AND NANOMECHANICS OF HUMAN LUNG CANCER AND BREAST CANCER CELLS EXAMINED BY COMBINED RAMAN MICROSPECTROSCOPY AND ATOMIC FORCE MICROSCOPY³

4.1 ABSTRACT

Nanostructures and hydrophobic properties of cancer cell membranes are important in membrane fusion and cell adhesion. These are directly related to cancer cell biophysical properties, including aggressive growth and migration. Additionally, chemical component analysis of the cancer cell membrane could potentially be applied in clinical diagnosis of cancer by identification of specific biomarker receptors expressed on cancer cell surfaces. In the present work, a combined Raman microspectroscopy (RM) and atomic force microscopy (AFM) technique was applied to detect the difference in membrane chemical components and nanomechanics of three cancer cell lines; human lung adenocarcinoma epithelial cells (A549), and human breast cancer cells (MDA-MB-435 with and without BRMS1 metastasis suppressor). Raman spectral analysis indicated similar bands between A549, 435 and 435/BRMS1 including $\sim 720\text{ cm}^{-1}$ (guanine band of DNA), 940 cm^{-1} (skeletal mode polysaccharide), 1006 cm^{-1} (symmetric ring breathing phenylalanine), and 1451 cm^{-1} (CH deformation). The membrane surface adhesion forces for these cancer cells were measured by AFM in culture medium: $0.478\pm 0.091\text{ nN}$ for A549 cells, $0.253\pm 0.070\text{ nN}$ for 435 cells, and $1.114\pm 0.281\text{ nN}$ for 435/BRMS1 cells,

³ Gerald D. McEwen, Y. Wu, M. Tang, X. Qi, Z. Xiao, S. M. Baker, T. Yu, T. A. Gilbertson, D. B. DeWald, A. Zhou, (*manuscript in preparation*).

and the cell spring constant was measured at 2.62 ± 0.682 mN/m for A549, 2.105 ± 0.691 mN/m for 435, and 5.448 ± 1.081 mN/m for 435/BRMS1.

4.2 INTRODUCTION

The mechanical properties of cells play a fundamental role in the regulation of cell structures and functions, such as intracellular and/or intercellular forces sensing and transmitting, biochemical signals transducing, and generating cellular responses [1]. The mechanical properties (including adhesion, elasticity, and stiffness) of cancer cells have been recognized as a contributing factor in cellular adherence, mobility, transformation, invasion, and metastasis [2]. It is known that the mechanical properties, cell topography, membrane surface nanostructures, and cellular biochemical components change among different cancer cell lines, and these differences are connected to the development of new clinical diagnostic approaches [2-5]. Therefore, it is of importance to characterize these cellular differences at the single cell and sub-cellular level. However, this type of characterization remains largely uninvestigated due to the lack of applicable technologies that can reach nanoscale resolutions. The development and application of atomic force microscopy (AFM) and Raman microspectroscopy (RM) provide new access to cell mechanics, cytoarchitectures, and biochemical components of cancer cells [2-8] at the single cell and sub-cellular levels.

4.2.1 Breast cancer metastasis suppressor 1 (BRMS1) gene

It has been shown that breast cancer metastasis suppressor 1 (BRMS1) gene can suppress the formation of metastasis without affecting orthotopic tumor growth [9], and BRMS1 expression in breast adenocarcinoma cells (MDA-MB-435) can be restored

using microcell mediated chromosome transfer and thus result in suppression of metastasis [10, 11]. However, it is unclear how BRMS1 expression could alter cell topographical structures, membrane surface nanostructures, cytoskeleton, cell mechanics, and cellular biochemical compositions, or, how these biophysical and biochemical parameters for MDA-MB-435 cells differ from those of other cancer cell line like epithelial A549 cells (human lung adenocarcinoma cell line). Knowledge of these differences could facilitate new applications of AFM and RM for early diagnosis of human cancers.

4.2.2 Raman microspectroscopy

RM is a nondestructive vibrational classification routine that can be utilized to identify characteristic spectroscopic fingerprints of living cells based on chemical compositions and molecular structures [12]. Briefly, Raman spectral frequencies are recorded in wavenumber units which are proportional to vibrational energies based on molecular polarizability [13]. Many former RM studies mainly focused on physical and structural investigations. Over the past few decades, due to advances within instrumentation design [14, 15], biological applications [16, 17], and methods for biochemical information extraction [18, 19], RM has exhibited increased popularity in the field of mammalian cell biology [7, 20]. Short *et al.* demonstrated the use of RM to detect biochemical changes, in tumorigenic versus nontumorigenic cells, as a result of proliferation [21]. More recently, Abramczyk *et al.* reported the hallmarks of normal, malignant, benign breast tissue characterized by Raman studies [22]. Several other studies reported the appearance of cellular biopolymers (including DNA/RNA, lipids, proteins, and carbohydrates) in cell growth [7, 19, 23]. As RM has increased in

popularity, new analysis routines have emerged to extract useful chemical composition information from Raman spectra. Advances have been made to obtain Raman scattering from inherent background fluorescence through automation [24, 25], while other groups move toward an automated pre- and post-processing routine to eliminate natural user variability [26] and categorize Raman spectra [27]. Also new and emerging methods have been explored to enhance the usefulness of Raman spectral maps/images. Principal component analysis (PCA) was used to evaluate maps of freeze dried and living cells [28]. Ling *et al.* demonstrated image-processing algorithms to restore Raman image degradation in the study of anticancer drug distribution within living cells [12]. When key molecular components are used, RM becomes a powerful tool for rapid characterization of normal and transformed breast epithelial cell-lines [7] and multivariate analysis classification models can discriminate normal from abnormal tissue in cervical cancer progression [19].

4.2.3 Atomic force microscopy

Previously, AFM had been widely used in cell biology studies, because it can simultaneously obtain surface structures and mechanics of cells. This has allowed researchers to better understand the relationship between cell functions and biophysical alterations, such as to assess the biophysical alterations of mammalian cells associated with functional gene expressing or oncogenic transformation. Until now, there are only a few AFM applications in cancer cell line studies, which revealed that cancerous cells are largely softer and less adhesive [2, 3] and have a lower Young's modulus [8, 29] compared to normal/benign cells. This work and others [4, 5, 29, 30] demonstrate the

importance of AFM detection of nano-biomechanics and the potential for early cancer diagnosis.

Our aim in this study was to assess the usefulness of combining AFM/Raman technologies to distinguish differences in cellular biochemical markers, topography, membrane nanostructures and mechanics, among the following cancer cell lines: human lung adenocarcinoma epithelial cells (A549), metastatic human breast carcinoma cells MDA-MB-435 (435) and non-metastatic MDA-MB-435/BRMS1 (435/BRMS1). This study is directed at understanding potential fundamental links between biochemical makeup, cytoarchitectural, and biomechanical changes among these various cancer cell lines. Our results show that A549 cells possess a rougher cell membrane, and larger adhesion force and cell elasticity than 435 cells, and that BRMS1-expression increased membrane surface roughness, adhesion force and cell elasticity in 435/BRMS1 cells. This work revealed the potential of applying a combined AFM and RM approach to study the relationship of cell biochemical composition and biomechanics of cancer cell lines.

4.3 MATERIALS AND METHODS

4.3.1 Preparation of human breast cancer cell line 435 and 435/BRMS1 and human lung adenocarcinoma cell A549

The 435/BRMS1 cells were transfected with a lentiviral vector construct expressing full length BRMS1 cDNA under the control of a cytomegalovirus promoter. 435 and 435/BRMS1 cells were cultured in a 1:1 mixture of Dulbecco's-modified eagle's medium (DMEM) and Ham's F-12 medium supplemented with 5% fetal bovine serum (HyClone, Logan, UT). Cells were cultured in 25-cm² Corning tissue culture dishes at 37 °C with 5% CO₂ in a humidified atmosphere. Cells were subcultured at 80-90%

confluency using 2 mM EDTA in $\text{Ca}^{2+}/\text{Mg}^{2+}$ -free phosphate buffered saline (PBS, 0.01 M, pH 7.4, Thermo Scientific). Cell lines were confirmed to be free of mycoplasma contamination using PCR (TaKaRa, Japan). No antibiotics or antimycotics were used in either cell cultures.

Human (*Homo sapiens*) lung carcinoma A549 cells (ATCC, USA) were cultured in F-12k medium containing 10% fetal bovine serum at 37°C with 5% CO_2 in a humidified atmosphere. Cells were sub-cultured at 80-90% confluency and used for experiments. No antibiotics or antimycotics were used in cell cultures.

For AFM experiments, cells were seeded in poly-L-lysine coated Petri dishes at 5×10^4 cells/ml. The same seeding density was used for Raman spectroscopy; however, cells were seeded in quartz dishes (Quartz Scientific Inc., 313R020, USA) to minimize background fluorescence.

4.3.2 Raman microspectroscopy

Raman spectra were acquired using a Renishaw inVia Raman spectrometer (controlled by WiRE 3.0 software) connected to a DMLM Leica microscope (Leica, Germany). The Raman spectrometer was equipped with a 785 nm near-IR laser (laser spot $10 \times 3 \mu\text{m}$ line) that was focused through a 63x NA = 0.90 water immersion objective (Leica, Germany). The spectrometer was calibrated with silicon at a static spectrum centered at 520.5 cm^{-1} for 1 second using a pinhole to partially block some of the laser. Each cell line, A549, 435, and 435/BRMS1 were cultured in quartz dishes to 80-90% confluency, then mounted on the microscope stage and imaged. Raman spectra were collected in static mode at 1 accumulation with 10 second laser exposure over a wavenumber range of $500 - 1800 \text{ cm}^{-1}$ for cells. A background spectrum was obtained at

the same focal plane [31]. Five spectra were used to obtain an average for each cell line and background. Averaged background spectra were subtracted from averaged cell line spectra by finding a local minimum area (GRAMS/AI 8.0, Thermo Electron Corp., USA). Each spectrum was then baseline corrected for fluorescence (Vancouver Raman Algorithm) [25], then normalized using peak intensity at 1450 cm^{-1} [32], which represents a CH deformation that is not significantly affected by intercellular changes [31]. Raman spectral maps were collected in a “StreamLine” mode for 30 seconds exposure time at wavenumber center of 910 cm^{-1} . If necessary, Cosmic Ray Removal (CRR) was performed and signal-to-baseline intensity was analyzed.

4.3.3 Chemometric analysis of Raman spectra and spectral images

First, a moving average smoothing was done to the Raman spectra to filter high-frequency noise. Then, the second derivative of smoothed spectra was obtained to eliminate baseline drifts and background interference. This pre-treatment is often used to distinguish overlapping peaks and improve resolution and sensitivity of spectra [33-35]. The Raman spectra were analyzed by principal components analysis (PCA) to extract information from raw spectral data and eliminate overlapped information, and then an unsupervised Ward’s hierarchical cluster analysis (HCA) with Euclidean distances [36] was performed to qualitatively distinguish the differences among three cell lines. All algorithms were implemented in MATLAB R2010b (MathWorks, Natick, USA).

PCA was employed to analyze Raman spectra for single cell Raman images. The detailed steps to obtain PC1 (the 1st principal component) and PC2 (the 2nd principal component) score images for the single cell Raman spectral image, which was corrected for cosmic rays and smoothed, are described briefly. The spectral data of each single cell

was read and arranged into matrix A , whose width is the number of cells in the spectral image and whose height is the length of the spectral data in each cell. Then the covariance matrix U was computed according to equation 1.

$$U = \frac{1}{M} \sum_{i=1}^M [A_i - \mu] [A_i - \mu]^T \quad (1)$$

Where μ is the average spectra data of all cells in the image, M is the number of cells in the image, and A_i corresponds to the i^{th} column in A (i.e., the spectral data of the i^{th} cell). Eigenvalues and eigenvectors of the covariance matrix U were computed and eigenvalues were sorted in descending order and eigenvectors were reorganized in matrix D , where $D = [D_1 D_2 \dots D_n]$ with D_i corresponding to the eigenvector of the i^{th} largest eigenvalue and n being the number of distinct eigenvalues. The PC1 scores were computed (i.e., projected values in the first PC direction) by multiplying D_1^T by $A - \mu$ and rearrange the PC1 scores to the corresponding cells in the PC1 score image. Similarly, PC2 scores (i.e., projected values in the second PC direction) were computed by multiplying D_2^T by $A - \mu$ and rearranging the PC2 scores to the corresponding cells in the PC2 score image.

4.3.4 Atomic force microscopy

In order to image viable carcinoma cells *in vitro* via AFM, two sample preparation approaches were utilized. In the first approach, cultured cells were measured directly *in situ* in culture medium without pre-treatment to record biomechanical properties (e.g. adhesion behavior and cellular spring constant). For the second approach, cells were visualized topographically and then pre-treated by a fixative (1% glutaraldehyde plus 1% paraformaldehyde dissolved in $1 \times \text{Ca}^{2+}/\text{Mg}^{2+}$ -free phosphate

buffered saline) for 5 minutes. After fixation, cells were gently rinsed with PBS and then imaged in PBS.

The contact mode PicoPlus AFM controlled by PicoScan 5.4 software (PicoPlus, Agilent Technologies, USA) was used to measure cells at 22 ~ 25 °C in PBS (0.01 M, pH 7.4) or directly in cell culture medium. The spring constant of the cantilever was calibrated at 0.06 ~ 0.11 N/m (Veeco, USA) with tip length between 0.4 ~ 0.7 μm, and Si₃N₄ tip curvature radius of approximately 10 nm. The approach/retract velocity applied throughout deflection (nm) vs. distance (nm) curve acquiring was 6.1 μm/second. The values for the adhesion force (the detachment force between bare AFM tip and cell membrane in the process of AFM cantilever retracting) were extracted from the deflection (nm) vs. distance (nm) curves via the Scanning Probe Image Processor (SPIP) software (Image Metrology, Denmark). The compliance slope portion of the deflection-distance curves was used to evaluate cellular elasticity and the cellular spring constants (k_{cell}) were calculated using a previously proposed formula [37, 38] equation 2.

$$k_{cell} = -k_{tip} \frac{s}{1+s} \quad (2)$$

where s is the linear slope of the approaching branch, the ratio of *deflection (nm)* to *distance (nm)*; k_{cell} and k_{tip} represent the spring constants of cell and cantilever, respectively.

In addition, the average roughness (R_a) and root-mean-square roughness (R_{rms}) were obtained according to equation 3 and 4 [39].

$$R_a = \frac{1}{N} \cdot \sum_{n=1}^N |z_n - z| \quad (3)$$

$$R_{rms} = \sqrt{\frac{\sum_{n=1}^N (z_n - \bar{z})^2}{N-1}} \quad (4)$$

where N represents the total number of data points in a selected area, z_n is the height of the n^{th} point, and \bar{z} is the mean height.

Furthermore, to assess statistically significant differences in nano-mechanics including adhesion force and cellular elasticity among these cancer cell lines, the data were reported as mean \pm SD (standard deviation of mean), and analyzed using Student's t-test. The data used to graph histograms or created force maps were measured from the whole cell body, and the histograms were graphed using OriginPro 7.5 (OriginLab Corp., USA). The adhesion force or cellular spring constant maps were graphed with as 256 color maps created by MATLAB version R2010b (MathWorks, Inc.).

4.4 RESULTS

4.4.1 Raman spectral analysis - Biochemical markers of three cell lines

In this study, RM was utilized as a method to characterize cellular biochemical composition for each cancer cell line; A549, 435 and 435/BRMS1. Figure 4.1 is a stacked view of the averaged raw data for A549, 435, 435/BRMS1, and the quartz/culture medium background, respectively (offset vertically for clarity).

To better understand the differences between each cell line, the Raman spectra were post-processed as previously described (section 4.2). Figure 4.2 depicts stacked Raman spectra normalized at 1450 cm^{-1} . These spectra exhibit minor differences, which are probably minimized based on the semi-confocal probing approach of the cellular

regions. The post-processing procedure assists to reveal subtle variations among each spectrum, yet maintain similarities for spectra of the same cell type.

Mean RM spectra are illustrated in Figure C4.11 (Appendix C) with only minor variations based on the selected normalization band represented. In the 1450 cm^{-1} normalized Figure 4.2, the overall spectral fingerprint for A549, 435 and 435/BRMS1, are very similar. However, initial fluorescence in Figure 4.2-B and -C obscure the

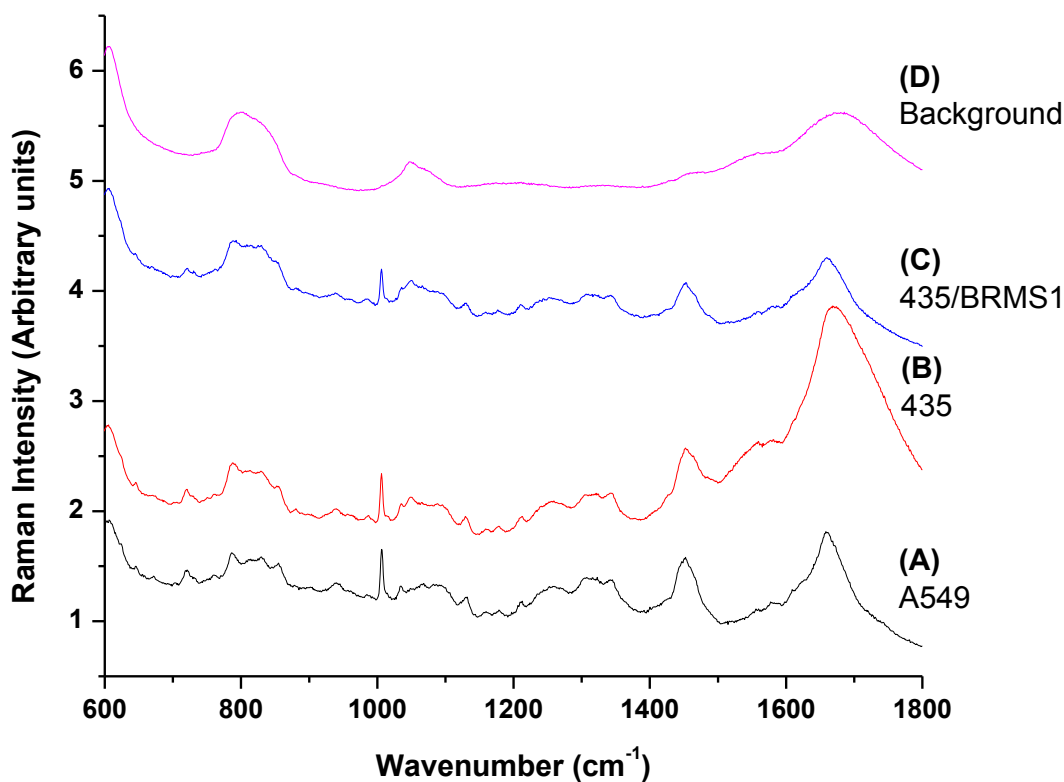


Figure 4.1. Averaged Raman spectra for three cancer cell lines and background, respectively: A549 (A-black), 435 (B-red), 435/BRMS1 (C-blue), and background (D-magenta). For each cell line the Raman spectrum represent an average of five separate spectra and the background is an average of fifteen spectra. Spectra are offset vertically for clarity.

624 cm^{-1} (protein) band of 435 and 435/BRMS1, another likely fluorescent artifact is present between $\sim 770 - 872$ and $1023 - 1148$ cm^{-1} , which could be caused by the quartz substrate. Further, a very weak shoulder peak at 1606 cm^{-1} (protein) is visible for both 435 and 435/BRMS1 and the Amide I band at 1660 cm^{-1} for 435 is blue shifted from ~ 1660 to 1665 cm^{-1} . On the other hand, the 813 cm^{-1} (one of two RNA bands) is missing in Figure 4.2-A for A549 along with the previously mentioned fluorescent artifacts.

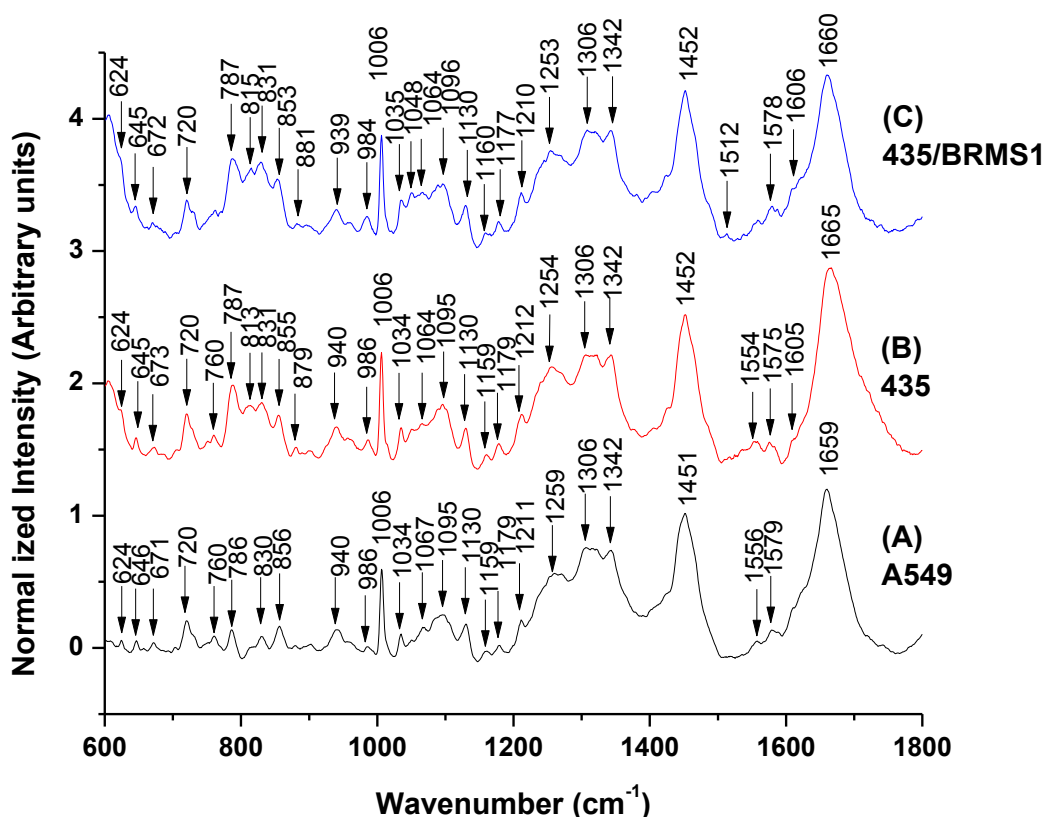


Figure 4.2. Mean Raman spectra of three cancer cell lines: A549 (A-black), 435 (B-red), and 435/BRMS1 (C-blue). Each spectrum is the average of five spectra, the averaged background was subtracted by finding a local minimum area, spectra were baseline corrected, and then normalized using peak intensity at 1450 cm^{-1} [32]. Spectra are offset vertically for clarity.

Table 4.1. Tentative Raman band assignments for human lung adenocarcinoma epithelial cell (A549) and human metastatic (435) and non-metastatic (435/BRMS1) breast carcinoma cells

Raman shift (cm ⁻¹)			Band assignment
A549	435	435/BRMS1	
624			Phenylalanine
646	645	645	C-C twist Phenylalanine
671	672	672	
720	720	720	DNA
760	760		Tryptophan
786	788	787	DNA & phosphodiester bands DNA
	813	814	Phosphodiester bands RNA
830	830	829	PO ₂ ⁻ stretch nucleic acids
856	855	853	Tyrosine
	880		Tryptophan
940	940	939	Skeletal modes (polysaccharides)
984	986	984	
1006	1006	1006	Phenylalanine
1034	1034	1035	Phenylalanine
		1050	
1066			PO ₂ ⁻ stretching (DNA/RNA); chain stretching (lipids); C-O, C-C stretching (carbohydrates)
1095	1095	1096	Lipid
1130	1129	1129	C-C skeletal stretch transconformation
1160	1160		
1179	1178	1178	Cytosine, guanine
1211	1211	1211	Tyrosine, phenylalanine
1259	1255	1254	Lipid; A,T breathing mode (DNA/RNA); Amide III (protein)
1306	1306	1308	C-N stretching aromatic amines
1343	1342	1342	G (DNA/RNA); CH deformation (proteins and carbohydrates)
1451	1452	1452	CH ₂ deformation (nucleic acid, proteins, lipids)
	1553		
1579	1575	1579	Pyrimidine ring (nucleic acids)
1659	1666	1660	Amide I

Band assignments are based on [7, 40].

In Figure C4.10, normalized at 1660 cm⁻¹, the same spectral difference are noted that were described for Figure C4.11 with relative intensity changes based on the ratio of the 1450 to 1660 cm⁻¹ Raman bands. Additionally, data mining is required to extract

useful biochemical information to further compare each cell line. The first step is to assign various vibrational modes to each mean spectrum to provide a primary level of understanding. Tentative Raman band assignments are listed in Table 4.1.

An approach that is somewhat better than direct comparison (as in Figure 4.2 and Figure C4.10) is to compute difference spectra by subtracting one mean normalized spectrum from another [32, 40]. Figure 4.3 and Figure C4.11 are the computed difference spectra from Figure 4.2 and Figure C4.10, respectively.

PCA of pre-processed Raman data was performed and the score plot of the first three principal components is shown in Figure 4.4. In the score plot, each sample is represented by a single point and the origin of the graph is the data set average. The x-axis, labeled PC1, is the score values for the first principal component; the y-axis, PC2, the second principal component, and the z-axis, PC3, the third principal component. The samples are color coded according to the sample type. The score plot demonstrates that the three cell line samples are distinguishable into three distinct clusters.

Figure 4.5 shows the dendrogram resulting from HCA performed on a total of 29 spectra (9 spectra for A549, 9 spectra for 435, 11 spectra for 435/BRMS1). The first six principal components were used as the input parameters, which account for 97.2% of the variation in the data set. The dendrogram was generated using Ward's clustering algorithm and the squared Euclidean distance. The Euclidean distance method is a simple approach for the classification of multivariate data. In Figure 4.5, the horizontal axis

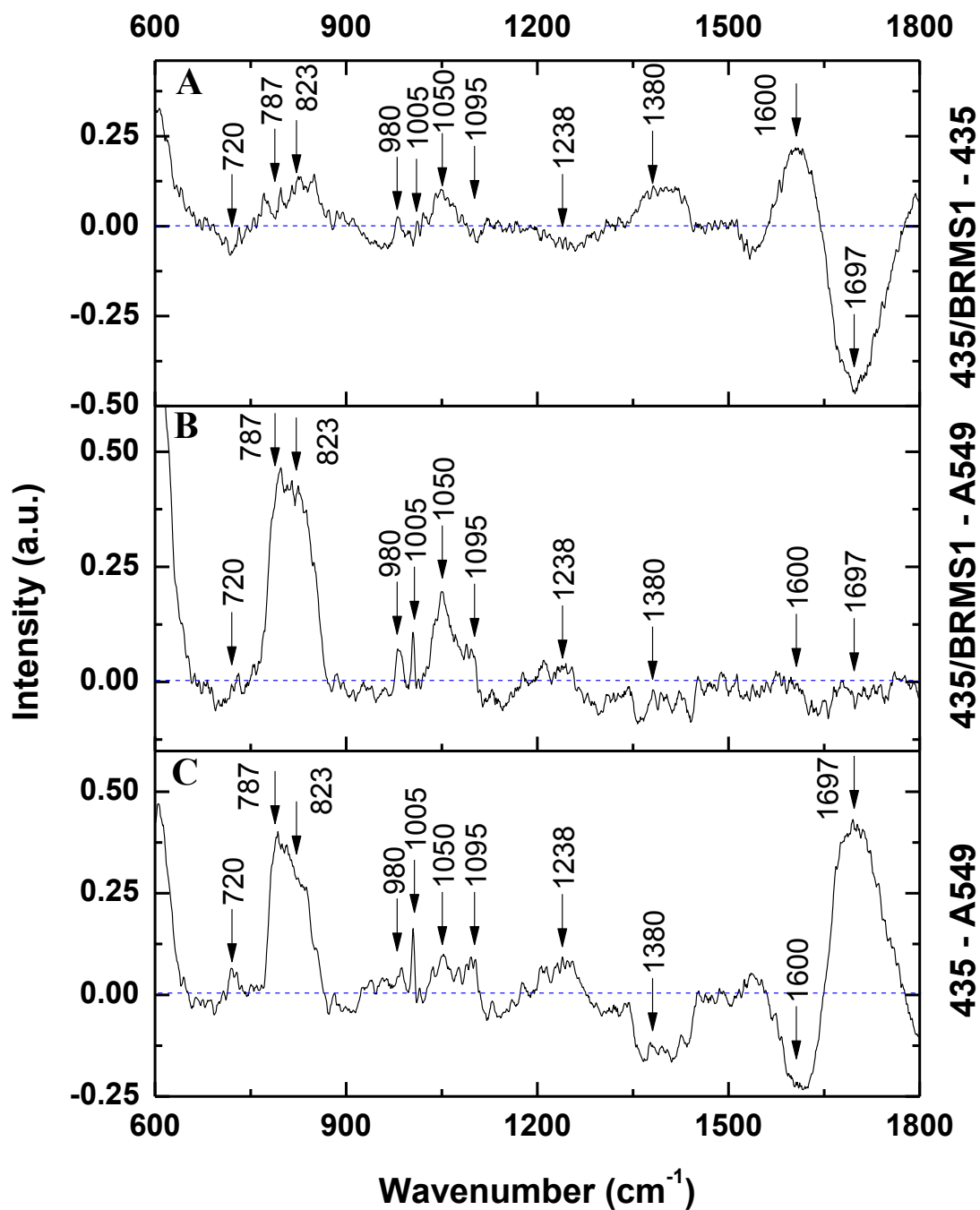


Figure 4.3. Difference spectra computed from the 1450 cm^{-1} normalized spectrum in Figure 4.2 using A549, 435, and 435/BRMS1: 435/BRMS1 - A549 (A), 435/BRMS1 - A549 (B), A549 - 435 (C).

stands for the labeling of the 29 cells, and the vertical axis represents the heterogeneity (or dissimilarity) distance between two cells or clusters. Apparently, the 29 spectra (or cells) formed three separated clusters, one per cell type. The dendrogram shows that the Raman spectra of these three cell lines and illustrates that the 435/BRMS1 and 435 cell lines are much more similar to each other than to the A549 cell line.

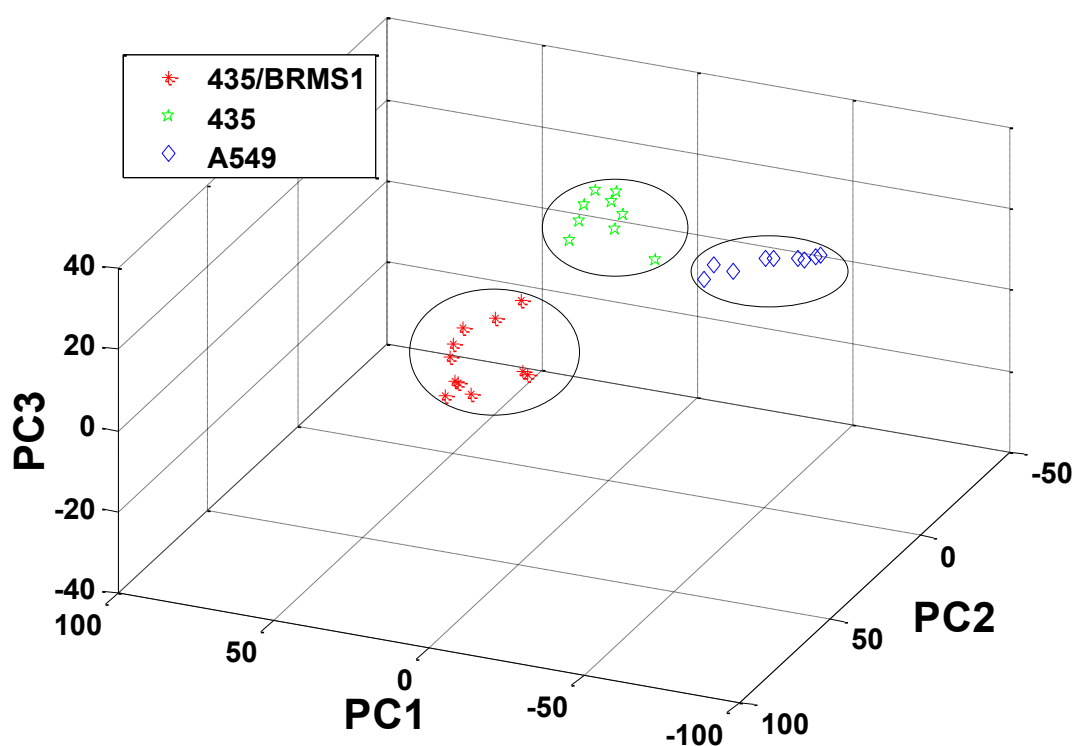


Figure 4.4. PCA score plot of pre-processed Raman spectra for each cell line. Each cancer cell line is coded by color and shape (435/BRMS1 - red star, 435 - green pentagram, and A549 - blue diamond)

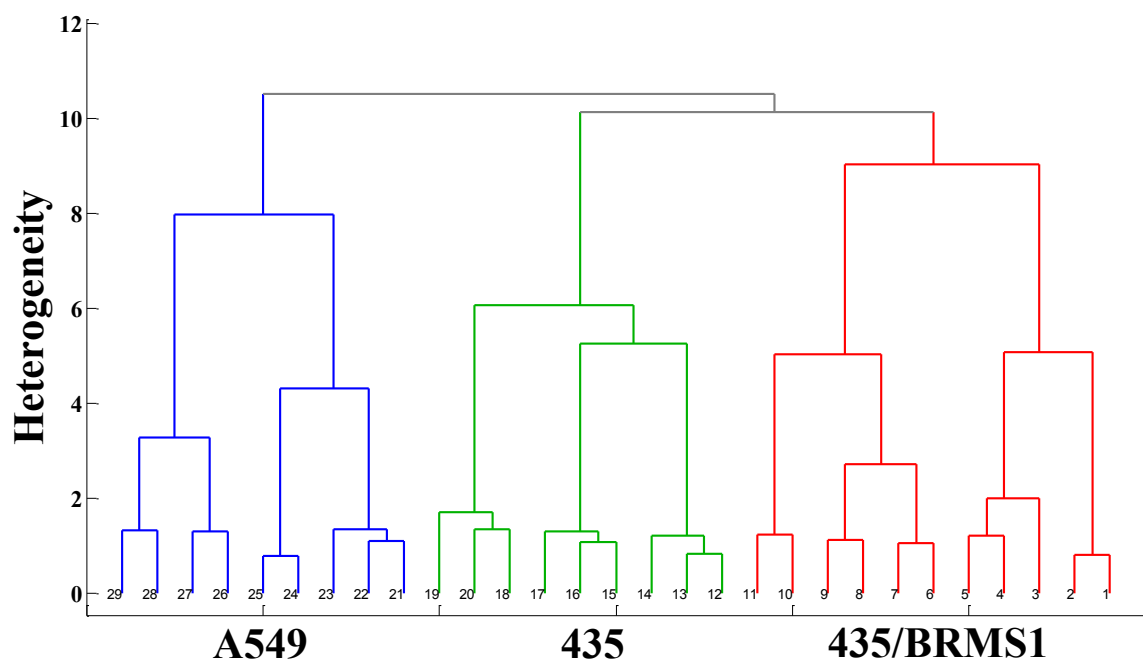


Figure 4.5. Dendrogram analysis based on PCA score values for the first six principal components. The data is color coded into three groups. By including six PCs, the dendrogram shows that the spectral data can be correctly categorized according to cancer cell line type.

4.4.2 Raman spectral image analysis – Biochemical markers of three cell lines

Figure 4.6-A through -C represent white light images for A549, 435, and 435/BRMS1 along with overlaid spectral maps for specific Raman bands which correspond to biochemical components of interest: DNA (Figure 4.6-D through -F), carbohydrate (Figure 4.6-G through -I), protein (Figure 4.6-J through -L), and lipid (Figure 4.6-M through -O). Characteristic Raman band intensity analysis provides spectral maps or images with spatial and temporal distribution for major biochemical components at single and sub-cellular levels.

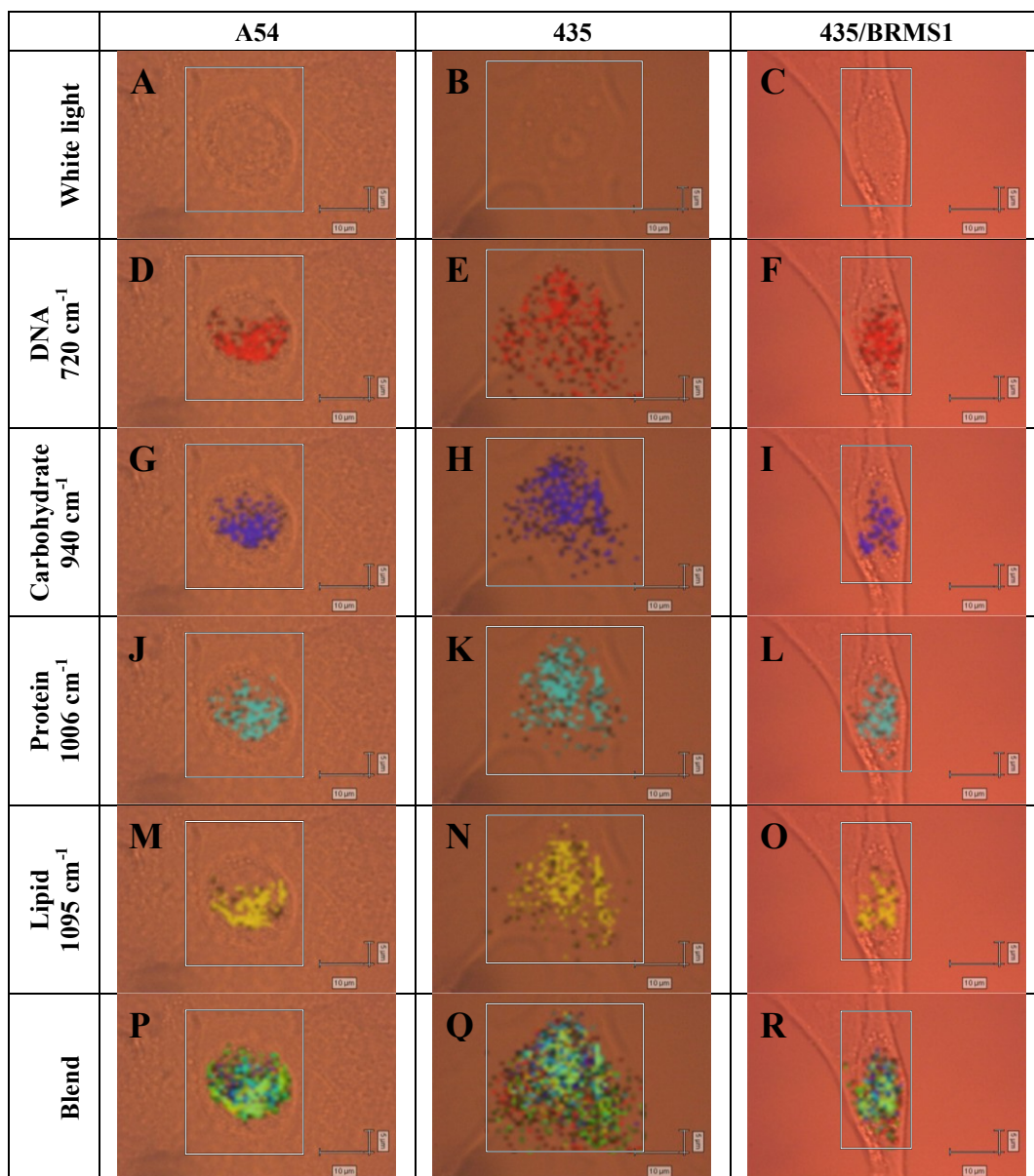


Figure 4.6. Raman spectral images for relative biochemical distribution within single cells; A549, 435 and 435/BRMS1. White light images (A-C). Different biochemical components were identified by characteristic wavenumber as follows; DNA (D-F, red) – 720 cm^{-1} , carbohydrate (G-I, blue) – 940 cm^{-1} , protein (J-L, cyan) – 1006 cm^{-1} , and lipid (M-O, yellow) – 1095 . Complete biochemical distribution overlays (P-R). Scale bar: $10 \mu\text{m}$ (horizontal), $5 \mu\text{m}$ (vertical).

Figure 4.7 represents the PC1 and PC2 score images for three single cell Raman images. Here, PC1 and PC2 score images account for the two most significant PC components and show the summary of variations at all wavenumbers used in the PCA. Each score image shows a separate variation that is linearly independent of the other score image. Specifically, PC1 and PC2 score images contain the largest and the second largest variation among all the choices of the PC component, respectively.

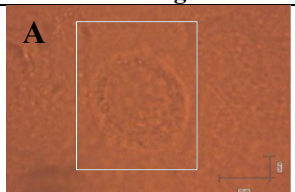
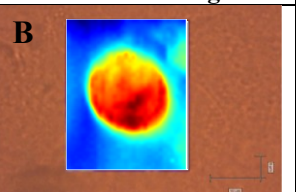
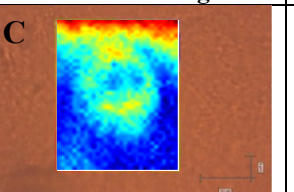
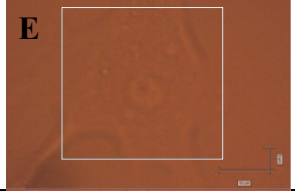
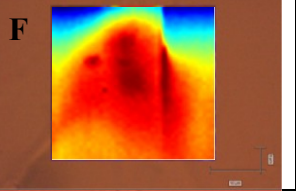
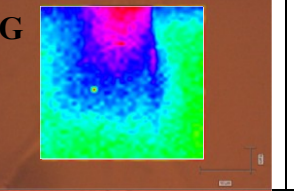
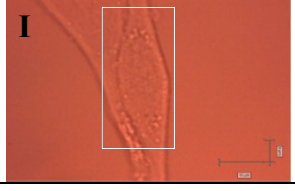
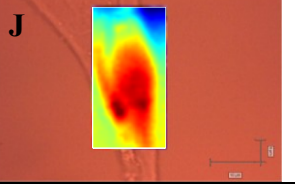
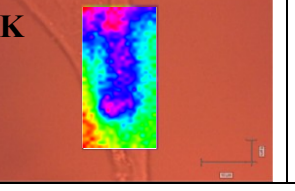
	White light	PC1 score image	PC2 score image	Comments
A549	A 	B 	C 	PC1 Variation 98.98% PC2 Variation 1.02%
435	E 	F 	G 	PC1 Variation 96.76% PC2 Variation 3.24%
435/BRMS1	I 	J 	K 	PC1 Variation 98.06% PC2 Variation 1.94%

Figure 4.7. Single cell Raman spectral image maps for A549, 435, 435/BRMS1: first column (white image), 2nd column (PCA1 score image), 3rd column (PCA2 score image). The colors were scaled for better visualization and displaying purpose. Scale bar: 10 μm (horizontal), 5 μm (vertical).

4.4.3 AFM observation of cell membrane nanostructure

To assess the differences in cell topography and cell membrane surface nanostructures among each cancer cell line, fixed cells were imaged by contact mode AFM in PBS, and the results are shown in Figure 4.8. The first column gives the representative images of single A549 and 435 cells and multiple 435/BRMS1 cells. The second column shows their respective deflection mode images. The third and fourth columns show the nanostructures of the cellular membrane at two different locations for each individual cell type.

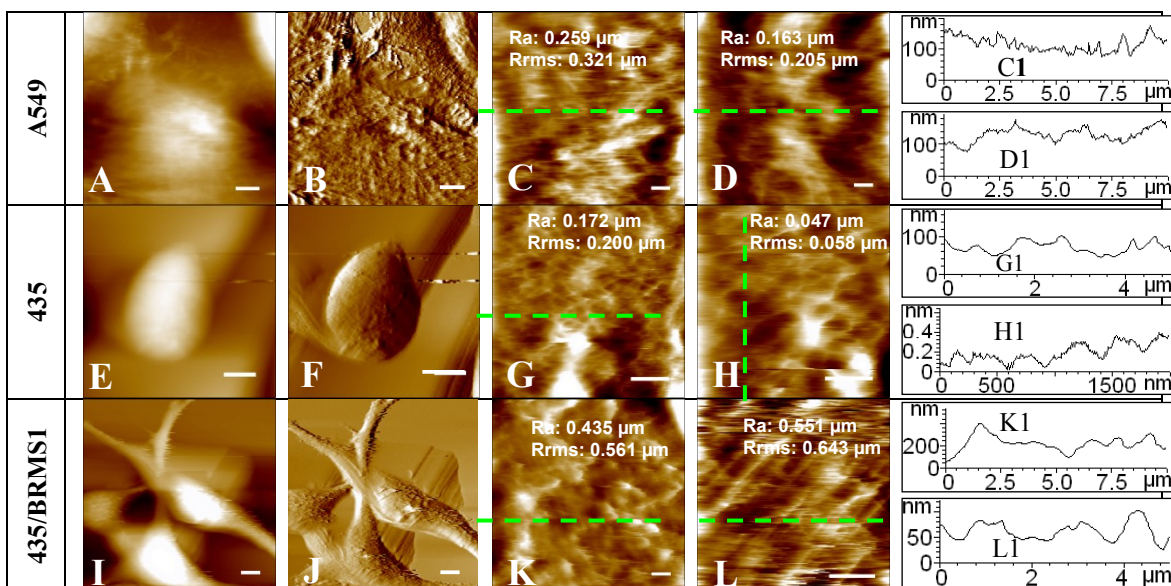


Figure 4.8. Topography and membrane surface nanostructures of A549, 435, and 435/BRMS1 acquired in PBS. The 1st column shows the topography images; 2nd column the respective deflection images, 3rd and 4th columns show the membrane surface nanostructures (roughness values marked) obtained at two different locations for each cell line. The 5th column presents the cross section profiles taken along the green dash lines. Scale bar: 5 μm (A,B,E,F,I,J), 1 μm (C,D,G,K,L), 500 nm (H).

4.4.4 Measurements of nanomechanical properties of cancer cell lines

Different cellular topography and membrane surface structures could alter cellular mechanics, for example, cellular elasticity and adhesion. To further evaluate the nanomechanical differences among each cell line, the adhesion interaction force (F) between the bare AFM tip and the cellular membrane surface cellular spring constant (k_{cell}), and Young's modulus (E) were analyzed in situ based on hundreds of force-distance curves for each cell type. These force-distance curves were acquired using AFM contact mode in culture media and the measured results are shown in Figure 4.9. Columns 1, 2 and 3 in Figure 4.9 indicate a representative AFM image and the corresponding nanomechanical results (row 2, F maps and histograms; row 3, k_{cell} maps and histograms; row 4, E maps and histograms) of A549, 435, and 435/BRMS1, respectively. The low resolution images in Figure 4.9 (row 1) may have resulted from the very soft cell membrane (evidenced by the low cellular spring constants as shown in Figure 4.9, row 3) and the presence and movement of membrane surface microvillus of living cells during tip scanning. Therefore, we mainly focused on the acquisition of deflection (nm) vs. distance (nm) curve to evaluate the nano-biomechanics of living cells.

The parametric statistical analysis (Student's t-test) indicated that the adhesion force, cell spring constant and Young's modulus measured among three cell lines were significantly different ($p < 0.01$). To clearly illustrate the variations of these three parameters, the statistical data (mean \pm SD) were marked on their respective histograms (Figure 4.9- rows 2-4).

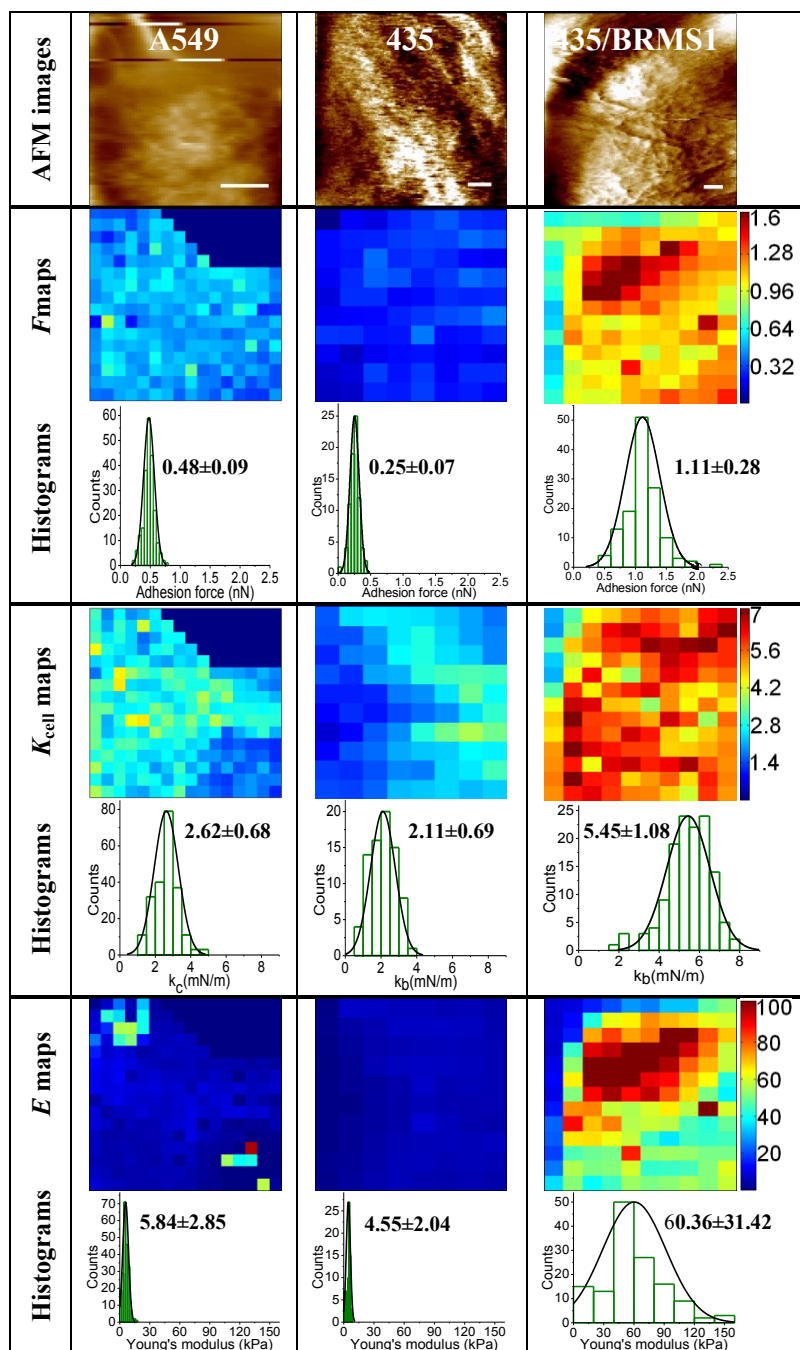


Figure 4.9. Biomechanical evaluation of A549 (column 1), 435 (column 2) and 435/BRMS1 (column 3). Row 1 shows representative topography images acquired in culture medium. The maps of adhesion force (F), spring constant (k_{cell}), and Young's modulus (E) of three cell lines are shown row 2, row 3, and row 4, respectively, and their respective distribution histogram (mean \pm SD is marked) is displayed under the corresponding map. The color bars arranged at the right of maps illustrate the value scale of color-coded maps of adhesion force (nN), k_{cell} (mN/m), and E (kPa). Scale bar: 5 μ m (A549), 1 μ m (435 and 435/BRMS1).

4.5 DISCUSSION

Qualitative and quantitative analysis of cell adhesion and elasticity of human cancer cells could advance the fundamental understanding of the biochemical and biomechanical developmental roles in cancer metastasis mechanisms. This present work exhibits a combined Raman microspectroscopy and atomic force microscopy approach to evaluate biochemical and biophysical properties of cellular membrane and nano-architectures of three different model human carcinoma cells.

4.5.1 Raman spectral analysis – Biochemical markers of three cell lines

Raman microspectroscopy results showed that these three cell lines possess very similar biochemical components on their cell membrane surfaces, more over small spectral differences could be detected through the use of difference spectra. We have previously shown that both 435 and 435/BRMS1 contain similar gross biochemical compositions [41] when imaged with RM. A direct comparison, as in Figure 4.1, does not reveal many spectral variations among the cancer cell lines.

In order to verify if spectral difference are affected by normalization band, we also compared the normalized 1450 cm^{-1} band (Figure 4.2 and Figure 4.3) with another at 1660 cm^{-1} (Figure C4.10 and Figure C4.11). To better interpret the spectral differences and gain insight into the biochemical variation of A549, 435 and 435/BRMS1: difference spectra were computed by subtracting the metastatic spectrum from the model spectrum ($435 - \text{A549}$), the non-metastatic from model spectrum ($435/\text{BRMS1} - \text{A549}$), and the non-metastatic from the metastatic ($435/\text{BRMS1} - 435$), respectively. Differences in the spectral profiles of the breast carcinoma cells (435 and 435/BRMS1) and the lung adenocarcinoma cells (A549) were more pronounced than those from the breast

carcinoma cells. This suggests that while the spectra appear to contain a similar overall fingerprint as seen in Figure 4.2 and Figure C4.10, there are some vital distinctions that are observed. Therefore, the overall spectral fingerprint does not change based on the normalization band, only the relative intensity based on the normalization band ratio.

It was found that these cancer cell lines share many of the same characteristic Raman bands as illustrated in Table 4.1 and are similar biochemically although cultured using slightly different cell culture protocols (4.3.1). Based on the phase of the cell cycle, many of the cell biochemical/biopolymer components are concentrated inside living cells [42] and typical biochemical molecules of interest are associated with DNA, carbohydrates, proteins, and lipids. When measured with RM, these biochemical molecules are typically reported based on each respective Raman band assignment (also designated Raman shift in cm^{-1}). Raman band assignments, for the above mentioned biochemical molecules of interest, are as follows; DNA are located at $\sim 720, 787, 830, 1178, \text{ and } 1579 \text{ cm}^{-1}$, while a distinct band for carbohydrates is 940 cm^{-1} , proteins are at $1006, 1130 \text{ and } 1660 \text{ cm}^{-1}$, and lipids are located at 1095 cm^{-1} , respectively [43]. Also, it is noted that there are bands that overlap; for example, 1066 cm^{-1} could be associated with the PO_2^- stretching of DNA/RNA, chain stretching in lipids, and C-O or C-C stretching of carbohydrates [43], 1255 cm^{-1} may be assigned as lipid, adenine or thymine breathing modes of DNA/RNA, and the amide III band of proteins [43], 1308 cm^{-1} might either be assigned as C-N stretching of aromatic amines [43], or CH_2 twist or bend associated with nucleic acids proteins and lipids [7], 1342 cm^{-1} may possibly be assigned as guanine in DNA/RNA or CH deformation in proteins and carbohydrates [43], and finally 1452 cm^{-1} could be assigned as CH_2 deformation in nucleic acids, proteins, and

lipids [43]. At present, we are not able to further distinguish the overlapping bands, yet it may be possible to use surface enhanced Raman scattering (SERS) to gain insight into the specific biochemical components of interest via a better enhanced/resolved spectra around the broad Raman bands.

In Figure 4.3-A, there is a two-fold decrease in the overall spectral intensity and all of the negative bands, 720, 1005, 1095, 1238, and 1697 cm^{-1} are due to the 435 spectrum. The majority of these peaks can be assigned as DNA (720 – DNA, and 1095 cm^{-1} – PO_2^- in nucleic acids), proteins (1005 – phenylalanine/protein, 1238 – Amide III, and 1697 cm^{-1} – Amide I), and lipids (1095 – lipids,) with overlap in the 1095 cm^{-1} band. The positive bands, 787, 823, 980, 1050, 1380, and 1600 cm^{-1} are from the 435/BRMS1 spectrum and can be similarly assigned; as DNA (787 – relative DNA, 823 – phosphodiester, and 1095 cm^{-1} – PO_2^- in nucleic acids), proteins (980 – protein, 1602 cm^{-1} – phenylalanine/Amide I), and lipids (1380 – δCH_3 symmetric) with no overlapping bands and one unassigned band (1050 cm^{-1}). Figure 4.3-B and -C show a two-fold increase in the overall spectral intensity when compared with Figure 4.3-A. The negative bands in Figure 4.3(-B and -C) are respectively: 1380 cm^{-1} and 1380, and 1600 cm^{-1} and were due to the A549 spectrum. Whereas the positive bands for Figure 4.3-B and -C are respectively; 787, 823, 980, 1005, 1050, 1095, and 1238 cm^{-1} due to the 435/BRMS1 spectrum and 720, 787, 823, 980, 1005, 1050, 1095, 1238, and 1697 cm^{-1} due to the 435 spectrum. These peaks have been previously assigned for Figure 4.3-A above. Difference spectra between 435/BRMS1 and 435 (Figure C4.11) yield negative bands at 720 and 1697 cm^{-1} which were due to the 435 spectrum. The positive bands; 787, 823, 980, 1005, 1050, 1095, 1238, 1380, 1441, and 1600 cm^{-1} are from the 435/BRMS1 spectrum. In

Figure C4.11-B and -C, the negative bands are respectively: 1441, 1697 cm^{-1} and 1380, 1441, and 1600 cm^{-1} , which were due to the A549 spectrum. Whereas the positive bands for Figure C4.11-B and -C are respectively: 720, 787, 823, 980, 1005, 1050, 1095, 1238, and 1441 cm^{-1} due to the 435/BRMS1 spectrum and 720, 787, 823, 980, 1005, 1050, 1095, 1238, and 1697 cm^{-1} due to the 435 spectrum. The previously mentioned fluorescence quartz artifact is visible in Figure 4.3-B and -C and Figure C4.11-B and -C compared to Figure 4.3-A and Figure C4.11-A.

From the difference spectra, it can be concluded that the variability within the difference spectra is associated with the differences related to the A549 spectrum. This is illustrated in Figure 4.3-A where the spectral features less pronounced as compared with both Figure 4.3-B and -C, which include stronger features at 787 and 823 cm^{-1} related to DNA and 1050 cm^{-1} (unassigned) and decreases at 1380 (lipid) and 1600 cm^{-1} (protein). Figure C4.11-A is similar to Figure 4.3-A and likewise Figure C4.11-B and -C are similar to Figure 4.3-B and -C with the exception of the addition of the Raman band at 1441 cm^{-1} (CH_2 scissoring & CH_3 bending in lipids). These slight spectral variations from the difference spectra are more insightful than Figure 4.2 and Figure C4.10, in that, we can now compare the relative ratios of Raman bands across each of the three cell lines. Each of the Raman band vibrational modes was assigned based on available literature [7, 43].

PCA of the processed Raman spectra aid to distinguish each cell line based on cell type. Figure 4.4 shows the scatter plots of the Raman spectra for these cancer cell lines projected into a three-dimensional subspace using principal component scores PC1, PC2, and PC3. It is seen that the first principal component (PC1) possess 60.3% variation, PC2 19.4% variation, PC3 9.8%. Thus the 3D PCA plots indicate that the Raman spectra of

these three cell lines are distinguishable into three distinct groups – according to the cell line type. The intrinsic difference in biomolecular composition and concentration for different cancer cells will cause the clusters to be separated from each other. In order to better view the similarity among these three cancer cell lines, hierarchical cluster analysis (HCA) was performed. HCA is used as an unsupervised method for obtaining information about the heterogeneity (dissimilarity) between spectra collected from different species. The dendrogram (Figure 4.5) shows that the three cell lines can be grouped based on the heterogeneity of each spectra, indicating that breast cancer cell lines (435 and 435/BRMS1) are much more similar to each other than to the lung cancer cell line (A549). The two breast cancer cell lines are more biologically similar each other, which makes sense as one is the parental cell line (435) and the other is progeny from that cell line (435/BRMS1).

4.5.2 Raman spectral image analysis – Biochemical markers of three cell lines

The spectral image at band 720 cm^{-1} in Figure 4.6-D through -F represents the guanine band distribution for DNA [43] and is concentrated centrally on the cells of A549 in Figure 4.6-D and 435/BRMS1 in Figure 4.6-F, compared to 435 cells in Figure 4.6-E where the map is more evenly distributed. Raman band 940 cm^{-1} in all three cell lines Figure 4.6-G through -I is assigned the skeletal mode vibrations of polysaccharides for carbohydrates [43] and these spectral image display similar distributions as seen in Figure 4.6-D,-E,-F with the similar even spread noted for 435 cells in Figure 4.6-E. The 1006 cm^{-1} band in Figure 4.6-J through -L is the symmetric ring breathing band of phenylalanine for protein [23, 43], which has a more even distribution near the center of each cell, although more broadly distributed in Figure 4.6-K. Finally, the 1095 cm^{-1} band

in Figure 4.6-M through -O is the chain C-C stretch band for lipid [23], and appears to be more narrowly distributed as in Figure 4.6-M and -O and more broad in Figure 4.6-N. Blended images are shown in Figure 4.6-P through -R and illustrate the overall combined biochemical distributions of these major biochemical components for A549, 435, and 435/BRMS1. Furthermore, the biochemical distributions of A549 cells are very similar to those for 435/BRMS1. Both of these cell lines appear to have most of the biochemical components centralized at the mass of the cell. On the contrary, 435 has a broad distribution for each biochemical component, which could be attributed to either the cellular adhesion or perhaps this cell is at a different phase cycle compared to A549 and 435/BRMS1 cells imaged.

In the PCA image analysis (Figure 4.4), all three cell lines possess >95% variations for the first principal component (PC1) among all the PC components. Specifically, the percentages of the variations in the first two principal components (PC1, PC2) of the spectra of the three cell lines are: A549 (98.98%, 1.02%), 435 (96.76%, 3.24%), 435/BRMS1 (98.06%, 1.94%), respectively. As a result, the major variability of within the Raman signal is captured in the principal component (PC1) score image. Figure 4.7 clearly shows several distinct clusters, where the different colors indicate distinct features within the cluster. That is, the areas with similar colors represent a cluster and indicate the spectral data of the cells have similar patterns. The three PC1 score images of the three cell lines demonstrate the major variability in the data and the dark red colored areas show the most informative sampling points in the single cell Raman spectral images.

4.5.3 Measurement of nanomechanical properties of cancer cell lines

The topographical images obtained in Figure 4.8-B,-F, and -J revealed cellular morphological and structural differences of the cell surface membranes of each cell line: A549 cells exhibit a round or elliptical shape and the lamellipodia can be readily seen (Figure 4.8-A and -B), and 435 cells also have a round or elliptical shape but no pseudopodium is seen (Figure 4.8- E and -F); in contrast, 435/BRMS1 cells were predominately elongated and are long spindle-like or triangular shaped (Figure 4.8-I and -J). Additionally, more details of the membrane surface nanostructures can be observed in the 3rd and 4th columns which were obtained using a more narrow scanning area: net-like cytoskeleton structures were present on A549 cells (Figure 4.8-C and -D) and 435 cells (Figure 4.8-G and -H); whereas the parallel arranged cytoskeleton structures (e.g., filamentous actin) were clearly visible on 435/BRMS1 cells (Figure 4.8-K and -L), indicating the reorganization of the cytoskeleton associated with BRMS1-expression. And the cross section profiles, shown in the 5th column, further depicted the corrugation of cell membranes, suggesting non-smooth features on the cellular membrane surface. Furthermore, the quantitative comparison of membrane surface roughness (R_a and R_{rms}) indicated that the 435/BRMS1 cells possessed a much rougher membrane surface compared to A549 and 435 cells (the roughness values are indicated on respective images in the 3rd and 4th columns).

Figure 4.9 indicates a representative AFM image and the corresponding nanomechanical results (adhesion force F maps and histograms; cell spring constant k_{cell} maps and histograms; Young's modulus E maps and histograms) of A549, 435, and 435/BRMS1, respectively. Statistical analysis of AFM results revealed that A549 cells

had rougher cell membrane; larger cell adhesion force and cell spring constant compared to 435 cells and 435/BRMS1. The membrane surface adhesion forces for these cancer cells were measured in culture medium: 0.478 ± 0.091 nN for A549 cells, 0.253 ± 0.070 nN for 435 cells, and 1.114 ± 0.281 nN for 435/BRMS1 cells, and the cell spring constant was measured at 2.62 ± 0.682 mN/m for A549 cells, 2.105 ± 0.691 mN/m for 435 cells, and 5.448 ± 1.081 mN/m for 435/BRMS1 cells. These differences could be attributed difference in the biochemical components and biophysical properties of each of the cell lines. Meanwhile, the increased membrane adhesion force and cell elasticity for 435/BRMS1 versus 435 could be caused by changes in the cell adhesion, cytoarchitecture and extracellular matrix in the context of BRMS1-expression [44].

4.6 CONCLUSIONS

It has been shown that the adhesion and motility of cancer cells is one of essential factors in the development of cancer cell metastasis [45, 46], for example, the inhibition of motility and enhancement of adhesion is very important for clinical treatment of cancer [45, 47, 48]. Therefore lower adhesion and a round shape may facilitate cell movement and migration. Alternatively, a stronger adhesion to the substratum may make these cells too adherent (or “sticky”) to migrate [45]. On the other hand, it has been reported that BRMS1 can suppress the development of metastasis without blocking orthotopic tumor growth [44, 49-53] and BRMS1-expression can probably induce cytoskeleton rearrangement and alterations in cell adhesion properties [44, 49], and suppress epidermal growth factor receptor (EGFR) expression [53].

Our AFM results presented in this work revealed that BRMS1 expression in 435 cells: a) altered cell topography from round (or elliptical shape) to triangular shape; b)

changed membrane cytoskeleton from net-like to parallel arrangement and thus induced a much rougher cell membrane; and c) increased the membrane surface adhesion force and cell spring constant. RM results indicated the overall similarity of the cellular surface biochemical compositions in A549, 435 and 435/BRMS1 cells, despite slightly weaker Raman band intensities that were observed in A549, the absence of the RNA band (813 cm^{-1}), and the increased amide I band (1660 cm^{-1}). These slight differences could possibly be enhanced utilizing a surface-enhanced Raman scattering (SERS) approach to gain new insight into the more subtle difference that may exist among these cell lines. The ability to differentiate cell biochemical components and cell biomechanics between native and metastasis biomarker gene expressed (e.g., BRMS1) cells could help in determining the role of related genes in cancer cell metastasis and the potential relationship to extracellular matrix and cell mobility [54, 55]. The alterations in cell and sub-cellular structures, nanomechanics and biochemical components arising from BRMS1-expression are likely to play an important role in the decrease of cell mobility and thus demonstrate a role in metastasis suppression. Altogether, this present work and the preliminary data revealed that the combination of AFM and RM are a promising technique for qualitatively and quantitatively assessing the differences in cell surface structures, surface biocomponents, and cell mechanics at the single cell, single molecule, and nanoscale level.

4.7 REFERENCES

- [1] P.A. Janmey, C.A. McCulloch, *Annu. Rev. Biomed. Eng.* 9 (2007) 1.
- [2] S.E. Cross, Y.S. Jin, J. Tondre, R. Wong, J. Rao, J.K. Gimzewski, *Nanotechnol.* 19 (2008) 384003.
- [3] S.E. Cross, Y.S. Jin, J. Rao, J.K. Gimzewski, *Nat. Nanotechnol.* 2 (2007) 780.

- [4] S. Suresh, *Nat. Nanotechnol.* 2 (2007) 748.
- [5] S. Suresh, *Acta Biomater.* 3 (2007) 413.
- [6] C. Kendall, M. Isabelle, F. Bazant-Hegemark, J. Hutchings, L. Orr, J. Babrah, R. Baker, N. Stone, *Analyst* 134 (2009) 1029.
- [7] C. Yu, E. Gestl, K. Eckert, D. Allara, J. Irudayaraj, *Cancer Detect. Prev.* 30 (2006) 515.
- [8] Q.S. Li, G.Y. Lee, C.N. Ong, C.T. Lim, *Biochem. Biophys. Res. Commun.* 374 (2008) 609.
- [9] L.J. Stafford, K.S. Vaidya, D.R. Welch, *Int J Biochem. Cell Biol.* 40 (2008) 874.
- [10] M.J. Seraj, R.S. Samant, M.F. Verderame, D.R. Welch, *Cancer Res.* 60 (2000) 2764.
- [11] R.S. Samant, M.J. Seraj, M.M. Saunders, T.S. Sakamaki, L.A. Shevde, J.F. Harms, T.O. Leonard, S.F. Goldberg, L. Budgeon, W.J. Meehan, C.R. Winter, N.D. Christensen, M.F. Verderame, H.J. Donahue, D.R. Welch, *Clin. Exp. Metastas.* 18 (2000) 683.
- [12] J. Ling, S.D. Weitman, M.A. Miller, R.V. Moore, A.C. Bovik, *Appl. Opt.* 41 (2002) 6006.
- [13] D.W. Ball, *Spectroscopy* 16 (2001) 32.
- [14] D. Pappas, B.W. Smith, J.D. Winefordner, *Talanta* 51 (2000) 131.
- [15] P. Carey, *Trac-Trend. Anal. Chem.* 2 (1983) 275.
- [16] P. Hildebrandt, S. Lecomte, C.L. John, *Encyclopedia of Spectroscopy and Spectrometry*, Elsevier, Oxford, 1999, p. 88.
- [17] H. Fabian, P. Anzenbacher, *Vib. Spectrosc.* 4 (1993) 125.
- [18] J.R. Baena, B. Lendl, *Curr. Opin. Chem. Biol.* 8 (2004) 534.
- [19] F.M. Lyng, E.Ó. Faoláin, J. Conroy, A.D. Meade, P. Knief, B. Duffy, M.B. Hunter, J.M. Byrne, P. Kelehan, H.J. Byrne, *Exp. Mol. Pathol.* 82 (2007) 121.
- [20] C.M. Krishna, G.D. Sockalingum, G. Kegelaer, S. Rubin, V.B. Kartha, M. Manfait, *Vib. Spectrosc.* 38 (2005) 95.
- [21] K.W. Short, S. Carpenter, J.P. Freyer, J.R. Mourant, *Biophys. J.* 88 (2005) 4274.
- [22] H. Abramczyk, J. Surmacki, B. Brozek-Pluska, Z. Morawiec, M. Tazbir, *J. Mol. Struct.* 924-926 (2009) 175.
- [23] I. Notingher, *Sensors* 7 (2007) 1343.

- [24] C.A. Lieber, A. Mahadevan-Jansen, *Appl. Spectrosc.* 57 (2003) 1363.
- [25] J. Zhao, H. Lui, D.I. McLean, H. Zeng, *Appl. Spectrosc.* 61 (2007) 1225.
- [26] F.W.L. Esmonde-White, M.V. Schulmerich, K.A. Esmonde-White, M.D. Morris, Automated Raman spectral preprocessing of bone and other musculoskeletal tissues, *Optics in Bone Biology and Diagnostics*, SPIE, San Jose, CA, USA, 2009, p. 716605.
- [27] E.M. Kanter, S. Majumder, E. Vargis, A. Robichaux-Viehoever, G.J. Kanter, H. Shappell, I. Howard W. Jones, A. Mahadevan-Jansen, *J. Raman Spectrosc.* 40 (2009) 205.
- [28] C. Krafft, T. Knetschke, A. Siegner, R.H.W. Funk, R. Salzer, *Vib. Spectrosc.* 32 (2003) 75.
- [29] M. Lekka, P. Laidler, D. Gil, J. Lekki, Z. Stachura, A.Z. Hrynkiwicz, *Eur. Biophys. J. Biophys.* 28 (1999) 312.
- [30] W.A. Lam, M.J. Rosenbluth, D.A. Fletcher, *Blood* 109 (2007) 3505.
- [31] G. Pyrgiotakis, T.K. Bhowmick, K. Finton, A.K. Suresh, S.G. Kane, J.R. Bellare, B.M. Moudgil, *Biopolymers* 89 (2008) 555.
- [32] M.V.P. Chowdary, K.K. Kumar, M. Stanley, R. Lakshmi, C.M. Krishna, K. Jacob, *Biopolymers* 91 (2009) 539.
- [33] I.T. Jolliffe, *Principal Component Analysis*, 2nd edition, Springer, New York, 2002.
- [34] J.M. Shaver, *Chemometrics for Raman spectroscopy*. In *Handbook of Raman Spectroscopy*, Lewis, I. R., Edwards, H. G. M. (eds), Marcel Dekker, New York, 2001.
- [35] R.J. Barnes, M.S. Dhanoa, S.J. Lister, *Appl. Spectrosc.* 43 (1989) 772.
- [36] A.K. Jain, Dubes, R. C. (Ed.), *Algorithms for Clustering Data*, Prentice Hall, Englewood Cliffs, NJ, 1988.
- [37] S.B. Velegol, B.E. Logan, *Langmuir* 18 (2002) 5256.
- [38] M. Arnoldi, M. Fritz, E. Bauerlein, M. Radmacher, E. Sackmann, A. Boulbitch, *Phys. Rev. E* 62 (2000) 1034.
- [39] Y.Z. Wu, Y. Hu, J. Cai, S.Y. Ma, X.P. Wang, Y. Chen, *Scanning* 30 (2008) 426.
- [40] C. Krishna, G. Sockalingum, R. Bhat, L. Venteo, P. Kushtagi, M. Pluot, M. Manfait, *Anal. Bioanal. Chem.* 387 (2007) 1649.
- [41] Y. Wu, G.D. McEwen, S. Harihar, S.M. Baker, D.B. DeWald, A. Zhou, *Cancer Lett.* 293 (2010) 82.

- [42] E.R. Hildebrandt, N.R. Cozzarelli, *Cell* 81 (1995) 331.
- [43] Z. Movasaghi, S. Rehman, I.U. Rehman, *Appl. Spectrosc. Rev.* 42 (2007) 493.
- [44] P.J. Champine, J. Michaelson, B.C. Weimer, D.R. Welch, D.B. DeWald, *Clin. Exp. Metastas.* 24 (2007) 551.
- [45] M.T. Debies, D.R. Welch, *J. Mammary Gland Biol.* 6 (2001) 441.
- [46] S. Zhang, Q.D. Lin, W. Di, *Int. J. Gynecol. Cancer* 16 (2006) 522.
- [47] J.M. Kirstein, K.C. Graham, L.T. MacKenzie, D.E. Johnston, L.J. Martin, A.B. Tuck, I.C. MacDonald, A.F. Chambers, *Clin. Exp. Metastas.* 26 (2009) 121.
- [48] L. Lu, F. Payvandi, L. Wu, L.H. Zhang, R.J. Hariri, H.W. Man, R.S. Chen, G.W. Muller, C.C.W. Hughes, D.I. Stirling, P.H. Schafer, J.B. Bartlett, *Microvasc. Res.* 77 (2009) 78.
- [49] D.B. DeWald, J. Torabinejad, R.S. Samant, D. Johnston, N. Erin, J.C. Shope, Y. Xie, D.R. Welch, *Cancer Res.* 65 (2005) 713.
- [50] C.W. Rinker-Schaeffer, J.P. O'Keefe, D.R. Welch, D. Theodorescu, *Clin. Cancer Res.* 12 (2006) 3882.
- [51] L.A. Shevde, D.R. Welch, *Cancer Lett.* 198 (2003) 1.
- [52] P.S. Steeg, *Nat. Rev. Cancer* 3 (2003) 55.
- [53] K.S. Vaidya, S. Harihar, P.A. Phadke, L.J. Stafford, D.R. Hurst, D.G. Hicks, G. Casey, D.B. DeWald, D.R. Welch, *J. Biol. Chem.* 283 (2008) 28354.
- [54] K. Bhadriraju, L.K. Hansen, *Exp. Cell. Res.* 278 (2002) 92.
- [55] D. Yamazaki, S. Kurisu, T. Takenawa, *Cancer Sci.* 96 (2005) 379.

CHAPTER 5**BRMS1 EXPRESSION ALTERS THE ULTRASTRUCTURAL,
BIOMECHANICAL AND BIOCHEMICAL PROPERTIES OF MDA-MB-435
HUMAN BREAST CARCINOMA CELLS: AN INSTRUMENTAL APPROACH
TO STUDY CANCER CELLS⁴****5.1 ABSTRACT**

Restoring breast cancer metastasis suppressor 1 (BRMS1) expression suppresses metastasis in MDA-MB-435 human breast carcinoma cells at ectopic sites without affecting tumor formation at orthotopic site in the body. BRMS1 expression induces many phenotypic alterations in 435 cells such as cell adhesion, cytoskeleton rearrangement, and the down-regulation of epidermal growth factor receptor (EGFR) expression. In order to better understand the role of cellular biomechanics in breast cancer metastasis, the qualitative and quantitative detection of cellular biomechanics and biochemical composition is urgently needed. In the present work, using atomic force microscopy (AFM) and fluorescent microscopy we revealed that BRMS1-expression in 435 cells induced reorganization of F-actin and caused alteration in cytoarchitectures (cell topography and ultrastructure). Results from AFM revealed increase in biomechanical properties which include cell adhesion, cellular spring constant, and Young's modulus in 435/BRMS1 cells. Raman microspectroscopy (RM) showed weaker vibrational spectroscopic bands in 435/BRMS1 cells, implying decrease in concentration of cellular biochemical components in these cells. This was despite similar spectral

⁴ Coauthored by Gerald D. McEwen, Yangzhe Wu, Sitaram Harihar, Sherry M. Baker, Daryll B. DeWald, and Anhong Zhou

patterns observed between 435 and 435/BRMS1 cells. Electric cell-substrate impedance sensing (ECIS) similarly revealed that 435 cells adhere more tightly to substrata and migrate more rapidly after wounding than BRMS1 cells. This work demonstrated the feasibility of applying AFM, RM, and ECIS techniques for *in situ* measurements of the cellular biomechanics, behavior, and biochemical components of breast carcinoma cells. It provides vital clues in understanding the role of cellular biomechanics in cancer metastasis, and further the development of new techniques for early diagnosis of breast cancer.

5.2 INTRODUCTION

The biomechanical properties of cancer cells such as adhesion, elasticity, and stiffness have been recognized as very important contributing to adherence, mobility, transformation, invasion, and metastasis [1]. Moreover, the cytoarchitectures and biophysical properties are often altered in cancer cells, and the latter has been implicated as a target area for the development of new clinical diagnostic approaches [1, 2, 3, 4]. Therefore, it is important to characterize the alterations in cellular biomechanics and membrane components in cancer cells with respect to normal or benign cells. However, such alterations have not yet been clearly elucidated, and one of the reasons is the lack of applicable technologies. Fortunately, studies using atomic force microscopy (AFM) and RM have provided important insights into cellular biomechanics and these important tools have been recently applied in cancer cell studies [1, 2, 3, 4, 5, 6, 7].

MDA-MB-435 are breast adenocarcinoma cells that when injected into the mammary fat pads of immune-compromised mice form progressively growing tumors culminating in metastases [8]. These cells show alterations in the long arm of

chromosome 11, a region containing the breast cancer metastasis suppressor 1 (BRMS1) gene, leading to the loss of BRMS1 expression. Restoration of BRMS1 expression in these cells using microcell mediated chromosome transfer resulted in suppression of metastasis, leading to the identification of BRMS1 as a legitimate member of the family of metastasis suppressor genes [9, 10]. Metastasis suppressor genes are defined by their ability to suppress the formation of metastasis without affecting orthotopic tumor growth [11]. BRMS1 belongs to this family of genes which also includes more than 25 other genes [12]. BRMS1 has been shown to associate with the SIN3-histone deacetylase complexes possibly altering the transcription of some genes [13]. Also, BRMS1 has been shown to regulate phosphoinositide signaling [14], expression of epidermal growth factor receptor [15], osteopontin [16], NF κ B [17], and connexins [18], all of which have been known to play a significant role in cancer progression, implicating BRMS1 in metastasis suppression.

In the past decades, atomic force microscopy (AFM), had been widely applied in cell biological studies as a valuable force (nN/pN)-sensitive technique. This technology can provide the surface topography and biomechanics of mammalian cells at nanoscale resolution under near-physiological conditions AFM has allowed researchers to better understand mammalian cell biology and biophysical functions such as expression of specific receptors or oncogenic transformation. To date, applications AFM have been widely applied for detecting cellular biomechanics. For example, using AFM Cross *et al.* found that cancer cells are largely softer and less adhesive compared to normal/benign cells [2, 19]. Lekka *et al.* reported that cancer cells have a lower Young's modulus than normal human epithelial cells (Hu609 and HCV29) [20], and Li *et al.* also found the

same variation tendency in non-malignant breast cells (MCF-10A) and malignant cells (MCF-7) [7]. These results along with others [3, 4, 20, 21] associated with cellular biomechanics have demonstrated the importance of AFM in nano-biomechanics studies and in early diagnosis of diseases like cancer.

RM is a nondestructive vibrational/structural characterization method that can be utilized to identify characteristic spectroscopic fingerprints of living cells based on chemical molecular compositions [22]. Raman spectral frequencies are recorded in wavenumber units which are proportional to vibrational energies based on molecular polarizability [23]. Earlier studies using RM focused mainly on physical and structural investigations. Over the past few decades, due to advances in instrument design [24, 25], biological applications [26, 27], and methods for biochemical information extraction [28, 29], RM has exhibited increased popularity in the field of mammalian cell biology [6, 30]. Short *et al.* demonstrated the use of RM to detect biochemical changes, in tumorigenic versus nontumorigenic cells, as a result of proliferation [31]. More recently, Abramczyk *et al.* reported the hallmarks of normal, malignant, benign breast tissue characterized by Raman studies [32]. Several other studies reported the appearance of surface biopolymers (including DNA/RNA, lipids, proteins, and carbohydrates) in cellular growth [6, 29, 33].

Introduced in 1991 [4] electric cell-substrate impedance sensing (ECIS) is an electrical method to observe mammalian cell behavior/mobility in real-time. Monitored behaviors include cell mobility, adhesion, and other cytoskeleton mediated activities. More than a decade ago ECIS was introduced to monitor cell attachment and cell spreading on artificial surfaces in real time and wound healing [5]. It was found that

wounding cells using ECIS is highly reproducible and can quantitatively measure cell line migration rates. A mini-review of ECIS as a non-invasive technique to study cancer cells addressed the importance of advantages for cancer biology and drug discovery [9]. Hong *et al.* further recognized how label-free and non-invasive measurements can be integrated with standard end point assays to achieve both optical and electrochemical observations.

The objective of the present study was to analyze and compare the differences in cell topography, ultrastructure, biomechanics, biochemical components, and mobility between metastatic MDA-MB-435 (435) and non-metastatic MDA-MB-435/BRMS1 (435/BRMS1) human breast carcinoma cells. In addition, we sought to understand potential links between cytoarchitectural, biomechanical changes and metastatic breast cancer. Our results show that BRMS1-expression induced alterations in cytoarchitecture including cell topography, ultrastructure, and biochemical properties, and increase in cell adhesion, elasticity, and stiffness in 435 cells. This work also illustrates the potential of applying a combined AFM and RM approach for the study of cancer cell metastasis.

5.3 MATERIALS AND METHODS

5.3.1 Preparation of breast cancer cell line 435 and 435/BRMS1

The 435/BRMS1 cells were transfected with a lentiviral vector construct expressing full length BRMS1 cDNA under the control of a cytomegalovirus promoter. 435 and 435/BRMS1 cells were cultured in a 1:1 mixture of Dulbecco's-modified eagle's medium (DMEM) and Ham's F-12 medium supplemented with 5% fetal bovine serum (HyClone, Logan, UT). Cells were cultured in 25-cm² Corning tissue culture dishes at 37 °C with 5% CO₂ in a humidified atmosphere. Cells were sub-cultured at 80-90%

confluency using 2 mM EDTA in $\text{Ca}^{2+}/\text{Mg}^{2+}$ -free PBS (PBS, 0.01M, pH7.4, Thermo Scientific). Cell lines were confirmed to be free of Mycoplasma contamination using PCR (TaKaRa, Japan). No antibiotics or antimycotics were used in both cells culturing.

For AFM experiments, cells were seeded on poly-L-lysine coated Petri dishes at a density of 1×10^5 cells per 2 mls of media. For RM a density of 1×10^5 cells per 2 mls of media was seeded on quartz cover slips (18×18 mm) to minimize the effects of background (Electron Microscopy Science Cat. # 72250-02). ECIS arrays were removed from the electrode holder and placed on a heating block ($37 \text{ }^\circ\text{C} \pm 1 \text{ }^\circ\text{C}$) within a laminar flow hood and inoculated with a 200 μl suspension of 5×10^5 cells/ml to yield a final concentration of 2×10^5 cells/well (400 μl total solution per well).

5.3.2 Atomic force microscopy

Because the 435 and 435/BRMS1 cells were too soft to be imaged by AFM, two approaches of sample preparation were adopted. 1) The *in situ* approach was used to measure the biomechanical properties such as adhesion behavior, cellular spring constant and Young's modulus. Cells grown on poly-L-lysine coated Petri dishes were directly transferred onto AFM scanner stage for measurements without any pretreatment, and whole measurements were conducted in culture medium; the acquired data thus reflected the physiological status of the observed living cells. 2) To compare the differences in topography and ultrastructures of the two cell lines, the cells were pretreated by fixing with $1 \times \text{Ca}^{2+}/\text{Mg}^{2+}$ -free phosphate buffered saline containing 1% glutaraldehyde plus 1% paraformaldehyde for 5 minutes, followed by gentle rinsing using PBS. The Petri dish containing the cells immersed in PBS was then transferred onto AFM scanner stage for imaging.

The contact mode AFM controlled by software PicoScan 5.4 (PicoPlus, Agilent Technologies, USA) was applied to 435 and 435/BRMS1 cells at room temperature in PBS (0.01 M, pH7.4) or directly in cell culture medium. During AFM imaging the height mode and deflection mode images were acquired simultaneously. Because the deflection mode image can provide very fine structural details it was employed in experimental analyses. The spring constant of the cantilever used in the experiments was 0.06 N/m (Veeco). The tip length was 0.4~0.7 μm , and the curvature radius of the Si_3N_4 tip was approximately 10 nm. Also, the approach/retract velocity applied throughout the experiments of deflection (nm) vs. distance (nm) curve acquirement was 6.1 $\mu\text{m/s}$. The values for the adhesion force (the detachment force between bare AFM tip and cell surface in the process of AFM cantilever retracting) were extracted from curves of deflection (nm) vs. distance (nm) via the Scanning Probe Image Processor (SPIP) software (Image Metrology, Denmark). By applying the AFM tip to the sample surface, the elasticity of cell membrane can be evaluated based on the slope of compliance portion of the deflection-force curve. To analyze cellular elasticity, the cellular spring constants (k_{cell}) were calculated using a previously presented formula [34, 35], as shown in Chapter 4 equation 2.

To further evaluate the difference in stiffness of the two cell lines, the Young's modulus was also calculated according to the following formula that has been widely accepted [36, 37]:

$$E_{\text{cell}} = \frac{4 \cdot F_{(\Delta z)} \cdot (1 - \nu_{\text{cell}}^2)}{3 \cdot \Delta z^{0.5} \cdot \tan \theta} \quad (2)$$

where E_{cell} , Young's modulus; F , loading force; ν_{cell} , Poisson ratio (assuming 0.5); Δz , indentation (shown in Figure 5.2); θ is the curvature tip half-angle that equals to 36° .

With this formula, we calculated the Young's modulus for each group based on hundreds of deflection-distance curves acquired.

Furthermore, to assess statistically significant differences in biophysical properties including adhesion force and cellular elasticity between these two breast cancer cell lines, the data were reported as mean \pm SE (standard error), and the statistical difference was analyzed by a Student's t-test or ANOVA. The data used to graph histogram or maps were measured from the whole cell body, and the histograms were drawn using OriginPro 7.5 (OriginLab Corp., USA). The mapping of adhesion force or cellular spring constant was graphed with a 256 color map created by MATLAB program version R2009a (MathWorks, Inc.).

5.3.3 Raman microspectroscopy

Raman spectra were acquired using a Renishaw inVia Raman spectrometer (controlled by WiRE 3.0 software) connected to a Leica microscope (Leica DMLM). The spectrometer was equipped with a 785 nm near-IR laser (laser spot 10 x 3 μ m line) that was focused through a 63x NA = 0.90 water immersion objective. The spectrometer was calibrated with silicon at a static spectrum centered at 520.5 cm^{-1} for 1 second. Samples of 435 and 435/BRMS1 cells were mounted on the microscope stage and imaged. Spectra were then collected in static mode for 1 accumulation at 10 second laser exposure over a wave number range of 500 – 1800 cm^{-1} . Five spectra were used to calculate an average for both cell lines. Each spectrum was then normalized using peak intensity at 805.7 cm^{-1} and baseline corrected by subtraction of quartz substrate and media spectrum. Savitsky-Golay smoothing [38] was performed with the smooth window equal to 9 and polynomial order equal to 2. Raman spectral maps were collected in a "StreamLine" mode at 30

seconds exposure time at wavenumber center 900 cm^{-1} . Cosmic Ray Removal (CRR) was performed and signal-to-baseline intensity was analyzed over a range of $700 - 1092\text{ cm}^{-1}$. The diffraction limited optical resolution for the 63x objective was calculated by the Abbe equation [22].

5.3.4 Electric cell-substrate impedance sensing

ECIS arrays were prepared, prior to use, according to the following steps; 200 μl of pre-warmed gelatin solution (0.15 M NaCl + 1000 $\mu\text{g/ml}$) was added to each well for 10 minutes or 10 mM L-cysteine in water (Electrode-stabilizing Solution, ABP, NY, USA) was added to each well for 15 minutes, electrodes were then rinsed with 400 μl of 0.15 M NaCl solution, and 200 μl of serum containing culture medium (DMEM:Ham's F-12) was added to each well. Electrode arrays were then placed in an array holder (ECIS Z0, ABP, NY, USA), incubated at $37\text{ }^{\circ}\text{C}$ and 5% CO_2 while an electrode stabilization was performed by the ECIS software. After stabilization, electrode arrays were monitored for an additional 30 minutes to verify proper electrode baseline prior to seeding with 435 and 435/BRMS1 cells. Once seeded the arrays were then returned to incubated electrode holder and monitored using ECIS Software (v1.2.35, ABP, NY, USA). For wounding assay setting were 60 kHz and 1400 μA for 20 seconds. Pre- and post-wounding images were acquired using an Olympus IX-70 inverted epifluorescence microscope with no further image processing.

5.3.5 Immuno-fluorescent staining for F-actin localization in 435 and 435/BRMS1 cells.

To evaluate F-actin localization, 435 and 435/BRMS1 cells grown on cover slips for 24 hours were fixed using 4% paraformaldehyde (Electron Microscopy Sciences,

Hatfield, PA) for 20 min, and permeabilized using 0.1% Triton X-100 (Union Carbide Corporation, Texas city, TX) for 10 minutes. F-actin was stained using Phalloidin (Invitrogen, Carlsbad, CA), nuclei were counter-stained using 4',6-diamidino-2-phenylindole (Vector laboratories Inc, Burlingame, CA), and cells were viewed with an Olympus IX-70 inverted epifluorescence microscope. Representative images were obtained, combined, and processed using IPLab (v3.7) deconvolution software (Scanalytics, Rockville, MD).

5.4 RESULTS

5.4.1 Topography and ultrastructure of 435 and 435/BRMS1 cells

Fixed cells were imaged by AFM in PBS solution. Figure 5.1-A through -F) shows representative images of 435 cells at a single cell (A-C) and ultrastructural level (D-F), and Figure 5.1-G through -L) are images of 435 /BRMS1 cells at a single cell (G-I) and ultrastructural level (J-L). Figure 5.1 vividly revealed the differences in topography and ultrastructures of these two cell lines, indicating that 435 cells possessed a more round or elliptical shape (Figure 5.1-A through -C). In contrast, 435/BRMS1 cells were predominately elongated (Figure 5.1-G) with lamellipodial-like projections (Figure 5.1-I). Moreover, the comparison of membrane surface ultrastructures indicated that the 435/BRMS1 (Figure 5.1-J through -L) cells also possessed a much rougher membrane surface than 435 cells (Figure 5.1-D through -F), which could be due to more abundant microvillus structures. These microvillus structures led to the low resolution (obscured) images (Figure 5.1-H, -K, and -L) because the microvillus floating in medium could move or be moved in the process of tip scanning. Mesh-like cytoskeleton structures were clearly visible on the membrane surface of 435 cells, whereas the cytoskeleton structures

(e.g., filamentous actin) (Figure 5.1-D through -F) of 435/BRMS1 cells were arranged in parallel, as shown in the deflection image (Figure 5.1-J).

5.4.2 Homogeneity in adhesion behavior and elasticity of membrane surface

The cytoskeleton, a supramolecular network mainly consisting of microfilaments, intermediate filaments and microtubules, is very important for determining cell shape and generating mechanical forces. It is possible that initiation of cytoskeletal rearrangements in 435 cells due to BRMS1 expression could affect cellular properties such as adhesion and elasticity. Therefore, it is of interest to evaluate the differences in viscoelasticity of the two cell lines (435 and 435/BRMS1). In 435 cells, both adhesion force and cellular spring constant (k_c) measured on cytoskeleton and on lipid (non-cytoskeleton region) were not statistically different. The measured adhesion force was 0.291 ± 0.018 nN for cytoskeleton and 0.298 ± 0.024 nN for lipid; the mean value of k_c was 9.45 ± 0.23 mN/m for the cytoskeleton, and 9.27 ± 0.20 mN/m for lipid, implying biophysical and biochemical homogeneity of the membrane surface of 435 cells. However in 435/BRMS1 cells the adhesion properties of the cytoskeleton region (below the green line in Figure 5.1-I) and the microvillus-abundant region (above the green line in Figure 5.1-I) were significantly different ($P < 0.01$): 0.173 ± 0.025 nN for the cytoskeleton region, and 0.477 ± 0.030 nN for the microvillus-abundant region. Also the difference in spring constants between these two regions were not statistically significant even though their mean spring constants were different (0.019 ± 0.002 N/m for the cytoskeleton region, and 0.006 ± 0.0001 N/m for the microvillus region). These findings suggested the lack of physicochemical homogeneity of the cell surface in 435/BRMS1 cells. These measurements indicated that BRMS1 expression induced changes in both membrane cytoskeleton and biomechanics,

which could be the result of differential expression of genes involved in the cytoskeleton and adhesion [39]. Because the reorganization of cytoskeleton is closely associated with cellular biomechanics [1, 7], it is more valuable to detect the difference in biomechanics including adhesion, elasticity and stiffness of living cells *in situ*.

5.4.3 Biomechanics of 435 and 435/BRMS1 cells.

To further analyze the biomechanics including adhesion behavior and elasticity of the two cell lines in the context of cytoskeleton rearrangements [15, 39], we measured the living cells, *in situ*, cultured on poly-L-lysine coated Petri dish in culture medium and the results are shown in Figure 5.2. Figure 5.2(-B, -D) and (-H, -J) show the statistical distribution of the adhesion force and cellular spring constant measured on 435 and

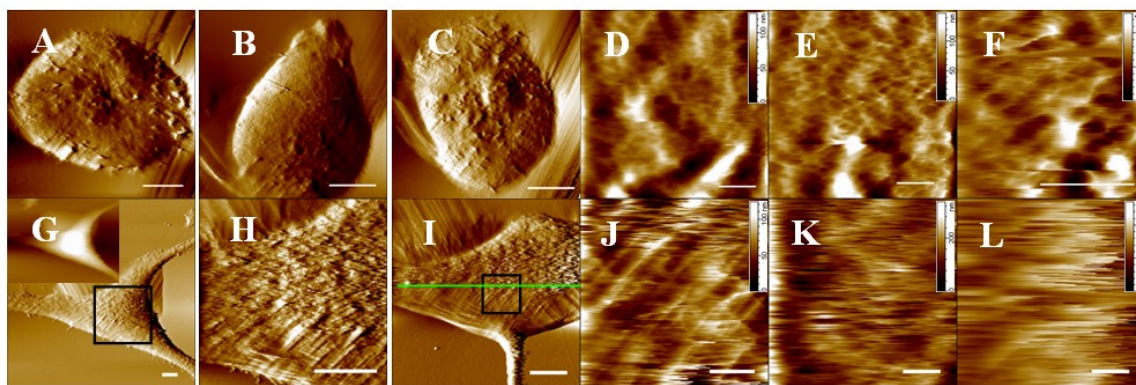


Figure 5.1. Comparison of topography, ultrastructures, and biomechanics of 435 (A-F) and 435/BRMS1 (G-L) cells. The cells were fixed by 1% glutaraldehyde plus 1% paraformaldehyde. (A-C) and (G-I) are deflection images of 435 and 435/BRMS1 cells, respectively; (D-F) and (J-L) present ultrastructures of 435 and 435/BRMS1 cells, respectively. The inset in (G) indicates the height mode image of cell (G). Images (H) and (J) are the magnified views of square frame in (G) and (I), respectively. Scale bar: A-C, G-I, 5 μm ; D-F, J-L, 1 μm .

435/BRMS1 cells and these respective maps are shown in Figure 5.2(-C, -E) and (-I, -K).

It was interesting to note that the filamentous actin that was previously observed in fluorescence images [14] was also seen in Figure 5.2-G (green arrows). The low resolution deflection images in Figure 5.2-A and -G may be a result of the very soft cell membrane (evidenced by the low cellular spring constants as shown in Figure 5.2-D, -J) and the presence and movement of membrane surface microvillus during the tip scanning. Figure 5.2-F shows representative deflection (nm) vs. distance (nm) curves acquired on 435 and 435/BRMS1 cells. The compliance portion of the approaching branch for the curves exhibited obvious non-linear interaction between the tip and cell membrane, revealing the existence of the effects of polymer brush of microvillus (steric effect), electrostatic interaction (charged group), and elastic interaction [40, 41]. On the other hand, the retracting branch of the curves indicated the non-specific binding force and long-range interaction (Figure 5.2-F) [41]. The culmination of these effects lowered the image resolution; therefore, we performed the acquisition of deflection (nm) versus distance (nm) curve to evaluate the biomechanics of the cell surface.

The analysis of variance (ANOVA) indicated that the adhesion behavior between the two cell lines were significantly different at the 0.05 level ($F=37.67$). The adhesion force of 435 cells was measured at 0.434 ± 0.010 nN, whereas that of 435 /BRMS1 cells was 0.826 ± 0.011 nN (statistics based on multiple cells). This adhesion force difference might be ascribed to the changes in cell adhesion, cytoarchitecture, and extracellular matrix in BRMS1-expressing cells [39]. Moreover, it was found that both 435/BRMS1 and 435 cells possessed very low cellular spring constants, 4.334 ± 0.066 mN/m for 435/BRMS1 and 3.443 ± 0.064 mN/m for 435 (data from multiple cells), and the

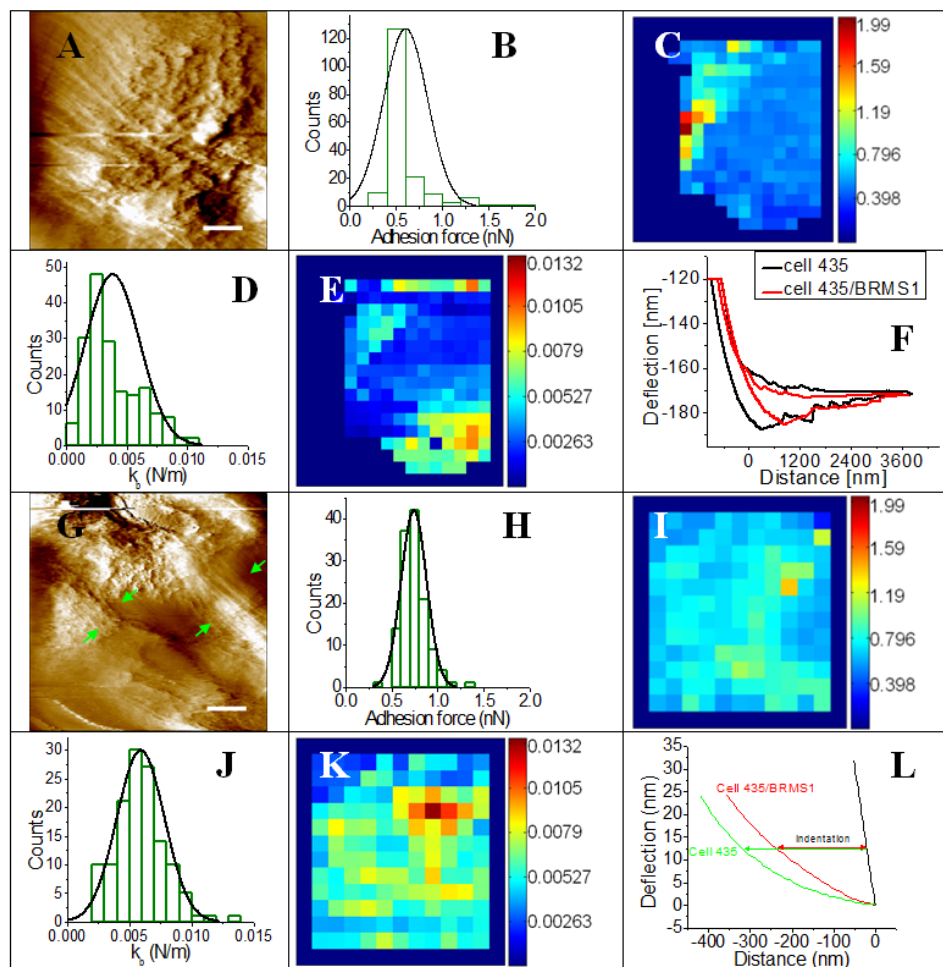


Figure 5.2. Biomechanical evaluation of living breast cancer cell line 435 (A-E) and 435/BRMS1 (G-K). (A) and (G) are representative deflection images of 435 and 435/BRMS1 cells scale acquired in culture medium, respectively, and their respective statistical results of adhesion force and spring constant (k_{cell}) are shown in (B, D) or in (H, J). The maps of adhesion force and k_c of 435 and 435/BRMS1 cells are shown in (C, E) and (I, K), respectively. (F) Two representative deflection (nm)-distance (nm) curves measured on 435 cells (black curve) and 435/BRMS1 cell (red curve). (L) presents the merged compliance portion of approaching branch of one deflection (nm)-distance (nm) curve acquired on 435 cell (green curve), 435/BRMS1 cell (red curve), or on Petri dish (black curve); the Young's moduli of the two cell lines were calculated by substituting the indentation depth and the corresponding compliance force into the equation (2). Scale bar for (A, G): $5\mu\text{m}$.

difference was also statistically significant. Furthermore, it should be noted that the Young's modulus of 435/BRMS1 (non-metastatic), 18.10 ± 0.94 kPa, was larger than the metastatic 435, 4.70 ± 0.28 kPa, which is similar to previous reported results for MCF7 breast cancer cells [7] and other cancer cell lines [2, 20]. The larger Young's modulus of 435/BRMS1 could be attributed to the reorganization of the cytoskeleton. In addition, it was noted that the adhesion force and spring constant measured for living cells differed from those for fixed cells (discussed in section 3.3.), which could be due to the different physiological status of the cell membranes.

5.4.4 Cellular components of 435 and 435/BRMS1 cells

RM provides a non-invasive tool to characterize the cellular biochemical composition of human tissues at different disease states [42]. Using this technique the predominance of lipids was reported in normal breast tissue whereas proteins were predominant in pathological breast tissue [43, 44]. Taking note of the previous observations the Raman spectra was compared between 435 and 435/BRMS1 cells in order to determine if the expression of BRMS1 could alter cell surface components. Stacked Raman spectra of 435 and 435/BRMS1 cells are shown in Figure 5.3. These spectra illustrate the overall similarities in biochemical composition between the metastatic 435 cells (upper in Figure 5.3) and the non-metastatic 435/BRMS1 cells (lower in Figure 5.3). It was found that the Raman spectra for 435 and 435/BRMS1 are very similar with the presence of bands corresponding to DNA/RNA, lipids, proteins, and carbohydrates. The main bands for DNA are assigned as 720 (adenine), 785 (cytosine and thymine), 1091 (O-P-O symmetric stretching), and 1341 cm^{-1} (adenine); all of which are

associated with the vibrations of the nucleic acid and sugar-phosphate backbone [33, 45, 46]. The band at 785 cm^{-1} can be taken as a measure for the relative quantity of nucleic acids [47]. Besides the nucleic acid and phosphate backbone bands, another characteristic band for RNA is assigned at 813 cm^{-1} (C'5-O-P-O-C'3 phosphodiester bands) which is one of the most distinct peaks for RNA [33, 46]. Lipids are present at 719 cm^{-1} ($\text{N}^+(\text{NH}_3)_3$ symmetric stretching), 1091 cm^{-1} (lipid), 1304 cm^{-1} (CH_2 deformation of phospholipids), and 1451 cm^{-1} (CH_2 bending mode in malignant tissue) [33, 46]. The characteristic peak for phospholipids at 719 cm^{-1} overlaps with the adenine peak at 720 cm^{-1} . Wavenumbers in the $1091 \sim 1095\text{ cm}^{-1}$ range can result from either lipids or phosphate backbone vibration in nucleic acids [33, 46], we tentatively assign 1091 cm^{-1} in 435 cells to lipid and use this peak for Raman spectral mapping. Compared to the normal breast tissue, the lipid band in breast cancer cells typically found at 1440 cm^{-1} (CH_2 bending mode) was red shifted to 1451 cm^{-1} , which is consistent with reported literature [44]. Proteins are assigned to 624 cm^{-1} (C-C twisting mode of phenylalanine), 645 cm^{-1} (C-C twisting mode of tyrosine), 856 cm^{-1} (ring breathing of tyrosine), 1006 cm^{-1} (ring breathing of phenylalanine), 1034 cm^{-1} (C-H in phenylalanine), 1128 cm^{-1} (C-N stretching in protein or C-O stretching in carbohydrates), 1209 cm^{-1} (C-C₆H₅ stretching mode in phenylalanine and tyrosine), 1254 cm^{-1} (Amide III β sheet), and 1661 cm^{-1} (Amide I) [33, 45]. It should be noted that the Amide I band, usually present at 1654 cm^{-1} in normal breast tissue, is also red shifted to 1661 cm^{-1} for both cancer cell-lines in this study. Also, the typical amide III at 1270 cm^{-1} (α helix of protein) was not observed here. Carbohydrates are assigned in the range of $800 - 1100\text{ cm}^{-1}$ are associated with glycosidic bonds and sugar ring vibrations [33], e.g., 939 or 940 cm^{-1} can be tentatively assigned to the skeletal mode of polysaccharides.

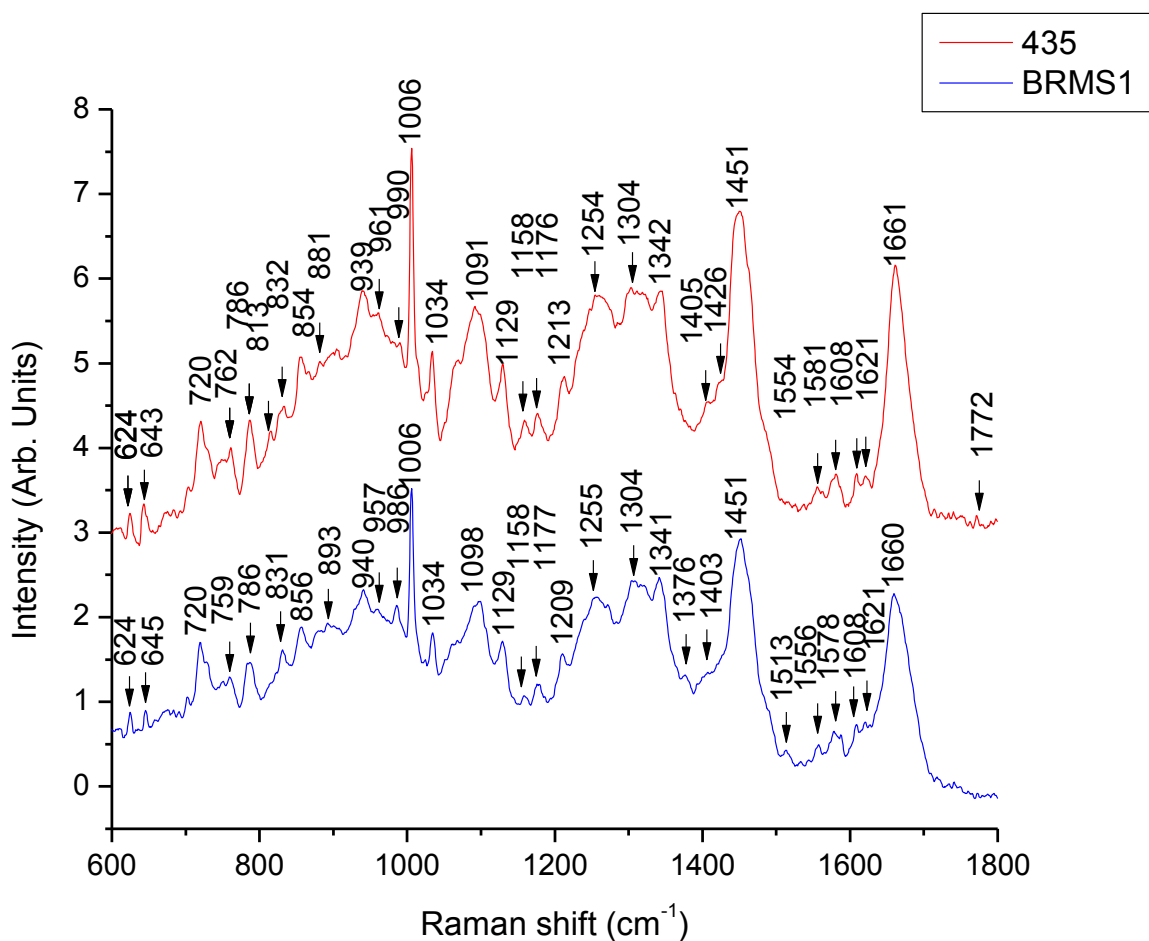


Figure 5.3. Raman spectra of 435 cells (upper) and 435/BRMS1 cells (lower).

Spectral differences between 435 and 435/BRMS1 cells are observed for the bands: 813 (C'5-O-P-O-C'3 phosphodiester bands in RNA), 1426 (deoxyribose or ν_s (COO⁻) of protein), and 1772 cm^{-1} (unidentified) in 435 cells; 1376 (CH_3 symmetric deformation) and 1513 cm^{-1} (cytosine or carotenoid pigments) in 435/BRMS1 cells [33, 46]. Also observed are relatively stronger bands at 1158 and 1176 cm^{-1} in 435, which can

be tentatively assigned as carotenoids, or C-C/C-N stretching in proteins and cytosine, or guanine or C-H bending in tyrosine [33, 46], and a relatively stronger band at 986 cm^{-1} in 435/BRMS1, which can be assigned as C-C or C-O in ribose [33, 46]. In addition, symmetric phosphate backbone stretching vibration of DNA band is red shifted from 1091 cm^{-1} in 435 cells to 1098 cm^{-1} in 435/BRMS1 cells. Overall, the band intensity of 435 is stronger than that of 435/BRMS1, implying a richer biochemical composition in 435 compared with 435/BRMS1 cells. The major spectral differences between these breast carcinoma cells and normal breast tissue [44] are: 435 carcinoma cells possess a relatively strong amide I band, a stronger and broader amide II band, a broader and red shifted CH_2 bending mode band, and a richer protein presence. The increased presence of proteins in cancer cells has been associated with inflammation and metastasis [48, 49].

Figure 5.4 shows Raman spectral mapping for both 435 (column 1) and 435/BRMS1 cells (column 2). The bottom row is a bright field image acquired prior to Raman spectral mapping. Each of the following rows (2-5 from bottom) is a specific cellular component distribution map, as characterized by using a wavenumber characteristic of each component layered over the bright field image. The top-most row is a blended image of each cellular component overlaid on the bright field image. Individual components were assigned as follows: 785 cm^{-1} for DNA, 939 cm^{-1} for carbohydrate, 1006 cm^{-1} for protein, and 1092 cm^{-1} for lipid. The overall component distribution for 435 and 435/BRMS1 appeared very similar, with the exception that 435 has a stronger

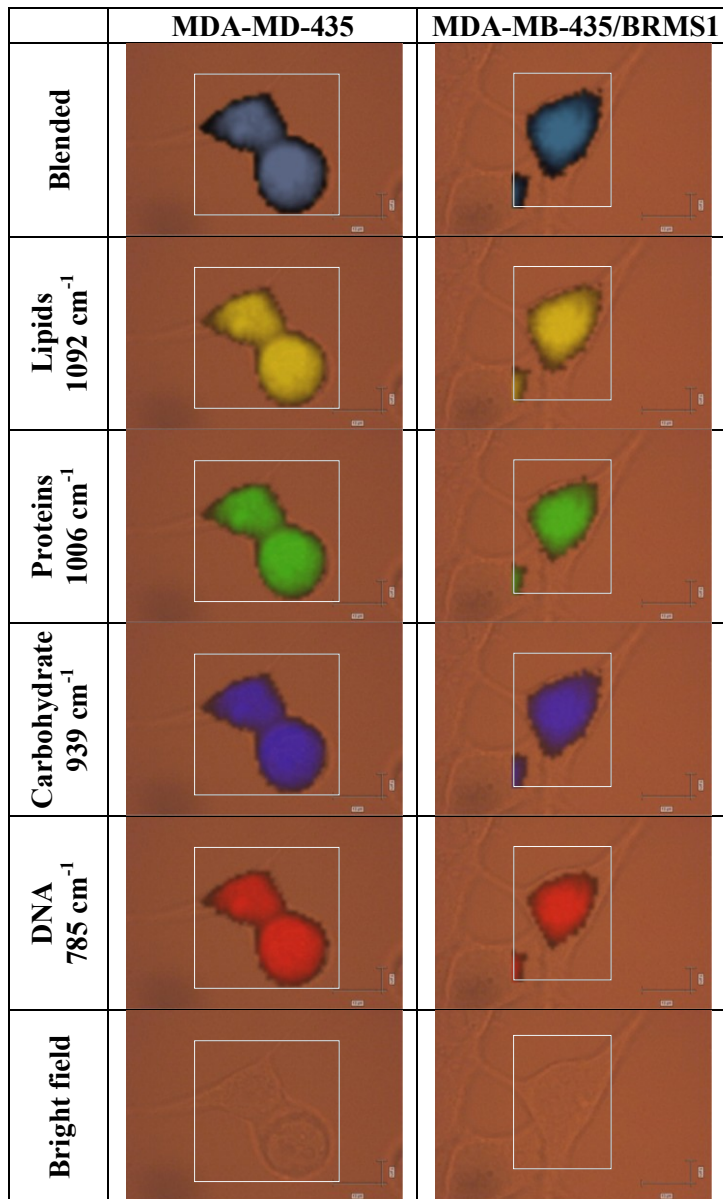


Figure 5.4. Raman mapping of biochemical information for cell line 435 and 435/BRMS1. Different biochemical components were identified by characteristic wavenumbers as follows; DNA (red) – 785 cm^{-1} , carbohydrate (blue) – 939 cm^{-1} , protein (green) – 1006 cm^{-1} , and lipid (yellow) – 1092 cm^{-1} . Scale bar: $10 \mu\text{m}$ (horizontal), $5 \mu\text{m}$ (vertical).

overall intensity than 435/BRMS1. Closer observation for the 435 maps revealed that the attached cell (column 1) has a different spectral intensity when compared to the rounded cell (column 2). This may be attributed to the spatial area distribution of components in a rounded cell compared with an attached cell which has a larger surface area. This could increase the likelihood of motility related proteins and metastatic potential [49].

Conversely for the 435 cell on the right the similarities with 435/BRMS1 is indistinguishable. Based on spatial resolution, Raman mapping gives a 2-D distribution (peak intensity mapping was used) for each of the cellular bio-components.

5.4.5 435 and 435/BRMS1 wound healing and migration rate

ECIS arrays seeded with both 435 cells and 435/BRMS1 cells were monitored over a time course of 50 hours. Figure 5.5 illustrates averaged time profiles of 435 and 435/BRMS1 cultured in separate arrays. During this time, cells were seeded (1) and allowed to attach and proliferate (2). Next each array was wounded (3) and allowed to recover (4) for ~12 hours. Then a second wounding was performed (5) and cells were allowed to continue in culture until termination (6). During the initial growth phase (2), both cell lines appear very similar with the exception of the red profile for 435 cells, which has an overall lower capacitance. After the first wounding (3), there are clear separations between each cell line (4). Replicates of 435 cells return to a lower capacitance level, indicating cell re-population of the working electrode, as compared with 435/BRMS1 which do not fully recover. When the capacitance values were close to the initial baseline values prior to the first wounding (4), a second wounding (5) was performed and the both cell line continued in culture. After the second wounding, there is

a greater separation in relative capacitance values for both 435 and 435/BRMS1 cell lines. This separation indicates that 435 cells recover and re-populate the working electrode versus little to no recovery for 435/BRMS1 cells. From the wound/healing assay, we calculated an average migration rate for 435 of 37 $\mu\text{m}/\text{hour}$ whereas 435/BRMS1 did not recover from the wounding and a migration rate could not be calculated. Similar wound healing results have been reported using traditional scrape assay for 435 and 435/BRMS1 cells and implicate the expression of BRMS1 gene in reduction specific to matrix metalloproteinase (MMP) MMP-9 and MMP-2, which could be responsible for the decreased invasiveness of 435/BRMS1 compared with 435 cells [50]. Another point to consider is the adhesion of each cell line. For the measured capacitance values and resistance values (not shown) for each cell line, 435 reach a greater capacitive low of ≤ 1.5 nF and resistance of 6 k Ω while 435/BRMS1 are around $\leq 2 - 2.5$ nF and 2.1 k Ω .

Figure 5.6 are bright field images from array A for each electrode pre- and post-wounding (profile not shown). Wells A2 – A4 contained 435 cells and A6 – A8 contained 435/BRMS1 cells and medium controls were in A1 and A5. Visually, without trypan blue exclusion or fluorescent staining, it is difficult to distinguish morphological difference between the pre- and post-wounded cells in the wells. However, slight differences were observed for in A4, A6, A7, and A8. Migration rates were not calculated for ECIS data in Figure 5.5, however a second study was conducted and electrode coverage and migration rates were calculated and indicated that there was incomplete electrode coverage and therefore wound/healing migration rates may have been too high

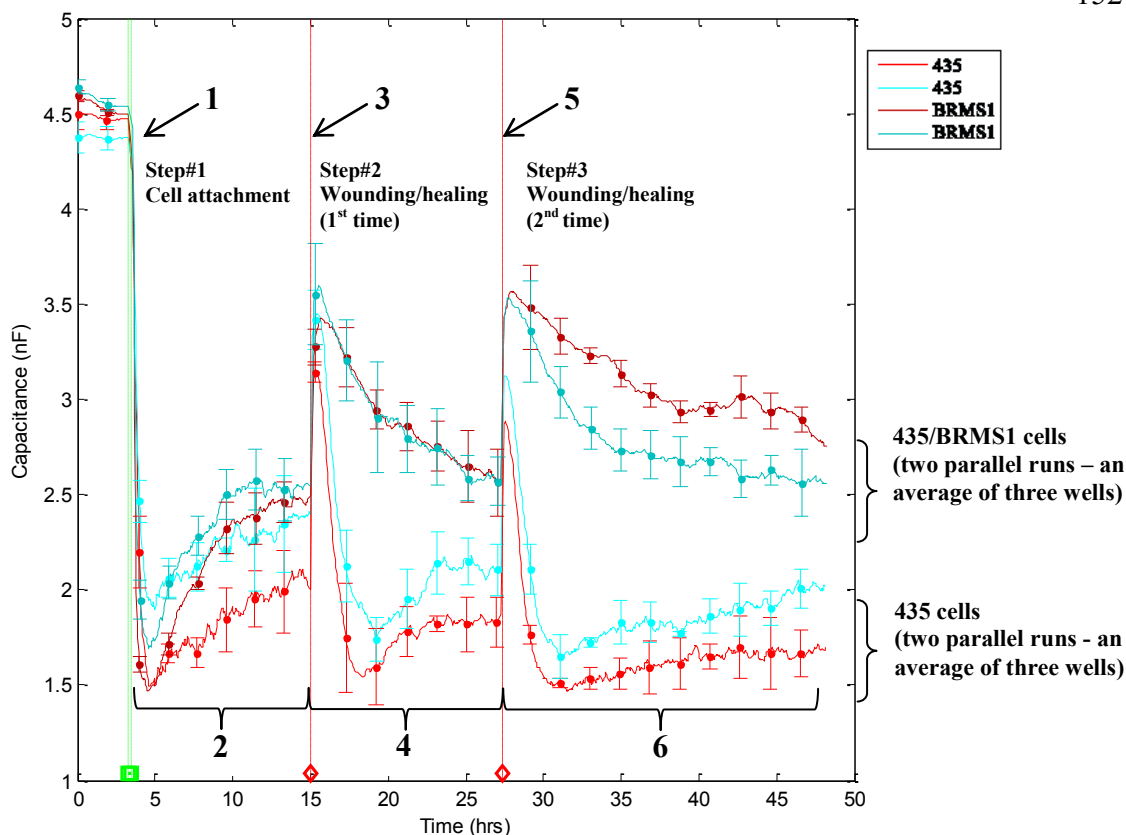


Figure 5.5. Electric cell-substrate impedance sensing (ECIS) of wounding and healing for 435 and 435/BRMS1. Each cell line was seeded, in culture-ware containing integrated electrodes on the substrate, at a final density of 2×10^5 cells/well (1). A confluent layer was allowed to form after initial attachment and proliferation (2). Arrays were charged with a $1400 \mu\text{A}$ pulse for 20 seconds at 60 kHz to wound cells attached on the electrode surface (3), time then allowed for the cell layer to recover – migrate/proliferate back over electrode surface (4). Re-wounding was performed (5) and then more time was allowed for healing (6).

5.4.6 Immuno-fluorescent imaging for F-actin localization in 435 and 435/BRMS1 cells

For cancer cells to successfully metastasize they must complete all the steps starting from invasion through the basement membrane to successful colonization at the secondary site to form micrometastasis followed by macrometastasis. Cytoskeletal

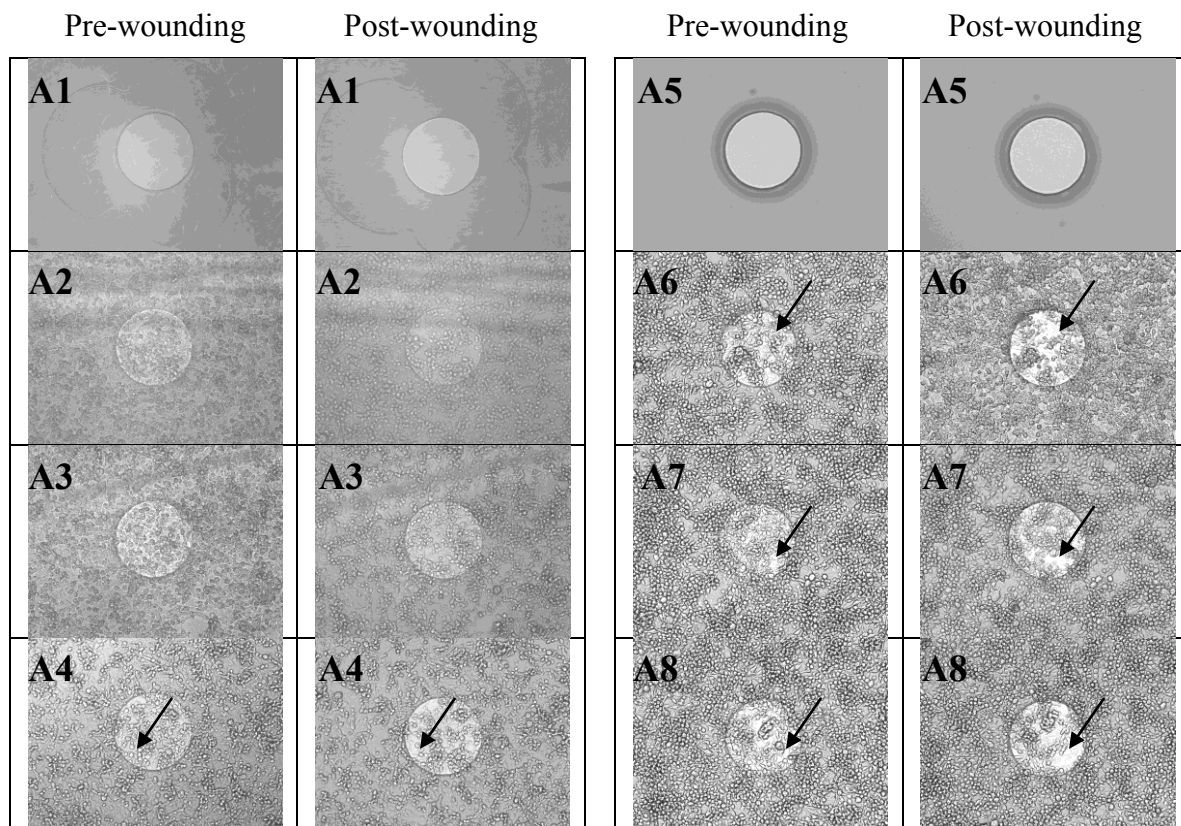


Figure 5.6. Bright field images of array A wells imaged with IX – 71 Olympus Microscope at 10 x magnifications. Well were imaged pre- and post-wounding. Note wells A1 and A5 contained only culture medium, A2, A3, A4 contained 435 cells and A6, A7, A8 contained 435/BRMS1 cells. Arrows indicated areas where cell monolayer has changed after wounding.

reorganization is critical in accomplishing some of these steps; metastatic cells reorganize their F-actin filaments to minimize adhesion to substratum leading to easier dissociation.

Figure 5.7 (A and B) shows the difference in F-actin organization in 435 and 435/BRMS1 cells stained with phalloidin. 435 cells show irregular distribution of F-actin mainly localized on the membrane surface, whereas 435/BRMS1 cells show a more organized cytoskeleton, providing the 435/BRMS1 cells with a stronger attachment to the

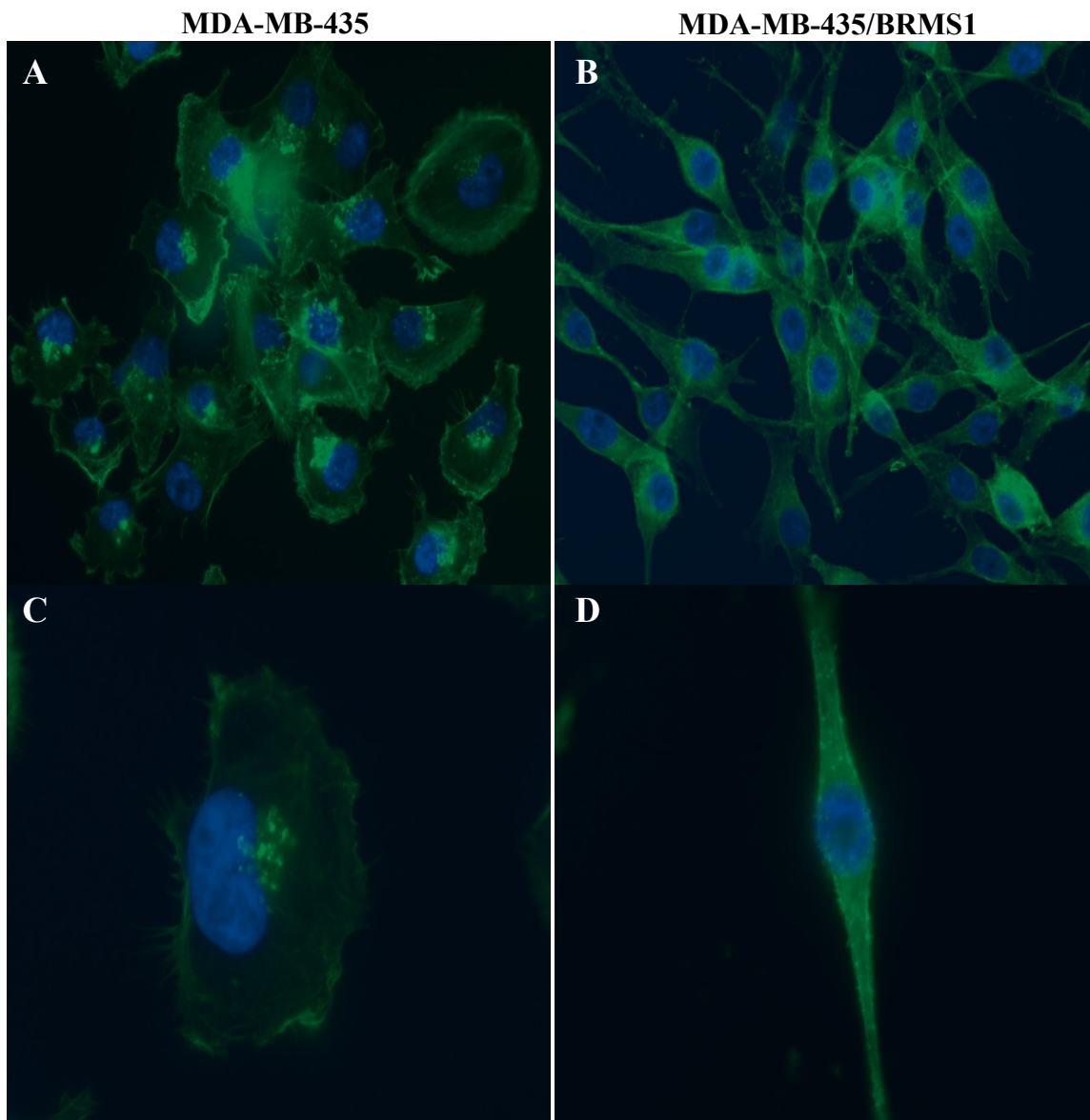


Figure 5.7. F-actin localization in 435 and 435/BRMS1 cells: Cells were cultured on cover slips for 24 hours; F-actin was visualized by phalloidin staining. Multiple cells and single cells were imaged for 435 (A and C) and 435/BRMS1 (B and D).

substratum. This is consistent with the increased adhesion force observed when BRMS1 was expressed in 435 cells. Figure 5.7 (C and D) also shows distinct differences in the morphology of 435 and 435/BRMS1 cells supporting the concept that cytoskeletal

organization determines the shape of the cell. The cell shape observed by fluorescence images is similar to what was observed by AFM and RM images: 435 cells are more round while 435/BRMS1 cells are more elongated.

5.5 DISCUSSION

It is well known that adhesion to the substratum is a critical component in cell survival. However, this requirement is not necessary for cancer cells as they do not undergo anoikis [51]. Unlike normal cells, the adhesion motility of cancer cells is one of the essential factors in the development of cancer cell metastasis [51, 52]. For this reason, cancer cells often possess very low adhesive behavior and a round shape that can facilitate the metastatic process and promote invasion, because a stronger adhesion to the substratum makes these cells too adherent (or “sticky”) to move and migrate [51]. Therefore, the inhibition of motility and the enhancement of adhesion are very important in the clinical treatment of cancer [51, 53, 54].

It has been shown that BRMS1 can suppress the development of metastasis without blocking orthotopic tumor growth [14, 15, 39, 55, 56, 57]. Also, previous work suggested that the mechanism of BRMS1-mediated metastasis suppression might correlate with the secretion of metastasis-associated proteins and/or extracellular matrix effects [39]. Also the expression of BRMS1 in 435 cells probably induced changes in cell adhesion, cytoskeleton rearrangement [14, 39], and suppressed epidermal growth factor receptor (EGFR) expression [15]. Because EGFR can be activated by its specific ligands such as epidermal growth factor (EGF) and transforming growth factor α (TGF α) leading to the growth and spread of tumor [58], down regulation of EGFR by BRMS1 helps suppress metastasis by modulating metastatic-associated phenotypes [52] like cell

migration and adhesion. Our qualitative and quantitative AFM results presented in this study revealed that the expression of BRMS1 in 435 cells, i) altered cell topography from round or elliptical shape to triangular shape, ii) induced membrane cytoskeleton changes from mesh-like to parallel arrangement, iii) resulted in the much rougher cell membrane, and iv) increased membrane surface adhesion force. These alterations in cell topography and the reorganization of sub-cellular structures arising from BRMS1 expression are very likely to play an important role in the decrease of cell mobility and thus demonstrate its role as a metastasis suppressor [59, 60]. Raman microspectroscopy results indicate overall similarity of cell surface biochemical composition in 435 and 435/BRMS1 cells, despite a slightly weaker Raman band intensity that was observed in 435/BRMS1 cells. That means the BRMS1 suppressor gene expression may not significantly change the cellular biochemical compositions (or these changes are not detectable under the current experimental conditions), but may alter the intensities of these biochemical components on the cell surface. ECIS also verified that the 435/BRMS1 cells have a stronger adhesion to the substratum compared to 435 cells. Also, 435 recover more completely from wounding whereas 435/BRMS1 cells do not fully recover. In future studies, it would be useful to verify complete surface coverage (by ECIS modeling and fluorescent staining) and then to extract further parameters of interest (i.e. α and h) to verify morphological/attachment differences between these two related cell lines.

In conclusion, the role of the biomechanical properties of cells in human diseases has been studied considerably in the past decades [1, 2, 3, 4, 61, 62]. Previous studies have demonstrated that malignant cells are less adherent and much softer compared to normal or benign cells [1, 2, 20, 62], which could be used as a “biomechanical marker”

for the development of a new tool for early diagnosis of cancer [1, 2, 3, 4, 62]. As shown in our work, the increase in cell adhesion, cellular spring constant, and Young's modulus, which were associated with the alteration in cytoarchitectures of BRMS1 expressing cells, altogether contributed to the low metastasis ability of 435/BRMS1 cells compared to 435 cells. This study revealed that the expression of BRMS1 altered the physiochemical and biomechanical properties of the parental cell membrane surface and induced an increase in cell adhesion, cell elasticity, and stiffness, suggesting why 435/BRMS1 cells are not metastatic and why 435 cells are metastatic. These findings were consistent with previous observations that non-metastatic cells possessed higher adhesion and stiffer cell membrane than malignant or metastatic cells [1, 2, 7, 20, 62].

5.6 REFERENCES

- [1] S.E. Cross, Y.S. Jin, J. Tondre, R. Wong, J. Rao, J.K. Gimzewski, AFM-based analysis of human metastatic cancer cells. *Nanotechnol.* 19 (2008) 384003-384011.
- [2] S.E. Cross, Y.S. Jin, J. Rao, J.K. Gimzewski, Nanomechanical analysis of cells from cancer patients. *Nat. Nanotechnol.* 2 (2007) 780-783.
- [3] S. Suresh, Nanomedicine - elastic clues in cancer detection. *Nat. Nanotechnol.* 2 (2007) 748-749.
- [4] S. Suresh, Biomechanics and biophysics of cancer cells. *Acta Biomater.* 3 (2007) 413-438.
- [5] C. Kendall, M. Isabelle, F. Bazant-Hegemark, J. Hutchings, L. Orr, J. Babrah, R. Baker, N. Stone, Vibrational spectroscopy: a clinical tool for cancer diagnostics. *Analyst* 134 (2009) 1029-1045.
- [6] C.X. Yu, E. Gestl, K. Eckert, D. Allara, J. Irudayaraj, Characterization of human breast epithelial cells by confocal Raman micro spectroscopy. *Cancer Detect. Prev.* 30 (2006) 515-522.
- [7] Q.S. Li, G.Y. Lee, C.N. Ong, C.T. Lim, AFM indentation study of breast cancer cells. *Biochem. Biophys. Res. Commun.* 374 (2008) 609-613.

- [8] R. Cailleau, M. Olive, Q.V. Cruciger, Long-term human breast carcinoma cell lines of metastatic origin: preliminary characterization. *In Vitro* 14 (1978) 911-915.
- [9] M.J. Seraj, R.S. Samant, M.F. Verderame, D.R. Welch, Functional evidence for a novel human breast carcinoma metastasis suppressor, BRMS1, encoded at chromosome 11q13. *Cancer Res.* 60 (2000) 2764-2769.
- [10] R.S. Samant, M.J. Seraj, M.M. Saunders, T.S. Sakamaki, L.A. Shevde, J.F. Harms, T.O. Leonard, S.F. Goldberg, L. Budgeon, W.J. Meehan, C.R. Winter, N.D. Christensen, M.F. Verderame, H.J. Donahue, D.R. Welch, Analysis of mechanisms underlying BRMS1 suppression of metastasis. *Clin. Exp. Metastas.* 18 (2001) 683-693.
- [11] L.J. Stafford, K.S. Vaidya, D.R. Welch, Metastasis suppressors genes in cancer. *Int. J. Biochem. Cell. Biol.* 40 (2008) 874-891.
- [12] M.D. Edmonds, D.R. Hurst, K.S. Vaidya, L.J. Stafford, D. Chen, D.R. Welch, Breast cancer metastasis suppressor 1 coordinately regulates metastasis-associated microRNA expression. *Int. J. Cancer* (2009) 1778-1785.
- [13] W.J. Meehan, D.R. Welch, Breast cancer metastasis suppressor 1: update. *Clin. Exp. Metastas.* 20 (2003) 45-50.
- [14] D.B. DeWald, J. Torabinejad, R.S. Samant, D. Johnston, N. Erin, J.C. Shope, Y. Xie, D.R. Welch, Metastasis suppression by breast cancer metastasis suppressor 1 involves reduction of phosphoinositide signaling in MDA-MB-435 breast carcinoma cells. *Cancer Res.* 65 (2005) 713-717.
- [15] K.S. Vaidya, S. Harihar, P.A. Phadke, L.J. Stafford, D.R. Hurst, D.G. Hicks, G. Casey, D.B. DeWald, D.R. Welch, Breast cancer metastasis suppressor-1 differentially modulates growth factor signaling. *J. Biol. Chem.* 283 (2008) 28354-28360.
- [16] R.S. Samant, D.W. Clark, R.A. Fillmore, M. Cicek, B.J. Metge, K.H. Chandramouli, A.F. Chambers, G. Casey, D.R. Welch, L.A. Shevde, Breast cancer metastasis suppressor 1 (BRMS1) inhibits osteopontin transcription by abrogating NF-kappaB activation. *Mol. Cancer* 6 (2007) 1-6.
- [17] M. Cicek, R. Fukuyama, D.R. Welch, N. Sizemore, G. Casey, Breast cancer metastasis suppressor 1 inhibits gene expression by targeting nuclear factor-kappaB activity. *Cancer Res.* 65 (2005) 3586-3595.
- [18] M.M. Saunders, M.J. Seraj, Z. Li, Z. Zhou, C.R. Winter, D.R. Welch, H.J. Donahue, Breast cancer metastatic potential correlates with a breakdown in homospecific and heterospecific gap junctional intercellular communication. *Cancer Res.* 61 (2001) 1765-1767.

- [19] S.E. Cross, Y.S. Jin, J. Tondre, R. Wong, J. Rao, J.K. Gimzewski, AFM-based analysis of human metastatic cancer cells. *Nanotechnology* 19 (2008) 384003-384008.
- [20] M. Lekka, P. Laidler, D. Gil, J. Lekki, Z. Stachura, A.Z. Hryniewicz, Elasticity of normal and cancerous human bladder cells studied by scanning force microscopy. *Eur. Biophys. J. Biophys.* 28 (1999) 312-316.
- [21] W.A. Lam, M.J. Rosenbluth, D.A. Fletcher, Chemotherapy exposure increases leukemia cell stiffness. *Blood* 109 (2007) 3505-3508.
- [22] J. Ling, S.D. Weitman, M.A. Miller, R.V. Moore, A.C. Bovik, Direct Raman imaging techniques for study of the subcellular distribution of a drug. *Appl. Opt.* 41 (2002) 6006-6017.
- [23] D.W. Ball, Theory of Raman Spectroscopy. *Spectroscopy* 16 (2001) 32-34.
- [24] D. Pappas, B.W. Smith, J.D. Winefordner, Raman spectroscopy in bioanalysis. *Talanta* 51 (2000) 131-144.
- [25] P. Carey, Raman spectroscopy for the analysis of biomolecules. *Trac-Trend Anal. Chem.* 2 (1983) 275-277.
- [26] P. Hildebrandt, S. Lecomte, C.L. John, Biochemical Applications of Raman Spectroscopy, in *Encyclopedia of Spectroscopy and Spectrometry*, Elsevier, Oxford, 1999, pp. 88-97.
- [27] H. Fabian, P. Anzenbacher, New developments in Raman spectroscopy of biological systems. *Vib. Spectrosc.* 4 (1993) 125-148.
- [28] J.R. Baena, B. Lendl, Raman spectroscopy in chemical bioanalysis. *Curr. Opin. Chem. Biol.* 8 (2004) 534-539.
- [29] F.M. Lyng, E.Ó. Faoláin, J. Conroy, A.D. Meade, P. Knief, B. Duffy, M.B. Hunter, J.M. Byrne, P. Kelehan, H.J. Byrne, Vibrational spectroscopy for cervical cancer pathology, from biochemical analysis to diagnostic tool. *Exp. Mol. Pathol.* 82 (2007) 121-129.
- [30] C.M. Krishna, G.D. Sockalingum, G. Kegelaer, S. Rubin, V.B. Kartha, M. Manfait, Micro-Raman spectroscopy of mixed cancer cell populations. *Vib. Spectrosc.* 38 (2005) 95-100.
- [31] K.W. Short, S. Carpenter, J.P. Freyer, J.R. Mourant, Raman spectroscopy detects biochemical changes due to proliferation in mammalian cell cultures. *Biophys. J.* 88 (2005) 4274-4288.
- [32] H. Abramczyk, J. Surmacki, B. Brozek-Pluska, Z. Morawiec, M. Tazbir, The hallmarks of breast cancer by Raman spectroscopy. *J. Mol. Struct.* 924-926 (2009) 175-182.

- [33] I. Notingher, Raman spectroscopy cell-based biosensors. *Sensors* 7 (2007) 1343-1358.
- [34] S.B. Velegol, B.E. Logan, Contributions of bacterial surface polymers, electrostatics, and cell elasticity to the shape of AFM force curves. *Langmuir* 18 (2002) 5256-5262.
- [35] M. Arnoldi, M. Fritz, E. Bauerlein, M. Radmacher, E. Sackmann, A. Boulbitch, Bacterial turgor pressure can be measured by atomic force microscopy. *Phys. Rev. E* 62 (2000) 1034-1044.
- [36] H.J. Butt, B. Cappella, M. Kappl, Force measurements with the atomic force microscope: technique, interpretation and applications. *Surf. Sci. Rep.* 59 (2005) 1-152.
- [37] M.J. Rosenbluth, W.A. Lam, D.A. Fletcher, Force microscopy of nonadherent cells: A comparison of leukemia cell deformability. *Biophys. J.* 90 (2006) 2994-3003.
- [38] A. Savitzky, M.J.E. Golay, Smoothing and Differentiation of Data by Simplified Least Squares Procedures. *Anal. Chem.* 36 (1964) 1627-1639.
- [39] P.J. Champine, J. Michaelson, B.C. Weimer, D.R. Welch, D.B. DeWald, Microarray analysis reveals potential mechanisms of BRMS1-mediated metastasis suppression. *Clin. Exp. Metastas.* 24 (2007) 551-565.
- [40] T.A. Camesano, B.E. Logan, Probing bacterial electrosteric interactions using atomic force microscopy. *Environ. Sci. Technol.* 34 (2000) 3354-3362.
- [41] W.F. Heinz, J.H. Hoh, Spatially resolved force spectroscopy of biological surfaces using the atomic force microscope. *Trends Biotechnol.* 17 (1999) 143-150.
- [42] S.Y. Lin, M.J. Li, W.T. Cheng, FT-IR and Raman vibrational microspectroscopies used for spectral biondiagnosis of human tissues. *Spectrosc. Int. J.* 21 (2007) 1-30.
- [43] C.J. Frank, R.L. McCreery, D.C.B. Redd, Raman-spectroscopy of normal and diseased human breast tissues. *Anal. Chem.* 67 (1995) 777-783.
- [44] M.V.P. Chowdary, K.K. Kumar, J. Kurien, S. Mathew, C.M. Krishna, Discrimination of normal, benign, and malignant breast tissues by Raman spectroscopy. *Biopolymers* 83 (2006) 556-569.
- [45] S. Verrier, I. Notingher, J.M. Polak, L.L. Hench, In situ monitoring of cell death using Raman microspectroscopy. *Biopolymers* 74 (2004) 157-162.
- [46] Z. Movasaghi, S. Rehman, I.U. Rehman, Raman spectroscopy of biological tissues. *Appl. Spectrosc. Rev.* 42 (2007) 493-541.

- [47] D. Naumann, Infrared and NIR Raman spectroscopy in medical microbiology, in Proc. SPIE (1998) 245-257.
- [48] A. Mantovani, Cancer: inflaming metastasis. *Nature* 457 (2009) 36-37.
- [49] M.R. Ray, D.M. Jablons, Hallmarks of metastasis, in Lung Cancer Metastasis, (2009) 29-46.
- [50] S.M. Baker, Metastasis Suppression in Carcinoma and Melanoma Cells. Undergraduate honors theses. Paper 41. (2010) 1-23.
- [51] M.T. Debies, D.R. Welch, Genetic basis of human breast cancer metastasis. *J. Mammary Gland Biol.* 6 (2001) 441-451.
- [52] S. Zhang, Q.D. Lin, W. Di, Suppression of human ovarian carcinoma metastasis by the metastasis-suppressor gene, BRMS1. *International J. Gynecol. Cancer* 16 (2006) 522-531.
- [53] J.M. Kirstein, K.C. Graham, L.T. MacKenzie, D.E. Johnston, L.J. Martin, A.B. Tuck, I.C. MacDonald, A.F. Chambers, Effect of anti-fibrinolytic therapy on experimental melanoma metastasis. *Clin. Exp. Metastas.* 26 (2009) 121-131.
- [54] L. Lu, F. Payvandi, L. Wu, L.H. Zhang, R.J. Hariri, H.W. Man, R.S. Chen, G.W. Muller, C.C.W. Hughes, D.I. Stirling, P.H. Schafer, J.B. Bartlett, The anti-cancer drug lenalidomide inhibits angiogenesis and metastasis via multiple inhibitory effects on endothelial cell function in normoxic and hypoxic conditions. *Microvasc. Res.* 77 (2009) 78-86.
- [55] C.W. Rinker-Schaeffer, J.P. O'Keefe, D.R. Welch, D. Theodorescu, Metastasis suppressor proteins: discovery, molecular mechanisms, and clinical application. *Clin. Cancer Res.* 12 (2006) 3882-3889.
- [56] L.A. Shevde, D.R. Welch, Metastasis suppressor pathways--an evolving paradigm. *Cancer Lett.* 198 (2003) 1-20.
- [57] P.S. Steeg, Metastasis suppressors alter the signal transduction of cancer cells. *Nat. Rev. Cancer* 3 (2003) 55-63.
- [58] R. Singh, P. Lei, S.T. Andreadis, PKC-delta binds to E-cadherin and mediates EGF-induced cell scattering. *Exp. Cell. Res.* (2009) 2899-2913.
- [59] K. Bhadriraju, L.K. Hansen, Extracellular matrix- and cytoskeleton-dependent changes in cell shape and stiffness. *Exp. Cell. Res.* 278 (2002) 92-100.
- [60] D. Yamazaki, S. Kurisu, T. Takenawa, Regulation of cancer cell motility through actin reorganization. *Cancer Sci.* 96 (2005) 379-386.
- [61] C. Brunner, A. Niendorf, J.A. Kas, Passive and active single-cell biomechanics: a new perspective in cancer diagnosis. *Soft Matter* 5 (2009) 2171-2178.

- [62] N. Bao, Y.H. Zhan, C. Lu, Microfluidic electroporative flow cytometry for studying single-cell biomechanics. *Anal. Chem.* 80 (2008) 7714-7719.

CHAPTER 6**TOXIC EFFECTS OF DIESEL EXHAUST PARTICLES AND ANTI-OXIDANT
PROTECTIVE ACTIVITIES ON HUMAN LUNG EPITHELIAL CELLS:
ENHANCED STUDIES USING ELECTRIC-CELL SUBSTRATE IMPEDANCE
SENSING AND RAMAN MICROSPECTROSCOPY⁵****6.1 ABSTRACT**

Research using epithelial cell lines is required to understand underlying mechanisms which lead to abnormalities that cause airway or pulmonary disease. A novel arrangement of electric cell-substrate impedance sensing (ECIS) and Raman microspectroscopy (RM) was used to explore cytotoxic response in A549 cell line exposed to diesel exhaust particles (DEP). For ECIS, ≤ 10 -fold DEP concentration (≤ 100 $\mu\text{g/ml}$) exposure caused clastogenic DNA degradation whereas ≥ 25 -fold DEP (≥ 250 $\mu\text{g/ml}$) exposure caused cytotoxic results compare to 10 $\mu\text{g/ml}$ DEP. 10 μM treatments of the natural phytoalexin, resveratrol (RES), showed minimal to mild protection against DEP before and after exposure and aided in improving injury recovery. RM also revealed decreases in nucleic acid and protein specific Raman bands. In conclusion, our setup with A549 proved useful for cytotoxic response to DEP exposure and we report a reproducible method to study cell attachment and proliferation, and biochemical changes with respect to culture time.

⁵ Figures 6.28 – 6.31 used with permission from Mingjie Tang

6.2 INTRODUCTION

Cell death mechanisms can be classified as either necrotic or accidental and as apoptotic or programmed [1]. Over the past three decades, the interest in apoptosis has gained attention based on the cascade of events that can be manipulated to trigger this natural programmed pathway for cell death. In apoptosis studies, at the cellular level, cytotoxic and genotoxic effects are generally studied utilizing either fluorescence staining techniques with *in vivo* or *in vitro* studies and also incorporated with flow cytometry [2]. Cytotoxicity refers to the state or quality of being toxic to mammalian cells. Whereas genotoxicity refers to the degree, to which, something will damage or mutate DNA. Common staining techniques require cells to be stained while live and then fixed as dead to then image using microscopy. Although fluorescent staining techniques offer specific advantages; there are disadvantages to these terminal type studies. Electric cell-substrate impedance sensing (ECIS) offers a non-invasive approach to monitor cell behavior. Alternatively, Raman microspectroscopy (RM) is a non-destructive vibration spectroscopy technique that may offer a real-time method to monitor cellular viability. This work investigated the feasibility of utilizing ECIS and RM to monitor cell behavior and biochemical changes with respect to culture time versus DEP exposure and RES treatment.

6.3 ELECTRIC CELL-SUBSTRATE IMPEDANCE SENSING

Invented in 1984 [3] and commercially introduced in 1991 [4], ECIS is an electrical method used to observe mammalian cell behavior. Monitored behaviors include cell mobility, adhesion, and other cytoskeleton mediated activities. More than a decade ago ECIS was introduced to monitor cell attachment and cell spreading on

artificial surfaces in real time and wound healing [5]. ECIS has also been used in numerous studies, for example cytotoxicity has been monitored, as a function of time and concentration, for the inhibitors: cadmium chloride, sodium arsenate, and benzalkonium chloride were compared to a standard neutral red assay [6] with good agreement. Xiao *et al.* showed that exposure to these toxicants made attached cells die and/or detach from the ECIS electrode, which correspond to a decrease in the measured capacitance.

Another study focused on wound-healing initiated and monitored by ECIS as compared to traditional “scrap” wounding studies [7]. It was found that wounding cells using ECIS is highly reproducible and can quantitatively measure cell line migration rates. More recently ECIS illustrated important differences in airway epithelial cell types [8]. The most remarkable aspect of this study was that each of the four cell lines (16HBE14o-, BEAS-2B, NCI-H292, and A549) has distinct phenotypic differences for the adhesion/spreading, barrier function, and wounding healing as measured with ECIS.

These differences divide the cell lines into good candidates for either barrier function studies (16HBE14o-) or cell-matrix translational research (BEAS-2B and A549) [8]. A mini-review of ECIS as a non-invasive technique to study cancer cells addressed the importance of advantages for cancer biology and drug discovery [9]. Hong *et al.* further recognized how label-free and non-invasive measurements can be integrated with standard end-point assays to have both optical and electrochemical observations. Our studies targeted this type of application and focused on the cytotoxic effects of diesel exhaust particles (DEP) on confluent layers of A549 cells. Further, we observed the inhibitory (hence forth termed “protective”) effect of resveratrol against premature cell death for both DEP treated and untreated A549 cells.

ECIS electrode arrays (8W10E and 8W10E+) were obtained from Applied BioPhysics (ABP, NY, USA). Each array slide consisted of eight individually addressable wells with modified surface for mammalian cell culture. On each well base, there were either 1 (8W1E) or <10 (8W10E+) active electrodes and one large counter electrode. Wells contained a maximum fluidic volume of $\sim 600 \mu\text{l}$ and $\sim 0.8 \text{ cm}^2$ substrate for active cell culture [7].

Some of our ECIS experiments utilized 8W10E+ arrays (Figure 6.1-A). The 8W10E+ arrays contain a total of 40 electrodes per well or two sets of 20 circular $250 \mu\text{m}$ diameter active electrodes. These arrays are generally useful to monitor extracellular matrix (ECM) protein interactions, barrier function measurements (modeling), and cell proliferation. We also decided to utilize 8W1E arrays (Figure 6.1-B), which contain a single $250 \mu\text{m}$ diameter active electrode and are useful in measuring cell migration via wound healing, agent effects on cell motion and morphology, and correlated microscopy/ECIS experiments. The 8W1E arrays measure approximately 50 – 100 cells in a confluent layer whereas the 8W10E+ array measures approximately 1000 – 2000 cells. Another advantage of the 8W1E array is that they reveal increased details of

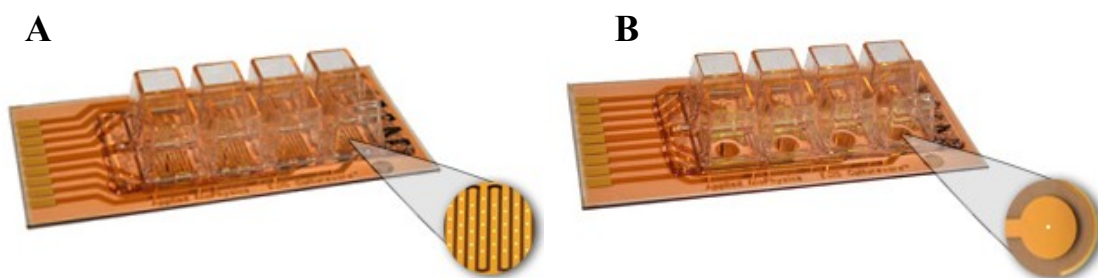


Figure 6.1. An 8W10E+ array containing >40 working electrodes (A) compared with 8W1E array that has a single working electrode (B) [images courtesy of ABP, NY, USA].

cellular mobility (compare signal-to-noise in an 8W1E array (Figure 6.7) to an 8W10E+ array (Figure 6.4)) as these arrays are not an average of multiple electrodes, but a measurement of one working electrode.

As stated in previous chapters, RM is a nondestructive vibrational classification routine that can be utilized to identify characteristic spectroscopic fingerprints of living cells based on chemical compositions and molecular structures [10]. Briefly, Raman spectral frequencies are recorded in wavenumber units which are proportional to vibrational energies based on molecular polarizability [11]. Many former RM studies focused mainly on physical and structural investigations. Over the past few decades, due to advances within instrumentation design [12, 13], biological applications [14, 15], and methods for biochemical information extraction [16, 17], RM has exhibited increased popularity in the field of mammalian cell biology [18, 19]. Short *et al.* demonstrated the use of RM to detect biochemical changes, in tumorigenic versus non-tumorigenic cells, as a result of proliferation [20]. More recently, Abramczyk *et al.* reported the hallmarks of normal, malignant, benign breast tissue characterized by Raman studies [21]. Several other studies reported the appearance of cellular biopolymers (including DNA/RNA, lipids, proteins, and carbohydrates) in cell growth [17, 19, 22]. As RM has increased in popularity, new analysis routines have emerged to extract useful information from Raman spectra. Advances have been made to obtain Raman scatter from inherent background fluorescence through automation [23, 24], while other groups move toward an automated pre- and post-processing routine to eliminate natural user variability [25] and categorize Raman spectra [26]. Also new and emerging methods have been explored to enhance the usefulness of Raman spectral maps/images. Principal component analysis (PCA) has

been used to evaluate maps of freeze dried and living cells [27]. Ling *et al.* demonstrated image processing algorithms to restore Raman image degradation in the study of anticancer drug distribution within living cells [10]. When key molecular components are used, RM becomes a powerful tool for rapid characterization of normal and transformed breast epithelial cell-lines [19] and multivariate analysis classification models can discriminate normal from abnormal tissue in cervical cancer progression [17]. We employed RM to track changes in DNA/RNA, lipids, proteins, and carbohydrates during cell growth and treatment with DEP and RES.

6.4 MATERIAL AND METHODS

6.4.1 Chemicals

DEP was a generous gift from Dr. Daniel Costa and Dr. Ian Gilmour from the U.S. EPA National Health and Environmental Effects Research Laboratory (NEERL). A DEP stock was prepared fresh for each experiment by dissolving 8 mg DEP in 80 μ l methanol and sonicate for 15 minutes at room temperature and then adding 1920 μ l fresh culture medium. A 20 μ M resveratrol (CAS: 501-36-0, Sigma, St. Louis, MO, USA) stock solution was prepared daily in fresh culture medium. Earle's balanced salt solution (EBSS) was prepared as described previously [28].

6.4.2 Cell culture

Human (*Homo sapiens*) lung carcinoma A549 cells (ATCC, USA) were cultured in F-12K medium (Gibco F12K #21127, Invitrogen) containing 10% fetal bovine serum (FBS) (HyClone, UT, USA) at 37 °C with 5% CO₂ in a humidified atmosphere. Cells were sub-cultured at 80-90% confluency and used for experiments. No antibiotics or antimycotics were used in cell cultures.

6.4.3 Electric cell-substrate impedance sensing

Briefly, ECIS arrays were prepared, prior to use, according to the following steps: 200 μ l of pre-warmed gelatin solution (0.15 M NaCl + 1000 μ g/ml) was added to each well for 10 minutes or 10 mM L-cysteine in water (Electrode-stabilizing Solution, ABP, NY, USA) was added to each well for 15 minutes, electrodes were then rinsed with 400 μ l of 0.15 M NaCl solution, and 200 μ l of serum containing culture medium (Gibco F12K #21127, Invitrogen) was added to each well. Electrode arrays were then placed in an array holder (ECIS Z0, ABP, NY, USA), incubated at 37 °C and 5% CO₂ while an electrode stabilization was performed using the ABP ECIS monitoring software. After stabilization, electrode arrays were monitored for an additional 30 minutes to verify proper electrode baseline prior to seeding with A549 cells. To seed, arrays were placed on a heating block (37 °C \pm 1 °C) within a laminar flow hood and inoculated with a 200 μ l suspension of 5×10^5 cells/ml to yield a final concentration of 2×10^5 cells/well (400 μ l total solution per well). Arrays were then returned to incubated electrode holder and monitored appropriately for each experiment. All additional treatments were performed aseptically in a laminar flow hood.

6.4.4 Cell viability staining

The live/dead viability/cytotoxicity kit was obtained from Molecular Probes (Eugene, OR, USA). Samples were prepared post-ECIS measurement by incubating arrays in EBSS containing 2 μ M calcein AM and 4 μ M ethidium homodimer-1 for 30 minutes at room temperature. Dye solution was then replaced with Earle's buffered salt solution (EBSS) for fluorescence microscopy.

6.4.5 Raman microspectroscopy

Raman spectra were acquired using a Renishaw inVia Raman spectrometer (WiRE 3.0 software) connected to a Leica microscope (Leica DMLM). The spectrometer was equipped with a 785 nm near-IR laser (laser spot 3 x 3 μm) that was focused through a 63x NA = 0.90 water immersion objective. The spectrometer was calibrated with silicon at a static spectrum centered at 520.5 cm^{-1} for 1 second. Samples of A549, were cultured, on 13 mm magnesium fluoride optic windows, to ~65-80% confluent and then transferred into a 50 mm glass Petri dish lined with an inert reflective metal substrate. Spectra were collected in static mode for 2 accumulation at 20 s laser exposure over a wavenumber range of 600 – 1800 cm^{-1} for cells and culture media at the same focal plane [29]. If necessary, Cosmic Ray Removal (CRR) was performed and four spectra per location (nucleus, cytoplasm, membrane, and background) for each cell were imaged. Then four cells were averaged (16 total spectra per location) for the A549 cells and background. Spectra were then analyzed over a range of ~600 – 1800 cm^{-1} .

6.4.6 Raman data processing

Raman spectra are affected by physical properties of the samples and other noises, therefore, it was necessary to use a mathematical process to reduce systematic noises and enhance resolution of the chemical compositions from the target cells. Raman spectra were smoothed by a moving average smoothing filter for high-frequency noises. Then the second derivative of the smoothed spectra was used to eliminate baseline drift and background interferences. This data processing method can help distinguish overlapping peaks and improve the resolution and sensitivity of the spectra.

The Raman spectral data include an array of ~1300 cross-sensitive variables which contain overlapping spectral information. Multivariate data analysis was employed to overcome these inherent difficulties of data analysis. Our approach utilized principal component analysis (PCA) which make it possible to extract useful information from a sample, and eliminate overlapping information [30, 31]. In this work, we utilized a PCA method based on moving average smoothing and second derivative pre-processing to extract the main information from raw spectral data. Then we used an unsupervised Ward's hierarchical cluster analysis (HCA) with Euclidean distances [32] to qualitatively examine the differences among cell location and the DEP and DEP/RES treated and untreated groups versus culture time. All algorithms were implemented in MATLAB V7.1 (MathWorks, USA) in Windows XP.

6.5 RESULTS AND DISCUSSION

Due to the amounts of tables and figures used to describe the ECIS experiments reported hence forth, Table 6.1 briefly outlines the major distinctions in section 6.5.1 and 6.5.2. Individual results direct the reader to comparable studies placed in Appendix D.

Table 6.1. Sectional overview for the ECIS experimental setup.

Section		Array Type		Treatment		Wounding		Average wells	
6.5.1	6.5.2	8W1E	8W10E+	DEP	RES	Array A	Array B	Yes	No
1			x	x				x	
2			x	x	x	x	x		x
3		x		x	x				x
4		x		x		x	x	x	
5		x		x	x			x	
6		x		x	x	x		x	
	1		x	x				x	
	2		x	x	x	x	x		x
	3	x		x	x		x	x	

6.5.1 Approach #1 – Sequential array modification

6.5.1.1 Multi-electrode monitoring of methanol treated versus DEP exposed cells

Because DEP is insoluble in culture medium we had to dissolve them in methanol (1.6.1). We first decided to evaluate the toxicity of increasing amounts of methanol to determine if it would be a good solvent for DEP. Cell seeding densities and methanol concentrations are listed in Table 6.2, where text color corresponds to profile color. Figure 6.2 illustrates the averaged normalized capacitance measured at 64 kHz from two 8W10E+ arrays. The time profiles are an average of two wells and show the impedance of A549 cells inoculated in 14 identical wells with 2 control wells (Table 6.2). Insert in Figure 6.2 represents the ECIS array configuration for array A and B and well color also correlates to profile color. Approximately 2×10^5 cells/well were inoculated at zero hour and allowed to settle, attach and proliferate on the bottom of each well. When a confluent layer of cells was established (≤ 25 hours), each well was treated with culture medium mixed with increasing amounts of methanol (≥ 25 hours, see Table 6.2). After

Table 6.2. Array seeding density and treatment for array A and B in Figure 6.2.

A1 – 2×10^5 cells/well (media only)	B1 – 2×10^5 cells/well (media only)
A2 – 2×10^5 cells/well (0.02% MTH + media)	B2 – 2×10^5 cells/well (0.02% MTH + media)
A3 – 2×10^5 cells/well (0.05% MTH + media)	B3 – 2×10^5 cells/well (0.05% MTH + media)
A4 – 2×10^5 cells/well (0.2% MTH + media)	B4 – 2×10^5 cells/well (0.2% MTH + media)
A5 – 2×10^5 cells/well (0.5% MTH + media)	B5 – 2×10^5 cells/well (0.5% MTH + media)
A6 – 2×10^5 cells/well (1.0% MTH + media)	B6 – 2×10^5 cells/well (1.0% MTH + media)
A7 – 2×10^5 cells/well (2.0% MTH + media)	B7 – 2×10^5 cells/well (2.0% MTH + media)
A8 – media only (media only)	B8 – media only (media only)

treatment with methanol, the cells continue in culture until ~50 hours. Next cells were wounded (50 hours – red dashed line) at 60 kHz and 5000 μ A for 20 seconds and then allowed to recover until ~90 hours.

From the experimental setup outlined in Table 6.2 and illustrated in Figure 6.2, we observe that increasing concentrations of methanol are not immediately toxic to A549 cells after cell attachment on the ECIS electrode working surface (~20 – 25 hours, compare Figure D6.32 Appendix). The arrow in Figure 6.2 indicates increasing concentration of methanol. In Figure 6.2 at 50 hours the adherent cells were wounded and allowed to recover until 90 hours. Because the capacitance signal does not return to the previous capacitance plateau baseline, prior to wounding, the cells do not fully recover from the wounding assay (\geq 50 hours). Furthermore, the increased capacitance, post wounding, indicates facilitated electron flow at the working surface of the ECIS electrode and hence a non-confluent layer of cells, implicating cell death, compromised integrity, and detachment. In this case, cell death is likely caused by nutrient metabolite depletion accompanied with toxic byproduct accumulation along with culture medium evaporation and perhaps medium component degradation.

Figure 6.3 illustrates uniform seeding and attachment (0 – 28 hours) followed by DEP treatment (28 hours, see Table 6.3 for increasing concentrations), and then cells continued in culture until termination (29 – 52 hours).

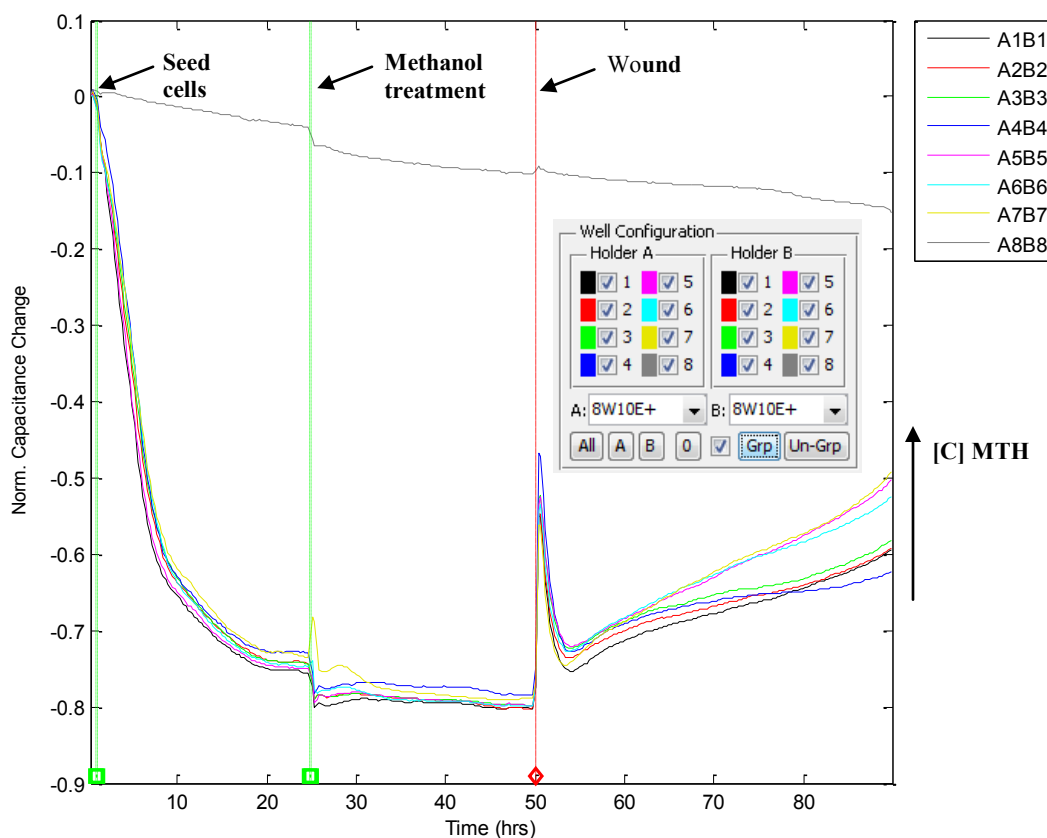


Figure 6.2. Two 8W10E+ arrays were seeded with 2×10^5 cells/well (A1 – A7 and B1 – B7) with control wells containing culture medium (A8 and B8). When the cells were confluent at ~ 25 hours an increasing amount of methanol was added to each well, and then at 50 hours wells were wounded (60 kHz, 5000 μ A, for 20 sec) and allowed to recover. The experiment was performed twice with similar results. Legend “AnBn” refers to averaging the responses in duplicate wells An and Bn (where n = 1, 2, 3 ... 8 see insert of well configuration).

The arrow in Figure 6.3 indicates increasing concentration of DEP. The highest three concentrations (250, 500, and 1000 μ g/ml) tend to disrupt the confluent cells as illustrated by increasing capacitance values (29 – 52 hours). The middle concentration (100 μ g/ml) also affects the cells as indicated by an increase in capacitance compared to the lower concentrations (10 and 25 μ g/ml), which do not seem to affect the adherent

Table 6.3. Array seeding density and treatment for array A and B in Figure 6.3.

A1 – 2×10^5 cells/well	(media only)	B1 – 2×10^5 cells/well	(media only)
A2 – 2×10^5 cells/well	(0.01% MTH/10 $\mu\text{g/ml}$ DEP + media)	B2 – 2×10^5 cells/well	(0.01% MTH/10 $\mu\text{g/ml}$ DEP + media)
A3 – 2×10^5 cells/well	(0.025% MTH/25 $\mu\text{g/ml}$ DEP + media)	B3 – 2×10^5 cells/well	(0.025% MTH/25 $\mu\text{g/ml}$ DEP + media)
A4 – 2×10^5 cells/well	(0.1% MTH/100 $\mu\text{g/ml}$ DEP + media)	B4 – 2×10^5 cells/well	(0.1% MTH/100 $\mu\text{g/ml}$ DEP + media)
A5 – 2×10^5 cells/well	(0.25% MTH/250 $\mu\text{g/ml}$ DEP + media)	B5 – 2×10^5 cells/well	(0.25% MTH/250 $\mu\text{g/ml}$ DEP + media)
A6 – 2×10^5 cells/well	(0.5% MTH/500 $\mu\text{g/ml}$ DEP + media)	B6 – 2×10^5 cells/well	(0.5% MTH/500 $\mu\text{g/ml}$ DEP + media)
A7 – 2×10^5 cells/well	(1.0% MTH/1000 $\mu\text{g/ml}$ DEP + media)	B7 – 2×10^5 cells/well	(1.0% MTH/1000 $\mu\text{g/ml}$ DEP + media)
A8 – media only	(media only)	B8 – media only	(media only)

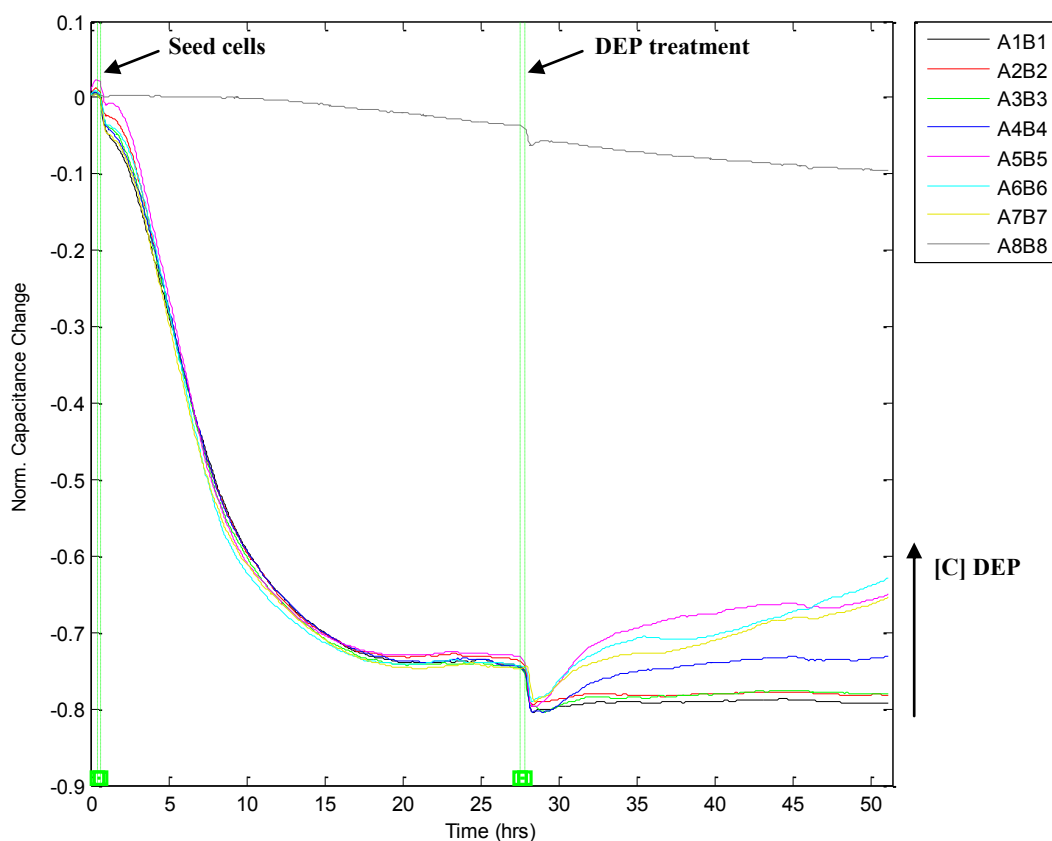


Figure 6.3. Two 8W10E+ arrays were seeded with 2×10^5 cells/ml (A1 – A7 and B1 – B7) with control wells containing culture medium (A8 and B8). When the cells were confluent at ~ 28 hours, then an increasing amount of DEP (ranging from 10 $\mu\text{g/ml}$ to 1000 $\mu\text{g/ml}$), dissolved in methanol, was added to each of the wells. Each data line is an average of two wells, except for A6 (B6 data was erroneous).

cells. Control wells continued to have the lowest raw capacitance values ($\sim 10 - 11$ nF) and are similar to values in Figure 6.2 and are in agreement with literature [5]. We determined that fresh DEP solutions had an effect on adherent A549 cells in Figure 6.3 ($\sim 28 - 50$ hours) when compared to methanol treated A549 cells in Figure 6.2 ($\sim 25 - 50$ hours).

6.5.1.2 *Protective effects of resveratrol against DEP exposure and wounding*

Figure 6.4 illustrates uniform seeding of two 8W10E+ arrays. Wells were seeded at 2×10^5 cells/well (0 – 23 hours), culture medium was replaced in array A, and array B was treated with medium containing 10 μ M resveratrol (23 – 45 hours). Next cells were treated with increasing concentrations of DEP (45 hours, see Table 6.4) allowed to continue to culture in medium containing increasing concentrations of DEP. At 70 hours, fresh medium was added (70 – 90 hours), and arrays were wounded at 60 kHz and

Table 6.4. Array seeding density and treatment for array A and B in Figure 6.4.

A1 – 2×10^5 cells/well	(media only)	B1 – 2×10^5 cells/well	(media + 10 μ M RES)
A2 – 2×10^5 cells/well	(0.01% MTH/2 μ g/ml DEP + media)	B2 – 2×10^5 cells/well	(0.01% MTH/2 μ g/ml DEP + media + 10 μ M RES)
A3 – 2×10^5 cells/well	(0.025% MTH/7 μ g/ml DEP + media)	B3 – 2×10^5 cells/well	(0.025% MTH/7 μ g/ml DEP + media + 10 μ M RES)
A4 – 2×10^5 cells/well	(0.1% MTH/20 μ g/ml DEP + media)	B4 – 2×10^5 cells/well	(0.1% MTH/20 μ g/ml DEP + media + 10 μ M RES)
A5 – 2×10^5 cells/well	(0.25% MTH/50 μ g/ml DEP + media)	B5 – 2×10^5 cells/well	(0.25% MTH/50 μ g/ml DEP + media + 10 μ M RES)
A6 – 2×10^5 cells/well	(0.5% MTH/100 μ g/ml DEP + media)	B6 – 2×10^5 cells/well	(0.5% MTH/100 μ g/ml DEP + media + 10 μ M RES)
A7 – 2×10^5 cells/well	(1.0% MTH/500 μ g/ml DEP + media)	B7 – 2×10^5 cells/well	(1.0% MTH/500 μ g/ml DEP + media + 10 μ M RES)
A8 – media only	(media only)	B8 – media only	(media only)

6500 μA for 20 seconds and then allowed to recover for ~ 30 hours (90 – 120 hours) and were finally wounded a second time and allowed to recover (120 – 164 hours) until termination. Figure 6.5 and Figure 6.6 represents ECIS profiles of array A and array B for clarity.

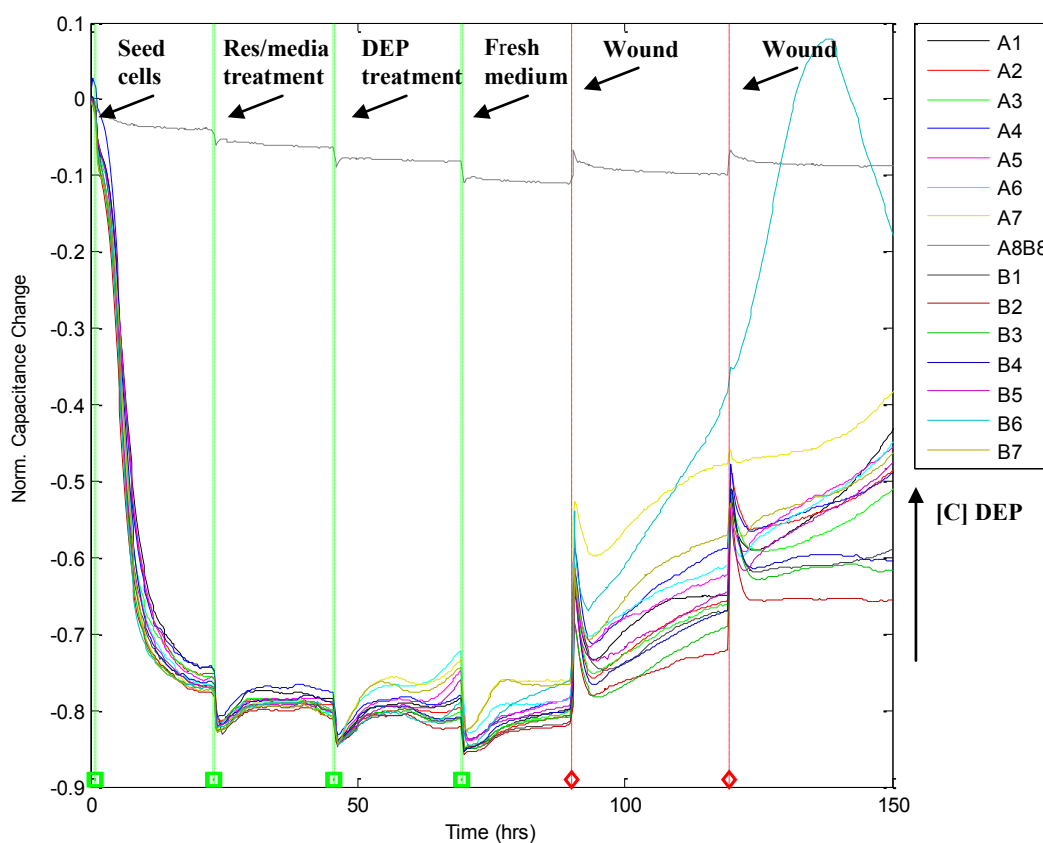


Figure 6.4. Two 8W10E+ arrays (array A and B) were seeded with 2×10^5 cells/ml of A549 (A1 – A7 and B1 – B7). After attachment and proliferation (0 – 24 hours), the media in wells A1 – A8 was replaced with fresh media (~ 24 hours) and wells B1 – B8 was replaced with medium containing 10 μM resveratrol. Next cells were treated with different concentrations of DEP (45 – 70 hours), then media was changed again and cells were allowed to adjust to new media (70 – 90 hours), next cells were wounded (90 hours) and allowed to recover (90~120 hours), and finally cells were re-wounded (~ 120 hours) and allowed to recover (120 – 165 hours).

During the first 90 hours of the experiment, there are no obvious differences for the time profile of control wells (medium only) versus 10 μM resveratrol treated wells. Figure 6.5 reiterates the trend of attachment, spreading and proliferation (0 – 45 hours; compare Figure 6.2, 0 – 50 hours) along with decreasing capacitance for increasing DEP concentrations (54 – 70; compare Figure 6.3, 28 – 51 hours). Conversely, from

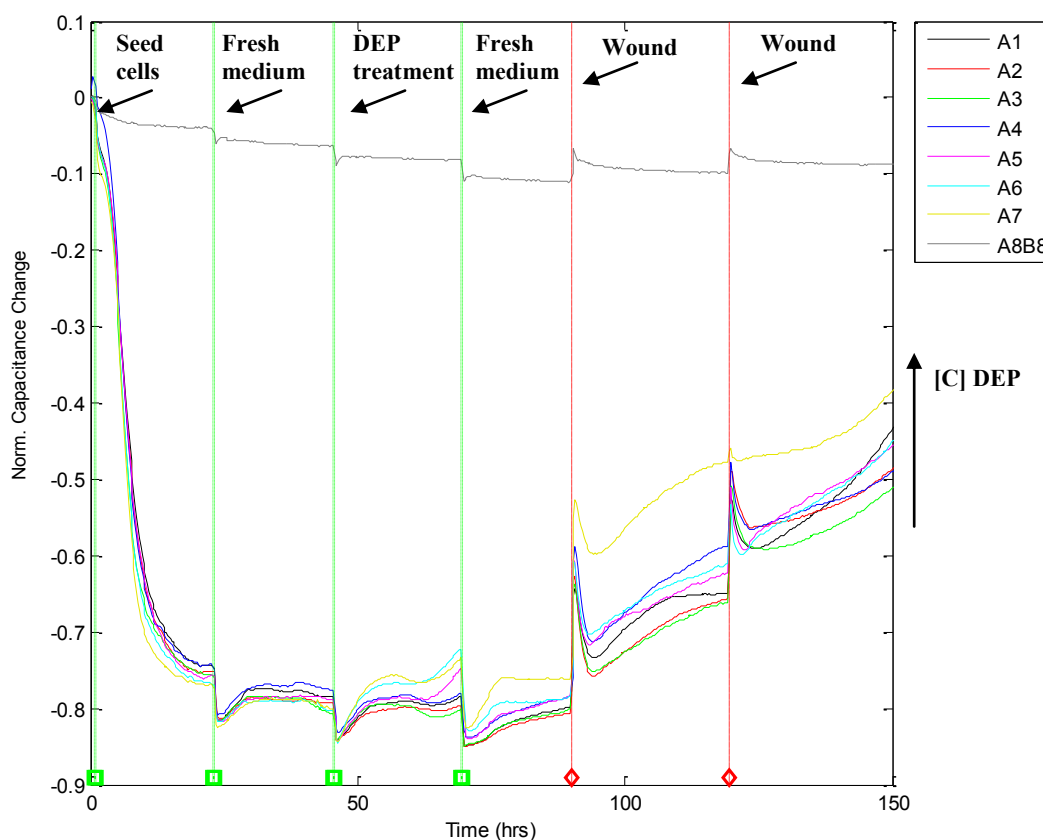


Figure 6.5. Array A. A549 was seeded at 2×10^5 cells/well in 8W10E+ arrays. After attachment and proliferation (0 – 24 hours), the media in the wells was replaced with fresh media (~24 hours). Next cells were treated with different concentrations of DEP (45 – 70 hours), then media was changed again and cells were allowed to adjust to new media (70 – 90 hours), next cells were wounded (90 hours) and allowed to recover (90~120 hours), and finally cells were re-wounded (~120 hours) and allowed to recover (120 – 165 hours).

≥ 90 hours onward there are two distinct features that were observed. The first feature is evident in the initial wounding (with the exception of well B6) where the capacitance values decreased following the trend of increasing DEP concentration. Wells with lower concentrations of DEP (2, 7, and 20 $\mu\text{g/ml}$ DEP) tend to have greater capacitive values whereas wells with higher concentrations of DEP (50, 100, and 500 $\mu\text{g/ml}$) have

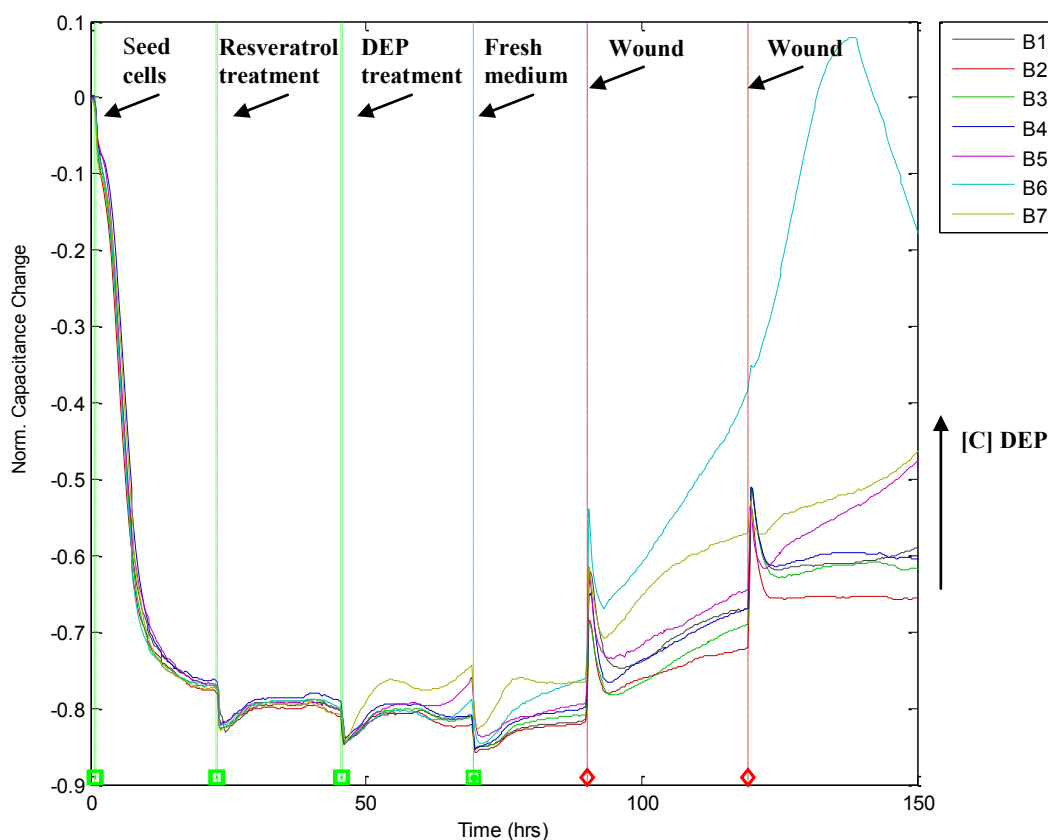


Figure 6.6. Array B. After attachment and proliferation (0 – 24 hours), the cells were treated with 10 μM resveratrol (~24 – 45 hours). Next cells were treated with different concentrations of DEP (45 – 70 hours), then media was changed and cells were allowed to recover (70 – 90 hours), next cells were wounded (90 hours) and allowed to recover (90 – 120 hours), and finally cells were re-wounded and allowed to recover (120 – 165 hours).

decreasing capacitive values. The increased capacitive values are an indication of cell attachment and are associated with cell re-population on the working area of the electrode within that well. When the capacitance values decrease, it signals loss of cell integrity or a decrease in population numbers attached to the electrode surface. The second feature is evident in the final wounding where all wells (array A see Figure 6.5 >120 hours) show marked decreases in capacitive values and indicate a declining cell population based on factors such as: wounding, DEP toxicity, and medium depletion. On the other hand, four wells (B1, B2, B3, and B4) from the 10 μ M resveratrol treated array (array B see Figure 6.6 >120 hours) show steady capacitive values compared to the declining values of the same untreated wells (see A1, A2, A3, and A4). These four wells, the control well (B1) along with the wells containing the three lowest concentrations of DEP: B2 = 2 μ g/ml, B3 = 7 μ g/ml, and B4 = 20 μ g/ml, continue to survive (indicated by the flat capacitance response) after recovering from DEP treatment and wounding. Figure 6.5 clearly shows the decreasing capacitance trend in array A and Figure 6.6 shows steady capacitance in array B after the final wounding. These results imply a protective advantage for the 10 μ M resveratrol treated A549 cells that were exposed to <20 μ g/ml DEP.

6.5.1.3 Single electrode monitoring of resveratrol treatment versus DEP exposure

Figure 6.7 illustrates the time profile for cells that were cultured in two 8W1E arrays. (Note: the aforementioned experiments; Figure 6.2, Figure 6.3, Figure 6.4, Figure 6.5, and Figure 6.6 were cells cultured in 8W10E+ arrays containing multi-electrode

wells). Cells were seeded at 2×10^5 cells/well and allowed to attach and proliferate until confluent (~27 hours), then culture medium in array A (Figure 6.8) was replaced with fresh medium and array B (Figure 6.9) was also replaced with medium containing 10 μM resveratrol. After ~24 hours, array A and B were treated with increasing concentrations of DEP (50 – 74 hours, see Table 6.5).

Figure 6.7 shows the combined arrays whereas Figure 6.8 and Figure 6.9 show each separate array A (no resveratrol) and B (10 μM resveratrol). Figure 6.8 and Figure 6.9 show similar signal-to-noise for the initial seeding and proliferation (0 – 27 hours), however there is a distinct decrease in cellular mobility (micro-motion) when Figure 6.9 is treated with 10 μM resveratrol (27 – 50 hours) compared to the control wells containing only culture medium in Figure 6.8. On the other hand, the opposite is true for

Table 6.5. Array seeding density and treatment for array A and B in Figure 6.7.

A1 – 2×10^5 cells/well	(media only)	B1 – 2×10^5 cells/well	(media + 10 μM RES)
A2 – 2×10^5 cells/well	(0.01% MTH/10 $\mu\text{g/ml}$ DEP + media)	B2 – 2×10^5 cells/well	(0.01% MTH/10 $\mu\text{g/ml}$ DEP + media + 10 μM RES)
A3 – 2×10^5 cells/well	(0.025% MTH/25 $\mu\text{g/ml}$ DEP + media)	B3 – 2×10^5 cells/well	(0.025% MTH/25 $\mu\text{g/ml}$ DEP + media + 10 μM RES)
A4 – 2×10^5 cells/well	(0.1% MTH/100 $\mu\text{g/ml}$ DEP + media)	B4 – 2×10^5 cells/well	(0.1% MTH/100 $\mu\text{g/ml}$ DEP + media + 10 μM RES)
A5 – 2×10^5 cells/well	(0.25% MTH/250 $\mu\text{g/ml}$ DEP + media)	B5 – 2×10^5 cells/well	(0.25% MTH/250 $\mu\text{g/ml}$ DEP + media + 10 μM RES)
A6 – 2×10^5 cells/well	(0.5% MTH/500 $\mu\text{g/ml}$ DEP + media)	B6 – 2×10^5 cells/well	(0.5% MTH/500 $\mu\text{g/ml}$ DEP + media + 10 μM RES)
A7 – 2×10^5 cells/well	(1.0% MTH/1000 $\mu\text{g/ml}$ DEP + media)	B7 – 2×10^5 cells/well	(1.0% MTH/1000 $\mu\text{g/ml}$ DEP + media + 10 μM RES)
A8 – media only	(media only) Not shown	B8 – media only	(media only)

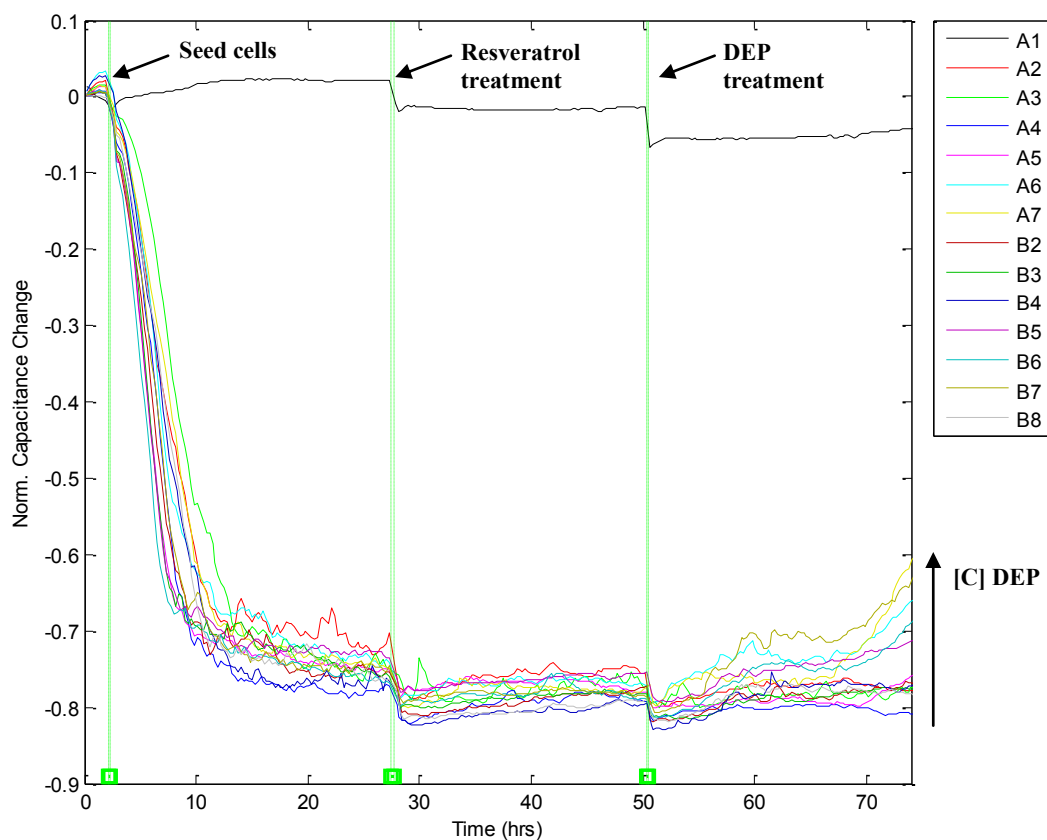


Figure 6.7. Two 8W1E arrays were seeded with 2×10^5 cells/ml of A549 (A1 – A7) and (B1 – B7) with control wells containing culture medium (A8 and B8). Cells were monitored until approximately confluent (27 hours), then 10 μ M (final) resveratrol was added to array B for 24 hours (culture medium, without resveratrol, in array A), DEP was added for the final ~24 hours.

treatment with DEP, the lower concentrations of DEP in Figure 6.8 (A2 = 10 μ g/ml, A3 = 25 μ g/ml, B4 = 100 μ g/ml and B5 = 250 μ g/ml) have an overall increase in cell micro-motion whereas the same wells in Figure 6.9 pre-treated with resveratrol and exposed to DEP have a decrease in micro-motion. The highest concentrations of DEP (500 and 1000 μ g/ml) for both array A and B show a similar trend of increasing micro-motion (A6 & B6 and A7 & B7). Interestingly the decrease in micro-motion of A549

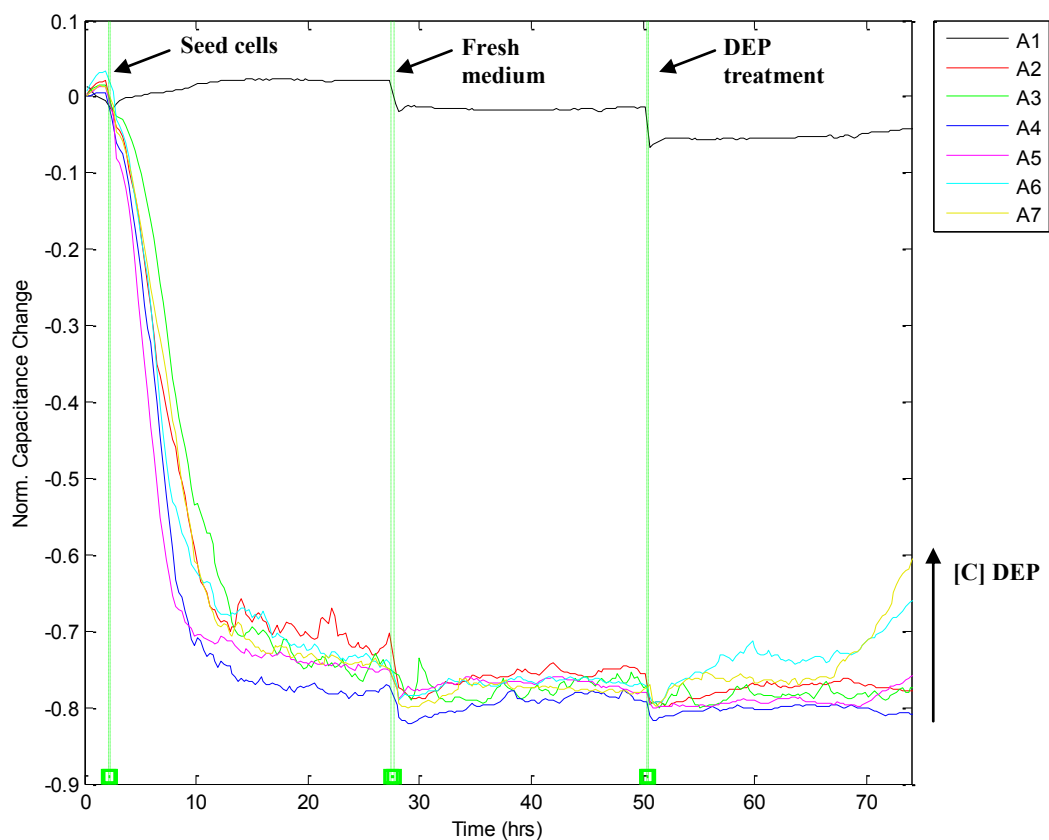


Figure 6.8. Array A. A549 was seeded at 2×10^5 cells/well in an 8W1E array. After attachment and proliferation (0 – 27 hours), the medium in each well was replaced with fresh medium (~27 hours) and cells were allowed to continue in culture (28 – 50 hours). Next cells were treated with different concentrations of DEP (50 – 75 hours).

cells was not apparent in Figure 6.6 (45 – 70 hours) when treated with $10 \mu\text{M}$ resveratrol and is likely due to the average of $\sim 1000 - 2000$ cells on the 40 electrodes per well of the 8W10E+ array compared with 50 – 100 cells of the 8W1E array. The overall trend for cell response to increasing concentrations of DEP is consistent between the 8W10E+ (Figure 6.3 and Figure 6.4) and 8W1E (Figure 6.7) arrays.

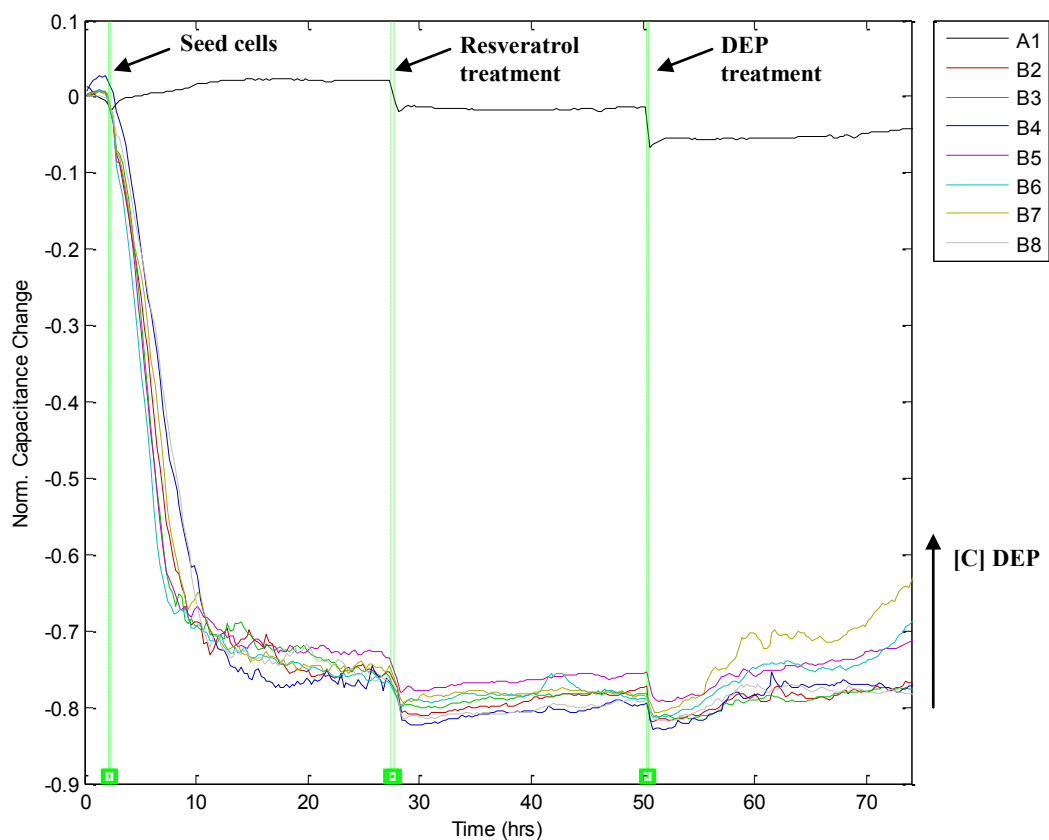


Figure 6.9. Array B. A549 was seeded at 2×10^5 cells/well in an 8W1E array. After attachment and proliferation (0 – 27 hours), the medium in each well was replaced with fresh medium containing a final concentration of $10 \mu\text{M}$ resveratrol (~ 27 hours) and cells were allowed to continue in culture (28 – 50 hours). Next cells were treated with different concentrations of DEP (50 – 75 hours).

ECIS modeling was performed for raw data in Figure 6.7 and is illustrated in Figure D6.33-A through -C. Means comparison ($\text{mean} \pm \text{SD}$) was calculated for a 10 hour span during seeding ($\sim 15 - 25$ hours), resveratrol treatment (35 – 45 hours), and DEP exposure (55 – 65 hours). Figure D6.33-A illustrates the overall mean changes in R_b for array A and B. For array A the R_b value increases after the medium exchange and the DEP exposure, suggesting an increase in cell-to-cell junctions. In array B the R_b value is

greatest at the medium exchange/resveratrol treatment, and then decreases during the DEP exposure, perhaps indicating protective effects of resveratrol in maintaining cell-to-cell integrity. A similar trend is seen for α in Figure D6.33-B as in Figure D6.33-A; perhaps suggesting that cell morphology (area) or basal membrane to substratum (h) may change due to resveratrol treatment. In Figure D6.33-C there is an increase in C_m , which may indicate that the cell area decreases with resveratrol treatment and may contribute to a decrease in cell micro-motion during this period.

6.5.1.4 Single electrode monitoring of DEP exposure on wound healing with wounding verified by fluorescent staining

Figure 6.10 illustrates the averaged time profiles of A549 in 8W1E arrays (see Table 6.6). Cells were seeded at 2×10^5 cells/well and allowed to attach and proliferate until confluent (~24 hours), then fresh culture medium was added to wells A1, B1, A5, and B5 in both arrays and followed by increasing concentrations of DEP in A2, A3, A4, A6, A7, A8 and B2, B3, B4, B6, B7, B8. After the addition of medium to each array,

Table 6.6. Array seeding density and treatment for array A and B in Figure 6.10.

A1 – 2×10^5 cells/well (serum containing media)	B1 – 2×10^5 cells/well (serum containing media)
A2 – 2×10^5 cells/well (serum containing media + 50 $\mu\text{g/ml}$ DEP)	B2 – 2×10^5 cells/well (serum containing media + 50 $\mu\text{g/ml}$ DEP)
A3 – 2×10^5 cells/well (serum containing media + 125 $\mu\text{g/ml}$ DEP)	B3 – 2×10^5 cells/well (serum containing media + 125 $\mu\text{g/ml}$ DEP)
A4 – 2×10^5 cells/well (serum containing media + 500 $\mu\text{g/ml}$ DEP)	B4 – 2×10^5 cells/well (serum containing media + 500 $\mu\text{g/ml}$ DEP)
A5 – 2×10^5 cells/well (serum containing media)	B5 – 2×10^5 cells/well (serum containing media)
A6 – 2×10^5 cells/well (serum containing media + 50 $\mu\text{g/ml}$ DEP)	B6 – 2×10^5 cells/well (serum containing media + 50 $\mu\text{g/ml}$ DEP)
A7 – 2×10^5 cells/well (serum containing media + 125 $\mu\text{g/ml}$ DEP)	B7 – 2×10^5 cells/well (serum containing media + 125 $\mu\text{g/ml}$ DEP)
A8 – 2×10^5 cells/well (serum containing media + 500 $\mu\text{g/ml}$ DEP)	B8 – 2×10^5 cells/well (serum containing media + 500 $\mu\text{g/ml}$ DEP)

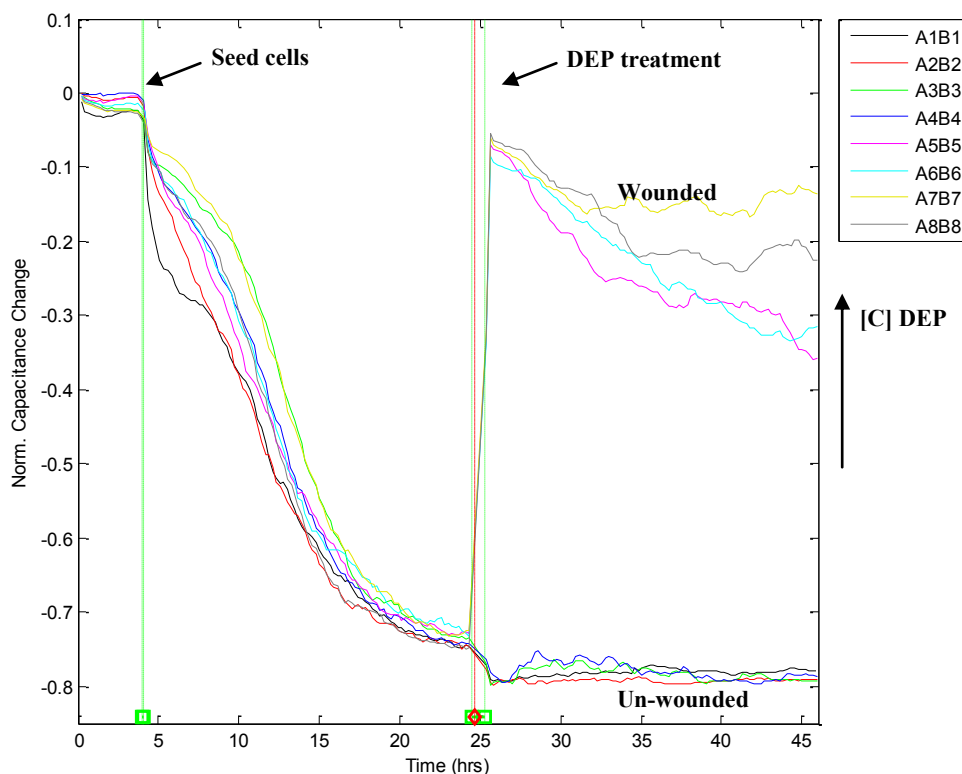


Figure 6.10. Two 8W1E arrays were seeded with 2×10^5 cells/well of A549 (A1–A8 and B1–B8) and cells were allowed to become confluent. After ~ 24 hours, the medium was changed and medium with DEP (50, 125, and 500 $\mu\text{g}/\text{ml}$) was added to the arrays. The arrays were then wounded (A5 – 8 and B5 – 8 @ 180 seconds, 3000 μA and 60 kHz), and then allowed to recover. It appears each of the wells begin to recover, but not to the baseline of the un-wounded wells.

wells of array B were wounded at 60 kHz and 3000 μA for 180 seconds and then allowed to recover until ~ 46 hours.

From the averaged wells in Figure 6.10, the partial recovery of the wounded wells (A5, A6, A7, A8 and B5, B6, B7, B8) and the trend for cell recovery is consistent with previous runs of DEP exposed and wounded cells (Figure 6.2 after wounding at 50 hours

and Figure 6.4 after 90 hours). The unwounded wells appear to have similar micro-motion as compared to the DEP exposed cells in Figure 6.9 after resveratrol treatment (27 hours).

Figure 6.11 and Figure 6.12 are both the bright field images of array A and B, from Figure 6.10, along with accompanying live/dead assay (Molecular Probes, Eugene, OR, USA) of array A and B. Green cells were stained using calcein and represent live cells while red cells were stained with ethidium homodimer (EthD) and represent cells with compromised cellular membranes. The same wells were wounded in both array A and B (A5, A6, A7, A8 and B5, B6, B7, B8). For array A, it is possible that the wounded cells were washed off the electrode during the staining procedure. In contrast, more care was taken for array B and the dead cells are easily spotted in the wounded wells (B5, B6, B7, B8) and especially in B6 and B7 where there are a greater number of red cells in the working electrode area outlined with a white circle.

From the wounding at the electrode, we can see that the settings which were used have an effect to permeate the cell membrane and allow for EthD to enter these cells and bind to nucleic acids. Likewise DEP can also cause reactive oxygen species (ROS) mediated damage to these compromised cells.

For comparison, in Figure D6.34 we observe that the concentrations of DEP (50 and 125 $\mu\text{g/ml}$) do not significantly affect the attached A549 cells; however, after wounding the healing/migration rate is altered and the lower DEP concentration (50 $\mu\text{g/ml}$) has a minimal affect on the recovering cells as compared with the higher

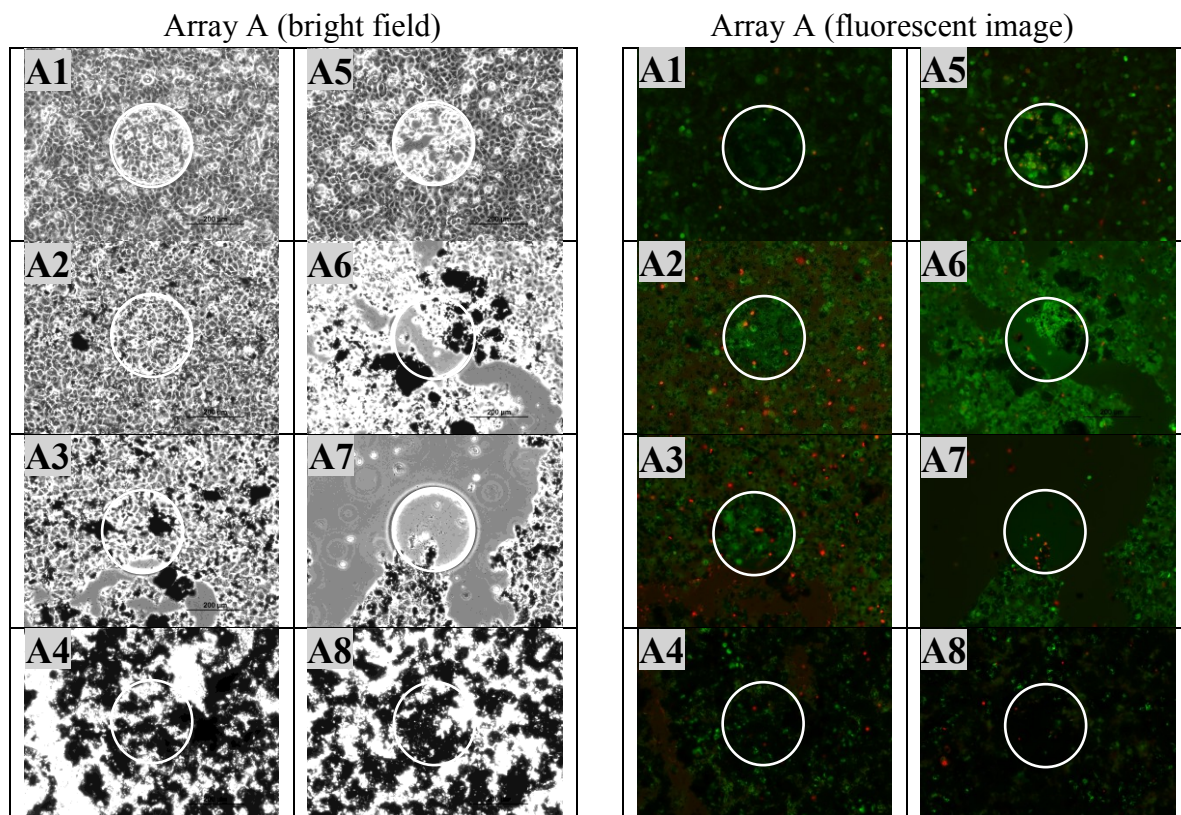


Figure 6.11. Bright field and fluorescent images of array A imaged with IX – 71 Olympus Microscope at 10x magnification. Note that the first column (A1 – A4) was not wounded and the second column (A5 – A8) was wounded and the 250 μm electrode is still covered after partial recovery.

concentration (125 $\mu\text{g/ml}$). Figure D6.35 illustrates an example of decreasing the frequency applied to the electrodes for the wounding assay. A frequency of 32 kHz was too low and increased the likelihood that the cells would not recover after the wounding assay. From Figure D6.34, Figure D6.35, and Figure D6.38, we determined that 180 seconds, 2600 μA (or 3000 μA), and 64 kHz was ideal for wounding A549 in our experimental setup.

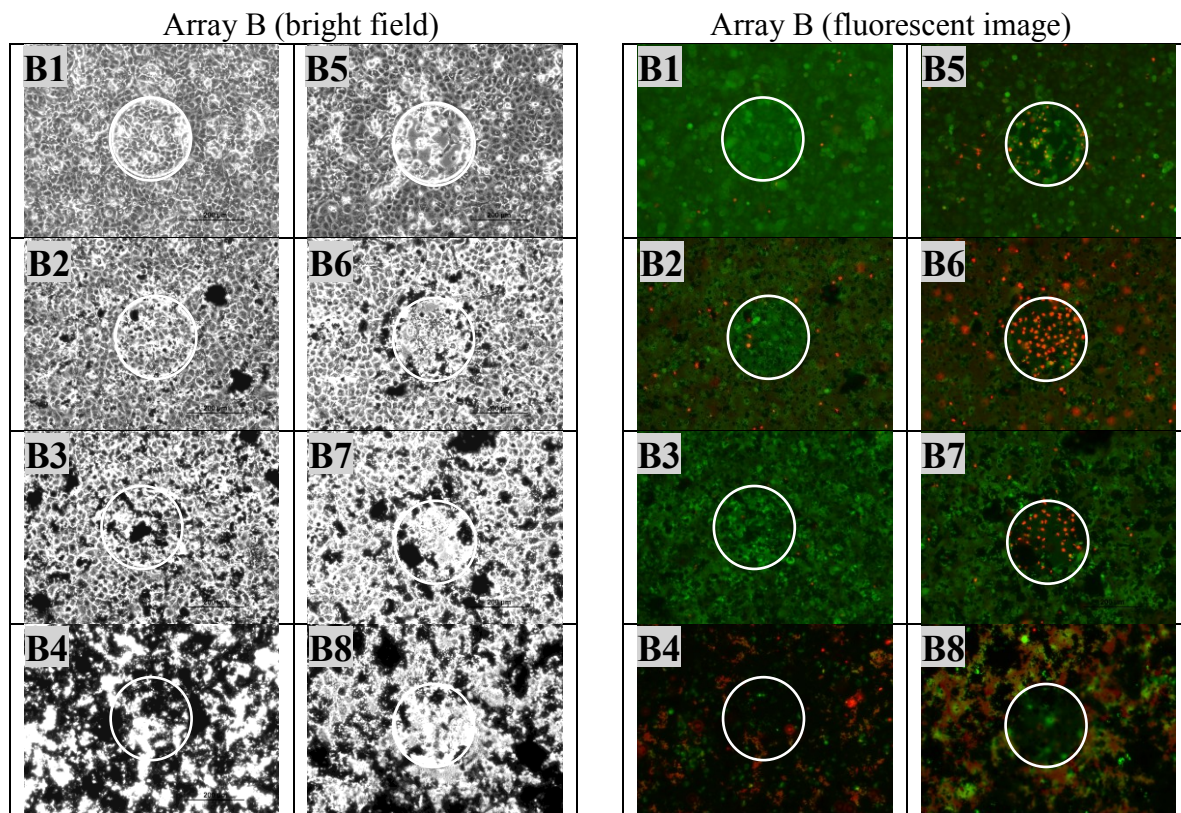


Figure 6.12. Bright field and fluorescent images of array B imaged with IX – 71 Olympus Microscope at 10x magnification. Note that the first column (B1 – B4) was not wounded and the second column (B5 – B8) was wounded and the 250 μm electrode is mostly covered, but the dead cells are visible above the electrode.

The bright field images (Appendix – Figure D6.36 and Figure D6.37) show two important distinctions among the wells from each array. First, the overall color differences associated with increasing concentrations of DEP listed in Table D6.15. Second, wounding causes the cells to roundup on the electrode as compared with the insulated background (compare Figure D6.37-A1 and -A5). Also, we can see damage to the electrode perimeter in Figure D6.37-A1 compared to -A5 (arrow) and -B1 compared with -B5 (arrow). Wells A1 and B1 were un-wounded and appear to have an intact

perimeter, whereas A5 and B5 were wounded and the perimeter of the electrode appears to be compromised (i.e. gold flaking around the electrode perimeter).

6.5.1.5 *Single electrode monitoring of DEP exposure versus simultaneous DEP/RES treatment*

Figure 6.13 and Figure 6.14 illustrate time profiles for A549 cells (each profile an average of two wells) cultured in 8W1E arrays. Cells were seeded at 1×10^5 cells/well and allowed to attach and proliferate until confluent (~30 hours). Next, according to Table 6.7, wells were randomly treated with either DEP (Figure 6.13) or a combination of DEP plus 10 μ M resveratrol (Figure 6.14). Following treatments cells continued in culture another ~24 hours. Arrow indicates increasing concentration of DEP.

Table 6.7. Well seeding density and treatment for array A and B in Figure 6.13 and Figure 6.14.

A1 – 2×10^5 cells/well	(serum containing media + 50 μ g/ml DEP)	B1 – 2×10^5 cells/well	(serum containing media + 125 μ g/ml DEP + 10 μ M RES)
A2 – 2×10^5 cells/well	(serum containing media + 10 μ M RES)	B2 – 2×10^5 cells/well	(serum containing media + 500 μ g/ml DEP + 10 μ M RES)
A3 – 2×10^5 cells/well	(serum containing media + 50 μ g/ml DEP + 10 μ M RES)	B3 – 2×10^5 cells/well	(serum containing media + 500 μ g/ml DEP)
A4 – 2×10^5 cells/well	(serum containing media + 50 μ g/ml DEP + 10 μ M RES)	B4 – 2×10^5 cells/well	(serum containing media + 50 μ g/ml DEP)
A5 – 2×10^5 cells/well	(serum containing media + 10 μ M RES)	B5 – 2×10^5 cells/well	(serum containing media)
A6 – 1.0×10^5 cells/well	(serum containing media)	B6 – 2×10^5 cells/well	(serum containing media + 125 μ g/ml DEP)
A7 – 2×10^5 cells/well	(serum containing media + 500 μ g/ml DEP)	B7 – 2×10^5 cells/well	(serum containing media + 125 μ g/ml DEP)
A8 – 2×10^5 cells/well	(serum containing media + 500 μ g/ml DEP + 10 μ M RES)	B8 – 2×10^5 cells/well	(serum containing media + 125 μ g/ml DEP + 10 μ M RES)

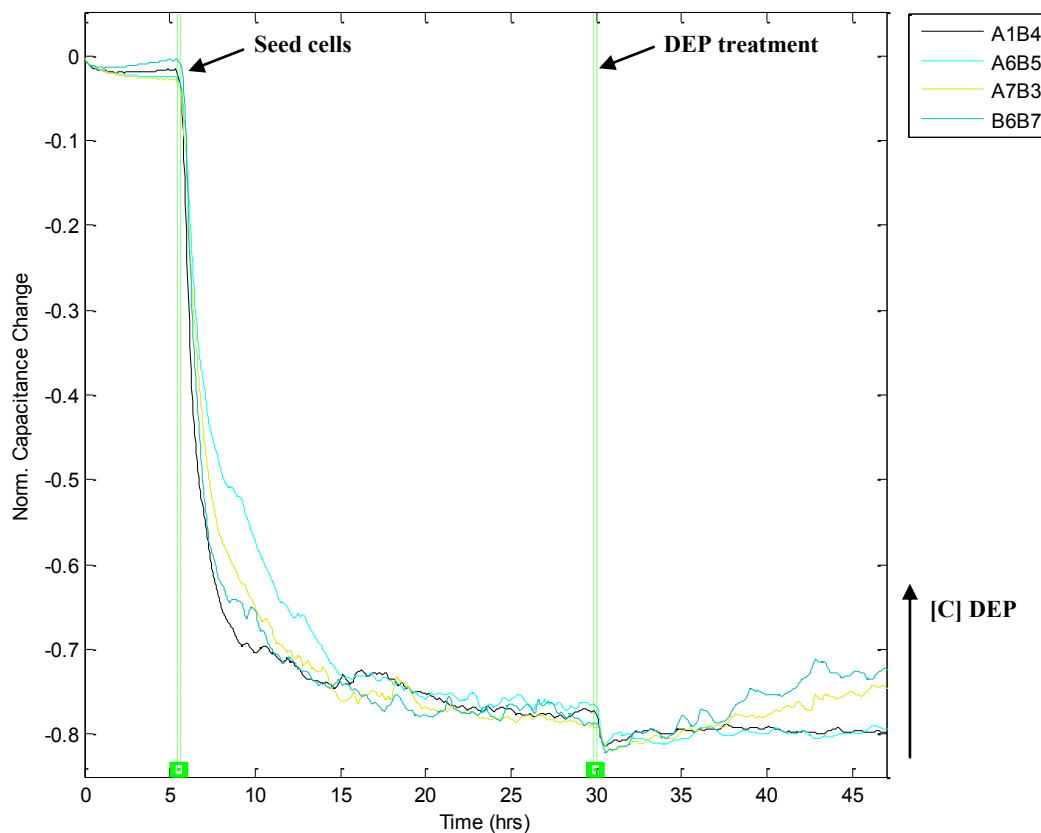


Figure 6.13. A549 cells were seeded at 1×10^5 cells/well, allowed to attach and spread until 30 hours. Next cells were treated with increasing concentrations of DEP and allowed to continue to grow for ~ 15 hours (note each data line is an average of two wells).

Figure 6.13 illustrates two averaged wells per profile for DEP exposure. After culture exposure ($\sim 35 - 47$ hours) the two highest concentrations of DEP (125 and 500 $\mu\text{g/ml}$) caused cells to die and detach as the overall DEP trend is similar to that shown in Figure 6.3 as indicated by the increasing DEP concentration (arrow). In Figure 6.14, the DEP plus resveratrol treated cells show three distinct differences: 1) cell viability appears

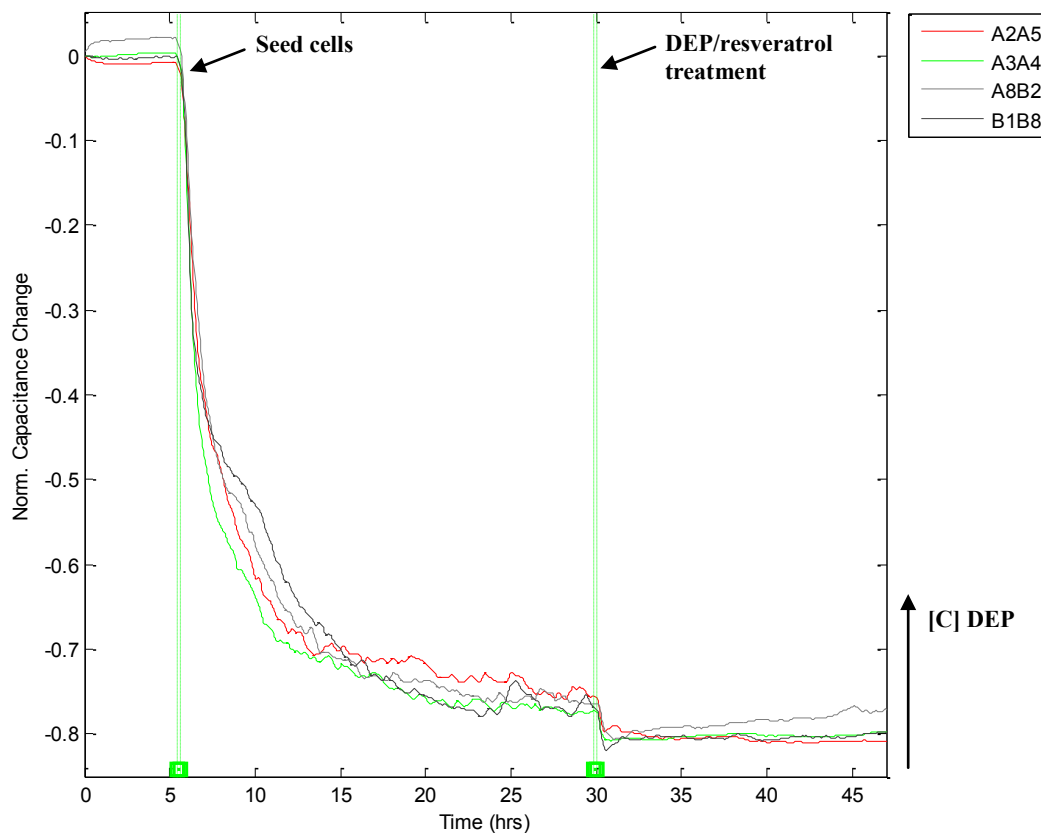


Figure 6.14. A549 cells were seeded at 1×10^5 cells/well, allowed to attach and spread until 30 hours. Next cells were treated with increasing concentrations of DEP combined with 10 μ M resveratrol and allowed to continue to grow for ~ 15 hours (note each data line is an average of two wells).

unaffected except for a higher capacitance value for the 500 μ g/ml DEP treated wells, 2) the micro-motion of the cells is reduced as previously seen in Figure 6.9, and 3) an overall decrease in the total capacitance values for each well could indicate a stronger attachment to the electrode or other morphological changes.

6.5.1.6 Single electrode monitoring of RES pretreatment and followed with DEP exposure and wounding versus no wounding and fluorescent imaging

Figure 6.15 and Figure 6.16 illustrate time profiles for two averaged wells of A549 cultured in 8W1E arrays. Cells were seeded at 2×10^5 cells/well plus 10 μ M resveratrol and allowed to attach and proliferate until confluent (~30 hours). Next, arrays were exposed to increasing amounts of DEP (Table 6.8) and wells: A2, A3, A4, A5, A6, A7, A8, and B1 were wounded (60 kHz and 3000 μ A for 180 seconds). All wells were allowed to continue in culture another 40 hours. Post-ECIS measurement the arrays were stained using a live/dead assay (Molecular Probes, Eugene, OR, USA) and imaged with an IX – 71 Olympus microscope.

Table 6.8. Array seeding density and treatment for array A and B in Figure 6.15 and Figure 6.16.

A1 – 2×10^5 cells/well	(serum containing media + 10 μ M RES)	B1 – No cells	(serum containing media + 10 μ M RES)
A2 – 2×10^5 cells/well	(serum containing media + 10 μ M RES then 50 μ g/ml DEP)	B2 – 2×10^5 cells/well	(serum containing media + 50 μ g/ml DEP + 10 μ M RES)
A3 – 2×10^5 cells/well	(serum containing media + 10 μ M RES then 125 μ g/ml DEP)	B3 – 2×10^5 cells/well	(serum containing media + 10 μ M RES then 125 μ g/ml DEP)
A4 – 2×10^5 cells/well	(serum containing media + 10 μ M RES then 500 μ g/ml DEP)	B4 – 2×10^5 cells/well	(serum containing media + 10 μ M RES then 500 μ g/ml DEP)
A5 – 2×10^5 cells/well	(serum containing media + 10 μ M RES)	B5 – No cells	(serum containing media + 10 μ M RES)
A6 – 1.0×10^5 cells/well	(serum containing media + 10 μ M RES then 50 μ g/ml DEP)	B6 – 1.0×10^5 cells/well	(serum containing media + 10 μ M RES then 50 μ g/ml DEP)
A7 – 2×10^5 cells/well	(serum containing media + 10 μ M RES then 125 μ g/ml DEP)	B7 – 2×10^5 cells/well	(serum containing media + 10 μ M RES then 125 μ g/ml DEP)
A8 – 2×10^5 cells/well	(serum containing media + 10 μ M RES then 500 μ g/ml DEP)	B8 – 2×10^5 cells/well	(serum containing media + 10 μ M RES then 500 μ g/ml DEP)

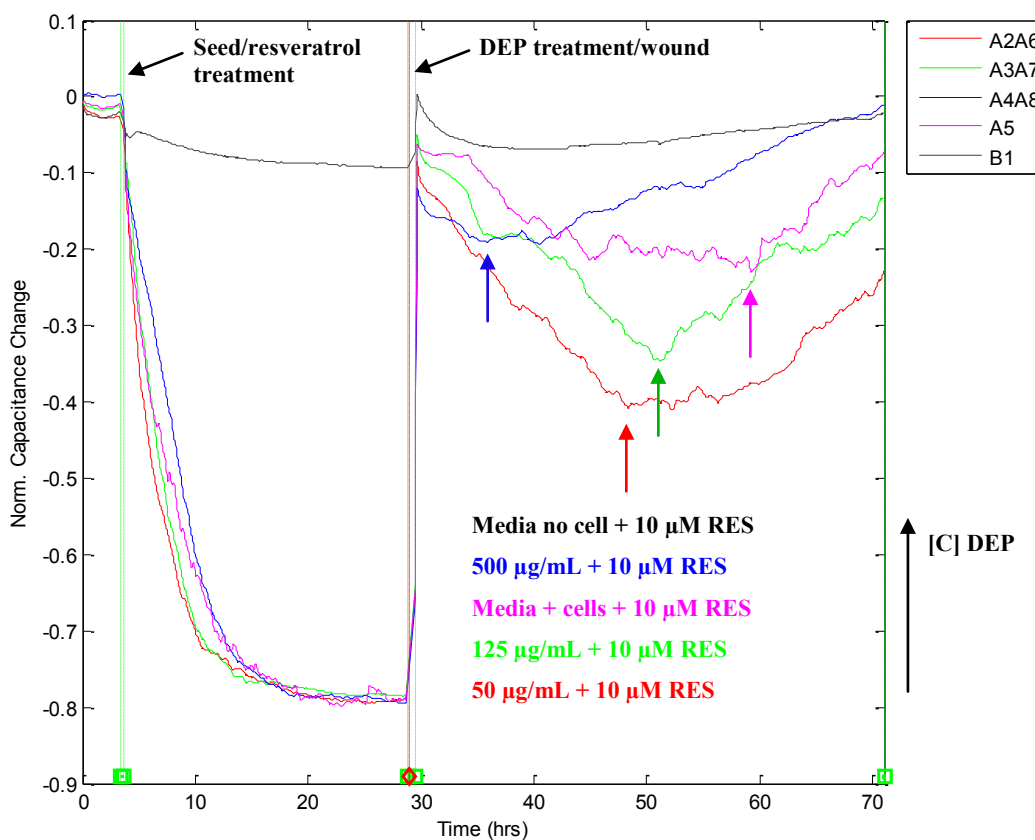


Figure 6.15. A549 cells were seeded at 2×10^5 cells/well plus $10 \mu\text{M}$ resveratrol, allowed to attach and spread until ~ 30 hours. Then cells were treated with increasing concentrations of DEP, wounded (60 kHz and $3000 \mu\text{A}$ for 180 seconds) and allowed to continue to grow for ~ 36 hours (note each data line is an average of two wells, expect for the media and media + cells wells).

Figure 6.15 illustrates the wounding assay and it is interesting to see the trend for the resveratrol treated cells once they are exposed to DEP and then wounded. The most notable recovery is $50 \mu\text{g/ml}$ DEP followed by $125 \mu\text{g/ml}$ and then the medium control and finally $500 \mu\text{g/ml}$ DEP. At first glance, it appears that the control (well A5, no replicate) may not have been representative for the recovery after wounding; however, similar trends were seen in Figure 6.10 and Figure D6.38. Conversely, cells treated with

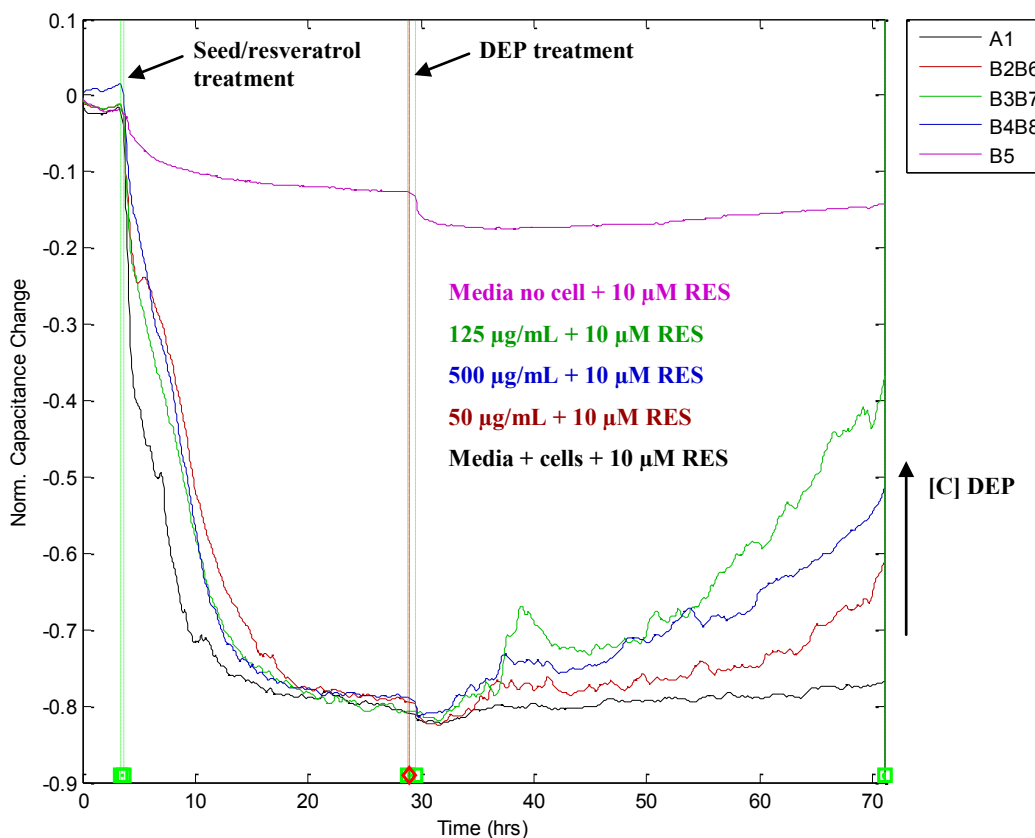


Figure 6.16. A549 cells were seeded at 2×10^5 cells/well + 10 μM resveratrol, allowed to attach and spread until ~ 30 hours. Then cells were treated with increasing concentrations of DEP and allowed to continue to grow for ~ 36 hours (note each data line is an average of two wells, expect for the media and media +cells wells).

B4, B6, B7, and B8) stained resveratrol and the lowest concentration of DEP (50 and 125 $\mu\text{g/ml}$) may exhibit better recovery compared to control cells, as seen with the low capacitance flat line in Figure 6.6-B2.

A second way to understand the response of the treated wells would be to look at the inflection points of the profiles post-wounding (Figure 6.15 colored arrows). The trend for longest to shortest survival is 59.8 hours, (no DEP), 56.6 hours (50 $\mu\text{g/ml}$ DEP),

51.7 hours (125 $\mu\text{g/ml}$ DEP), and 40.9 hours (500 $\mu\text{g/ml}$ DEP). The latter response in Figure 6.15 coincides with the un-wounded wells in Figure 6.16 for array B.

Figure 6.17 and Figure 6.18 are bright field and fluorescent images of array A (Figure 6.15) and array B (Figure 6.16) at 40x magnification. From the images of array A only wells A4 and A6 appear to contain dead cells. The other wells appear to be cell free on the working area of the electrode. This may, again, be due to the cells washing off the surface of the electrode in the wash step of the staining protocol. It is interesting to compare the Figure 6.17-A4 with Figure 6.12-B6, where the majority of the wounded cells are on the working electrode. For the un-wounded array, the treated wells (B2, B3,

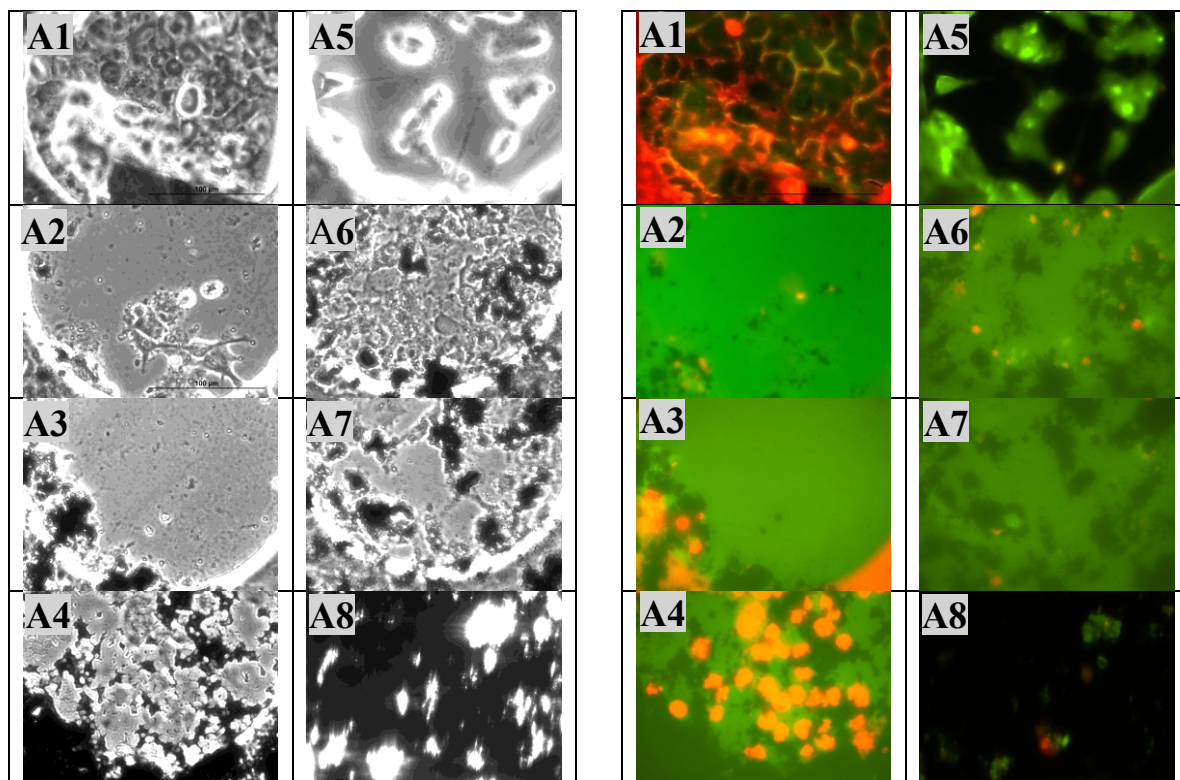


Figure 6.17. Bright field and fluorescent images of Array A imaged with IX – 71 Olympus Microscope at 40x magnification. Note that most of the wounded cells detached and may have washed away – except for well A4 and some in well A6.

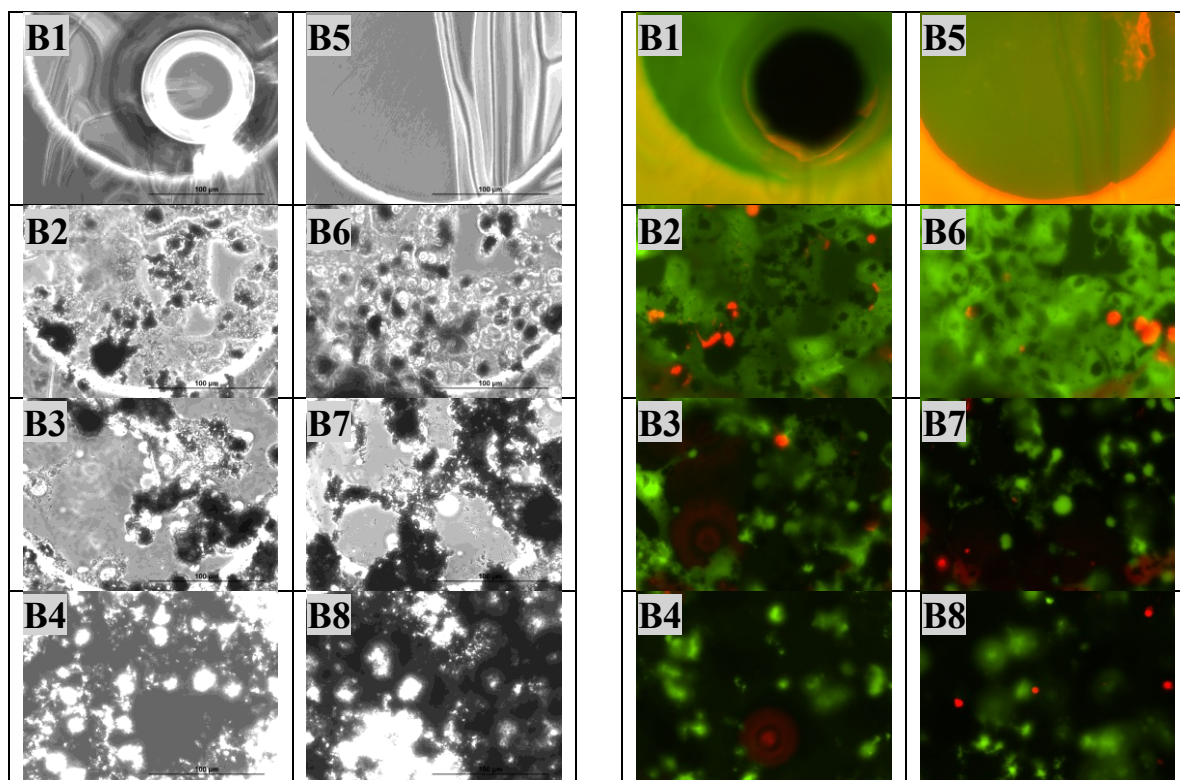


Figure 6.18. Bright field and fluorescent images of Array A imaged with IX – 71 Olympus Microscope at 40x magnification. It also appears that some of the cells have washed off in the rinsing with EBSS.

approximately the same with the noted increase in DEP, however surprisingly sparse dead cells.

In summary, Approach #1 (6.5.1) shows that increasing concentrations of methanol were not immediately toxic to A549 cells; however, increasing concentrations of DEP begin to interfere with cell integrity and lead to cell death and detachment compared to control. The “higher” DEP concentrations (125, 250, and 500 $\mu\text{g/ml}$) appear to cause a cytotoxic response in A549 that leads to outright cell death. Whereas the “lower” concentrations of DEP (5, 17.5, and 50 $\mu\text{g/ml}$) illicit non to mild genotoxic responses in A549 cells. Moreover, treatment with 10 μM resveratrol exhibits protective

effects against cell death, notably, for DEP concentrations ($>20 \mu\text{g/ml}$) that are not readily cytotoxic to cells. It is thought that these inhibitory effects are mediated by resveratrol as a scavenger of ROS or by inhibiting some apoptotic machinery. Also resveratrol has a visible effect on cell micro-motion, which could also be linked to cell recovery and survival.

6.5.2 Approach #2 – Simultaneous array modification

6.5.2.1 Multi-electrode monitoring of methanol treated cell versus DEP pre-exposed cells, prior to seeding

Figure 6.19 shows the averaged normalized capacitive portion for measured impedance at 64 kHz of A549 inoculated in 14 identical wells with 2 blank wells. Cells were seeded in 8W10E+ arrays according to Table 6.9. Cells were seeded with medium plus increasing concentrations of methanol and then allowed to settle, attach, and proliferate on the bottom of each well (~25 hours).

Table 6.9. Array seeding density and treatment for array A and B in Figure 6.19.

A1 – 2×10^5 cells/well	(media only)	B1 – 2×10^5 cells/well	(media only)
A2 – 2×10^5 cells/well	(0.01% MTH + media)	B2 – 2×10^5 cells/well	(0.01% MTH + media)
A3 – 2×10^5 cells/well	(0.025% MTH + media)	B3 – 2×10^5 cells/well	(0.025% MTH + media)
A4 – 2×10^5 cells/well	(0.1% MTH + media)	B4 – 2×10^5 cells/well	(0.1% MTH + media)
A5 – 2×10^5 cells/well	(0.25% MTH + media)	B5 – 2×10^5 cells/well	(0.25% MTH + media)
A6 – 2×10^5 cells/well	(0.5% MTH + media)	B6 – 2×10^5 cells/well	(0.5% MTH + media)
A7 – 2×10^5 cells/well	(1.0% MTH + media)	B7 – 2×10^5 cells/well	(1.0% MTH + media)
A8 – media only	(media only)	B8 – media only	(media only)

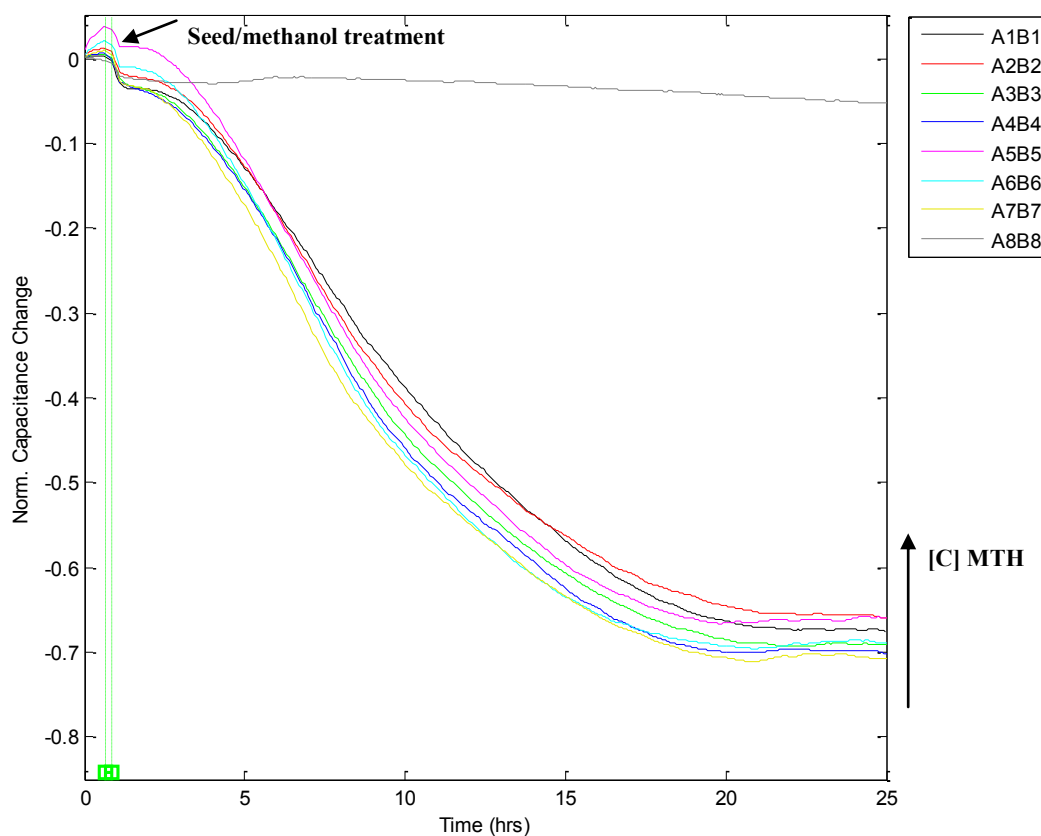


Figure 6.19. Two 8W10E+ arrays were seeded with 2×10^5 cells/well + methanol (A1 – A7 and B1 – B7) and culture media without methanol in the other two wells (A8 and B8). A549 cells become confluent at ~24 hours.

In Figure 6.19, we observe that increasing concentrations of methanol mixed with cells, prior to attachment, are not immediately toxic to the A549 cells as attachment is uniform for all wells. A similar trend was observed for attached cells treated with increasing concentrations of methanol (compare Figure 6.2 and Figure D6.32). Figure 6.20 illustrates uniform seeding of two 8W10E+ arrays where cells were combined with increasing concentrations of DEP (see Table 6.10). Cultures were allowed to continue in culture until termination at ~46 hours.

Table 6.10. Array seeding density and treatment for array A and B in Figure 6.20.

A1 – 2×10^5 cells/well	(media only)	B1 – 2×10^5 cells/well	(media only)
A2 – 2×10^5 cells/well	(0.01% MTH/10 $\mu\text{g/ml}$ DEP + media)	B2 – 2×10^5 cells/well	(0.01% MTH/10 $\mu\text{g/ml}$ DEP + media)
A3 – 2×10^5 cells/well	(0.025% MTH/25 $\mu\text{g/ml}$ DEP + media)	B3 – 2×10^5 cells/well	(0.025% MTH/25 $\mu\text{g/ml}$ DEP + media)
A4 – 2×10^5 cells/well	(0.1% MTH/100 $\mu\text{g/ml}$ DEP + media)	B4 – 2×10^5 cells/well	(0.1% MTH/100 $\mu\text{g/ml}$ DEP + media)
A5 – 2×10^5 cells/well	(0.25% MTH/250 $\mu\text{g/ml}$ DEP + media)	B5 – 2×10^5 cells/well	(0.25% MTH/250 $\mu\text{g/ml}$ DEP + media)
A6 – 2×10^5 cells/well	(0.5% MTH/500 $\mu\text{g/ml}$ DEP + media)	B6 – 2×10^5 cells/well	(0.5% MTH/500 $\mu\text{g/ml}$ DEP + media)
A7 – 2×10^5 cells/well	(1.0% MTH/1000 $\mu\text{g/ml}$ DEP + media)	B7 – 2×10^5 cells/well	(1.0% MTH/1000 $\mu\text{g/ml}$ DEP + media)
A8 – media only	(media only)	B8 – media only	(media only)

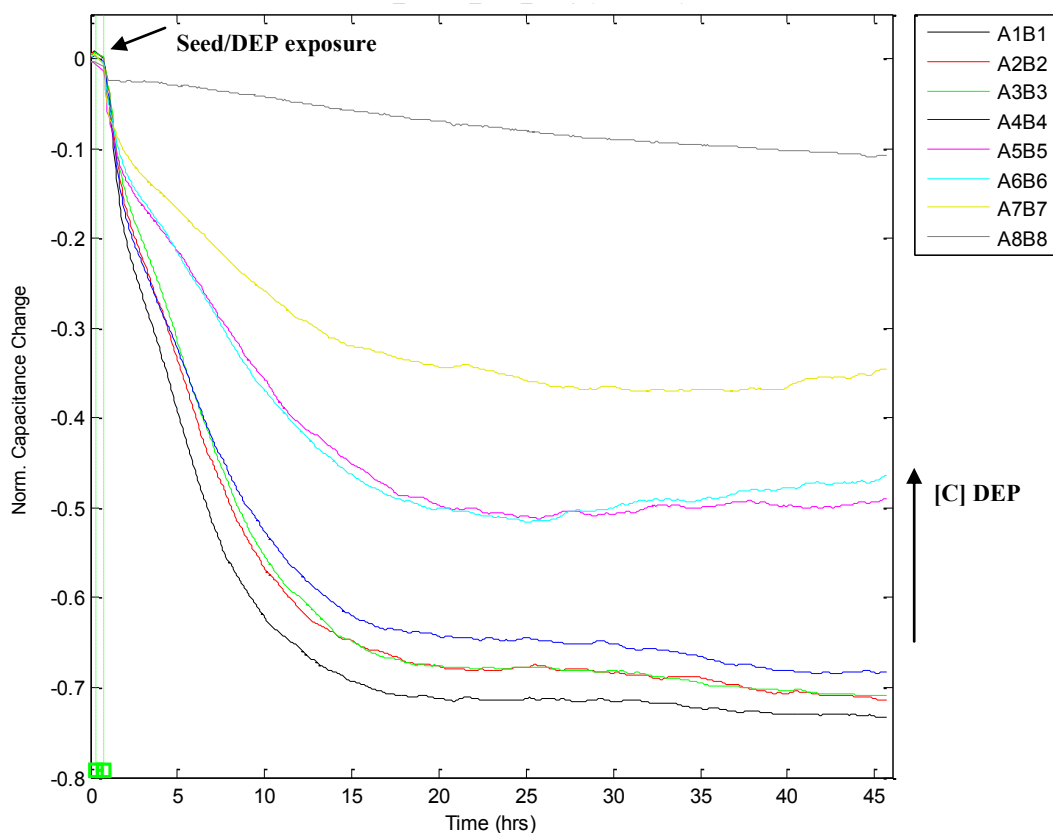


Figure 6.20. Two 8W10E+ arrays were seeded with 2×10^5 cells/ml + DEP/MTH (A1 – A7 and B1 – B7) and culture media in the other two wells (A8 and B8). A549 cells become confluent at ~15 – 20 hours.

In Figure 6.20, the arrow indicates increasing concentration of DEP, the highest three concentrations (250, 500, and 1000 $\mu\text{g/ml}$) tend to interrupt the attachment of cells as illustrated by increasing capacitance values (compare 15 – 30 hours among averaged wells in Figure 6.20). The middle concentration (100 $\mu\text{g/ml}$) also affect the cells as indicated with the increase in capacitance compared to the lower concentrations (10 and 25 $\mu\text{g/ml}$), which do not seem to affect the adherent cells as adversely as the higher concentrations (250, 500, and 1000 $\mu\text{g/ml}$). Control wells continued to have the lowest raw capacitance values ($\sim 15 - 16$ nF). As seen previously in Figure 6.3, the attached cells treated with DEP and the concurrent mixture of cells and DEP prior to seeding yield very similar trends. The lowest concentrations (10 and 25 $\mu\text{g/ml}$) appear to do the least amount of damage whereas the highest concentrations (250, 500, and 1000 $\mu\text{g/ml}$ DEP) cause the greatest increase in capacitance compared to control.

6.5.2.2 Multi-electrode monitoring of effects for DEP exposed cells versus DEP + RES treated cells and wound healing

Figure 6.21 and Figure 6.22 were setup according to Table 6.11, where two 8W10E+ arrays were seeded with 2×10^5 cells/well that were treated with either increasing amounts of DEP (array A) or DEP plus 10 μM resveratrol (array B). After 23 hours, both arrays were wounded and allowed to recover until termination at ~ 45 hours.

There are two main differences that are readily observed between Figure 6.21 (array A) and Figure 6.22 (array B). In Figure 6.21 the attachment and proliferation follow a similar trend when compared with Figure 6.20; where there is an overall decrease in the capacitance values with increasing DEP concentrations. In Figure 6.22,

Table 6.11. Array seeding density and treatment for array A in Figure 6.21 and B in Figure 6.22.

A1 – 2×10^5 cells/well	(media only)	B1 – 2×10^5 cells/well	(media+ 10 μ M RES)
A2 – 2×10^5 cells/well	(0.01% MTH/2 μ g/ml DEP + media)	B2 – 2×10^5 cells/well	(0.01% MTH/2 μ g/ml DEP + media + 10 μ M RES)
A3 – 2×10^5 cells/well	(0.025% MTH/7 μ g/ml DEP + media)	B3 – 2×10^5 cells/well	(0.025% MTH/7 μ g/ml DEP + media + 10 μ M RES)
A4 – 2×10^5 cells/well	(0.1% MTH/20 μ g/ml DEP + media)	B4 – 2×10^5 cells/well	(0.1% MTH/20 μ g/ml DEP + media + 10 μ M RES)
A5 – 2×10^5 cells/well	(0.25% MTH/50 μ g/ml DEP + media)	B5 – 2×10^5 cells/well	(0.25% MTH/50 μ g/ml DEP + media + 10 μ M RES)
A6 – 2×10^5 cells/well	(0.5% MTH/100 μ g/ml DEP + media)	B6 – 2×10^5 cells/well	(0.5% MTH/100 μ g/ml DEP + media + 10 μ M RES)
A7 – 2×10^5 cells/well	(1.0% MTH/500 μ g/ml DEP + media)	B7 – 2×10^5 cells/well	(1.0% MTH/500 μ g/ml DEP + media + 10 μ M RES)
A8 – media only	(media only)	B8 – media only	(media + 10 μ M RES)

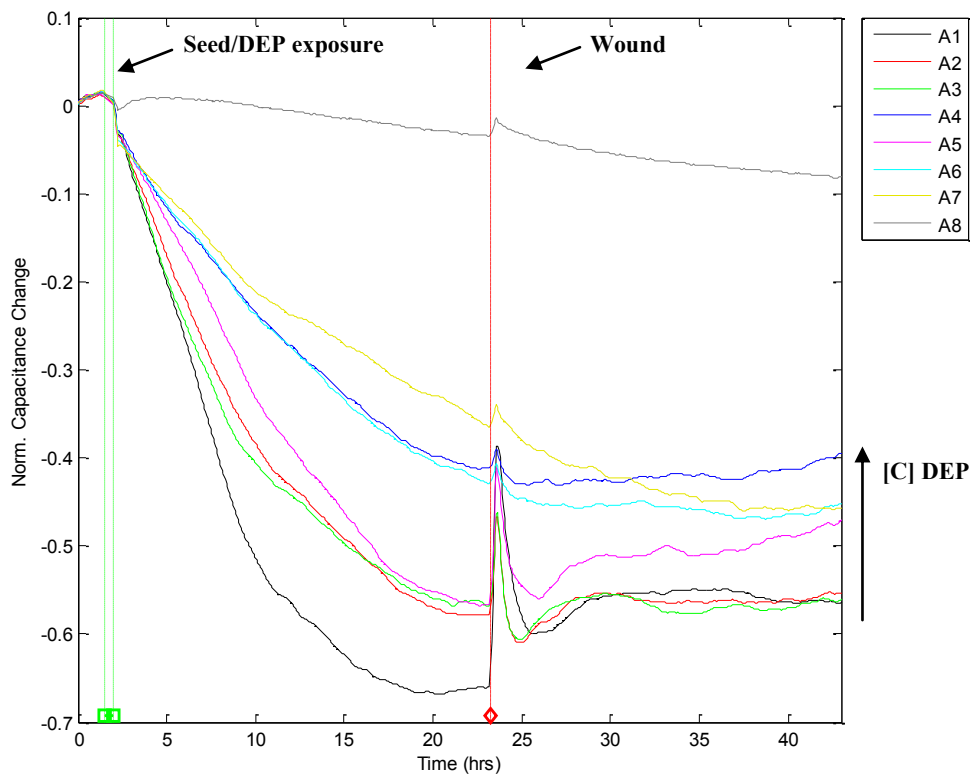


Figure 6.21. Array A (8W10E+ array) seeded with 2×10^5 cells/ml of A549 + media/DEP (A1–A7) and culture medium in A8. Cells were monitored until approximately confluent (~23 hours) and were wounded at 6500 μ A, 20 seconds, and 60 kHz.

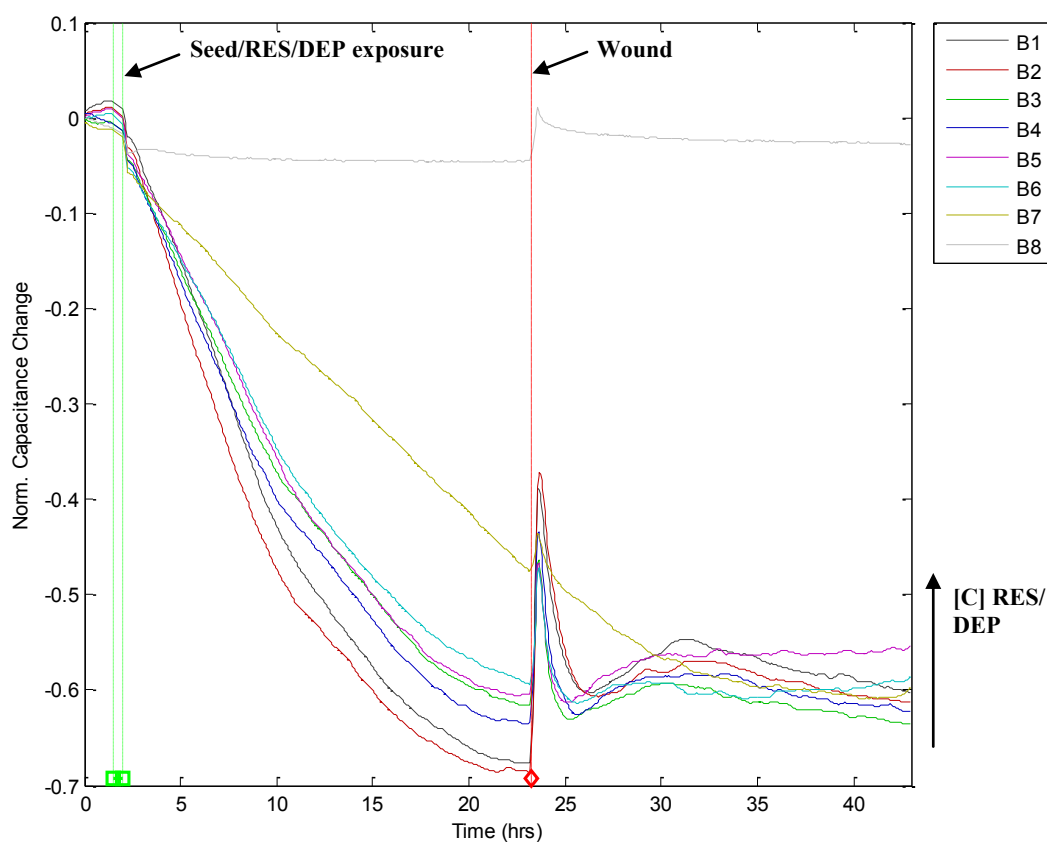


Figure 6.22. Array B (8W10E+ array) seeded with 2×10^5 cells/ml of A549 + media/RES/DEP (B1–B7) and culture medium + RES in B8. Cells were monitored until approximately confluent (~ 23 hours) and were wounded at $6500 \mu\text{A}$, 20 seconds, and 60 kHz.

the DEP plus $10 \mu\text{M}$ resveratrol mixture combined with cells prior to seeding have a negligible effect on the capacitance values except for the greatest amount of DEP ($1000 \mu\text{g/ml}$) used in well B7. The respective profile in Figure 6.22 is more similar to the untreated wells in Figure 6.19 when compared to the DEP exposed wells in Figure 6.20, and Figure 6.21. The partially wounded cells in both Figure 6.21 and Figure 6.22 appear to recover quickly and surprisingly those that were treated with resveratrol are very similar in final capacitive values. Based on the smaller spread of the profiles in Figure

6.22 compared to Figure 6.21, it appears that resveratrol inhibits the DEP damage to cells more easily when mixed directly with DEP (compare Figure 6.4, Figure 6.5, and Figure 6.6).

6.5.2.3 *Single-electrode monitoring of DEP + RES treated cells and wounding versus non-wounding*

Figure 6.23 and Figure 6.24 were both setup according to Table 6.12, where two 8W1E arrays were seeded with 2×10^5 cells/well that were treated with increasing amounts of DEP plus 10 μ M resveratrol. After 25 hours, array B was wounded and both arrays were allowed to continue in culture another ~45 hours.

Table 6.12. Array seeding density and treatment for array A in Figure 6.23 and B in Figure 6.24.

A1 – 2×10^5 cells/well	(serum containing media + 10 μ M RES)	B1 – 2×10^5 cells/well	(serum containing media + 10 μ M RES)
A2 – 2×10^5 cells/well	(serum containing media + 10 μ M RES + 50 μ g/ml DEP)	B2 – 2×10^5 cells/well	(serum containing media + 10 μ M RES + 50 μ g/ml DEP)
A3 – 2×10^5 cells/well	(serum containing media + 10 μ M RES + 125 μ g/ml DEP)	B3 – 2×10^5 cells/well	(serum containing media + 10 μ M RES + 125 μ g/ml DEP)
A4 – 2×10^5 cells/well	(serum containing media + 10 μ M RES + 500 μ g/ml DEP)	B4 – 2×10^5 cells/well	(serum containing media + 10 μ M RES + 500 μ g/ml DEP)
A5 – 2×10^5 cells/well	(serum containing media + 10 μ M RES)	B5 – 2×10^5 cells/well	(serum containing media + 10 μ M RES)
A6 – 1.0×10^5 cells/well	(serum containing media + 10 μ M RES + 50 μ g/ml DEP)	B6 – 1.0×10^5 cells/well	(serum containing media + 10 μ M RES + 50 μ g/ml DEP)
A7 – 2×10^5 cells/well	(serum containing media + 10 μ M RES + 125 μ g/ml DEP)	B7 – 2×10^5 cells/well	(serum containing media + 10 μ M RES + 125 μ g/ml DEP)
A8 – 2×10^5 cells/well	(serum containing media + 10 μ M RES + 500 μ g/ml DEP)	B8 – 2×10^5 cells/well	(serum containing media + 10 μ M RES + 500 μ g/ml DEP)

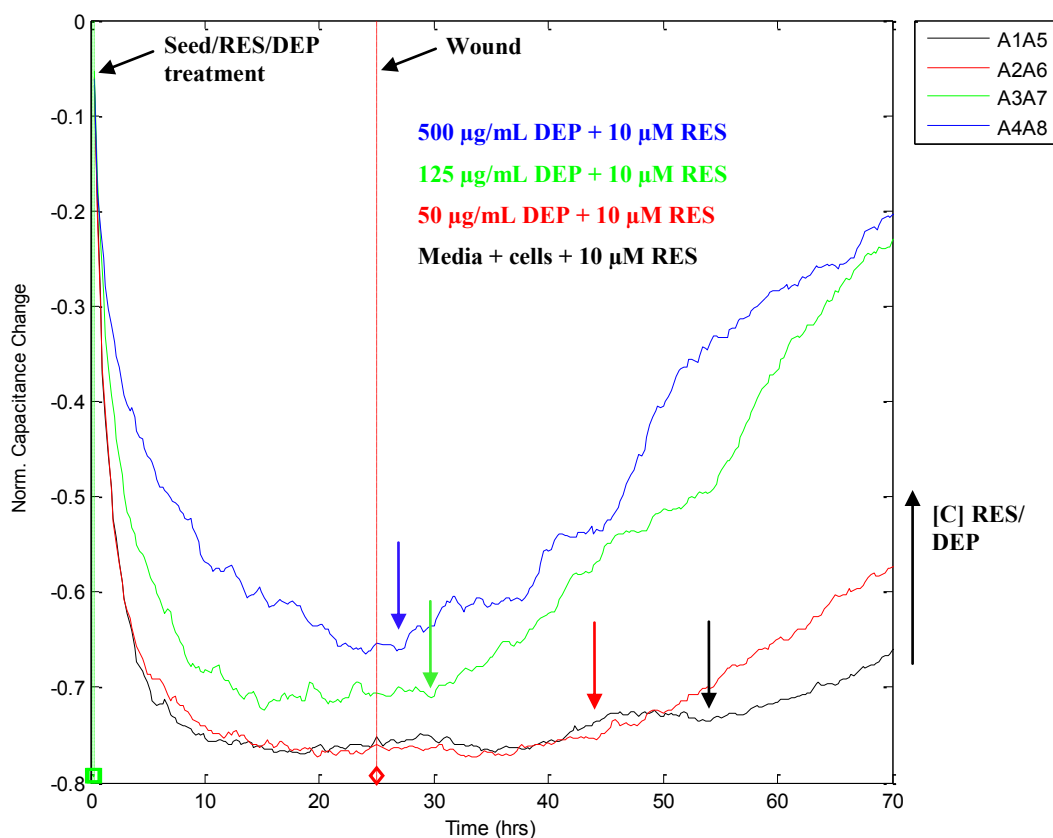


Figure 6.23. Array A (8W1E array) was seeded with 2×10^5 cells/ml of A549 + DEP (50, 125, and 500 $\mu\text{g/ml}$) + 10 μM resveratrol (A1–A8 and B1–B8) and cells were allowed to become confluent. After ~ 28 hours, the arrays were then wounded (B1–B8 @ 180 seconds, 3000 μA and 60 kHz), then the wells were allowed to recover.

Figure 6.24 illustrates a similar setup when compared to Figure 6.15; however, this time the recovery follows a different pattern where the best recovery is the media control, then the 125 $\mu\text{g/ml}$, followed by 50 $\mu\text{g/ml}$, and finally 500 $\mu\text{g/ml}$ DEP. Although the trend of increasing DEP concentration does not follow suit with decreasing viability for Figure 6.10, Figure 6.24, or Figure D6.38; it does follow a similar pattern for both Figure 6.16 and Figure 6.23.

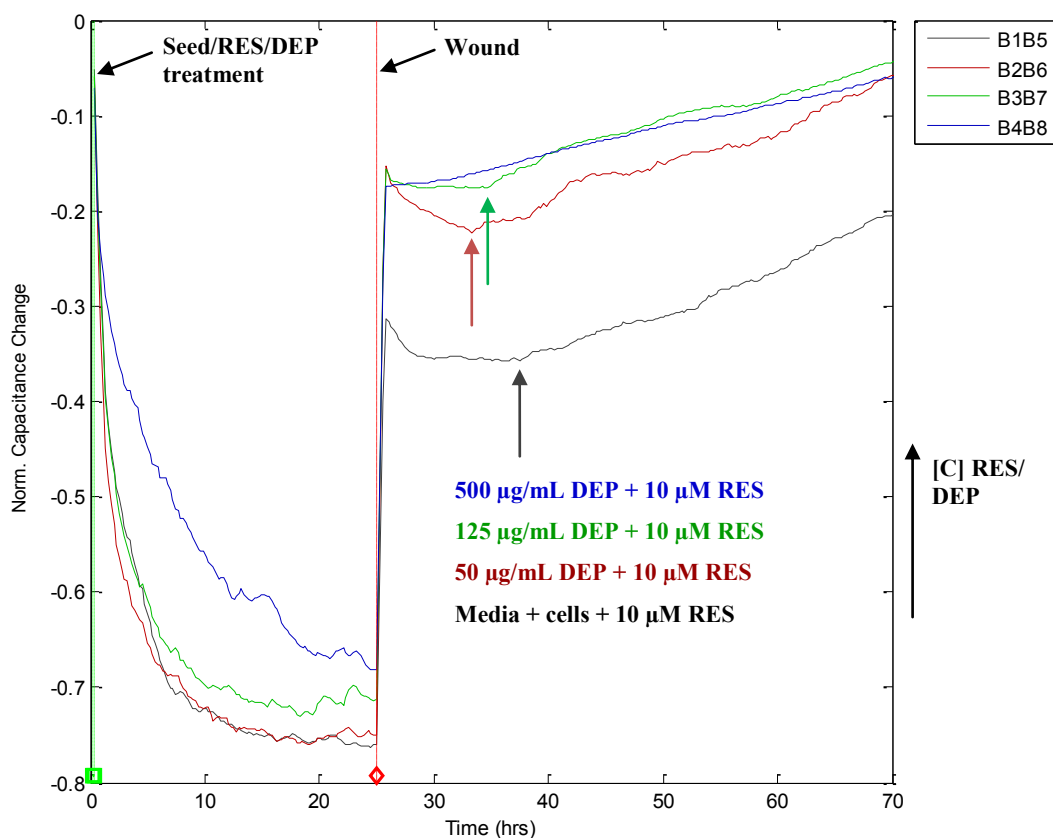


Figure 6.24. Array B (8W1E array) was seeded with 2×10^5 cells/ml of A549 + DEP (50, 125, and 500 $\mu\text{g/ml}$) + 10 μM RES (A1–A8 and B1–B8) and cells were allowed to become confluent. After ~ 28 hours, the arrays were then wounded (B1–B8 @ 180 seconds, 3000 μA and 60 kHz), then the wells were allowed to recover.

In summary Approach #2, like Approach #1, showed similar results for methanol treatment where methanol was not readily toxic to cells and increasing concentrations of DEP were toxic to A549 cells. Also, DEP treated cells that are wounded do not fully recover; however, resveratrol aids in protecting cells from DEP toxicity and in wound healing. Moreover, extensive wounding ultimately leads to no recovery of DEP exposed cell as well as control cells.

6.6 RAMAN MICROSPECTROSCOPY

6.6.1 Raman spectra and light images of DEP exposure A549 with and without resveratrol protection

Raman microspectroscopy (RM) was performed to better understand induced biochemical changes and analyze cellular bio-compositions of single A549 cells using two concentrations of DEP (25 and 50 $\mu\text{g/ml}$) with and without 10 μM resveratrol treatment. Results for confocal Raman spectra and bright field images of A549 cells are illustrated in Figure 6.25, Figure 6.26, and Figure 6.27. Each Raman figure represents four different spectral profiles (nucleus – black, cytoplasm – red, cellular membrane – blue, and background substrate – magenta), which are an average of four individual cells with four spectral acquisitions per cell (16 total spectra per profile). Row 1 shows Raman spectra of A549 control group and rows 2 through 5 show the treated groups over a 48 hour period of culture/DEP exposure (0, 4, 8, 16, 24, and 48 hours). These four imaged locations exhibit biochemical differences among the four cellular locations imaged. For example, the 0 hour figure in row 1 exhibit a peak rich profile for the nucleus (black) and cytoplasm (red) compared with the membrane (blue) and background (magenta). As the culture time increases, for the control group, the Raman bands become more defined and distinguishable with the best resolution at 24 and 48 hours. Notable peaks of interest are located at ~ 720 , 940, 1006, and 1451 cm^{-1} and are representative of DNA, carbohydrates, proteins, and lipids. Furthermore, changes in Raman spectra of A549 cells with respect to increases in DEP exposure time combined with 10 μM resveratrol treatments are seen in rows 2 – 5. The 0 hour spectra for each of the treated groups illustrate the best Raman resolution (with the exception of anomalies in the 25 $\mu\text{g/ml}$ DEP control group). In the 4

– 48 hour treated groups, DEP exposure illicit two broad fluorescent bands at ~ 1320 and $\sim 1620 \text{ cm}^{-1}$, which overpower all but the strongest Raman bands (1006 and 1451 cm^{-1}). Figure D6.41-A is a Raman spectrum of DEP acquired in air and it illustrates two main peaks (1318 and 1600 cm^{-1}) that are associated with crystalline graphite and are commonly referred to in literature as disorder-induced models D and D', respectively [33, 34]. Figure D6.41-A shows a similar overall trend as seen in Figure 6.25, Figure 6.26, and Figure 6.27 for the DEP treated samples. Figure D6.41-B is a bright field image of DEP powder. Additional morphology of amorphous clusters can be seen in Figure D6.42-A through -D, where DEP clusters range in size from $3.0 \mu\text{m}$, 500 nm , 333 nm , and 231 nm .

Likewise, Figure D6.43-A is a Raman spectrum for dry resveratrol powder; which is rich with many Raman bands. Figure D6.44 is an overlay of Raman spectra for A549, DEP, and resveratrol. This figure illustrates how crystalline solids give intense Raman bands and produce a peak rich spectrum that can be used as a “finger-print” for Raman active substances. However, due to the low concentration of resveratrol in our aqueous medium, and overlapping peaks from A549 and DEP, it is difficult to pin-point a specific characteristic band or bands for resveratrol. Therefore, more data mining is necessary to achieve these specific bands and a way to segregate information. RM spectral peak assignments of A549 cells had been given in the literatures [35-39] and are listed in Table 4.1. Moreover, Raman spectra show significant differences of overall spectral patterns between row 1 (control groups) and rows 2 - 5 (treatment groups) and can be seen in Figure 6.25, Figure 6.26, and Figure 6.27. Bright field images show the overall morphology of the cells versus time and DEP exposure. Clumps of DEP can be seen and

are similar to the previous images of the ECIS arrays (compare Figure 6.11, Figure 6.12, Figure 6.17, Figure 6.18, Figure 5.6, and Figure D6.37) and other images in Figure D6.42 and Figure D6.43.

6.6.2 Hierarchical Cluster Analysis of DEP exposed A549 with and without resveratrol protection

The dendrogram in Figure 6.28 and Figure 6.29 show the heterogeneity of each group location (nucleus, cytoplasm, membrane, and background) for the control (red), 25 $\mu\text{g/ml}$ DEP (green), and 50 $\mu\text{g/ml}$ DEP (blue) treated groups versus time. Whereas Figure 6.30 and Figure 6.31 show dendrogram, grouped by location, of the control (red), 25 $\mu\text{g/ml}$ DEP (green), and 25 $\mu\text{g/ml}$ DEP + 10 μM RES (blue) treated cells versus time. These statistical evaluations of the RM spectra showed that there are inherent compositional differences among the different locations on A549 cells and that these biochemical changes of A549 cells were time-dependent. Such results indicated heterogeneity property of mammalian cells and hierarchical cluster analysis (HCA) conducted on multiple spectra showed that RM could achieve detection and identification of specific molecular components and biochemical changes such as nucleic acids, lipids and proteins at the single cell level.

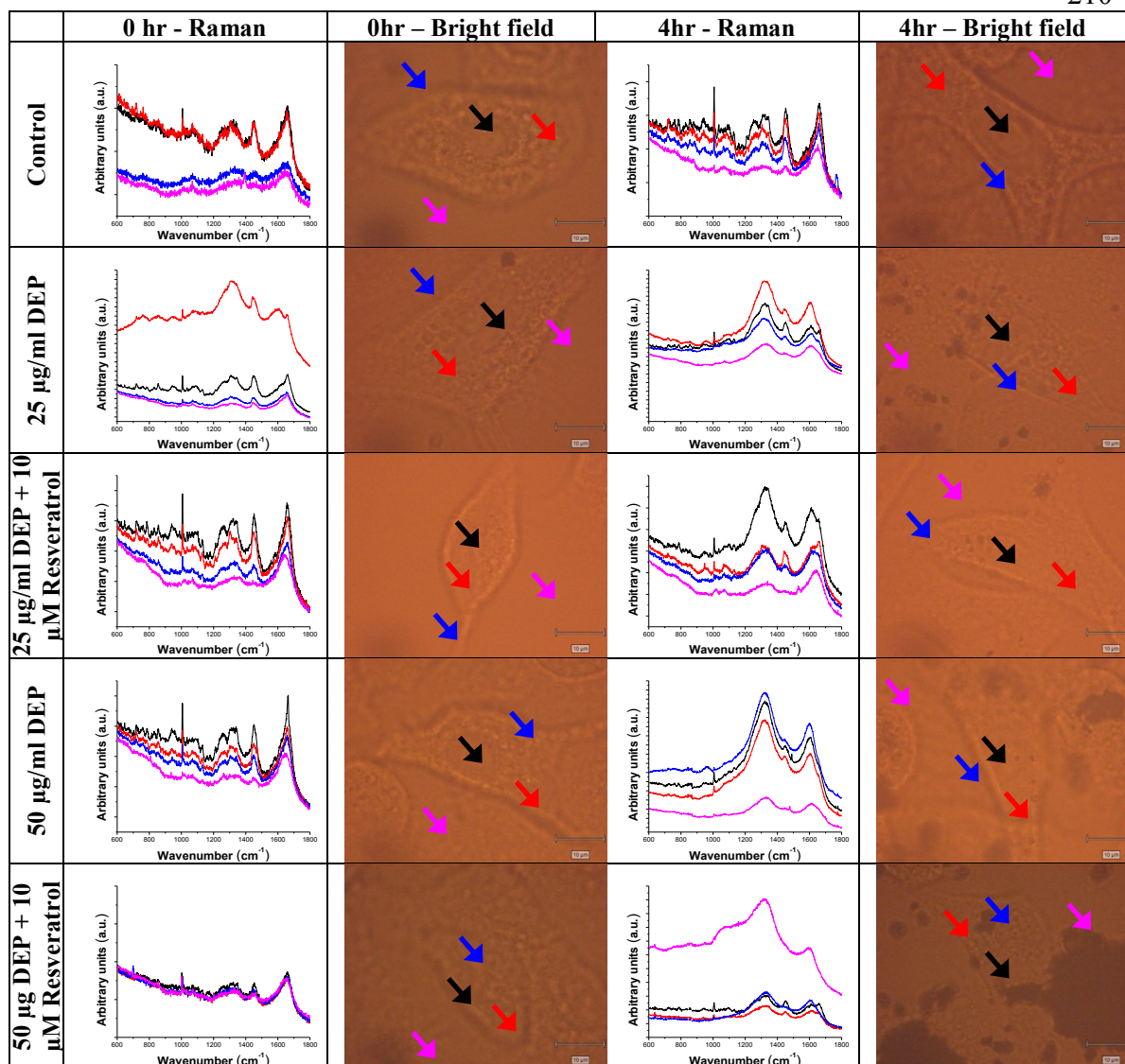


Figure 6.25. Raman spectra and bright field images of A549 cells during culture/treatment. Row 1 – Raman spectra of untreated A549 cells for 0 and 4 hours of culture. Row 2 – Raman spectra of 25 µg/ml DEP treated A549 cells. Row 3 – Raman spectra of 25 µg/ml DEP + 10 µM RES treated A549 cells. Row 4 – Raman spectra of 50 µg/ml DEP treated A549 cells. Row 5 – Raman spectra of 50 µg/ml DEP + 10 µM RES treated A549 cells. Each Raman spectral profile represent the following locations of A549; nucleus (black), cytoplasm (red), cellular membrane (blue), and background substrate (magenta) and corresponding arrows accompany bright filed images. Raman spectra are an average of four spectra per cell for four separate imaged cells (16 total spectra per profile). Scale bar = 10 µm.

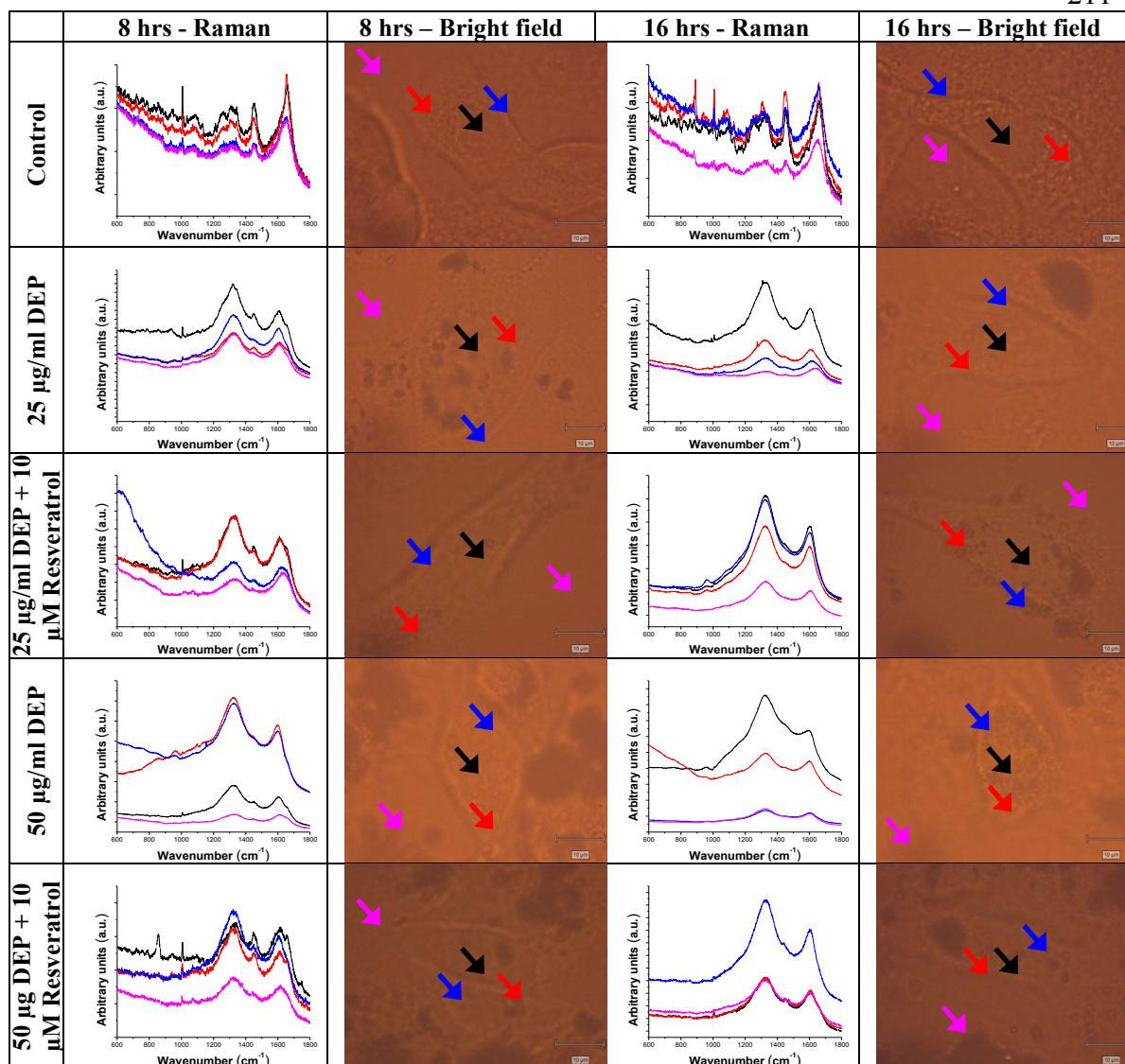


Figure 6.26. Raman spectra and bright field images of A549 cells during culture/treatment. Row 1 – Raman spectra of untreated A549 cells for 8 and 16 hours of culture. Row 2 – Raman spectra of 25 µg/ml DEP treated A549 cells. Row 3 – Raman spectra of 25 µg/ml DEP + 10 µM RES treated A549 cells. Row 4 – Raman spectra of 50 µg/ml DEP treated A549 cells. Row 5 – Raman spectra of 50 µg/ml DEP + 10 µM RES treated A549 cells. Each Raman spectral profile represent the following locations of A549; nucleus (black), cytoplasm (red), cellular membrane (blue), and background substrate (magenta) and corresponding arrows accompany bright filed images. Raman spectra are an average of four spectra per cell for four separate imaged cells (16 total spectra per profile). Scale bar = 10 µm.

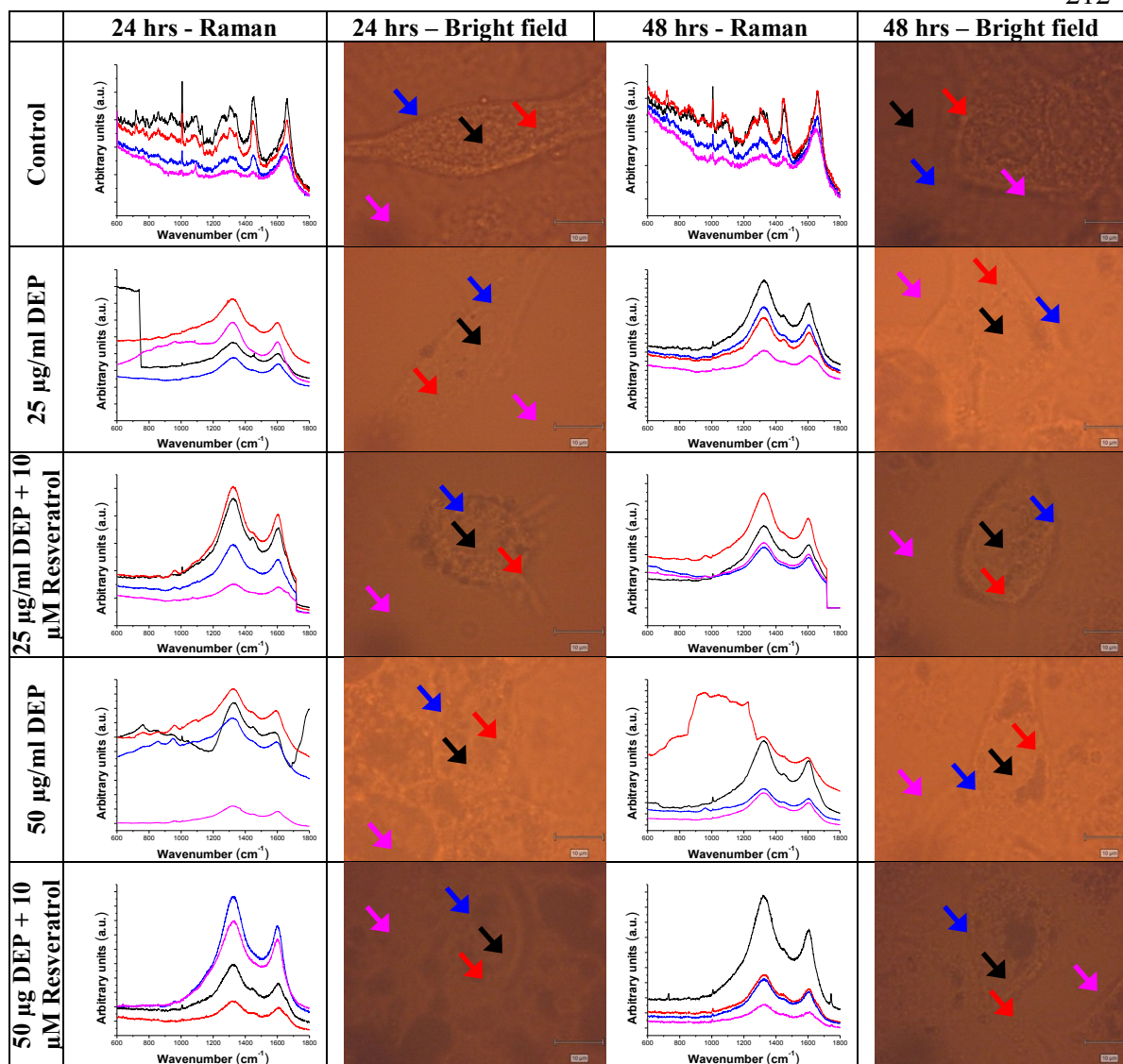


Figure 6.27. Raman spectra and bright field images of A549 cells during culture/treatment. Row 1 – Raman spectra of untreated A549 cells for 24 and 48 hours of culture. Row 2 – Raman spectra of 25 µg/ml DEP treated A549 cells. Row 3 – Raman spectra of 25 µg/ml DEP + 10 µM RES treated A549 cells. Row 4 – Raman spectra of 50 µg/ml DEP treated A549 cells. Row 5 – Raman spectra of 50 µg/ml DEP + 10 µM RES treated A549 cells. Each Raman spectral profile represent the following locations of A549; nucleus (black), cytoplasm (red), cellular membrane (blue), and background substrate (magenta) and corresponding arrows accompany bright filed images. Raman spectra are an average of four spectra per cell for four separate imaged cells (16 total spectra per profile). Scale bar = 10 µm

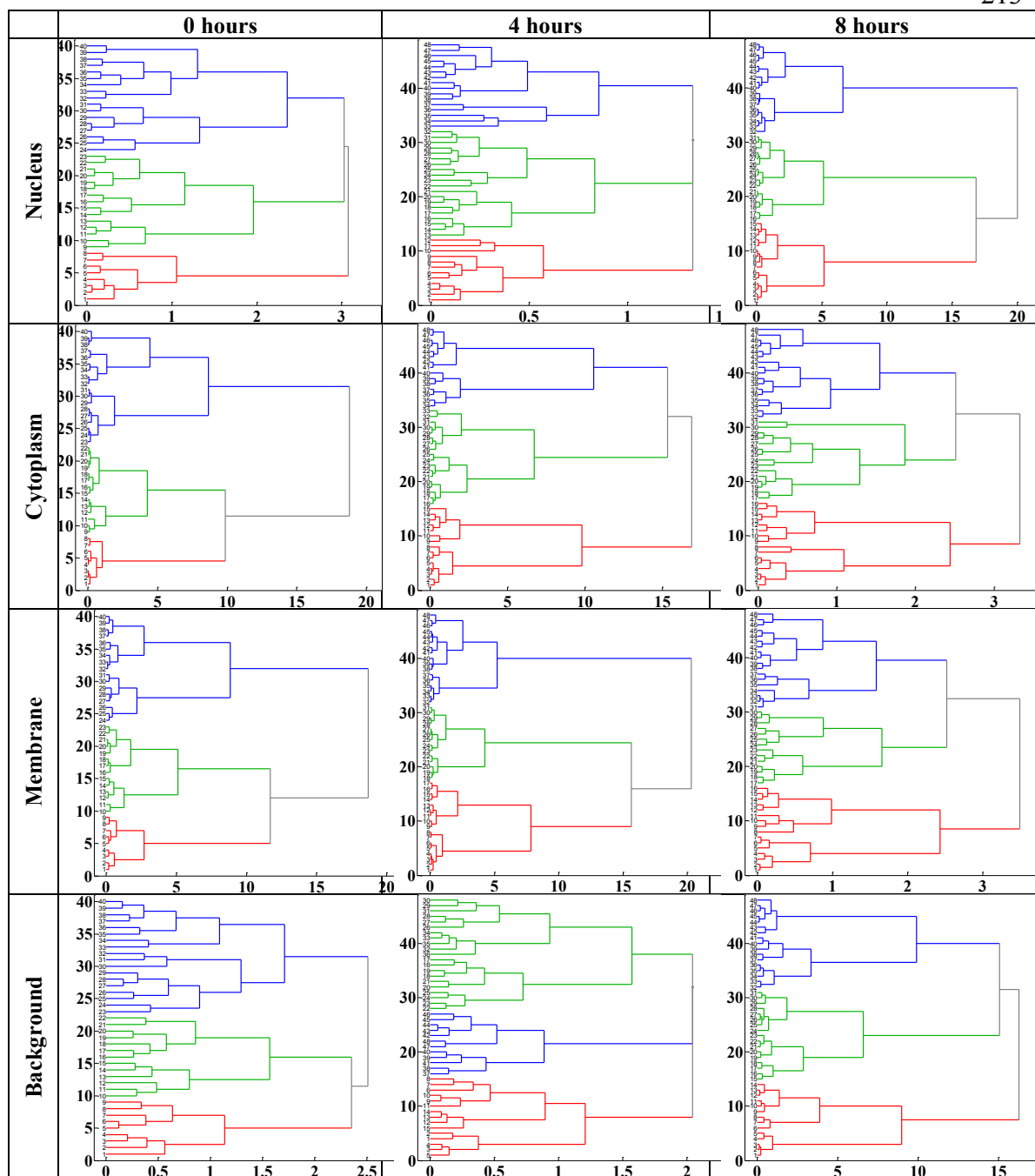


Figure 6.28. Dendrogram obtained by hierarchical cluster analysis of Raman spectra of A549 cells during 48 hour culture period. Each tree, three per figure, represent a different set of cell culture treatment conditions; control (red), 25 $\mu\text{g/ml}$ DEP (green), and 50 $\mu\text{g/ml}$ DEP (blue). Row 1 – Dendrogram clusters of A549 nucleus at 0, 4, and 8 hours of culture. Row 2 – Dendrogram clusters of A549 cytoplasm. Row 3 – Dendrogram clusters of A549 membrane. Row 4 – Dendrogram clusters of A549 background.

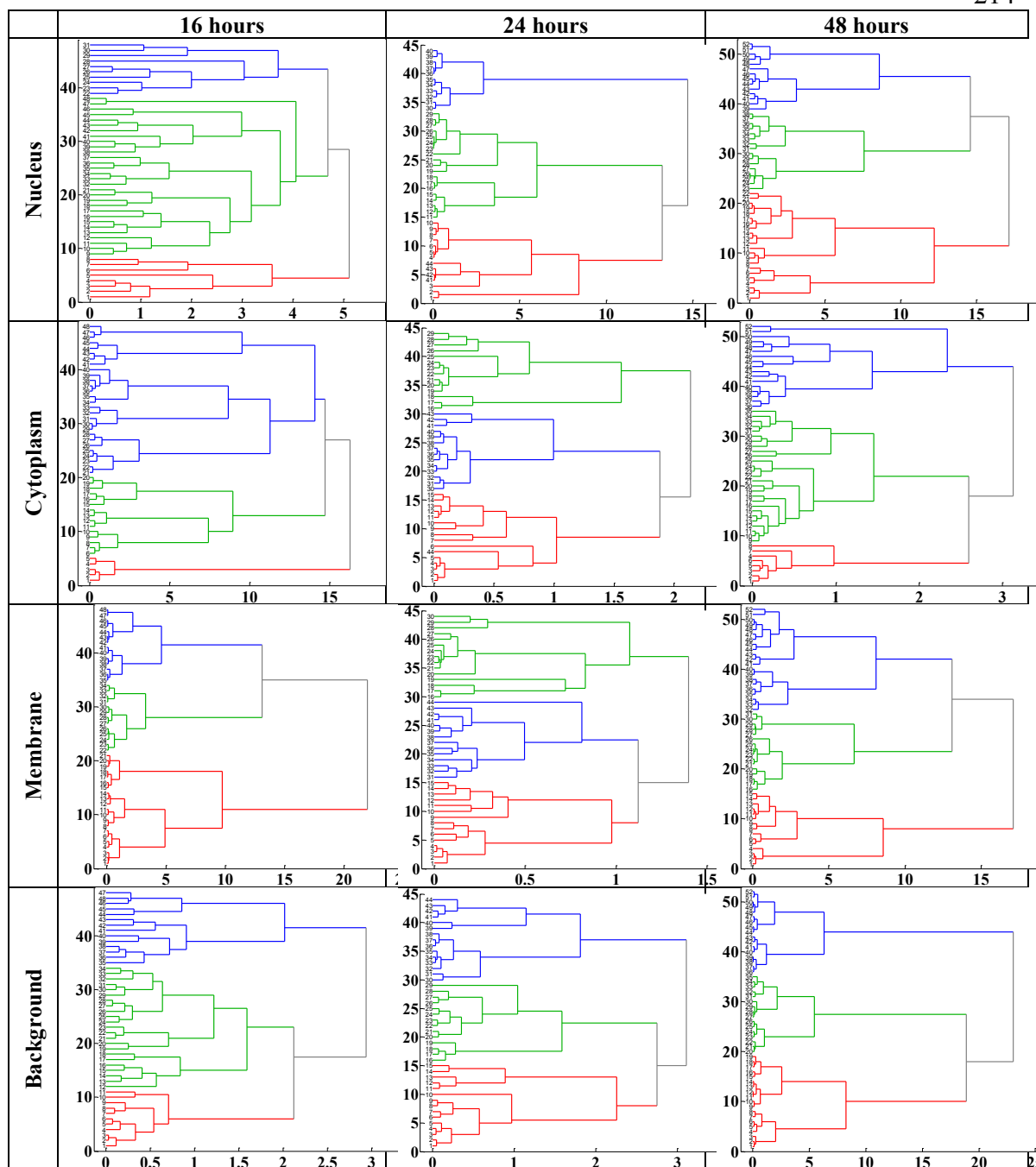


Figure 6.29. Dendrogram obtained by hierarchical cluster analysis of Raman spectra of A549 cells during 48 hour culture period. Each tree, three per figure, represent a different set of cell culture treatment conditions; control (red), 25 $\mu\text{g/ml}$ DEP (green), and 50 $\mu\text{g/ml}$ DEP (blue). Row 1 – Dendrogram clusters of A549 nucleus at 16, 24, and 48 hours of culture. Row 2 – Dendrogram clusters of A549 cytoplasm. Row 3 – Dendrogram clusters of A549 membrane. Row 4 – Dendrogram clusters of A549 background.

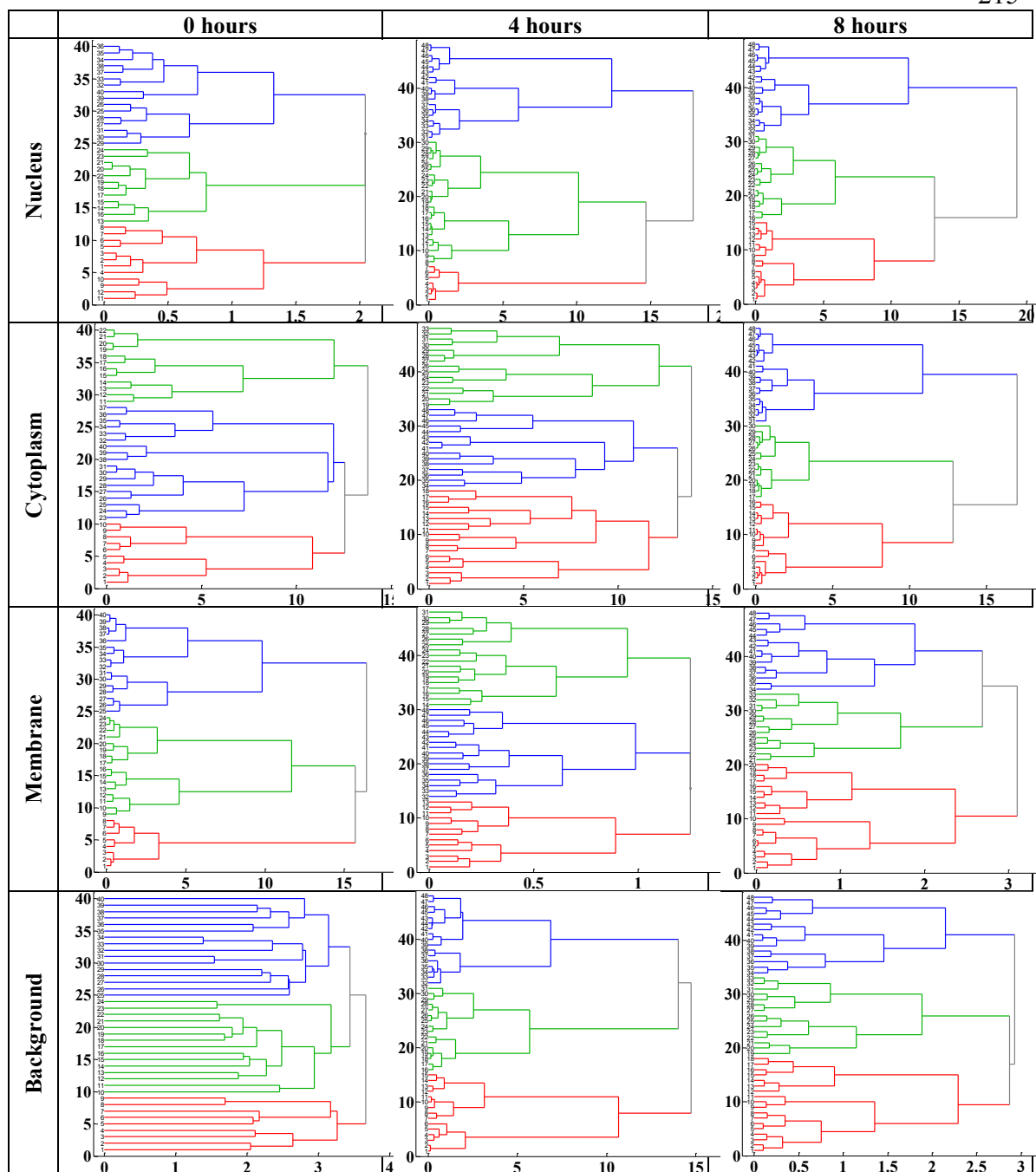


Figure 6.30. Dendrogram obtained by hierarchical cluster analysis of Raman spectra of A549 cells during 48 hour culture period. Each tree, three per figure, represent a different set of cell culture treatment conditions; control (red), 25 $\mu\text{g/ml}$ DEP (green), and 25 $\mu\text{g/ml}$ DEP + 10 μM RES (blue). Row 1 – Dendrogram clusters of A549 nucleus at 0, 4, 8, 16, 24, and 48 hours of culture. Row 2 – Dendrogram clusters of A549 cytoplasm. Row 3 – Dendrogram clusters of A549 membrane. Row 4 – Dendrogram clusters of A549 background.

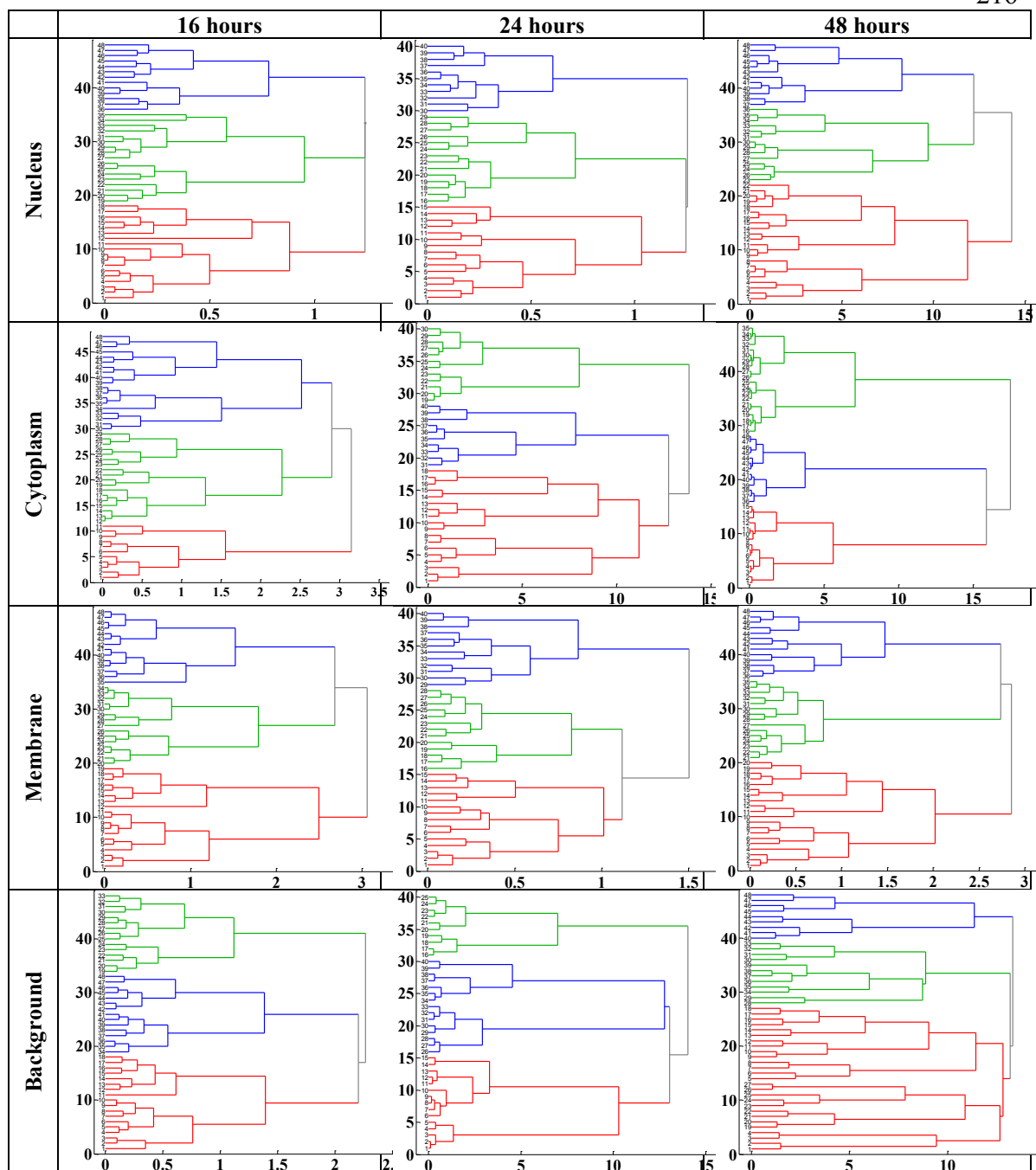


Figure 6.31. Dendrogram obtained by hierarchical cluster analysis of Raman spectra of A549 cells during 48 hour culture period. Each tree, three per figure, represent a different set of cell culture treatment conditions; control (red), 25 µg/ml DEP (green), and 25 µg/ml DEP + 10 µM RES (blue). Row 1 – Dendrogram clusters of A549 nucleus at 0, 4, 8, 16, 24, and 48 hours of culture. Row 2 – Dendrogram clusters of A549 cytoplasm. Row 3 – Dendrogram clusters of A549 membrane. Row 4 – Dendrogram clusters of A549 background.

6.7 CONCLUSION

In conclusion, ECIS makes it possible to non-invasively real-time monitor cell behavior and related morphological activities of mammalian cells in culture. This can provide insight into cell integrity and viability, be used to screen toxic substances and agents that protect against toxicity (i.e. pharmaceuticals, biologicals, etc.), and to quantify mobility/migration rates. This was important in our studies to explore the toxicity of DEP to A549 cells and protective activities of resveratrol for DEP treated cells.

It was found that increasing concentrations of methanol were not toxic to A549 cells, however increasing concentrations of DEP begin to interfere with cell integrity and lead to cell death and detachment compared to control. Concentrations greater than 125 $\mu\text{g/ml}$ appear to cause cytotoxic response in A549 and leads to outright cell death. The lower concentrations of DEP (10, 25, and 100 $\mu\text{g/ml}$) had no effect to mild genotoxic responses in A549 cells. Moreover, treatment with 10 μM resveratrol exhibits protective effects against cell death, notably, for DEP concentrations that are not readily cytotoxic to cells (2, 7, 10, 25, 100, and 125 $\mu\text{g/ml}$). Also it was observed that resveratrol had a visible effect on cell micro-motion, which could be linked to cell survival and recovery. DEP treated cells that are wounded did not fully recover however resveratrol did aid to protect cells from DEP toxicity and in wound healing. Finally, extensive wounding ultimately lead to non-recovery of DEP exposed and control cells and further studies with additional epithelial cell lines would reveal more information for barrier function and recovery from DEP exposure and resveratrol treatment.

In future work, the multi-frequency modeling could provide more information into cell mobility/migration rates, barrier resistance (R_b), current flow (α), and average

capacitance of cell plasma membrane (C_m). These values might then be further used to elucidate particular morphological changes on the cellular level.

Raman microspectroscopy also provided insight into the biochemical response of A549 cells when exposed to DEP. These responses were based on biochemical changes in Raman bands characteristic of nucleic acid, protein, carbohydrate, and lipid concentrations and with respect to culture/treatment time. RM findings suggest that, under our current experiment conditions, DEP mediated cell death involved a decrease in DNA ($726, 782, 788 \text{ cm}^{-1}$) and a decrease in protein (1006 and 1037 cm^{-1}) of the cells. Raman further illustrated that cellular viability decreases with time and exposure to increasing DEP concentrations. This is evident in the light images (similar to Figure 5.6 and Figure D6.37), where morphology visibly changes with time and DEP exposure. These findings suggest DEP exposure could be triggering important biochemical and biophysical changes that are interrelated with pathological changes of human lung cells, providing further insights into cytotoxicity of DEP to human lung cells.

6.8 REFERENCES

- [1] R.A. Lockshin, J. Beaulaton, *Life Sci.* 15 (1974) 1549.
- [2] J.J. Wang, B.J.S. Sanderson, H. Wang, *Mutat. Res.-Gen. Tox. En.* 628 (2007) 99.
- [3] I. Giaever, C.R. Keese, *P. Natl. Acad. Sci.* 81 (1984) 3761.
- [4] I. Giaever, C.R. Keese, *P. Natl. Acad. Sci.* 88 (1991) 7896.
- [5] J. Wegener, C.R. Keese, I. Giaever, *Exp. Cell Res.* 259 (2000) 158.
- [6] C. Xiao, B. Lachance, G. Sunahara, J.H.T. Luong, *Anal. Chem.* 74 (2002) 5748.
- [7] C.R. Keese, J. Wegener, S.R. Walker, I. Giaever, *P. Natl. Acad. Sci. USA* 101 (2004) 1554.
- [8] I.H. Heijink, S.M. Brandenburg, J.A. Noordhoek, D.S. Postma, D.J. Slebos, A.J.M. van Oosterhout, *Eur. Respir. J.* 35 (2010) 894.

- [9] J. Hong, K. Kandasamy, M. Marimuthu, C.S. Choi, S. Kim, *Analyst* 136 237.
- [10] J. Ling, S.D. Weitman, M.A. Miller, R.V. Moore, A.C. Bovik, *Appl. Opt.* 41 (2002) 6006.
- [11] D.W. Ball, *Spectroscopy* 16 (2001) 32.
- [12] D. Pappas, B.W. Smith, J.D. Winefordner, *Talanta* 51 (2000) 131.
- [13] P. Carey, *Trac-Trend. Anal. Chem.* 2 (1983) 275.
- [14] P. Hildebrandt, S. Lecomte, C.L. John, *Encyclopedia of Spectroscopy and Spectrometry*, Elsevier, Oxford, 1999, p. 88.
- [15] H. Fabian, P. Anzenbacher, *Vib. Spectrosc.* 4 (1993) 125.
- [16] J.R. Baena, B. Lendl, *Curr. Opin. Chem. Biol.* 8 (2004) 534.
- [17] F.M. Lyng, E.Ó. Faoláin, J. Conroy, A.D. Meade, P. Knief, B. Duffy, M.B. Hunter, J.M. Byrne, P. Kelehan, H.J. Byrne, *Exp. Mol. Pathol.* 82 (2007) 121.
- [18] C.M. Krishna, G.D. Sockalingum, G. Kegelaer, S. Rubin, V.B. Kartha, M. Manfait, *Vib. Spectrosc.* 38 (2005) 95.
- [19] C. Yu, E. Gestl, K. Eckert, D. Allara, J. Irudayaraj, *Cancer Detect. Prev.* 30 (2006) 515.
- [20] K.W. Short, S. Carpenter, J.P. Freyer, J.R. Mourant, *Biophys. J.* 88 (2005) 4274.
- [21] H. Abramczyk, J. Surmacki, B. Brozek-Pluska, Z. Morawiec, M. Tazbir, *J. Mol. Struct.* 924-926 (2009) 175.
- [22] I. Notingher, *Sensors* 7 (2007) 1343.
- [23] C.A. Lieber, A. Mahadevan-Jansen, *Appl. Spectrosc.* 57 (2003) 1363.
- [24] J. Zhao, H. Lui, D.I. McLean, H. Zeng, *Appl. Spectrosc.* 61 (2007) 1225.
- [25] F.W.L. Esmonde-White, M.V. Schulmerich, K.A. Esmonde-White, M.D. Morris, *Automated Raman spectral preprocessing of bone and other musculoskeletal tissues*, *Optics in Bone Biology and Diagnostics*, SPIE, San Jose, CA, USA, 2009, p. 716605.
- [26] E.M. Kanter, S. Majumder, E. Vargis, A. Robichaux-Viehoever, G.J. Kanter, H. Shappell, I. Howard, W. Jones, A. Mahadevan-Jansen, *J. Raman Spectrosc.* 40 (2009) 205.
- [27] C. Krafft, T. Knetschke, A. Siegner, R.H.W. Funk, R. Salzer, *Vib. Spectrosc.* 32 (2003) 75.
- [28] J.C. Bryant, *Method. Cell Sci.* 1 (1975) 185.

- [29] G. Pyrgiotakis, T.K. Bhowmick, K. Finton, A.K. Suresh, S.G. Kane, J.R. Bellare, B.M. Moudgil, *Biopolymers* 89 (2008) 555.
- [30] M. O'Farrell, E. Lewis, C. Flanagan, W.B. Lyons, N. Jackman, *Sensor. Actuat. B-Chem.* 107 (2005) 104.
- [31] Y. Roggo, L. Duponchel, J.P. Huvenne, *Anal. Chim. Acta* 477 (2003) 187.
- [32] A.K. Jain, Dubes, R. C. (Ed.), *Algorithms for Clustering Data*, Prentice Hall, Englewood Cliffs, NJ, 1988.
- [33] M. Odziemkowski, J.A. Koziel, D.E. Irish, J. Pawliszyn, *Anal. Chem.* 73 (2001) 3131.
- [34] S.K. Sze, N. Siddique, J.J. Sloan, R. Escibano, *Atmos. Environ.* 35 (2001) 561.
- [35] S. Verrier, I. Notingher, J.M. Polak, L.L. Hench, *Biopolymers* 74 (2004) 157.
- [36] I. Notingher, C. Green, C. Dyer, E. Perkins, N. Hopkins, C. Lindsay, L.L. Hench, *J. R. Soc. Interface* 1 (2004) 79.
- [37] C.A. Owen, J. Selvakumaran, I. Notingher, G. Jell, L.L. Hench, M.M. Stevens, *J. Cell. Biochem.* 99 (2006) 178.
- [38] I. Notingher, S. Verrier, S. Haque, J.M. Polak, L.L. Hench, *Biopolymers* 72 (2003) 230.
- [39] I. Notingher, J. Selvakumaran, L.L. Hench, *Biosens. Bioelectron.* 20 (2004) 780.

CHAPTER 7

SUMMARY AND FUTURE DIRECTIONS

7.1 SUMMARY

The overall aim of the various studies performed within the breadth my dissertation was to look at different bio-interfaces by using traditional and non-traditional instrumentation in the specific study designs. A wide-ranging amount of work was performed and the following are a review of the main findings from each of the technical chapters.

In Chapter 2 we observed that the DNA surface density (Γ_{DNA}) changed according to self-assembled monolayer order as follows: $\Gamma_{\text{DNA}} (\text{dsS-DNA/Au}) > \Gamma_{\text{DNA}} (\text{MCH/dsS-DNA/Au}) > \Gamma_{\text{DNA}} (\text{dsS-DNA/MCH/Au})$. The electro-oxidation of the DNA modified gold surface involved the oxidation of guanine and adenine nucleotides with a 5.51 electron transfer rate. The oxidative desorption of DNA and MCH molecules were caused by a 3 electron transfer rate. Also, it was observed that STM topography and current images increased in conductivity according to this order: $\text{dsS-DNA/Au} < \text{MCH/dsS-DNA/Au} < \text{oxidized MCH/dsS-DNA/Au} < \text{Hoechst/oxidized MCH/dsS-DNA/Au}$. Raman identified characteristic peaks for nucleic acids and may prove useful in verifying DNA electro-oxidation. Knowledge of interfacial electron transfer for gold modified surfaces, oxidative damage to DNA related electron transfer, and biochemical information of DNA modified gold surface may lead to better applications for DNA-based biosensors and the rapid detection of pathogenic organisms.

In Chapter 3 AFM and SEM images illustrated similar morphological features of Gram-positive and Gram-negative bacteria. Raman spectra showed that Gram-positive

bacteria contained more specifically defined Raman bands than did Gram-negative bacteria. Also, Gram-positive bacteria contained Raman bands that could be associated with pigmentation. DCLS aided to rapidly distinguish Gram-positive from Gram-negative bacteria even amid our simulated co-cultured strains. FTIR proved insightful for characteristic bands for Gram-positive; however, due to the aqueous sample the final resolution was poor for our particular region of interest. The combined AFM/Raman image revealed a nice colony of Gram-positive bacteria and Raman imaging revealed the areas of highest Raman intensity. Increased number of spectral points within the map or increased acquisition times will yield greater detailed information. Ultimately, this approach may prove useful to identify a mycobacterium species that can be used as a model organism in MTB studies.

Our results from Chapter 4 indicate that both A549, 435 and 435/BRMS1 cell lines contain several similar characteristic Raman bands. Moreover, there is a greater similarity between 435 and 435/BRMS1, respectively. The membrane surface adhesion forces and cell spring constants were measured for each cell line. These showed that 435/BRMS1 had physical forces that were greater than the other two cell lines, and may implicated BRMS1 as the key reason.

In Chapter 5, AFM revealed increases in biomechanical properties for 435/BRMS1 in the areas of cell adhesion, cell spring constant, and Young's modulus. Fluorescent staining showed the F-actin rearrangement for both cell lines. Raman showed a decrease in spectroscopic bands for 435/BRMS1 and implied a decrease in cellular biochemical components of these cells. ECIS revealed that 435 cells adhere

more tightly to substrata and migrate more rapidly compared with the metastasis suppressing cells.

From Chapter 6 it was found that for ECIS, ≤ 10 -fold DEP concentration exposure caused clastogenic DNA degradation whereas ≥ 25 -fold DEP exposure caused cytotoxic results. $10 \mu\text{M}$ treatments with the natural phytoalexin, resveratrol (RES), showed minimal to mild protection against DEP before and after exposure and aided in improving injury recovery. RM also revealed decreases in nucleic acid and protein specific Raman bands.

Toward the end of better understanding bio-interfaces, much of the research focused on the use of mammalian cells and how environmental factors affect their biochemical and biomechanical properties. It would be a good idea to explore ways to compare and correlate findings between RM, AFM, and ECIS.

7.2 FUTURE WORK

7.2.1 Raman outlook

Because a lot of the original work of this dissertation was exploratory, it would be worthwhile to take many of the processes that were developed throughout the course of this dissertation and continue to implement them in future studies. Three areas for future developments are discussed briefly.

Raman microspectroscopy is a powerful tool and it has been used to look at the different characteristic Raman bands associated with DNA, bacterial cell walls, and two different types of model cancers cell lines. In order to continue the viability of RM as tool for biological studies there are areas that need further development.

One area of particular interest is creating a database that contains Raman spectra for many different types of cancer and various stages of cancer development. Currently, there are several Raman databases that range from minerals and inorganics to artist pigments (<http://www.irug.org>). However, no standard database exists for cancerous samples and in order to achieve this work various factors would need to be considered. For example: cancer type and stage, Raman acquisition settings, laser wavelength, sample preparation, pre- and post-processing parameters, etc. As daunting as this task may appear, a simple beginning would be to setup a standardize method of collecting Raman spectra and then to sample numerous immortal cell lines. These spectra could be used as a preliminary group for creating algorithms that can then be used to classify a particular type of cancer cell line based on characteristic Raman bands and overall spectral fingerprint. Then the database could be further augmented with primary cell lines established for specific cancerous tumor sites. This type of information could then be used to look at the changes in the Raman signal over time, versus concentration, and chemical exposure. Then this database could be used in identifying potential cancerous specimens/biopsies in human diagnosis and later it could possibly be used to monitor treatment and recovery of cancer patients.

Another area that needs to be further developed is the use of our tandem AFM/RM system. The strength of the combined AFM/RM system is the fact that the same sample can be interrogated using both systems simultaneously. This instrumentation opens up the ability to look at the chemical properties of a sample and also the mechanical properties within the same location. This will lead to a more in-

depth look at biological specimens and allow studies that can draw correlations between chemical and mechanical properties of these samples.

The final area that will strengthen the use of RM is be able to accurately identify and assign Raman bands specifically to mineral, chemical, and biological species. Along the lines of the previously mentioned database, this would entail a large database of known Raman spectra and band assignments. A program could then be designed to take into account various parameters associated with the acquired Raman spectrum and use mathematical modeling and statistical analysis to create a best match for the components within that spectrum.

Although RM has great potential as an analytical tool, there are still barriers that need to be addressed. At the time of the writing of this dissertation, the Molecular and Cellular Sensing and Imaging Laboratory (MCSIL) at USU headed by Dr. Anhong Zhou is continually pursuing research to understand the fundamentals of cellular behavior and how these behaviors can be measured qualitatively and quantified using Raman microspectroscopy and other techniques.

7.2.2 Electric cell-substrate impedance sensing outlook

In our experiments, we utilized ECIS to monitor the attachment and viability of our culture cell lines in either 8W1E or 8W10E+ arrays. ECIS was used to monitor cell behavior of our cell population in real-time and was also used to electroporate cells or electrically wound cells attached to the working electrode. However, there is also the possibility to utilize different arrays that support different electrode architecture, such as, a linear line electrode that more naturally mimics a traditional scrap test used in wound healing or wound repair studies. Other cultureware include 96 well arrays that contain

one or multiple electrodes per well, flow cells for chemotaxis, and ibidi® products that can incorporate into the ECIS array holders. Along with these different options is the ability to use modules to prolong the culture times for incubated cells, such as, a perfusion system to exchange culture medium, a wound healing module, and a hypoxia/hyperoxia chamber incubator. I believe that the power of the ECIS system, as applied to our research, would be the ability to utilize a DOE approach for high throughput screening of toxic substances and also protective compounds. Then after the initial screening, we could narrow in on a range of our compound(s) of interest and use the more sensitive arrays to study subtle differences in cellular physical behaviors. The final key to ECIS would be to use the data modeling capabilities to extract the specific values for the model parameters as describe in Section 1.6. These parameters could them be used to describe a picture of how these cells compare to others and, more specifically, how they behave when exposed to various toxic or protective compounds.

7.2.3 Traditional biology methods to validate EC, RM, AFM, and ECIS

Due to the exploratory nature of this dissertation, there is a need to validate the EC, RM, AFM, and ECIS techniques that are presented throughout this dissertation. Currently there exist many time tested standard approaches that are used in traditional biology approaches that need to be investigated to validate the alternative methods that I have presented here. A few of the methods and studies that I feel would be most useful are described below.

The first study would be to perform typical growth and viability curves for the immortal cell lines that will be used throughout the studies. From the growth curves the average doubling time can be calculated and also the timing of the log growth phase can

be calculated. These results would be very useful, especially in comparison to the cancer cell studies in chapter 4 and 5 and the DEP/RES study performed in chapter 6. Along similar lines, the average cell cycle analysis would be very interesting to have, as cell cycle could affect our Raman results. A control experiment to measure the cell cycle could be easily performed by fixing and staining cells using a fluorescent dye, such as, propidium iodide (PI) and analysis events via flow cytometry. If we were to perform this analysis for our treated and untreated cells in chapter 6, it could give us a better idea about the way that cell cycle may influence both the AFM and RM results and possible the chemometric results. It would be very interesting to know if some of the Raman results and chemometric analysis is influenced by the cell cycle. The final set of experiments that I would perform would have to do with screening for cytokines and other inflammatory markers and mediators using enzyme-linked immunosorbent assay (ELISA). These results would benefit the studies that we performed in chapter 6 due to the inflammation and toxic response that the DEP illicit in the A549 cell line.

In conclusion, there are many future areas that can be further explored to enhance the research that has been described in detail in chapters 2 – 6. My primary work was to show the feasibility of utilizing EC, RM, AFM, and ECIS to characterize bio-interfaces that included biological samples, such as, molecular DNA, bacteria cell walls, and mammalian cell lines.

APPENDICES

APPENDIX A

CHAPTER 2

Rightslink Printable License

<https://s100.copyright.com/CustomerAdmin/PLF.jsp?ID=2011110..>ELSEVIER LICENSE
TERMS AND CONDITIONS

Nov 10, 2011

This is a License Agreement between Gerald D McEwen ("You") and Elsevier ("Elsevier") provided by Copyright Clearance Center ("CCC"). The license consists of your order details, the terms and conditions provided by Elsevier, and the payment terms and conditions.

All payments must be made in full to CCC. For payment instructions, please see information listed at the bottom of this form.

Supplier	Elsevier Limited The Boulevard, Langford Lane Kidlington, Oxford, OX5 1GB, UK
Registered Company Number	1982084
Customer name	Gerald D McEwen
Customer address	843 West 2730 South Nibley, UT 84321
License number	2785710501696
License date	Nov 10, 2011
Licensed content publisher	Elsevier
Licensed content publication	Analytica Chimica Acta
Licensed content title	Immobilization, hybridization, and oxidation of synthetic DNA on gold surfa Electron transfer investigated by electrochemistry and scanning tunnelling microscopy
Licensed content author	Gerald D. McEwen, Fan Chen, Anhong Zhou
Licensed content date	8 June 2009
Licensed content volume number	643
Licensed content issue number	1-2
Number of pages	12
Start Page	26
End Page	37
Type of Use	reuse in a thesis/dissertation
Intended publisher of new work	other
Portion	full article
Format	both print and electronic
Are you the author of this Elsevier article?	Yes
Will you be translating?	No
Order reference number	

Title of your thesis/dissertation	AFM/Raman characterization of Bio-interfaces: molecular, bacteria, and mammalian cells
Expected completion date	May 2012
Estimated size (number of pages)	100
Elsevier VAT number	GB 494 6272 12
Permissions price	0.00 USD
VAT/Local Sales Tax	0.0 USD / 0.0 GBP
Total	0.00 USD
Terms and Conditions	

INTRODUCTION

1. The publisher for this copyrighted material is Elsevier. By clicking "accept" in connection with completing this licensing transaction, you agree that the following terms and conditions apply to this transaction (along with the Billing and Payment terms and conditions established by Copyright Clearance Center, Inc. ("CCC"), at the time that you opened your Rightslink account and that are available at any time at <http://myaccount.copyright.com>).

GENERAL TERMS

2. Elsevier hereby grants you permission to reproduce the aforementioned material subject to the terms and conditions indicated.

3. Acknowledgement: If any part of the material to be used (for example, figures) has appeared in our publication with credit or acknowledgement to another source, permission must also be sought from that source. If such permission is not obtained then that material may not be included in your publication/copies. Suitable acknowledgement to the source must be made, either as a footnote or in a reference list at the end of your publication, as follows:

"Reprinted from Publication title, Vol /edition number, Author(s), Title of article / title of chapter, Pages No., Copyright (Year), with permission from Elsevier [OR APPLICABLE SOCIETY COPYRIGHT OWNER]." Also Lancet special credit - "Reprinted from The Lancet, Vol. number, Author(s), Title of article, Pages No., Copyright (Year), with permission from Elsevier."

4. Reproduction of this material is confined to the purpose and/or media for which permission is hereby given.

5. Altering/Modifying Material: Not Permitted. However figures and illustrations may be altered/adapted minimally to serve your work. Any other abbreviations, additions, deletions and/or any other alterations shall be made only with prior written authorization of Elsevier Ltd. (Please contact Elsevier at permissions@elsevier.com)

6. If the permission fee for the requested use of our material is waived in this instance, please be advised that your future requests for Elsevier materials may attract a fee.

7. Reservation of Rights: Publisher reserves all rights not specifically granted in the

combination of (i) the license details provided by you and accepted in the course of this licensing transaction, (ii) these terms and conditions and (iii) CCC's Billing and Payment terms and conditions.

8. License Contingent Upon Payment: While you may exercise the rights licensed immediately upon issuance of the license at the end of the licensing process for the transaction, provided that you have disclosed complete and accurate details of your proposed use, no license is finally effective unless and until full payment is received from you (either by publisher or by CCC) as provided in CCC's Billing and Payment terms and conditions. If full payment is not received on a timely basis, then any license preliminarily granted shall be deemed automatically revoked and shall be void as if never granted. Further, in the event that you breach any of these terms and conditions or any of CCC's Billing and Payment terms and conditions, the license is automatically revoked and shall be void as if never granted. Use of materials as described in a revoked license, as well as any use of the materials beyond the scope of an unrevoked license, may constitute copyright infringement and publisher reserves the right to take any and all action to protect its copyright in the materials.

9. Warranties: Publisher makes no representations or warranties with respect to the licensed material.

10. Indemnity: You hereby indemnify and agree to hold harmless publisher and CCC, and their respective officers, directors, employees and agents, from and against any and all claims arising out of your use of the licensed material other than as specifically authorized pursuant to this license.

11. No Transfer of License: This license is personal to you and may not be sublicensed, assigned, or transferred by you to any other person without publisher's written permission.

12. No Amendment Except in Writing: This license may not be amended except in a writing signed by both parties (or, in the case of publisher, by CCC on publisher's behalf).

13. Objection to Contrary Terms: Publisher hereby objects to any terms contained in any purchase order, acknowledgment, check endorsement or other writing prepared by you, which terms are inconsistent with these terms and conditions or CCC's Billing and Payment terms and conditions. These terms and conditions, together with CCC's Billing and Payment terms and conditions (which are incorporated herein), comprise the entire agreement between you and publisher (and CCC) concerning this licensing transaction. In the event of any conflict between your obligations established by these terms and conditions and those established by CCC's Billing and Payment terms and conditions, these terms and conditions shall control.

14. Revocation: Elsevier or Copyright Clearance Center may deny the permissions described in this License at their sole discretion, for any reason or no reason, with a full refund payable to you. Notice of such denial will be made using the contact information provided by you. Failure to receive such notice will not alter or invalidate the denial. In no event will Elsevier or Copyright Clearance Center be responsible or liable for any costs, expenses or damage incurred by you as a result of a denial of your permission request, other than a refund of the amount(s) paid by you to Elsevier and/or Copyright

Clearance Center for denied permissions.

LIMITED LICENSE

The following terms and conditions apply only to specific license types:

15. Translation: This permission is granted for non-exclusive world **English** rights only unless your license was granted for translation rights. If you licensed translation rights you may only translate this content into the languages you requested. A professional translator must perform all translations and reproduce the content word for word preserving the integrity of the article. If this license is to re-use 1 or 2 figures then permission is granted for non-exclusive world rights in all languages.

16. Website: The following terms and conditions apply to electronic reserve and author websites:

Electronic reserve: If licensed material is to be posted to website, the web site is to be password-protected and made available only to bona fide students registered on a relevant course if:

This license was made in connection with a course,

This permission is granted for 1 year only. You may obtain a license for future website posting,

All content posted to the web site must maintain the copyright information line on the bottom of each image,

A hyper-text must be included to the Homepage of the journal from which you are licensing at <http://www.science-direct.com/science/journal/xxxxx> or the Elsevier homepage for books at <http://www.elsevier.com> , and

Central Storage: This license does not include permission for a scanned version of the material to be stored in a central repository such as that provided by Heron/XanEdu.

17. Author website for journals with the following additional clauses:

All content posted to the web site must maintain the copyright information line on the bottom of each image, and

the permission granted is limited to the personal version of your paper. You are not allowed to download and post the published electronic version of your article (whether PDF or HTML, proof or final version), nor may you scan the printed edition to create an electronic version,

A hyper-text must be included to the Homepage of the journal from which you are licensing at <http://www.science-direct.com/science/journal/xxxxx> , As part of our normal production process, you will receive an e-mail notice when your article appears on Elsevier's online service ScienceDirect (www.sciencedirect.com). That e-mail will include the article's Digital Object Identifier (DOI). This number provides the electronic link to the published article and should be included in the posting of your personal version. We ask that you wait until you receive this e-mail and have the DOI to do any posting.

Central Storage: This license does not include permission for a scanned version of the material to be stored in a central repository such as that provided by Heron/XanEdu.

18. Author website for books with the following additional clauses:

Authors are permitted to place a brief summary of their work online only.

A hyper-text must be included to the Elsevier homepage at <http://www.elsevier.com>

All content posted to the web site must maintain the copyright information line on the bottom of each image

You are not allowed to download and post the published electronic version of your chapter, nor may you scan the printed edition to create an electronic version.

Central Storage: This license does not include permission for a scanned version of the material to be stored in a central repository such as that provided by Heron/XanEdu.

19. Website (regular and for author): A hyper-text must be included to the Homepage of the journal from which you are licensing at <http://www.sciencedirect.com/science/journal/xxxxx>, or for books to the Elsevier homepage at <http://www.elsevier.com>

20. Thesis/Dissertation: If your license is for use in a thesis/dissertation your thesis may be submitted to your institution in either print or electronic form. Should your thesis be published commercially, please reapply for permission. These requirements include permission for the Library and Archives of Canada to supply single copies, on demand, of the complete thesis and include permission for UMI to supply single copies, on demand, of the complete thesis. Should your thesis be published commercially, please reapply for permission.

21. Other Conditions:

v1.6

If you would like to pay for this license now, please remit this license along with your payment made payable to "COPYRIGHT CLEARANCE CENTER" otherwise you will be invoiced within 48 hours of the license date. Payment should be in the form of a check or money order referencing your account number and this invoice number **RLNK500662870**.

Once you receive your invoice for this order, you may pay your invoice by credit card. Please follow instructions provided at that time.

Make Payment To:
Copyright Clearance Center
Dept 001
P.O. Box 843006
Boston, MA 02284-3006

For suggestions or comments regarding this order, contact RightsLink Customer Support: customer.care@copyright.com or +1-877-622-5543 (toll free in the US) or +1-978-646-2777.

Gratis licenses (referencing \$0 in the Total field) are free. Please retain this printable license for your reference. No payment is required.

To Whom It May Concern:

I hereby give permission to Gerald Dustin McEwen to use and reprint all of the material that I have contributed to Chapter 3 of his dissertation.

A handwritten signature in cursive script, appearing to read 'Fan Chen', is written above a horizontal line.

Fan Chen

10-21-2011

206-321-7639

CHAPTER 3

March 26, 2012

Dear Mingjie,

I am in the process of preparing my dissertation in the Department of Biological Engineering at Utah State University. I hope to complete my degree in May of 2012.

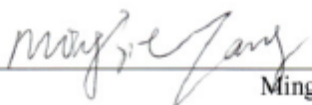
I am requesting permission to include the attached (submitted) paper, of which you are a coauthor, as a chapter in my dissertation. I will include acknowledgements to your contributions as indicated. Please advise me of any changes you require.

Please indicate your approval of this request by signing in the space provided, attaching any other form or instruction necessary to confirm permission. If you have any questions, please contact me.

Thank you,

Gerald D. McEwen

I hereby give permission to Gerald Dustin McEwen to use and reprint all of the material that I have contributed to Chapter 3 of his dissertation.


Mingjie Tang

CHAPTER 4

Rightslink Printable License

<https://s100.copyright.com/CustomerAdmin/PLF.jsp?ID=2011110..>

**JOHN WILEY AND SONS LICENSE
TERMS AND CONDITIONS**

Nov 10, 2011

This is a License Agreement between Gerald D McEwen ("You") and John Wiley and Sons ("John Wiley and Sons") provided by Copyright Clearance Center ("CCC"). The license consists of your order details, the terms and conditions provided by John Wiley and Sons, and the payment terms and conditions.

All payments must be made in full to CCC. For payment instructions, please see information listed at the bottom of this form.

License Number	2785710827335
License date	Nov 10, 2011
Licensed content publisher	John Wiley and Sons
Licensed content publication	Biopolymers
Licensed content title	Probing nanostructures of bacterial extracellular polymeric substances versus culture time by Raman microspectroscopy and atomic force microscopy
Licensed content author	Gerald D. McEwen, Yangzhe Wu, Anhong Zhou
Licensed content date	Feb 1, 2010
Start page	171
End page	177
Type of use	Dissertation/Thesis
Requestor type	Author of this Wiley article
Format	Print and electronic
Portion	Full article
Will you be translating?	No
Order reference number	
Total	0.00 USD

Terms and Conditions

TERMS AND CONDITIONS

This copyrighted material is owned by or exclusively licensed to John Wiley & Sons, Inc. or one of its group companies (each a "Wiley Company") or a society for whom a Wiley Company has exclusive publishing rights in relation to a particular journal (collectively WILEY"). By clicking "accept" in connection with completing this licensing transaction, you agree that the following terms and conditions apply to this transaction (along with the billing and payment terms and conditions established by the Copyright Clearance Center Inc., ("CCC's Billing and Payment terms and conditions"), at the time that you opened your Rightslink account (these are available at any time at <http://myaccount.copyright.com>)

Terms and Conditions

1. The materials you have requested permission to reproduce (the "Materials") are protected by copyright.
2. You are hereby granted a personal, non-exclusive, non-sublicensable, non-transferable, worldwide, limited license to reproduce the Materials for the purpose specified in the licensing

process. This license is for a one-time use only with a maximum distribution equal to the number that you identified in the licensing process. Any form of republication granted by this license must be completed within two years of the date of the grant of this license (although copies prepared before may be distributed thereafter). The Materials shall not be used in any other manner or for any other purpose. Permission is granted subject to an appropriate acknowledgement given to the author, title of the material/book/journal and the publisher. You shall also duplicate the copyright notice that appears in the Wiley publication in your use of the Material. Permission is also granted on the understanding that nowhere in the text is a previously published source acknowledged for all or part of this Material. Any third party material is expressly excluded from this permission.

3. With respect to the Materials, all rights are reserved. Except as expressly granted by the terms of the license, no part of the Materials may be copied, modified, adapted (except for minor reformatting required by the new Publication), translated, reproduced, transferred or distributed, in any form or by any means, and no derivative works may be made based on the Materials without the prior permission of the respective copyright owner. You may not alter, remove or suppress in any manner any copyright, trademark or other notices displayed by the Materials. You may not license, rent, sell, loan, lease, pledge, offer as security, transfer or assign the Materials, or any of the rights granted to you hereunder to any other person.

4. The Materials and all of the intellectual property rights therein shall at all times remain the exclusive property of John Wiley & Sons Inc or one of its related companies (WILEY) or their respective licensors, and your interest therein is only that of having possession of and the right to reproduce the Materials pursuant to Section 2 herein during the continuance of this Agreement. You agree that you own no right, title or interest in or to the Materials or any of the intellectual property rights therein. You shall have no rights hereunder other than the license as provided for above in Section 2. No right, license or interest to any trademark, trade name, service mark or other branding ("Marks") of WILEY or its licensors is granted hereunder, and you agree that you shall not assert any such right, license or interest with respect thereto.

5. NEITHER WILEY NOR ITS LICENSORS MAKES ANY WARRANTY OR REPRESENTATION OF ANY KIND TO YOU OR ANY THIRD PARTY, EXPRESS, IMPLIED OR STATUTORY, WITH RESPECT TO THE MATERIALS OR THE ACCURACY OF ANY INFORMATION CONTAINED IN THE MATERIALS, INCLUDING, WITHOUT LIMITATION, ANY IMPLIED WARRANTY OF MERCHANTABILITY, ACCURACY, SATISFACTORY QUALITY, FITNESS FOR A PARTICULAR PURPOSE, USABILITY, INTEGRATION OR NON-INFRINGEMENT AND ALL SUCH WARRANTIES ARE HEREBY EXCLUDED BY WILEY AND ITS LICENSORS AND WAIVED BY YOU.

6. WILEY shall have the right to terminate this Agreement immediately upon breach of this Agreement by you.

7. You shall indemnify, defend and hold harmless WILEY, its Licensors and their respective directors, officers, agents and employees, from and against any actual or threatened claims, demands, causes of action or proceedings arising from any breach of this Agreement by you.

8. IN NO EVENT SHALL WILEY OR ITS LICENSORS BE LIABLE TO YOU OR ANY OTHER PARTY OR ANY OTHER PERSON OR ENTITY FOR ANY SPECIAL, CONSEQUENTIAL, INCIDENTAL, INDIRECT, EXEMPLARY OR PUNITIVE DAMAGES, HOWEVER CAUSED, ARISING OUT OF OR IN CONNECTION WITH THE DOWNLOADING, PROVISIONING, VIEWING OR USE OF THE MATERIALS REGARDLESS OF THE FORM OF ACTION, WHETHER FOR BREACH OF CONTRACT, BREACH OF WARRANTY, TORT, NEGLIGENCE, INFRINGEMENT OR OTHERWISE (INCLUDING, WITHOUT LIMITATION, DAMAGES BASED ON LOSS OF PROFITS, DATA, FILES, USE, BUSINESS OPPORTUNITY OR CLAIMS OF THIRD PARTIES), AND WHETHER OR NOT THE PARTY HAS BEEN ADVISED OF THE POSSIBILITY OF SUCH DAMAGES. THIS LIMITATION SHALL APPLY NOTWITHSTANDING ANY FAILURE OF ESSENTIAL PURPOSE OF ANY LIMITED REMEDY PROVIDED HEREIN.

9. Should any provision of this Agreement be held by a court of competent jurisdiction to be illegal, invalid, or unenforceable, that provision shall be deemed amended to achieve as nearly as possible the same economic effect as the original provision, and the legality, validity and enforceability of the remaining provisions of this Agreement shall not be affected or impaired thereby.

10. The failure of either party to enforce any term or condition of this Agreement shall not constitute a waiver of either party's right to enforce each and every term and condition of this Agreement. No breach under this agreement shall be deemed waived or excused by either party

unless such waiver or consent is in writing signed by the party granting such waiver or consent. The waiver by or consent of a party to a breach of any provision of this Agreement shall not operate or be construed as a waiver of or consent to any other or subsequent breach by such other party.

11. This Agreement may not be assigned (including by operation of law or otherwise) by you without WILEY's prior written consent.

12. Any fee required for this permission shall be non-refundable after thirty (30) days from receipt.

13. These terms and conditions together with CCC's Billing and Payment terms and conditions (which are incorporated herein) form the entire agreement between you and WILEY concerning this licensing transaction and (in the absence of fraud) supersedes all prior agreements and representations of the parties, oral or written. This Agreement may not be amended except in writing signed by both parties. This Agreement shall be binding upon and inure to the benefit of the parties' successors, legal representatives, and authorized assigns.

14. In the event of any conflict between your obligations established by these terms and conditions and those established by CCC's Billing and Payment terms and conditions, these terms and conditions shall prevail.

15. WILEY expressly reserves all rights not specifically granted in the combination of (i) the license details provided by you and accepted in the course of this licensing transaction, (ii) these terms and conditions and (iii) CCC's Billing and Payment terms and conditions.

16. This Agreement will be void if the Type of Use, Format, Circulation, or Requestor Type was misrepresented during the licensing process.

17. This Agreement shall be governed by and construed in accordance with the laws of the State of New York, USA, without regards to such state's conflict of law rules. Any legal action, suit or proceeding arising out of or relating to these Terms and Conditions or the breach thereof shall be instituted in a court of competent jurisdiction in New York County in the State of New York in the United States of America and each party hereby consents and submits to the personal jurisdiction of such court, waives any objection to venue in such court and consents to service of process by registered or certified mail, return receipt requested, at the last known address of such party.

Wiley Open Access Terms and Conditions

All research articles published in Wiley Open Access journals are fully open access: immediately freely available to read, download and share. Articles are published under the terms of the [Creative Commons Attribution Non Commercial License](#), which permits use, distribution and reproduction in any medium, provided the original work is properly cited and is not used for commercial purposes. The license is subject to the Wiley Open Access terms and conditions: Wiley Open Access articles are protected by copyright and are posted to repositories and websites in accordance with the terms of the [Creative Commons Attribution Non Commercial License](#). At the time of deposit, Wiley Open Access articles include all changes made during peer review, copyediting, and publishing. Repositories and websites that host the article are responsible for incorporating any publisher-supplied amendments or retractions issued subsequently. Wiley Open Access articles are also available without charge on Wiley's publishing platform, **Wiley Online Library** or any successor sites.

Use by non-commercial users

For non-commercial and non-promotional purposes individual users may access, download, copy, display and redistribute to colleagues Wiley Open Access articles, as well as adapt, translate, text- and data-mine the content subject to the following conditions:

* The authors' moral rights are not compromised. These rights include the right of "paternity" (also known as "attribution" - the right for the author to be identified as such) and "integrity" (the right for the author not to have the work altered in such a way that the author's reputation or integrity may be impugned).

- Where content in the article is identified as belonging to a third party, it is the obligation of the user to ensure that any reuse complies with the copyright policies of the owner of that content.
- If article content is copied, downloaded or otherwise reused for non-commercial research and education purposes, a link to the appropriate bibliographic citation (authors, journal, article title, volume, issue, page numbers, DOI and the link to the definitive published version on Wiley Online Library) should be maintained. Copyright notices and disclaimers must not be deleted.
- Any translations, for which a prior translation agreement with Wiley has not been agreed, must prominently display the statement: "This is an unofficial translation of an article that appeared in a Wiley publication. The publisher has not endorsed this translation."

Use by commercial "for-profit" organisations

Use of Wiley Open Access articles for commercial, promotional, or marketing purposes requires further explicit permission from Wiley and will be subject to a fee.

Commercial purposes include:

- Copying or downloading of articles, or linking to such articles for further redistribution, sale or licensing;
- Copying, downloading or posting by a site or service that incorporates advertising with such content;
- The inclusion or incorporation of article content in other works or services (other than normal quotations with an appropriate citation) that is then available for sale or licensing, for a fee (for example, a compilation produced for marketing purposes, inclusion in a sales pack)
- Use of article content (other than normal quotations with appropriate citation) by for-profit organisations for promotional purposes
- Linking to article content in e-mails redistributed for promotional, marketing or educational purposes;
- Use for the purposes of monetary reward by means of sale, resale, licence, loan, transfer or other form of commercial exploitation such as marketing products
- Print reprints of Wiley Open Access articles can be purchased from:
corporatesales@wiley.com

Other Terms and Conditions:

BY CLICKING ON THE "I AGREE..." BOX, YOU ACKNOWLEDGE THAT YOU HAVE READ AND FULLY UNDERSTAND EACH OF THE SECTIONS OF AND PROVISIONS SET FORTH IN THIS AGREEMENT AND THAT YOU ARE IN AGREEMENT WITH AND ARE WILLING TO ACCEPT ALL OF YOUR OBLIGATIONS AS SET FORTH IN THIS AGREEMENT.

v1.7

If you would like to pay for this license now, please remit this license along with your payment made payable to "COPYRIGHT CLEARANCE CENTER" otherwise you will be invoiced within 48 hours of the license date. Payment should be in the form of a check or money order referencing your account number and this invoice number **RLNK500662873**.

Once you receive your invoice for this order, you may pay your invoice by credit card.

Rightslink Printable License

<https://s100.copyright.com/CustomerAdmin/PLF.jsp?ID=2011110..>

Please follow instructions provided at that time.

Make Payment To:
Copyright Clearance Center
Dept 001
P.O. Box 843006
Boston, MA 02284-3006

For suggestions or comments regarding this order, contact RightsLink Customer Support: customer@copyright.com or +1-877-622-5543 (toll free in the US) or +1-978-646-2777.

Gratis licenses (referencing \$0 in the Total field) are free. Please retain this printable license for your reference. No payment is required.

Dissertatin Permission Letter

Page 1 of 1

Dissertatin Permission Letter

Gerald McEwen

Sent: Thursday, October 20, 2011 10:55 PM**To:** Yangzhe Wu**Attachments:** Biopolymers_Dusti2k9_all.pdf (1 MB)

Dear Yangzhe,

I am in the process of preparing my dissertation in the Department of Biological Engineering at Utah State University. I hope to complete my degree in May of 2012.

I am requesting permission to include the attached paper, of which you are a coauthor, as a chapter in my dissertation. I will include acknowledgements to your contributions as indicated. Please advise me of any changes you require.

Please indicate your approval of this request by signing in the space provided or attaching any other form or instruction necessary to confirm permission. If you have any questions, please contact me.

Thank you,

Gerald D. McEwen

I hereby give permission to Gerald Dustin McEwen to use and reprint all of the material that I have contributed to Chapter 4 of his dissertation.

 10/26/2011
Yangzhe Wu

March 26, 2012

Dear Mingjie,

I am in the process of preparing my dissertation in the Department of Biological Engineering at Utah State University. I hope to complete my degree in May of 2012.

I am requesting permission to include the attached (submitted) paper, of which you are a coauthor, as a chapter in my dissertation. I will include acknowledgements to your contributions as indicated. Please advise me of any changes you require.

Please indicate your approval of this request by signing in the space provided, attaching any other form or instruction necessary to confirm permission. If you have any questions, please contact me.

Thank you,

Gerald D. McEwen

I hereby give permission to Gerald Dustin McEwen to use and reprint all of the material that I have contributed to Chapter 4 of his dissertation.


Mingjie Tang

March 26, 2012

Dear Tian,

I am in the process of preparing my dissertation in the Department of Biological Engineering at Utah State University. I hope to complete my degree in May of 2012.

I am requesting permission to include the attached (submitted) paper, of which you are a coauthor, as a chapter in my dissertation. I will include acknowledgements to your contributions as indicated. Please advise me of any changes you require.

Please indicate your approval of this request by signing in the space provided, attaching any other form or instruction necessary to confirm permission. If you have any questions, please contact me.

Thank you,

Gerald D. McEwen

I hereby give permission to Gerald Dustin McEwen to use and reprint all of the material that I have contributed to Chapter 4 of his dissertation.



Tian Yu

March 26, 2012

Dear Zhongmiao Xiao,

I am in the process of preparing my dissertation in the Department of Biological Engineering at Utah State University. I hope to complete my degree in May of 2012.

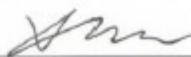
I am requesting permission to include the attached (submitted) paper, of which you are a coauthor, as a chapter in my dissertation. I will include acknowledgements to your contributions as indicated. Please advise me of any changes you require.

Please indicate your approval of this request by signing in the space provided, attaching any other form or instruction necessary to confirm permission. If you have any questions, please contact me.

Thank you,

Gerald D. McEwen

I hereby give permission to Gerald Dustin McEwen to use and reprint all of the material that I have contributed to Chapter 4 of his dissertation.



Zhongmiao Xiao

March 26, 2012

Dear Xiaojun Qi,

I am in the process of preparing my dissertation in the Department of Biological Engineering at Utah State University. I hope to complete my degree in May of 2012.

I am requesting permission to include the attached (submitted) paper, of which you are a coauthor, as a chapter in my dissertation. I will include acknowledgements to your contributions as indicated. Please advise me of any changes you require.

Please indicate your approval of this request by signing in the space provided, attaching any other form or instruction necessary to confirm permission. If you have any questions, please contact me.

Thank you,

Gerald D. McEwen

I hereby give permission to Gerald Dustin McEwen to use and reprint all of the material that I have contributed to Chapter 4 of his dissertation.


Xiaojun Qi



March 26, 2012

Dr. DeWald,

I am in the process of preparing my dissertation in the Department of Biological Engineering at Utah State University. I hope to complete my degree in May of 2012.

I am requesting permission to include the attached (submitted) paper, of which you are a coauthor, as a chapter in my dissertation. I will include acknowledgements to your contributions as indicated. Please advise me of any changes you require.

Please indicate your approval of this request by signing in the space provided, attaching any other form or instruction necessary to confirm permission. If you have any questions, please contact me.

Thank you,

Gerald D. McEwen

I hereby give permission to Gerald Dustin McEwen to use and reprint all of the material that I have contributed to Chapter 4 of his dissertation.

A handwritten signature in cursive script that reads "Daryll B. DeWald".

Daryll B. DeWald, Dean
College of Sciences

CHAPTER 5

Rightslink Printable License

<https://s100.copyright.com/CustomerAdmin/PLF.jsp?ED=2011110..>ELSEVIER LICENSE
TERMS AND CONDITIONS

Nov 10, 2011

This is a License Agreement between Gerald D McEwen ("You") and Elsevier ("Elsevier") provided by Copyright Clearance Center ("CCC"). The license consists of your order details, the terms and conditions provided by Elsevier, and the payment terms and conditions.

All payments must be made in full to CCC. For payment instructions, please see information listed at the bottom of this form.

Supplier	Elsevier Limited The Boulevard, Langford Lane Kidlington, Oxford, OX5 1GB, UK
Registered Company Number	1982084
Customer name	Gerald D McEwen
Customer address	843 West 2730 South Nibley, UT 84321
License number	2785710311619
License date	Nov 10, 2011
Licensed content publisher	Elsevier
Licensed content publication	Cancer Letters
Licensed content title	BRMS1 expression alters the ultrastructural, biomechanical and biochemical properties of MDA-MB-435 human breast carcinoma cells: An AFM and Raman microspectroscopy study
Licensed content author	Yangzhe Wu, Gerald D. McEwen, Sitaram Harihar, Sherry M. Baker, Daryll B. DeWald, Anhong Zhou
Licensed content date	1 July 2010
Licensed content volume number	293
Licensed content issue number	1
Number of pages	10
Start Page	82
End Page	91
Type of Use	reuse in a thesis/dissertation
Portion	full article
Format	both print and electronic
Are you the author of this Elsevier article?	Yes
Will you be translating?	No
Order reference number	

Title of your thesis/dissertation	AFM/Raman characterization of Bio-interfaces: molecular, bacteria, and mammalian cells
Expected completion date	May 2012
Estimated size (number of pages)	100
Elsevier VAT number	GB 494 6272 12
Permissions price	0.00 USD
VAT/Local Sales Tax	0.0 USD / 0.0 GBP
Total	0.00 USD
Terms and Conditions	

INTRODUCTION

1. The publisher for this copyrighted material is Elsevier. By clicking "accept" in connection with completing this licensing transaction, you agree that the following terms and conditions apply to this transaction (along with the Billing and Payment terms and conditions established by Copyright Clearance Center, Inc. ("CCC"), at the time that you opened your Rightslink account and that are available at any time at <http://myaccount.copyright.com>).

GENERAL TERMS

2. Elsevier hereby grants you permission to reproduce the aforementioned material subject to the terms and conditions indicated.

3. Acknowledgement: If any part of the material to be used (for example, figures) has appeared in our publication with credit or acknowledgement to another source, permission must also be sought from that source. If such permission is not obtained then that material may not be included in your publication/copies. Suitable acknowledgement to the source must be made, either as a footnote or in a reference list at the end of your publication, as follows:

"Reprinted from Publication title, Vol /edition number, Author(s), Title of article / title of chapter, Pages No., Copyright (Year), with permission from Elsevier [OR APPLICABLE SOCIETY COPYRIGHT OWNER]." Also Lancet special credit - "Reprinted from The Lancet, Vol. number, Author(s), Title of article, Pages No., Copyright (Year), with permission from Elsevier."

4. Reproduction of this material is confined to the purpose and/or media for which permission is hereby given.

5. Altering/Modifying Material: Not Permitted. However figures and illustrations may be altered/adapted minimally to serve your work. Any other abbreviations, additions, deletions and/or any other alterations shall be made only with prior written authorization of Elsevier Ltd. (Please contact Elsevier at permissions@elsevier.com)

6. If the permission fee for the requested use of our material is waived in this instance, please be advised that your future requests for Elsevier materials may attract a fee.

7. Reservation of Rights: Publisher reserves all rights not specifically granted in the

combination of (i) the license details provided by you and accepted in the course of this licensing transaction, (ii) these terms and conditions and (iii) CCC's Billing and Payment terms and conditions.

8. License Contingent Upon Payment: While you may exercise the rights licensed immediately upon issuance of the license at the end of the licensing process for the transaction, provided that you have disclosed complete and accurate details of your proposed use, no license is finally effective unless and until full payment is received from you (either by publisher or by CCC) as provided in CCC's Billing and Payment terms and conditions. If full payment is not received on a timely basis, then any license preliminarily granted shall be deemed automatically revoked and shall be void as if never granted. Further, in the event that you breach any of these terms and conditions or any of CCC's Billing and Payment terms and conditions, the license is automatically revoked and shall be void as if never granted. Use of materials as described in a revoked license, as well as any use of the materials beyond the scope of an unrevoked license, may constitute copyright infringement and publisher reserves the right to take any and all action to protect its copyright in the materials.

9. Warranties: Publisher makes no representations or warranties with respect to the licensed material.

10. Indemnity: You hereby indemnify and agree to hold harmless publisher and CCC, and their respective officers, directors, employees and agents, from and against any and all claims arising out of your use of the licensed material other than as specifically authorized pursuant to this license.

11. No Transfer of License: This license is personal to you and may not be sublicensed, assigned, or transferred by you to any other person without publisher's written permission.

12. No Amendment Except in Writing: This license may not be amended except in a writing signed by both parties (or, in the case of publisher, by CCC on publisher's behalf).

13. Objection to Contrary Terms: Publisher hereby objects to any terms contained in any purchase order, acknowledgment, check endorsement or other writing prepared by you, which terms are inconsistent with these terms and conditions or CCC's Billing and Payment terms and conditions. These terms and conditions, together with CCC's Billing and Payment terms and conditions (which are incorporated herein), comprise the entire agreement between you and publisher (and CCC) concerning this licensing transaction. In the event of any conflict between your obligations established by these terms and conditions and those established by CCC's Billing and Payment terms and conditions, these terms and conditions shall control.

14. Revocation: Elsevier or Copyright Clearance Center may deny the permissions described in this License at their sole discretion, for any reason or no reason, with a full refund payable to you. Notice of such denial will be made using the contact information provided by you. Failure to receive such notice will not alter or invalidate the denial. In no event will Elsevier or Copyright Clearance Center be responsible or liable for any costs, expenses or damage incurred by you as a result of a denial of your permission request, other than a refund of the amount(s) paid by you to Elsevier and/or Copyright

Clearance Center for denied permissions.

LIMITED LICENSE

The following terms and conditions apply only to specific license types:

15. Translation: This permission is granted for non-exclusive world **English** rights only unless your license was granted for translation rights. If you licensed translation rights you may only translate this content into the languages you requested. A professional translator must perform all translations and reproduce the content word for word preserving the integrity of the article. If this license is to re-use 1 or 2 figures then permission is granted for non-exclusive world rights in all languages.

16. Website: The following terms and conditions apply to electronic reserve and author websites:

Electronic reserve: If licensed material is to be posted to website, the web site is to be password-protected and made available only to bona fide students registered on a relevant course if:

This license was made in connection with a course,

This permission is granted for 1 year only. You may obtain a license for future website posting,

All content posted to the web site must maintain the copyright information line on the bottom of each image,

A hyper-text must be included to the Homepage of the journal from which you are licensing at <http://www.sciencedirect.com/science/journal/xxxxx> or the Elsevier homepage for books at <http://www.elsevier.com> , and

Central Storage: This license does not include permission for a scanned version of the material to be stored in a central repository such as that provided by Heron/XanEdu.

17. Author website for journals with the following additional clauses:

All content posted to the web site must maintain the copyright information line on the bottom of each image, and

the permission granted is limited to the personal version of your paper. You are not allowed to download and post the published electronic version of your article (whether PDF or HTML, proof or final version), nor may you scan the printed edition to create an electronic version,

A hyper-text must be included to the Homepage of the journal from which you are licensing at <http://www.sciencedirect.com/science/journal/xxxxx> , As part of our normal production process, you will receive an e-mail notice when your article appears on Elsevier's online service ScienceDirect (www.sciencedirect.com). That e-mail will include the article's Digital Object Identifier (DOI). This number provides the electronic link to the published article and should be included in the posting of your personal version. We ask that you wait until you receive this e-mail and have the DOI to do any posting.

Central Storage: This license does not include permission for a scanned version of the material to be stored in a central repository such as that provided by Heron/XanEdu.

18. Author website for books with the following additional clauses:

Authors are permitted to place a brief summary of their work online only.

A hyper-text must be included to the Elsevier homepage at <http://www.elsevier.com>

All content posted to the web site must maintain the copyright information line on the bottom of each image

You are not allowed to download and post the published electronic version of your chapter, nor may you scan the printed edition to create an electronic version.

Central Storage: This license does not include permission for a scanned version of the material to be stored in a central repository such as that provided by Heron/XanEdu.

19. Website (regular and for author): A hyper-text must be included to the Homepage of the journal from which you are licensing at <http://www.sciencedirect.com/science/journal/xxxxx>, or for books to the Elsevier homepage at <http://www.elsevier.com>

20. Thesis/Dissertation: If your license is for use in a thesis/dissertation your thesis may be submitted to your institution in either print or electronic form. Should your thesis be published commercially, please reapply for permission. These requirements include permission for the Library and Archives of Canada to supply single copies, on demand, of the complete thesis and include permission for UMI to supply single copies, on demand, of the complete thesis. Should your thesis be published commercially, please reapply for permission.

21. Other Conditions:

v1.6

If you would like to pay for this license now, please remit this license along with your payment made payable to "COPYRIGHT CLEARANCE CENTER" otherwise you will be invoiced within 48 hours of the license date. Payment should be in the form of a check or money order referencing your account number and this invoice number **RLNK500662869**.

Once you receive your invoice for this order, you may pay your invoice by credit card. Please follow instructions provided at that time.

Make Payment To:
Copyright Clearance Center
Dept 001
P.O. Box 843006
Boston, MA 02284-3006

For suggestions or comments regarding this order, contact RightsLink Customer Support: customer.care@copyright.com or +1-877-622-5543 (toll free in the US) or +1-978-646-2777.

Gratis licenses (referencing \$0 in the Total field) are free. Please retain this printable license for your reference. No payment is required.

Dissertatin Permission Letter

Page 1 of 1

Dissertatin Permission Letter

Gerald McEwen

Sent: Thursday, October 20, 2011 10:56 PM**To:** Yangzhe Wu**Attachments:** Yangzhe_BRMS1_AFM-Raman_2k9.pdf (2 MB)

Dear Yangzhe,

I am in the process of preparing my dissertation in the Department of Biological Engineering at Utah State University. I hope to complete my degree in May of 2012.

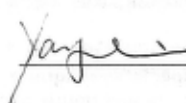
I am requesting permission to include the attached paper, of which you are a coauthor, as a chapter in my dissertation. I will include acknowledgements to your contributions as indicated. Please advise me of any changes you require.

Please indicate your approval of this request by signing in the space provided or attaching any other form or instruction necessary to confirm permission. If you have any questions, please contact me.

Thank you,

Gerald D. McEwen

I hereby give permission to Gerald Dustin McEwen to use and reprint all of the material that I have contributed to Chapter 6 of his dissertation.

 10/26/2011
Yangzhe Wu

Gerald McEwen

From: Sitaram Harihar [sharihar@kumc.edu]
Sent: Friday, October 21, 2011 4:16 PM
To: Gerald McEwen
Subject: Dear Gerald D. McEwen,

Dear Gerald D. McEwen,

I am happy to approve your request to include the cancer letters paper as part of your dissertation. Please let me know if you have any questions or concerns.

Regards,
Sitaram

Sitaram Harihar
Postdoctoral Fellow
Department of Cancer Biology
The University of Kansas Cancer Center
3020 Wahl Hall East, Mail Stop 3041
3901 Rainbow Blvd
Kansas City, KS 66160
Phone (lab): (913) 945-7798
E-mail: sharihar@kumc.edu
www.kucancercenter.org



College of Sciences

To Whom it May Concern:

I hereby give permission to Gerald Dustin McEwen to use and reprint all of the material that I have contributed to Chapter 6 of his dissertation.

A handwritten signature in blue ink that reads "Darryl B. DeWald". The signature is written in a cursive style and is positioned above a horizontal line.

Darryl B. DeWald
Dean and Professor

CHAPTER 6

March 26, 2012

Dear Mingjie,

I am in the process of preparing my dissertation in the Department of Biological Engineering at Utah State University. I hope to complete my degree in May of 2012.

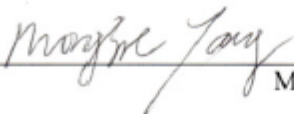
I am requesting permission to include the Raman profile and dendrogram figures, of which you helped process, in chapter 6 of my dissertation. I will include acknowledgements to your contributions as indicated. Please advise me of any changes you require.

Please indicate your approval of this request by signing in the space provided, attaching any other form or instruction necessary to confirm permission. If you have any questions, please contact me.

Thank you,

Gerald D. McEwen

I hereby give permission to Gerald Dustin McEwen to use and reprint all of the material that I have contributed to Chapter 6 of his dissertation.


Mingjie Tang

APPENDIX B

7.2.4 Electron transfer behaviors of the Hoechst/CV oxidation/dsS-DNA/MCH modified electrode surface

If the immobilization order between dsS-DNA and MCH is reversed, the electrochemical behaviors of the dsS-DNA modified gold electrode surface may be different. Figure B2.12 illustrates cyclic voltammograms of the gold electrode in 0.5 mM $\text{K}_3\text{Fe}(\text{CN})_6$ + 0.01 PBS with the following sequential modifications: bare Au (curve 1), 1 mM MCH for 6 hours (curve 2), 1 μM dsS-DNA for 24 hours (curve 3), CV oxidation (data not shown), and immersion in 100 μM Hoechst for 5 min (curve 5). The main difference between Figure 2.5 and Figure B2.12 is the immobilization order of dsS-DNA and MCH. As seen in Table B2.6, neither the immobilization of MCH nor of dsS-DNA give any diffusion coefficient (D_0) values for the $\text{Fe}(\text{CN})_6^{3-/4-}$ electroactive species due to the diffusive blockage between the self-assembly modified gold surface and the bulk solution.

EIS plots are shown in Figure B2.13 and the corresponding EIS parameters for these modifications are given in Table B2.7. It is worthwhile to note the difference in the simulated equivalent circuit parameters for the immobilization of MCH first (Table B2.7) and for the immobilization of dsS-DNA first (Table B2.5). For example, due to the chemical nature of both molecules MCH (uncharged small molecules) and dsS-DNA (charged macromolecules), the immobilization of dsS-DNA first leads to a larger C_d of 7.64 μF (as well as a small increase in Z_w) compared to the smaller capacitance C_d of 2.34 μF when MCH is immobilized first. Other than that, immobilization of MCH first results in the greater values of R_{ct} (7.5 $\text{K}\Omega$), θ_R (0.851), and d_i (9.51 nm), compared to 4.8 $\text{K}\Omega$, 0.766, and 2.91 nm, respectively, in the case of the immobilization of dsS-DNA

first. These larger values demonstrate that a more uniform multi-layer structure ($d_i = 9.51$ nm) of MCH is achieved on the gold surface if immobilization of MCH is conducted first. Moreover, this more uniform MCH multi-layer gives rise to a slightly smaller K_a^0 ($2.26 \times 10^{-3} \text{ cm s}^{-1}$), compared to the immobilization of dsS-DNA first ($3.54 \times 10^{-3} \text{ cm s}^{-1}$).

The second immobilization step (Figure B2.12) was to incubate the MCH-modified gold electrode with $1 \mu\text{M}$ dsS-DNA for 24 hours and the CV scan is shown in curve 3. In this immobilization step, it seems that the dsS-DNA molecules may still be able to replace the self-assembled MCH layers (or non-specifically attached MCH), which can be evidenced by the increase in C_d ($3.20 \mu\text{F}$) and decrease in d_i (6.95 nm).

It is noteworthy to compare the EIS parameters from the different immobilization orders: MCH/dsS-DNA/bare Au (Table B2.5), and dsS-DNA/MCH/bare Au (Table B2.7). After the immobilization of the second layer of molecules, the former immobilization approach (dsS-DNA/MCH) achieves the changes of C_d ($7.64 \mu\text{F}/3.10 \mu\text{F}$), R_{ct} ($4.8 \text{ K}\Omega/91 \text{ K}\Omega$), K_a^0 ($3.54 \times 10^{-3} \text{ cm s}^{-1}/1.86 \times 10^{-3} \text{ cm s}^{-1}$), θ_R ($0.766/0.988$), and d_i ($2.91 \text{ nm}/7.19 \text{ nm}$), respectively; while the later immobilization approach (MCH/dsS-DNA) gives C_d ($2.34 \mu\text{F}/3.20 \mu\text{F}$), R_{ct} ($7.5 \text{ K}\Omega/7.6 \text{ K}\Omega$), K_a^0 ($2.26 \times 10^{-3} \text{ cm s}^{-1}/2.21 \times 10^{-3} \text{ cm s}^{-1}$), θ_R ($0.851/0.854$), and d_i ($9.51 \text{ nm}/6.95 \text{ nm}$), respectively. It is found that 1) the interfacial capacitance C_d seems to be independent of the immobilization order; the magnitude of C_d follows the order: ss-DNA/Au ($9.64 \mu\text{F}$) > ds-DNA/Au ($7.64 \mu\text{F}$) > MCH/Au ($2.34 \mu\text{F}$). It has been reported that ss-DNA gives a larger C_d than ds-DNA when immobilized on a gold surface [60; 61]; 2) the electron transfer resistance (R_{ct}) or electron transfer rate (K_a^0) is dependent on the immobilization order between dsS-DNA and MCH; 3) surface coverage θ_R shows an increase with the dsS-DNA/MCH

immobilization order, while it remains almost unchanged with the MCH/dsS-DNA immobilization order; and 4) the layer thickness d_i seems to be dependent on the immobilization order. The dsS-DNA/MCH approach results in a significant increase in the surface layer thickness that may be due to the formation of a MCH multi-layer on the electrode surface. The MCH/dsS-DNA approach gives a decrease in surface layer thickness due to the replacement of MCH by the dsS-DNA molecules.

The subsequent cyclic voltammetric oxidation of MCH/dsS-DNA modification leads to a decrease in C_d (2.47 μF), R_{ct} (1.5 $\text{K}\Omega$), θ_R (0.276), and d_i (0.9 nm), all due to the oxidative damage of dsS-DNA and the oxidative removal of both MCH and dsS-DNA molecules from the gold surface.

From the comparison of Table 2.2, Table B2.5, and Table B2.7, the conclusion is that Hoechst prefers to bind with ds-DNA (rather than ss-DNA) and this binding facilitates the electron transfer between the DNA molecules and the electrode surface.

Table B2.5. Measured EIS parameters for successive modifications on bare gold by dsS-DNA, MCH, Hoechst, CV oxidation, and Hoechst binding.

Step	Modifications	${}^yR_{\Omega} / \Omega$	${}^yC_d / \mu\text{F}$	${}^yR_{ct} / \Omega$	${}^yZ_w / \mu\Omega \text{ s}^{-1/2}$	${}^zK_a^0 / \text{cm s}^{-1}$	${}^e\theta_R$	${}^y d_i / \text{nm}$
1	Bare gold	147.9	1.12	1120	80.4	1.51E-02	-	-
2	dsS-DNA	150.3	7.64	4792	81.3	3.54E-03	0.766	2.91
3	MCH	143	3.10	91200	67.8	1.86E-04	0.988	7.19
4	Hoechst (1)	--	--	--	--	--	--	--
5	CV Oxidation	150.5	2.63	4193	82.1	4.04E-03	0.733	0.85
6	Hoechst (2)	154.3	1.05	5581	63.4	3.04E-03	0.799	2.13

y Calculated based on the modified Randles equivalent circuit, z Calculated using Chapter 2 Equation 2, e Calculated using Chapter 2 Equation 3, and y Calculated using Chapter 2 Equation 4.

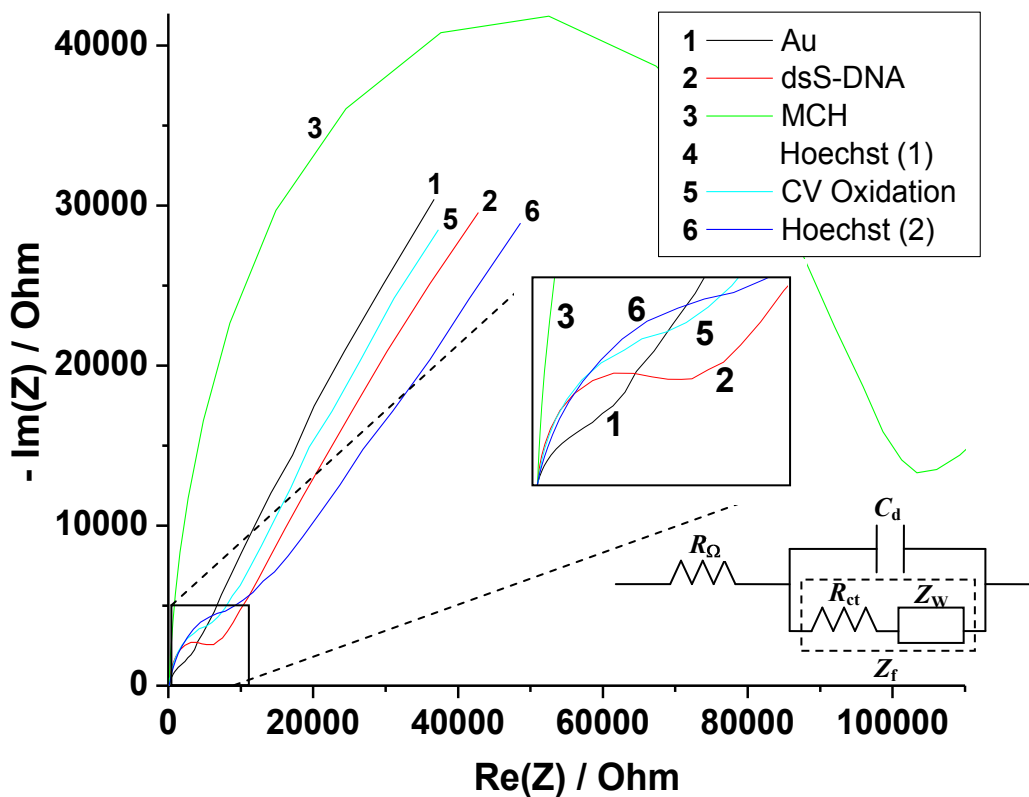


Figure B2.11. Electrochemical impedance spectroscopy (EIS) of step-by-step synthetic ds-DNA modified electrode: bare Au (1), dsS-DNA/Au (2), MCH/dsS-DNA/Au (3), Hoechst/MCH/dsS-DNA/Au (4), Oxidation/Hoechst/MCH/dsS-DNA/Au (5), and Hoechst/Oxidation/Hoechst/MCH/dsS-DNA/Au (6). Inset: modified equivalent Randles circuit used to model impedance data. EIS was conducted in 0.5 mM $\text{K}_3\text{Fe}(\text{CN})_6$ + 0.5 mM $\text{K}_4\text{Fe}(\text{CN})_6$ in 0.01 M PBS, pH 7.4 with 10 mV AC amplitude.

Table B2.6. Diffusion coefficients (D_0) for successive modifications on bare gold by MCH, dsS-DNA, CV oxidation, and Hoechst binding.

Step	Modifications	${}^{\varphi}D_0 / \text{cm}^2 \text{s}^{-1}$
1	Bare gold	6.59E-06
2	MCH	--
3	dsS-DNA	--
4	CV Oxidation	--
5	Hoechst	4.71E-06

${}^{\varphi}$ Calculated from Equation 1 by using cathodic peak currents.

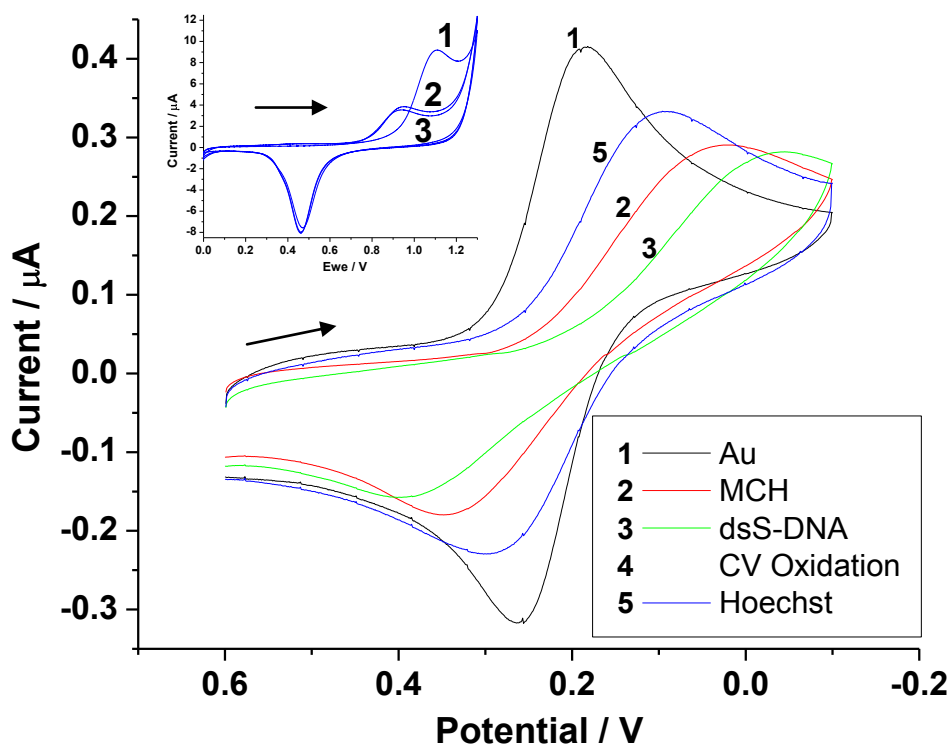


Figure B2.12. Voltammetric behaviors of $\text{Fe}(\text{CN})_6^{3-/4-}$ redox couple (0.5 mM $\text{K}_3\text{Fe}(\text{CN})_6$ + 0.01 PBS) on step-by-step synthetic ds-DNA modified electrodes: bare Au (1), MCH/Au (2), dsS-DNA/MCH/Au (3), Oxidation/dsS-DNA/MCH/Au (4), and Hoechst/Oxidation/dsS-DNA/MCH/Au (5). Inset: 5 mM Na_2HPO_4 + 5 mM NaH_2PO_4 between 0 - 1.3 V at 30 mV s^{-1} .

Table B2.7. Measured EIS parameters for successive modifications on bare gold by MCH, dsS-DNA, CV oxidation, and Hoechst binding.

Step	Modifications	${}^{\forall}R_{\Omega} / \Omega$	${}^{\forall}C_d / \mu\text{F}$	${}^{\forall}R_{ct} / \Omega$	${}^{\forall}Z_w / \mu\Omega \text{ s}^{-1/2}$	${}^{\ddagger}K_a^0 / \text{cm s}^{-1}$	${}^{\epsilon}\theta_R$	${}^{\psi}d_i / \text{nm}$
1	Bare gold	147.9	1.12	1120	80.4	1.51E-02	-	-
2	MCH	145.4	2.34	7506	78.3	2.26E-03	0.851	9.51
3	dsS-DNA	144.7	3.20	7684	73.6	2.21E-03	0.854	6.95
4	CV Oxidation	152.7	2.47	1547	79.2	1.09E-02	0.276	0.90
5	Hoechst	151.5	1.36	7183	66.3	2.36E-03	0.844	1.64

${}^{\forall}$ Calculated based on the modified Randles equivalent circuit, ‡ Calculated using Chapter 2

Equation 2, ${}^{\epsilon}$ Calculated using Chapter 2 Equation 3, and ${}^{\psi}$ Calculated using Chapter 2 Equation 4

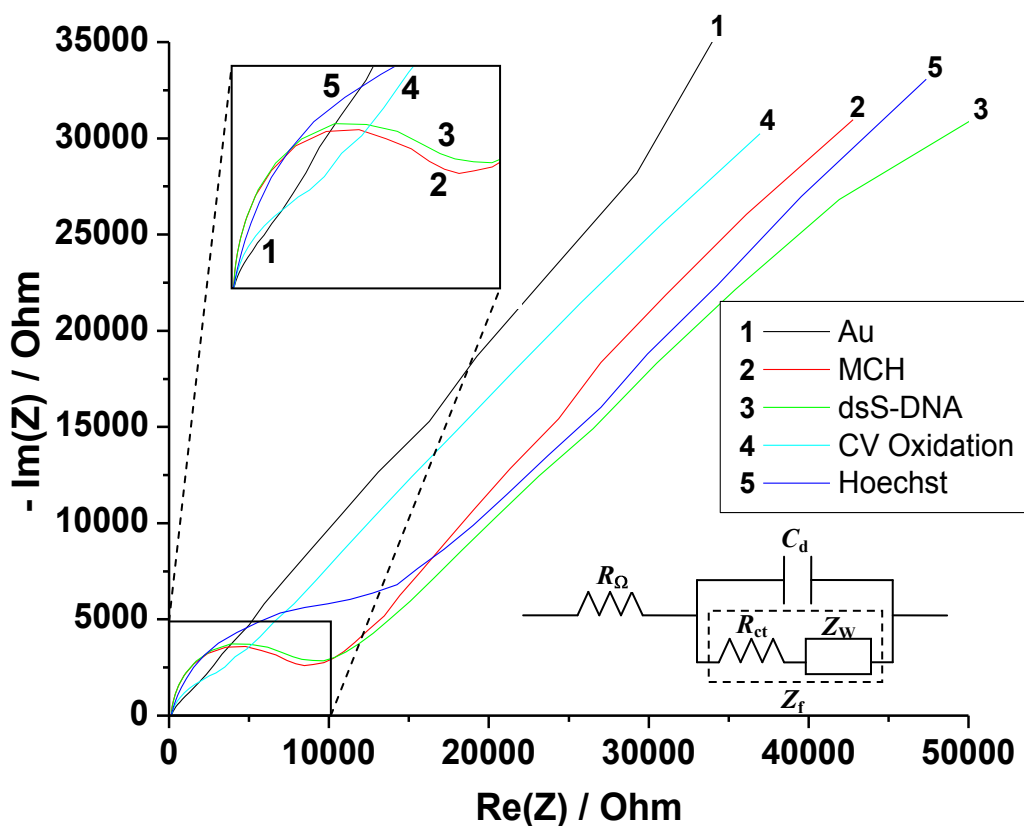


Figure B2.13. Electrochemical impedance spectroscopy (EIS) of step-by-step synthetic ds-DNA modified electrode: bare Au (1), MCH/Au (2), dsS-DNA/MCH/Au (3), Oxidation/dsS-DNA/MCH/Au (4), and Hoechst/Oxidation/dsS-DNA/MCH/Au (5). Inset: modified equivalent Randles circuit used to model impedance data. EIS was conducted in 0.5 mM $\text{K}_3\text{Fe}(\text{CN})_6$ + 0.5 mM $\text{K}_4\text{Fe}(\text{CN})_6$ in 0.01 M PBS, pH 7.4 with 10 mV AC amplitude.

7.2.5 Charges obtained from current vs. time curves

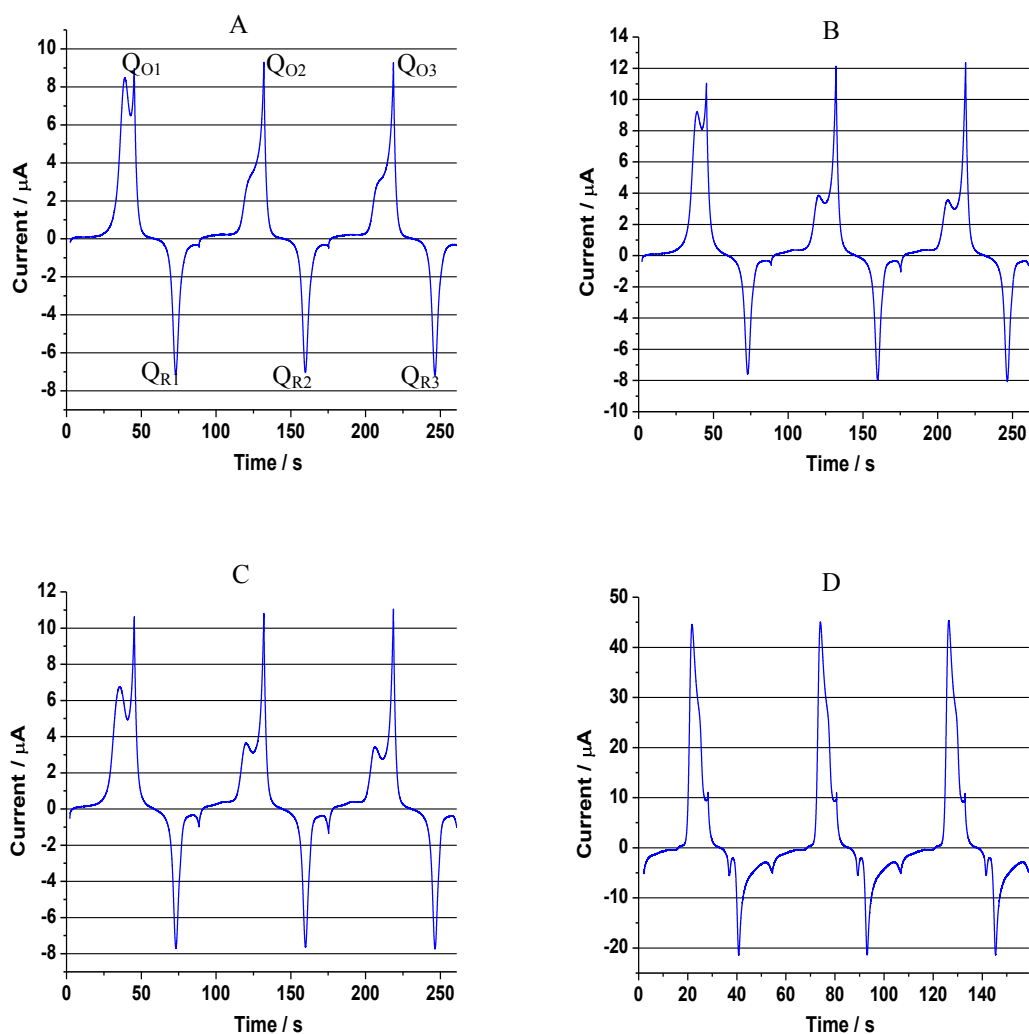


Figure B2.14. Depiction of current vs. time curves for three cases; (A) Hoechst 33258 (5 min)/MCH (6 hrs)/dsS-DNA (24 hrs)/Au (corresponding to the inset in Figure 2.5), (B) dsS-DNA (24 hrs)/MCH (6 hrs)/Au (corresponding to the inset in Figure B2.12), and (C) dsS-DNA (12 hrs)/Au (corresponding to the curves in Figure 2.7-A. Each CV illustrates the first three cyclic voltammetry scans numbered 1, 2, and 3.

It has been assumed that the immobilized ds-DNA would be oxidized in the first CV scan [54]. Under this assumption, we could speculate the following electro-oxidation and electro-reduction mechanisms on the ds-DNA immobilized gold electrodes during the first three CV scans (CVs in the insets of Figure 2.5, Figure B2.12, and Figure 2.7-A), which consists of DNA electro-oxidation (charge $Q_{\text{DNA,ox}}$), gold electro-oxidation ($Q_{\text{Au,ox}}$) or electro-reduction ($Q_{\text{AuO,Rd}}$), and oxidative desorption ($Q_{\text{ox-des (DNA/MCH)}}$). Here an example of the modification MCH/dsS-DNA/Au (case B in Table B2.8, inset of Figure B2.12) is given below:

$$\text{1st scan, } Q_{\text{O1}} = Q_{\text{DNA,ox}} + Q_{\text{Au,ox1}} + Q_{\text{ox-des1 (DNA/MCH)}} = 102.04 \mu\text{C};$$

$$Q_{\text{R1}} = Q_{\text{AuO,Rd1}} = Q_{\text{Au,ox1}} = 47.38 \mu\text{C}$$

$$\text{2nd scan, } Q_{\text{O2}} = Q_{\text{Au,ox2}} + Q_{\text{ox-des2 (DNA/MCH)}} = 77.18 \mu\text{C};$$

$$Q_{\text{R2}} = Q_{\text{AuO,Rd2}} = Q_{\text{Au,ox2}} = 48.33 \mu\text{C}$$

$$\text{3rd scan, } Q_{\text{O3}} = Q_{\text{Au,ox3}} + Q_{\text{ox-des3 (DNA/MCH)}} = 74.47 \mu\text{C};$$

$$Q_{\text{R3}} = Q_{\text{AuO,Rd3}} = Q_{\text{Au,ox3}} = 47.94 \mu\text{C}$$

Considering the charge difference of electro-oxidation charge between the 2nd scan and the 3rd scan, 77.18 μC and 74.47 μC , we define an “attenuation factor” (γ), $\gamma = 74.47 \mu\text{C}/77.18 \mu\text{C} = 96.49\%$. Taking this percentage as the same attenuation factor for the electro-oxidation charge between 1st scan and the 2nd scan, we could estimate the $Q_{\text{Au,ox1}} + Q_{\text{ox-des1 (DNA/MCH)}} = 79.98 \mu\text{C}$. Considering $Q_{\text{AuO,Rd1}} = Q_{\text{Au,ox1}} = 47.38 \mu\text{C}$, $Q_{\text{ox-des1 (DNA/MCH)}}$ is estimated to be 32.60 μC . Thus, $Q_{\text{DNA,ox}} = 102.04 \mu\text{C} - 79.98 \mu\text{C} = 22.06 \mu\text{C}$. Also, following the similar procedures for the modification dsS-DNA/MCH/Au and dsS-DNA/Au, we can obtain all the individual charges for the above three scans, shown in Table B2.8.

Table B2.8. The charges (μC) for individual electro-oxidation reactions on different modified gold electrodes.

Modifications		Q_{O1}	Q_{O2}	Q_{O3}
		$Q_{\text{DNA,ox}}$	$Q_{\text{Au,ox}}$	$Q_{\text{Au,ox}}$
		$Q_{\text{Au,ox}}$	$Q_{\text{ox-des}}$	$Q_{\text{ox-des}}$
		$Q_{\text{ox-des}}$	--	--
A	Hoechst 33258 (5 min)/MCH	22.05	48.34	47.94
	(6 hrs)/dsS-DNA (24 hrs)/Au	47.38	28.84	26.53
		32.60	--	--
B	dsS-DNA (24 hrs)/MCH	19.43	48.34	47.97
	(6 hrs)/Au	47.42	48.43	44.83
		53.49	--	--
C	dsS-DNA (12 hrs)/Au	25.92	47.48	48.51
		47.50	41.94	37.22
		45.65	--	--

All conditions are the same as Table 2.4. Q_{O1} , Q_{O2} , and Q_{O3} obtained in three modified electrodes are referred to Table 2.4.

7.2.6 Processing STM images

Shown in Figure 2.9 are the procedures for how we do the molecule conductance estimation from the STM current image. The STM topography image (left) and the current image (same time cited as current map) (right) are obtained using the constant current mode. In this mode, the feedback circuit moves the piezo, or the STM tip, in Z-direction to maintain constant current while the tip is scanning in X- and Y- directions.

We chose a few of the brightest points in the current image to do the rough estimation. We first carefully increased the “Z-range” in the PicoScan software to view only a few of the brightest points. Secondly, we adjusted the “Z-center offset” to make the background black so that the brightest points are easier to distinguish from the background. Third, we gradually increased the zoom around each spot until a clear spot

shape could be identified. Finally, a cross-section profile over each selected spot was done to measure the highest current.

APPENDIX C

Figure C4.10 depicts stacked Raman spectra normalized at 1660 cm^{-1} .

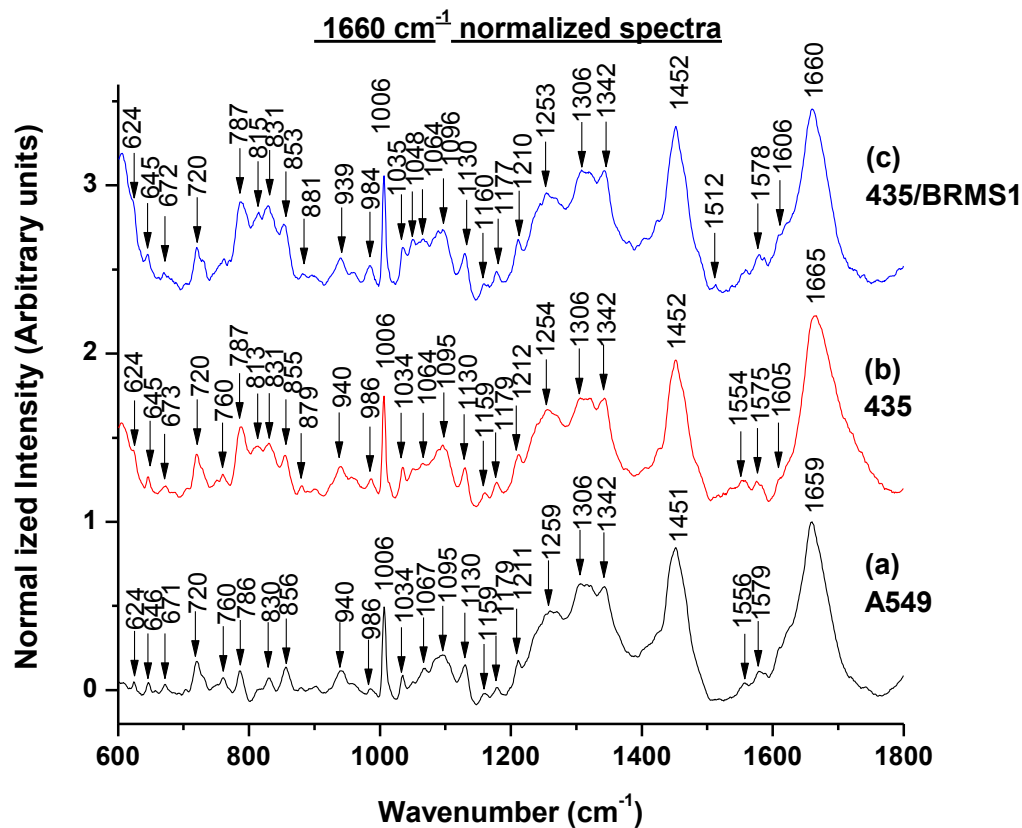


Figure C4.10. Mean Raman spectra of three cancer cell lines: A549 (a-black), 435 (b-red), and 435/BRMS1 (c-blue). Each spectrum is the average of five spectra, the averaged background was subtracted by finding a local minimum area, spectra were baseline corrected, and, then normalized using peak intensity at 1660 cm^{-1} . Spectra are offset vertically for clarity.

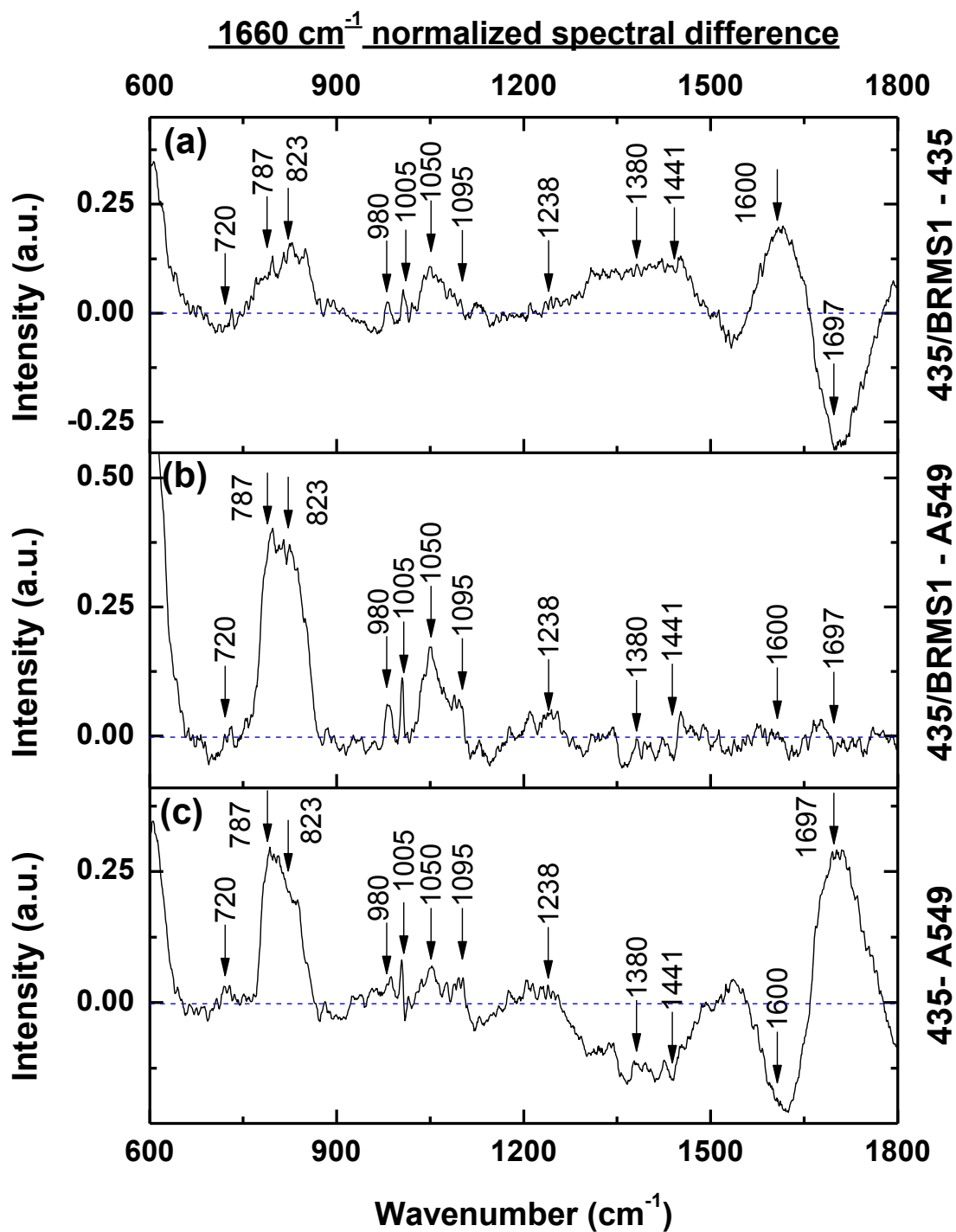


Figure C4.11. Difference spectra computed from the 1660 cm^{-1} normalized spectrum in Figure C4.10 using A549, 435, and 435/BRMS1: 435/BRMS1 – A549 (a); 435/BRMS1 – A549 (b); A549 – 435 (c)

APPENDIX D

Table D6.13. Array seeding density and treatment for array A and B in Figure D6.32.

A1 – 2×10^5 cells/well	(media only)	B1 – 2×10^5 cells/well	(media only)
A2 – 2×10^5 cells/well	(0.02% MTH + media)	B2 – 2×10^5 cells/well	(0.02% MTH + media)
A3 – 2×10^5 cells/well	(0.05% MTH + media)	B3 – 2×10^5 cells/well	(0.05% MTH + media)
A4 – 2×10^5 cells/well	(0.2% MTH + media)	B4 – 2×10^5 cells/well	(0.2% MTH + media)
A5 – 2×10^5 cells/well	(0.5% MTH + media)	B5 – 2×10^5 cells/well	(0.5% MTH + media)
A6 – 2×10^5 cells/well	(1.0% MTH + media)	B6 – 2×10^5 cells/well	(1.0% MTH + media)
A7 – 2×10^5 cells/well	(2.0% MTH + media)	B7 – 2×10^5 cells/well	(2.0% MTH + media)
A8 – media only	(media only)	B8 – media only	(media only)

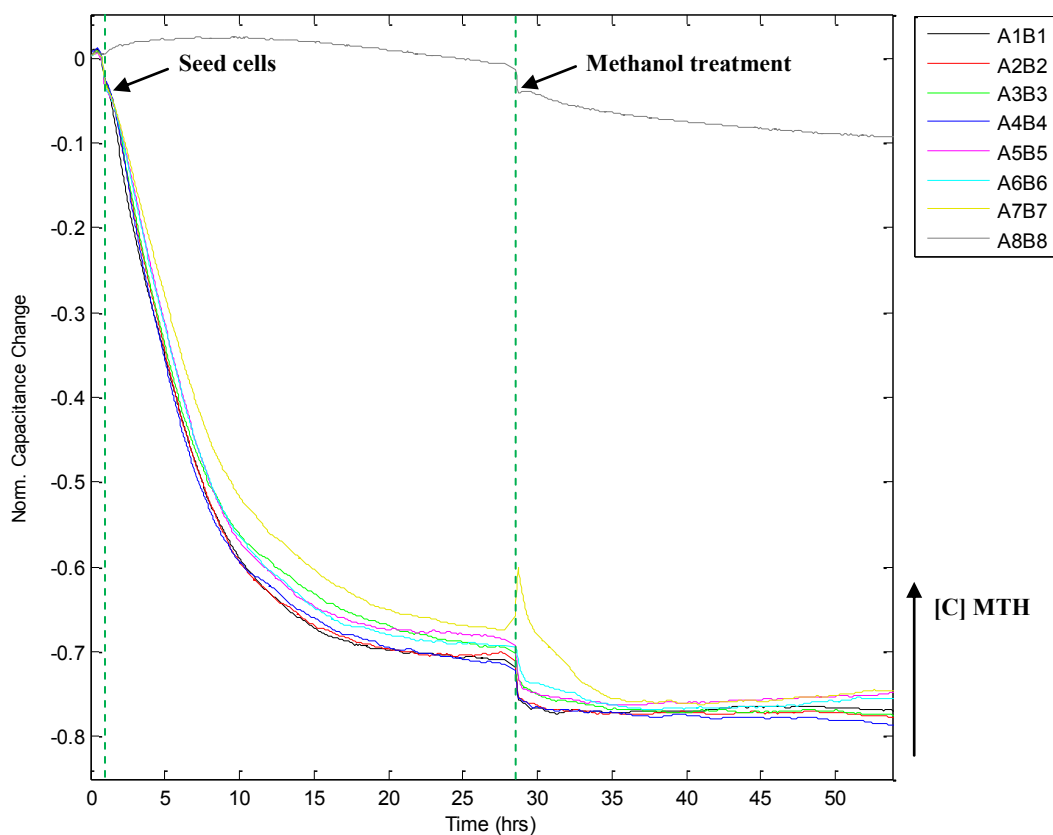


Figure D6.32. Two 8W10E+ arrays were seeded with 2×10^5 cells/ml (A1 – A7 and B1 – B7) and media in the other two wells (A8 and B8). When the cells were confluent at $\sim 27 - 28$ hours, an increasing amount of methanol was added to each of the wells.

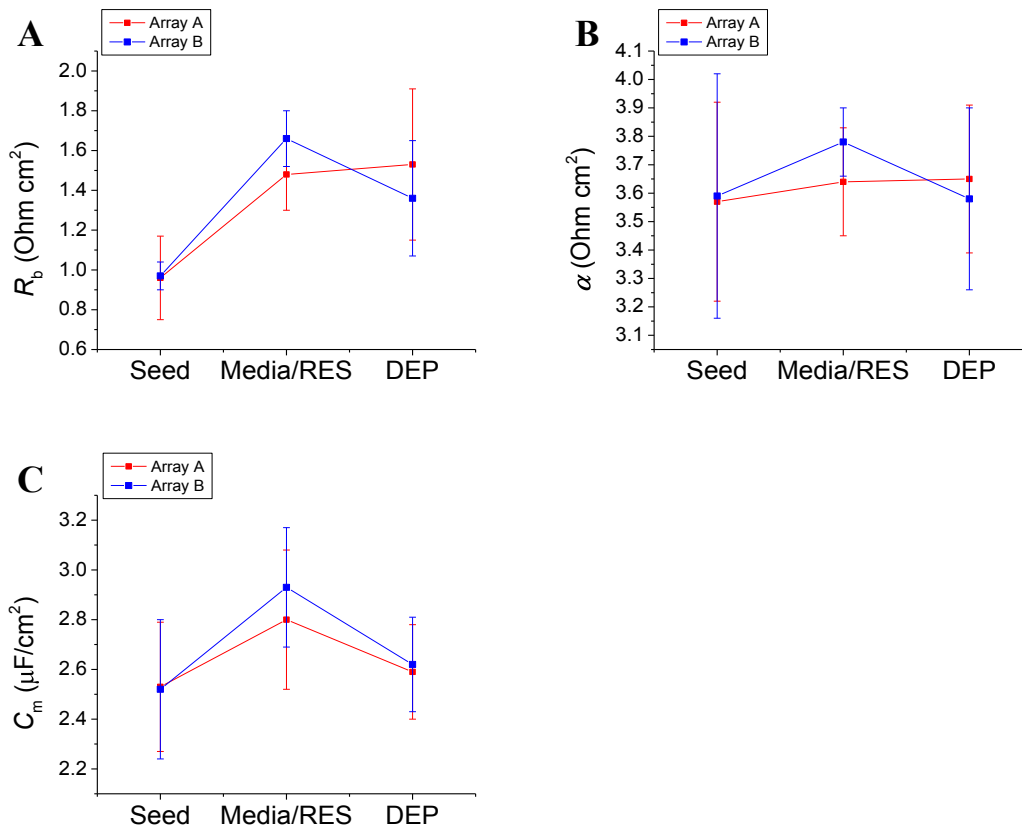


Figure D6.33. Means comparison (mean \pm SD) of modeled parameters R_b , α , and C_m obtained from Figure 6.7. Means were computed for six wells over a 10 hour period. Seed = 15 – 25 hours (A), Media/RES = 35 – 45 hours (B), and DEP = 55 – 65 hours (C). Array A and B were seeded at 0 hour, media was exchanged at 29 hour with medium control in array A and 10 μ M resveratrol plus medium in array B, and DEP exposure was at performed 50 hours.

Table D6.14. Array seeding density and treatment for array A and B in Figure D6.34.

A1 – 2×10^5 cells/well	(media) no wounding	B1 – 2×10^5 cells/well	(media) wounded
A2 – 2×10^5 cells/well	(media + 50 $\mu\text{g/ml}$ DEP) wounded	B2 – 2×10^5 cells/well	(media + 50 $\mu\text{g/ml}$ DEP) wounded
A3 – 2×10^5 cells/well	(media + 125 $\mu\text{g/ml}$ DEP) wounded	B3 – 2×10^5 cells/well	(media + 125 $\mu\text{g/ml}$ DEP) wounded
A4 – media only	(media) no wounding	B4 – media only	(media) no wounding
A5 – 2×10^5 cells/well	(media) no wounding	B5 – 2×10^5 cells/well	(media) wounded
A6 – 2×10^5 cells/well	(media + 50 $\mu\text{g/ml}$ DEP) wounded	B6 – 2×10^5 cells/well	(media + 50 $\mu\text{g/ml}$ DEP) wounded
A7 – 2×10^5 cells/well	(media + 125 $\mu\text{g/ml}$ DEP) wounded	B7 – 2×10^5 cells/well	(media + 125 $\mu\text{g/ml}$ DEP) wounded
A8 – media only	(media + 50 $\mu\text{g/ml}$ DEP) no wounding	B8 – media only	(media + 125 $\mu\text{g/ml}$ DEP) wounded

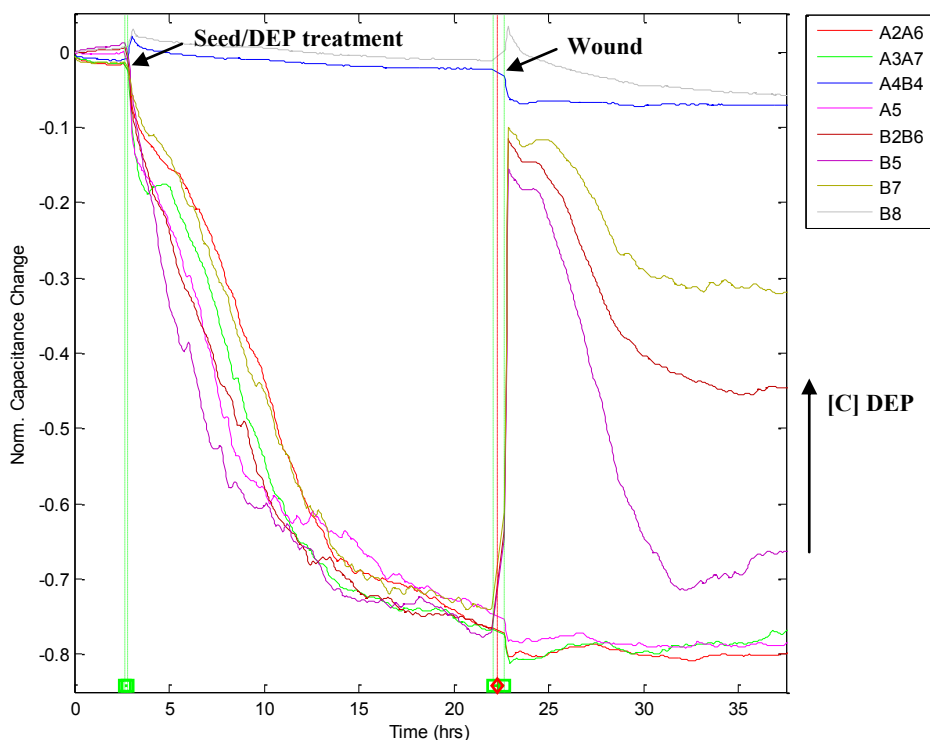


Figure D6.34. This was an experiment to test the migration rate of A549 at two different concentrations of DEP (50 and 125 $\mu\text{g/ml}$ – dark red and dark yellow) at the previously defined wounding settings of at 60 kHz, 2600 μA and 180 seconds. A549 cells were seeded as outlined above (see Table D6.14). At ~ 22.5 hours the experiment was paused, DEP was added to wells A2, 3, 4, 6, 7 and B2, 3, 4, 6, and 7. Arrays were replaced, values were checked and wounding was applied while measurements were still paused. Then measurement was resumed.

Table D6.15. Array seeding density and treatment for array A and B in Figure D6.35.

A1 – 2×10^5 cells/well	(serum containing media)	B1 – 2×10^5 cells/well	(serum containing media)
A2 – 2×10^5 cells/well	(serum containing media + 50 $\mu\text{g/ml}$ DEP)	B2 – 2×10^5 cells/well	(serum containing media + 50 $\mu\text{g/ml}$ DEP)
A3 – 2×10^5 cells/well	(serum containing media + 125 $\mu\text{g/ml}$ DEP)	B3 – 2×10^5 cells/well	(serum containing media + 125 $\mu\text{g/ml}$ DEP)
A4 – 2×10^5 cells/well	(serum containing media + 500 $\mu\text{g/ml}$ DEP)	B4 – 2×10^5 cells/well	(serum containing media + 500 $\mu\text{g/ml}$ DEP)
A5 – 2×10^5 cells/well	(serum containing media)	B5 – 2×10^5 cells/well	(serum containing media)
A6 – 2×10^5 cells/well	(serum containing media + 50 $\mu\text{g/ml}$ DEP)	B6 – 2×10^5 cells/well	(serum containing media + 50 $\mu\text{g/ml}$ DEP)
A7 – 2×10^5 cells/well	(serum containing media + 125 $\mu\text{g/ml}$ DEP)	B7 – 2×10^5 cells/well	(serum containing media + 125 $\mu\text{g/ml}$ DEP)
A8 – 2×10^5 cells/well	(serum containing media + 500 $\mu\text{g/ml}$ DEP)	B8 – 2×10^5 cells/well	(serum containing media + 500 $\mu\text{g/ml}$ DEP)

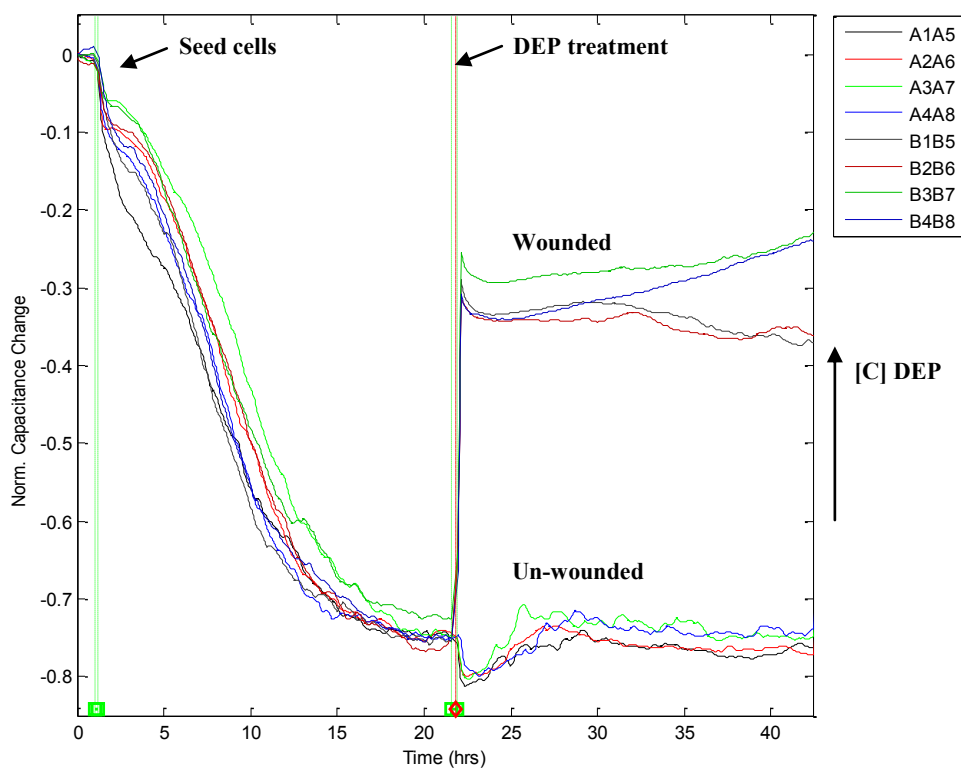


Figure D6.35. Two 8W1E arrays were seeded with 2×10^5 cells/ml of A549 cells and were allowed to become confluent. At ~ 22 hours the media was changed and DEP was added to wells A2, 3, 4, 6, 7, and 8. Cells were allowed to continue to culture for ~ 42 hours. Array B was then wounded at 2600 μA , for 30 seconds, and 32 kHz. Cells were allowed to heal until ~ 42 hours.

From the above wounding settings, it was determined that ~180 seconds at 2600 μ A and 64 kHz is the best for wounding A549 cells in our current configuration. Wounding at 32 kHz is too much for the cells to recover and it also possibly damages the electrodes and causes them to return erroneous values.

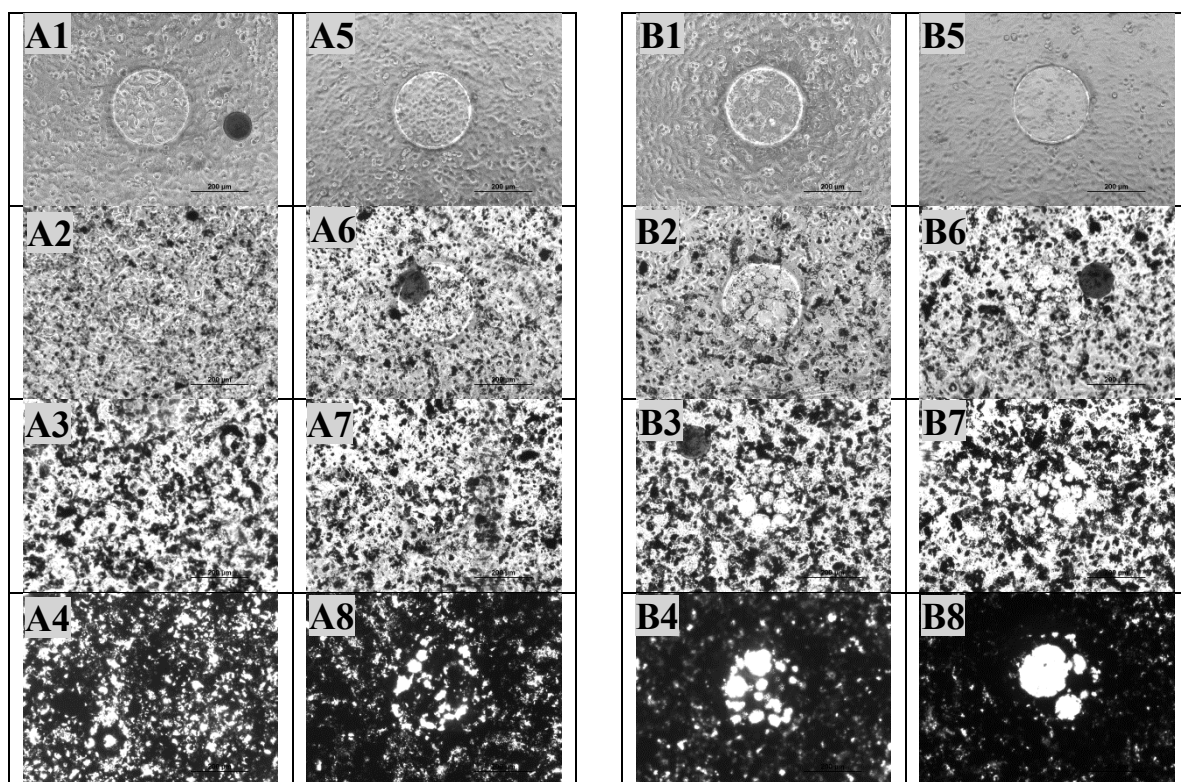


Figure D6.36. Bright field images of Array A and B imaged with IX – 71 Olympus Microscope at 10x magnification. Note increasing DEP concentrations in Wells A2 & 6, 3 & 7, 4 & 8 and B2 & 6, 3 & 7, 4 & 8 – respectively 50, 125, and 500 μ g/ml.

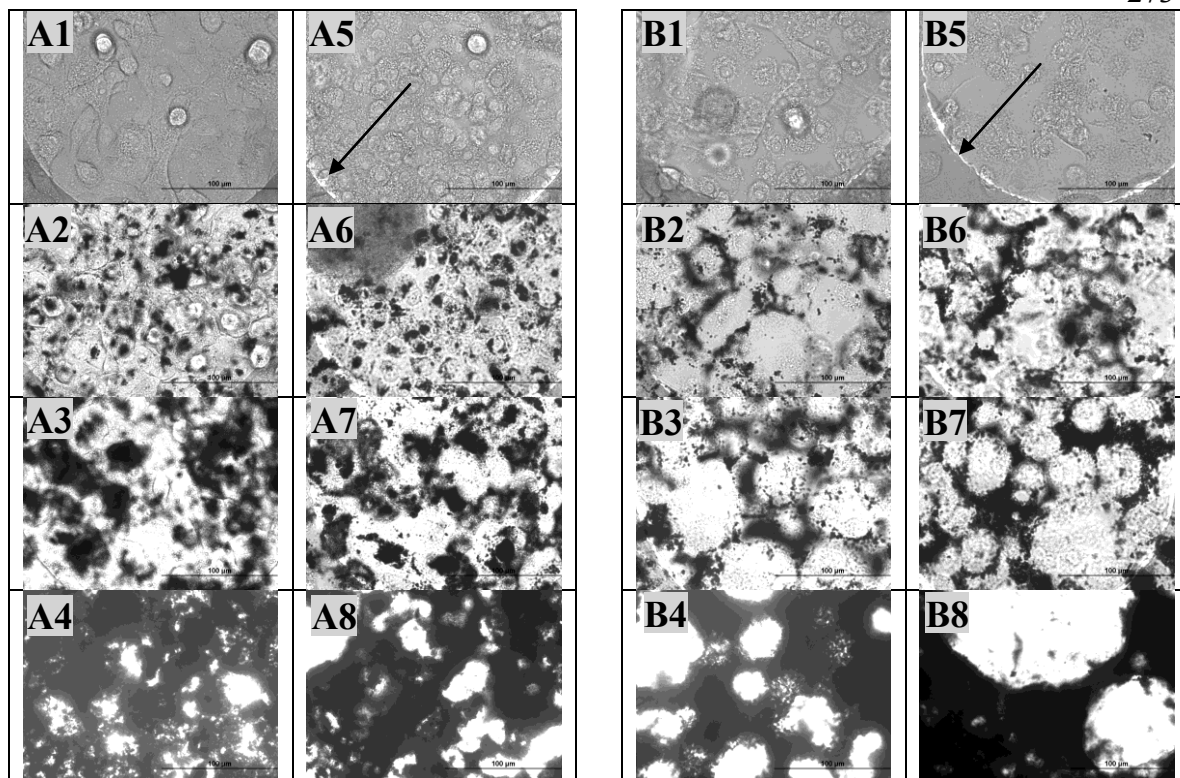


Figure D6.37. Bright field images of Array A and B imaged with IX – 71 Olympus Microscope at 40x magnification. Note increasing DEP concentrations in Wells A2 & 6, 3 & 8, 4 & 8 and B2 & 6, 3 & 7, 4 & 8 – respectively 50, 125, and 500 µg/ml.

Table D6.16. Array seeding density and treatment for array A and B in Figure D6.38.

A1 – 2×10^5 cells/well	(serum containing media)	B1 – 2×10^5 cells/well	(serum containing media)
A2 – 2×10^5 cells/well	(serum containing media + 50 µg/ml DEP)	B2 – 2×10^5 cells/well	(serum containing media + 50 µg/ml DEP)
A3 – 2×10^5 cells/well	(serum containing media + 125 µg/ml DEP)	B3 – 2×10^5 cells/well	(serum containing media + 125 µg/ml DEP)
A4 – 2×10^5 cells/well	(serum containing media + 500 µg/ml DEP)	B4 – 2×10^5 cells/well	(serum containing media + 500 µg/ml DEP)
A5 – 2×10^5 cells/well	(serum containing media)	B5 – 2×10^5 cells/well	(serum containing media)
A6 – 2×10^5 cells/well	(serum containing media + 50 µg/ml DEP)	B6 – 2×10^5 cells/well	(serum containing media + 50 µg/ml DEP)
A7 – 2×10^5 cells/well	(serum containing media + 125 µg/ml DEP)	B7 – 2×10^5 cells/well	(serum containing media + 125 µg/ml DEP)
A8 – 2×10^5 cells/well	(serum containing media + 500 µg/ml DEP)	B8 – 2×10^5 cells/well	(serum containing media + 500 µg/ml DEP)

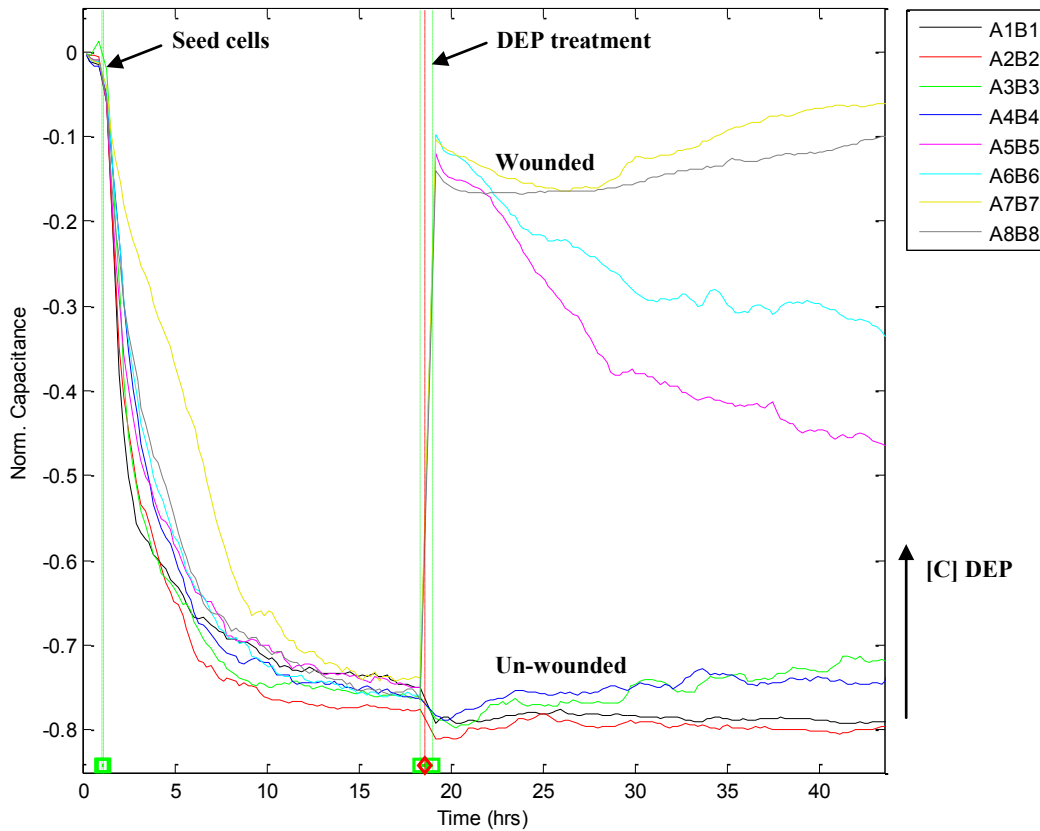


Figure D6.38. Two 8W1E arrays were seeded with 2×10^5 cells/ml of A549 (A1–A8 and B1–B8) and cells were allowed to become confluent. After ~18 hours, the media was changed and media and DEP (50, 125, and 500 $\mu\text{g/ml}$) were added to the arrays. The arrays were then wounded (A5 – 8 and B5 – 8 @ 180 seconds, 3000 μA and 64 kHz), then the wells were allowed to recover. It appears that control and the 50 $\mu\text{g/ml}$ DEP wells start to recover while the 125 and 500 $\mu\text{g/ml}$ treated wells do not recover.

Table D6.17. Array seeding density and treatment for array A and B in Figure D6.39.

A1 – 2×10^5 cells/well	(media only)	B1 – 2×10^5 cells/well	(media only)
A2 – 2×10^5 cells/well	(0.01% MTH + media)	B2 – 2×10^5 cells/well	(0.01% MTH + media)
A3 – 2×10^5 cells/well	(0.025% MTH + media)	B3 – 2×10^5 cells/well	(0.025% MTH + media)
A4 – 2×10^5 cells/well	(0.1% MTH + media)	B4 – 2×10^5 cells/well	(0.1% MTH + media)
A5 – 2×10^5 cells/well	(0.25% MTH + media)	B5 – 2×10^5 cells/well	(0.25% MTH + media)
A6 – 2×10^5 cells/well	(0.5% MTH + media)	B6 – 2×10^5 cells/well	(0.5% MTH + media)
A7 – 2×10^5 cells/well	(1.0% MTH + media)	B7 – 2×10^5 cells/well	(1.0% MTH + media)
A8 – media only	(media only)	B8 – media only	(media only)

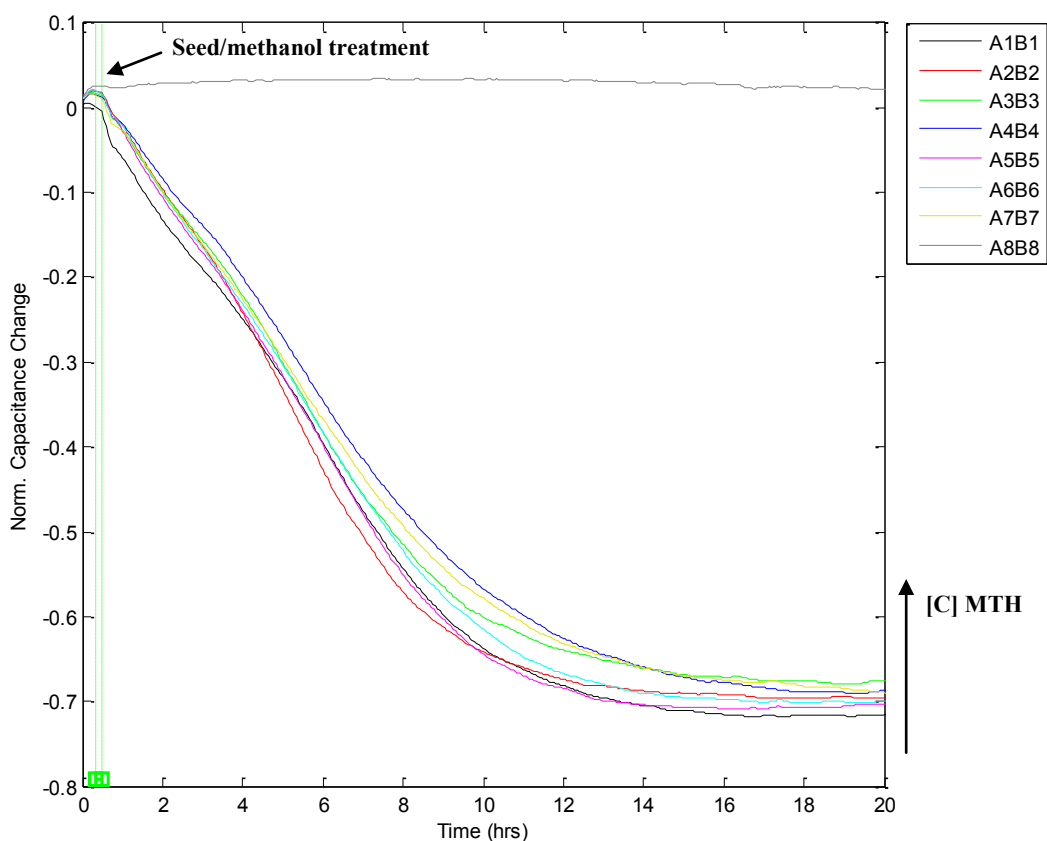


Figure D6.39. $8W10E+$ Second seeding using a final dilution (2×10^5 cells/well) combined with methanol + media treatment (~ 0 hours) *note MTH + media was prepared fresh on day of runs.

Table D6.18. Array seeding density and treatment for array A and B in Figure D6.40.

A1 – 2×10^5 cells/well	(media only)	B1 – 2×10^5 cells/well	(media only)
A2 – 2×10^5 cells/well	(0.01% MTH/10 $\mu\text{g/ml}$ DEP + media)	B2 – 2×10^5 cells/well	(0.01% MTH/10 $\mu\text{g/ml}$ DEP + media)
A3 – 2×10^5 cells/well	(0.025% MTH/25 $\mu\text{g/ml}$ DEP + media)	B3 – 2×10^5 cells/well	(0.025% MTH/25 $\mu\text{g/ml}$ DEP + media)
A4 – 2×10^5 cells/well	(0.1% MTH/100 $\mu\text{g/ml}$ DEP + media)	B4 – 2×10^5 cells/well	(0.1% MTH/100 $\mu\text{g/ml}$ DEP + media)
A5 – 2×10^5 cells/well	(0.25% MTH/250 $\mu\text{g/ml}$ DEP + media)	B5 – 2×10^5 cells/well	(0.25% MTH/250 $\mu\text{g/ml}$ DEP + media)
A6 – 2×10^5 cells/well	(0.5% MTH/500 $\mu\text{g/ml}$ DEP + media)	B6 – 2×10^5 cells/well	(0.5% MTH/500 $\mu\text{g/ml}$ DEP + media)
A7 – 2×10^5 cells/well	(1.0% MTH/1000 $\mu\text{g/ml}$ DEP + media)	B7 – 2×10^5 cells/well	(1.0% MTH/1000 $\mu\text{g/ml}$ DEP + media)
A8 – media only	(media only)	B8 – media only	(media only)

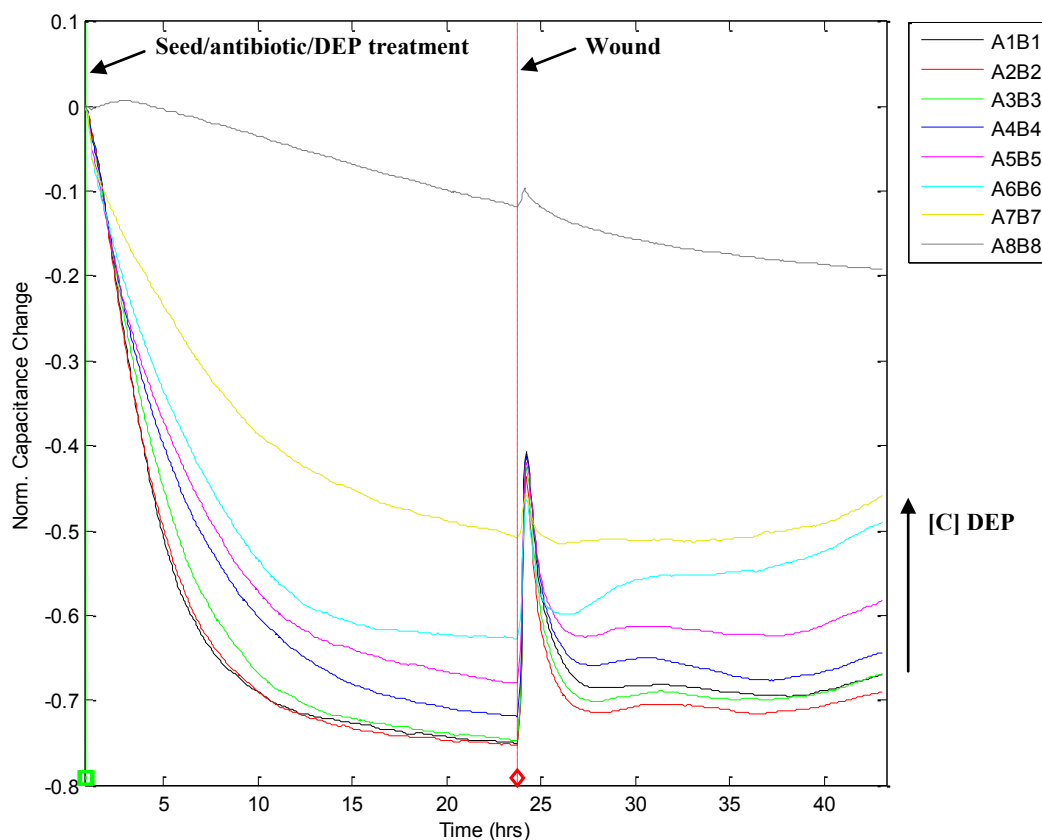


Figure D6.40. A repeat of the suspension/DEP work was performed to verify the concentration and test if media+ antibiotics make a difference in the bacterial contamination of the DEP. Two 8W10E+ arrays each seeded with A549 mixed with DEP, final density of A549 was 2×10^5 cells/well. Density of the DEP treatments is listed in the table below.

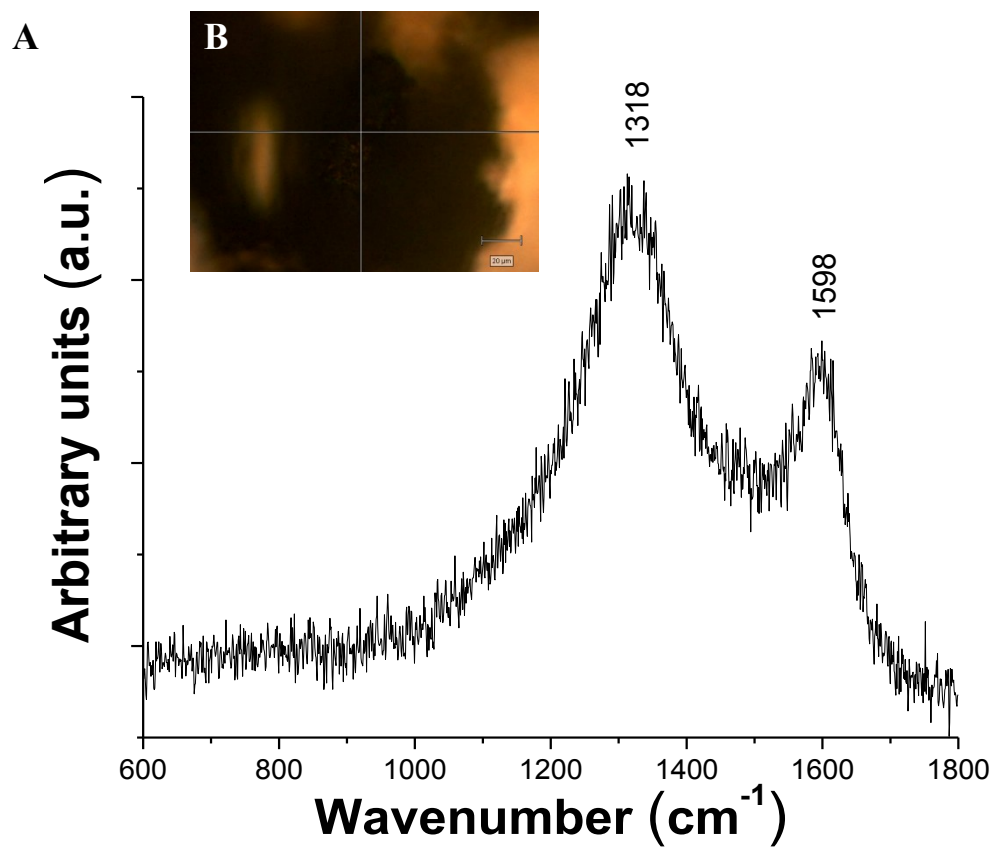


Figure D6.41. Raman spectrum of dry diesel exhaust particles collected over a wavenumber range of 100 – 3200 cm^{-1} at 2.5% laser power for 10 seconds (A). Bright field image of DEP (B). Scale bar = 20 μm .

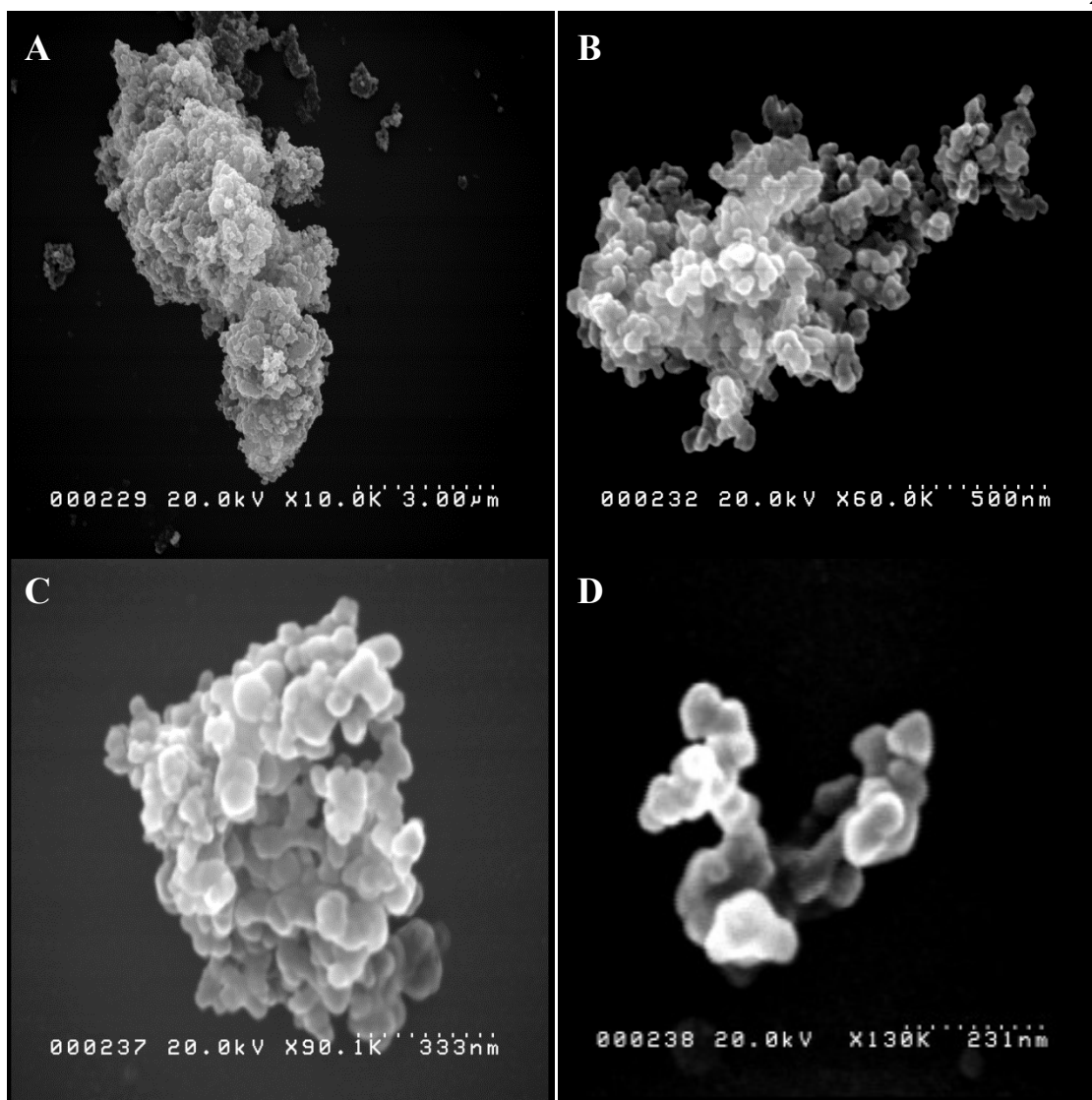


Figure D6.42. SEM images of DEP powder. Micrographs reveal DEP size and morphology. Size of DEP clusters range from 3.0 μm (A), 500 nm (B), 333 nm (C), and 231 nm (D).

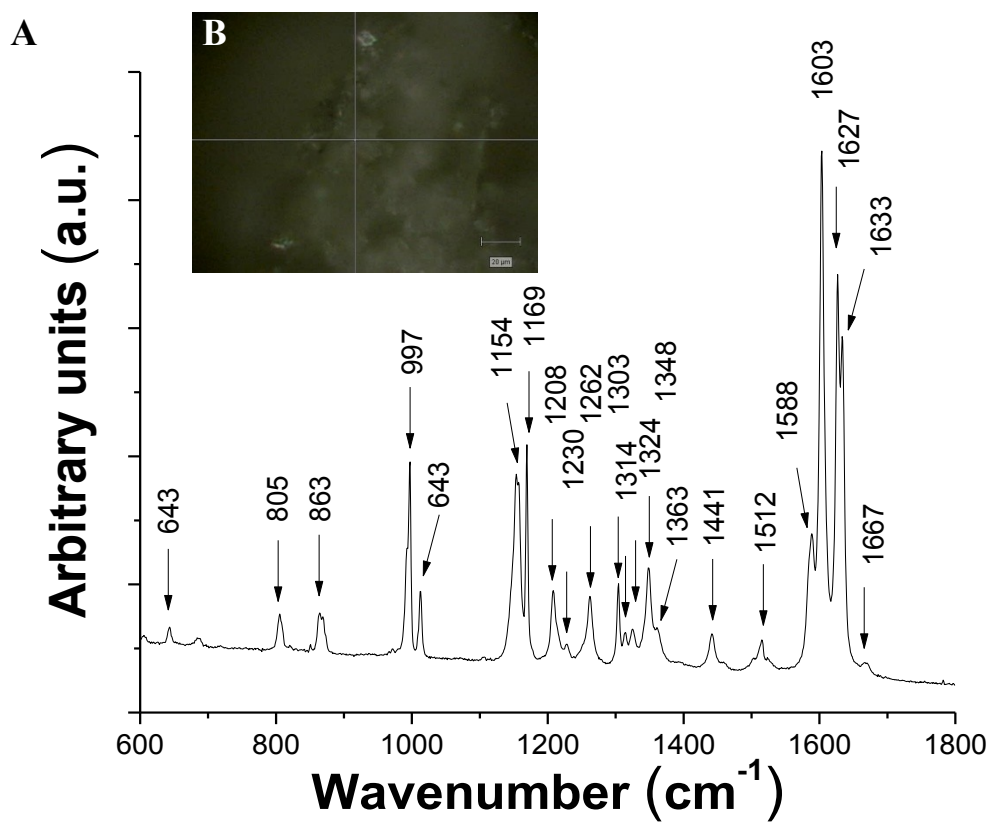


Figure D6.43. Raman spectrum of resveratrol powder collected over a wavenumber range of 200 – 3200 cm^{-1} at 0.5% laser power for 10 seconds (A). Bright field image of resveratrol powder (B). Scale bar = 20 μm .

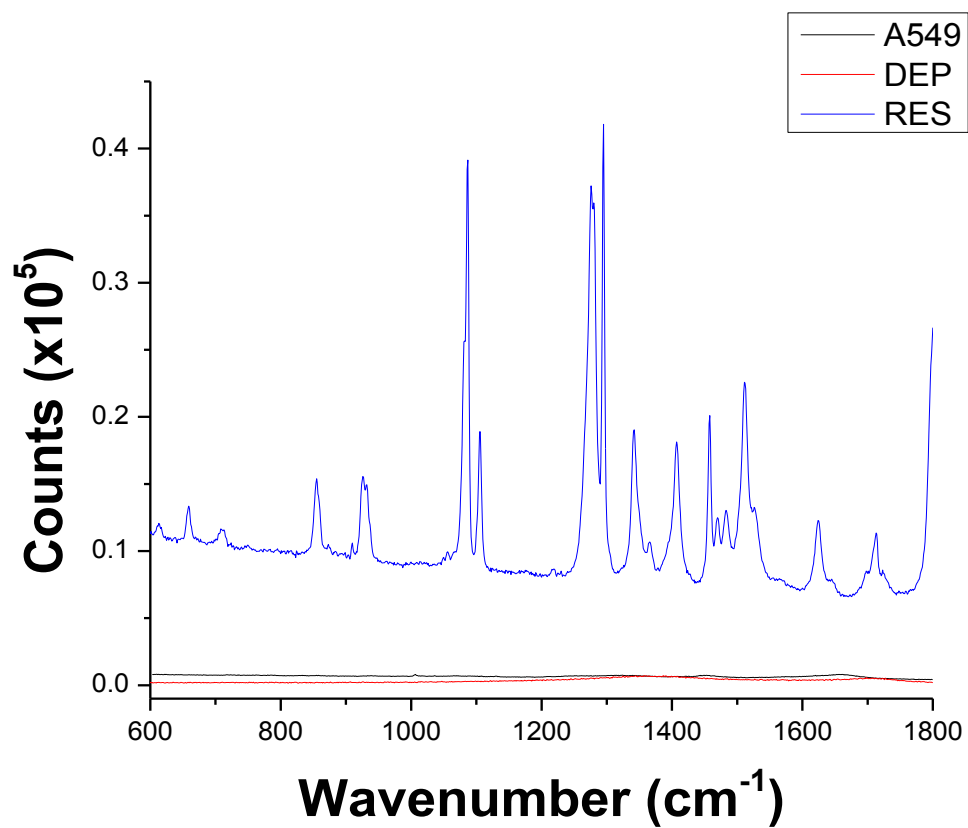


Figure D6.44. Raman spectral overlay of resveratrol powder (blue), DEP (red), and A549 (black). Count intensities are absolute values.

CURRICULUM VITAE

GERALD MCEWEN

gerald.d.mcewen@aggiemail.usu.edu

REFEREED PUBLICATIONS

(symbol * is designated to the corresponding author: IF: impact factor)

1. J. Lin, H. Xu, Y. Wu, M. Tang, **Gerald D. McEwen**, P. Liu, D. R. Hansen, T. A. Gilbertson*, A. Zhou*, *Biosensors and Bioelectronics*, 2012 (in preparation)
2. **Gerald D. McEwen**, Y. Wu, M. Tang, X. Qi, Z. Xiao, S. M. Baker, T. Yu, T. A. Gilbertson, D. B. DeWald, A. Zhou*, "Subcellular Spectroscopic Markers, Topography and Nanomechanics of Human Lung Cancer and Breast Cancer Cells Examined by Combined Confocal Raman microspectroscopy and Atomic Force Microscopy", *Analytica Chimica Acta*, (in-preparation)
3. M. Tang, **Gerald D. McEwen**, Y. Wu, C. D. Miller, A. Zhou*, "Characterization and analysis of Gram-positive and Gram-negative bacteria and co-culture mixtures by Raman microspectroscopy, FTIR, and atomic force microscopy" *Journal of Raman Spectroscopy* (in-preparation)
4. Y. Wu, **Gerald D. McEwen**, S. Harihar, S. M. Baker, D.B. DeWald, A. Zhou*, "BRMS1 expression alters the ultrastructural, biomechanical and biochemical properties of MDA-MB-435 human breast carcinoma cells: an AFM and Raman Microspectroscopy study", *Cancer Letters* 293 (2010) 82-89. (IF: 3.5)
(note: the first two authors contribute equally to this work)
5. **Gerald D. McEwen**, Y. Wu, and A. Zhou*, "Probing nanostructures of bacterial extracellular polymeric substances versus culture time by Raman microspectroscopy and atomic force microscopy", *Biopolymers* 93 (2010) 171-177. (IF: 2.8)
(note: this work was cited and reported by a large website SpectroscopyNow.com which has millions of subscribers all around the world)
6. N. Zaveri, **Gerald D. McEwen**, R. Karpagavalli, and A. Zhou*, "Biocorrosion Studies of TiO₂ Nanoparticle Coated Ti-6Al-4V Implant in Simulated Biofluids", *Journal of Nanoparticle Research*, 12 (2010) 1609-1623 (IF: 2.3)
7. **Gerald D. McEwen**, F. Chen, and A. Zhou*, "Immobilization, hybridization, and oxidation of synthetic DNA on gold surface: electron transfer investigated by electrochemistry and scanning tunneling microscopy", *Analytica Chimica Acta*, 643 (2009) 26-37. (IF: 3.1)

PROCEEDING PAPER

1. Y. Wu, **Gerald D. McEwen**, S. M. Baker, T. Yu, T. A. Gilbertson, D. B. DeWald, A. Zhou*, "Topography, Nanomechanics, and Cell Surface Components of Cancer Cells Examined by Combined Atomic Force Microscopy and Raman Microspectroscopy", Proc. SPIE, Vol. 7568, 75681T (2010); doi:10.1117/12.843098

BOOK CHAPTER

1. A.H. Zhou, **Gerald D. McEwen**, and Y.Z. Wu, "*Combined AFM/Raman microspectroscopy for characterization of living cells in near physiological conditions*" in: A. Méndez-Vilas and J. Díaz (Eds.), Microscopy Book Series - Volume # 4: Microscopy: Science, Technology, Applications and Education, Formatex Research Center, Badajoz, Spain (March, 2011).
2. Q. Chen, **Gerald D. McEwen**, N. Zaveri, R. Karpagavalli, and A. Zhou, "Corrosion Resistance of Ti6Al4V with Nanostructured TiO₂ Coatings" in Karthikeyan Subramani and Waqar Ahmed (Eds.), Emerging Nanotechnologies in Dentistry: Materials, Processes, and Applications, Elsevier (Dec, 2011).

LANGUAGES

- English – Native language
- Spanish – Speak, read, and write

EDUCATION

- Ph.D. Biological Engineering**, May 20123.59 GPA
Utah State University, Logan, UT
Thesis: AFM/Raman characterization of Bio-interfaces; molecular, bacteria, and mammalian cells
- B.S. Biological Engineering**, May 2007.....3.5 GPA
Utah State University, Logan, UT
Passed Fundamentals of Engineering Exam (FE) in Oct 2006
- A.S. Associate of Arts**, May 2003 3.75 GPA
Dixie State College, Saint George, UT
Graduated *Cum Laude*

INDUSTRY EXPERIENCE

Jan 2011-Present

Scientist, Cell Culture in the Research and Development Department

Thermo Fisher Scientific, Logan, UT

- Designed experiments to validate genetically engineered cell lines for recombinant protein production
- Measured protein production via colorimetric assay
- Observed cholesterol affinity to storage contain polymer to determine long term storage lose
- Utilized Design of Experiments (DOE) for formulation screening and new product development

Summer 2006

Summer intern in the Process Development Department

Amgen Inc., Longmont, CO

- Innovated a capillary zone electrophoresis protocol to measure protein charge versus pH
- Measured protein mass acetylation by use of high performance liquid chromatography (HPLC) and matrix assisted laser desorption/ionization time-of-flight (MALDI-TOF)
- Observed standards for Good Laboratory Practice (GLP) in an industrial laboratory setting
- Utilized Laboratory Information Management Systems (LIMS) for order supplies and training
- Collaborated in a team setting to troubleshoot instrumental/experimental issues

TEACHING EXPERIENCE

Sept. 2005-May 2010

Teaching Assistant for Bioinstrumentation Laboratory Section (BIE 3000)

Department of Biological and Irrigation Engineering, Utah State University, Logan, UT

- Created a protocol and instrumental setup for an electrocardiography laboratory module
- Developed another protocol and setup for an electroencephalography laboratory module
- Prearranged each laboratory session prior to instructing students during lab sessions
- Composed and modified laboratory protocols as needed to increase student efficiency and understanding
- Assisted students, one-on-one, in troubleshooting and performing experiments (note: with my input, this course has received very positive feedback to these hands-on lab modules)

Feb. 2005-May 2010

Teaching Assistant for Biosensors Laboratory Section (BIE 5910)

Department of Biological and Irrigation Engineering, Utah State University, Logan, UT

- Instructed an overview of laboratory requirements and illustrated an example laboratory report
- Demonstrated the use of surface plasmon resonance (SPR) and electrochemical analysis detectors
- Pre-performed and setup the laboratory equipment for each laboratory session
- Assisted students in troubleshooting and understanding experiments and theory

CONFERENCE PRESENTATIONS (6 PODIUMS + 16 POSTERS)

PODIUMS

1. **Gerald D. McEwen**, C. B. Bitner, K. Johnson, and M. E. Wight, “Design of Experiment Methodologies to Optimize Custom Cell Culture Medium for Increased Protein Quantity and Quality”, *Fourth Annual Institute of Biological Engineering (IBE) Regional Conference*, Engineering Building, USU, October 28, 2011. (*note: 2nd place award* in student presentation competition)
2. **Gerald D. McEwen**, Y. Wu, T. Yu, T. A. Gilbertson, R. A. Coulombe, Jr, A. Zhou, “Diesel exhaust particle toxicity to human lung cells: a study of cellular biochemical components and biomechanical alterations”, *2010 Intermountain Graduate Research Symposium*. Eccles Conference Center, Utah State University, Logan, Utah. March 31, 2010. (*note: 1st place award* in student presentation competition)
3. **Gerald D. McEwen** and A. Zhou, “Surface Enhanced Raman Spectroscopy (SERS) Characterization of Mycobacteria – A new twist on an emerging technique”, *Second Annual Institute of Biological Engineering (IBE) Regional Conference*, Merrill-Cazier Library, USU, December 4, 2009.
4. **Gerald D. McEwen**, F. Chen, and A. Zhou. “Electron Transfer (ET) Characteristics of ssDNA, hybridized dsDNA, and Oxidatively Damaged dsDNA on Gold Surface: Electrochemistry and Scanning Tunneling Microscopy (STM) Studies.” The Tenth World Congress on Biosensors. Shanghai International Convention Centre, Shanghai, China. May 14-16, 2008.
5. **Gerald D. McEwen**, A. Zhou. “Electron Transfer via Self-Assembled Monolayer (SAM) of Immobilized DNA on a Gold Electrode Surface.” *11th Annual Intermountain Graduate Student Research Symposium*. Taggart Student Center, Utah State University, Logan, Utah. April 2, 2008. (*note: 1st place award* in student presentation competition)
6. **Gerald D. McEwen** and A. Zhou, "Surface Enhanced Raman Spectroscopy (SERS) Characterization of Mycobacteria", *Graduate Student Support Program (CIBR)*, Center for Integrated Biosystems, USU, Nov 19th, 2008.

POSTERS

1. K. Johnson, **Gerald D. McEwen**, C. Bitner, and M. Wight, "Employing Design of Experiments During Custom Media Development to Increase Protein Quantity and Quality", *Bioprocess International Conference and Exhibition*, Long Beach, California, November 1 – 4, 2011.
2. **Gerald D. McEwen**, Y. Wu, T. Yu, S. Baker, T. A. Gilbertson, D. B. DeWald, A. Zhou, "Topography, Biomechanics, and Chemical Components of Human Cancer Cell Membranes Examined by Combined Atomic Force Microscopy and Raman Microspectroscopy", *2010 Intermountain Graduate Research Symposium*. Taggart Student Center, Utah State University, Logan, Utah. March 31, 2010.
3. A. Zhou, **Gerald D. McEwen**, Y. Wu, T. Yu, T. A. Gilbertson, R. A. Coulombe, Jr, "Toxicity effect of diesel exhaust particles on biomechanics and cell surface biopolymers of human lung carcinoma epithelial cells A549: preliminary study by Atomic Force Microscopy/Raman microspectroscopy", *49th Annual Meeting of the Society of Toxicology (SOT)*, Salt Lake City, Utah, March 7-11, 2010.
4. Y. Wu, **Gerald D. McEwen**, S. Baker, T. Yu, T. A. Gilbertson, D. B. DeWald, A. Zhou, "Topography, Biomechanics, and Chemical Components of Cancer Cell Membranes Exploited by Combined Atomic Force Microscopy and Raman Microspectroscopy", *SPIE Photonics West BiOS 2010*, San Francisco, California, 23 - 28 January 2010.
5. Y. Wu, A. Zhou, **Gerald D. McEwen**, C.D. Miller, R.C. Sims, T. Kar, "Real-time observation of cellular biomechanics of Ethambutol treated *M. JLS* using AFM/Raman", *2009 BMES Annual Meeting*, Pittsburgh, PA, October 7-10, 2009.
6. M. L. Davis, **Gerald D. McEwen**, A. Zhou, "Study of the effects of Magnesium ion on the thermal stability of a monomer-excimer molecular beacon that has potential in detection of synthetic DNA of human genotype *Cryptosporidium*", *237th ACS National Meeting & Exposition*, Salt Lake City, UT, March 22-26, 2009.
7. **Gerald D. McEwen**, A. Zhou, "Characterization of Nontuberculous Bioremediation Mycobacteria via Raman Microspectroscopy", *60th Pittsburgh Conference on Analytical Chemistry and Applied Spectroscopy (Pittcon®2009)*, Chicago, IL, USA, March 8-13, 2009.
8. Y. Peng, **Gerald D. McEwen**, A. Zhou, R. Sims, C. Miller, "Comparison analysis of Gram positive and Gram negative bacteria by atomic force microscope and Raman microspectroscopy", *2007 INRA Environmental and Subsurface Science Symposium (ESSS 07), featuring Biotechnology and Bioremediation*, Utah State University, Logan, Utah, July 25th ~ 27th, 2007.
9. **Gerald D. McEwen**, E. Griffiths, G. Olsen, A. Zhou, and T. Gilbertson, "Bio-Impedance Multi-Sensor Array to Test Cell Response in Real-Time", *2007 Annual Meeting of Institute of Biological Engineering (IBE)*, St. Louis, Missouri, March 30-April 1, 2007.
10. **Gerald D. McEwen**, E. Griffiths, G. Olsen, A. Zhou, and T. Gilbertson, "Multi-Sensor Array for Real Time Monitoring Cellular Apoptosis", *Undergraduate Research Day at the State Capitol*, Salt Lake City, January 16, 2007.

11. **Gerald D. McEwen**, E. Griffiths, G. Olsen, A. Zhou, and T. Gilbertson, "Multi-Sensor Bio Sensor Bio-impedance Array for Real impedance Array for Real-Time Monitoring of Cellular Relative Volume Change and Viability of Cellular Relative Volume Change and Viability", *Utah Conference on Undergraduate Research (UCUR)*, Olpin Student Union, University of Utah, February 2, 2007.
12. F. Chen, Y. Wang, **Gerald D. McEwen**, and A. Zhou, "DNA Hybridization and Oxidative Damage at Gold Surface: Electrochemical Scanning Tunneling Microscopy (STM) Study", *2006 Annual Biomedical Engineering Society*, Chicago, Illinois, Oct 11 - 14, 2006.
13. A. Zhou, **Gerald D. McEwen**, and Y. Wang, "Characterization of Single Nucleotide Polymorphism (SNP) Hybridization of *Cryptosporidium* Pathogen DNA: Electrochemistry, Surface Plasmon Resonance, Scanning Tunneling Microscope, and Fluorescence Spectroscopy/Microscope", *Biosensors 2006 – 9th World Congress on Biosensors*, Toronto, Canada, May 10 – 12, 2006.
14. **Gerald D. McEwen**, M. Grover, A. Zhou, "Investigation of Pathogenic DNA via Electrochemical Surveillance Techniques", *Utah Undergraduate Research Day at the State Capitol*, Salt Lake City, UT, January 26, 2006.
15. **Gerald D. McEwen**, M. Grover, A. Zhou, "Electrochemical and surface plasmon resonance detection of pathogenic DNA", *1st Annual Mountain Biomedical Engineering Conference*, Snowbird, Utah, Sept 16-17, 2005.
16. A. Zhou, M. Grover, **Gerald D. McEwen**, "Studies of pathogen DNA immobilization and hybridization on gold surface: electrochemical and SPR", *2005 Annual Biomedical Engineering Society*, Baltimore, Maryland, Sept 28 – Oct 1st, 2005.